SYNTHESIS OF BIMETALLIC IMMISCIBLE ALLOY NANOPARTICLES THROUGH GREEN AND GAMMA RADIOLYSIS APPROACHES FOR ENVIRONMENTAL REMEDIATION APPLICATIONS

By

SANDRINE KAMDOUM NOUKELAG

A thesis submitted in fulfillment of the requirements for the degree of Doctor of Philosophy in the Department of Physics and Astronomy, Faculty of Natural Sciences, University of the Western Cape

Supervisor: Prof. Malik Maaza

University of South Africa

Co-Supervisor: Prof. Christopher J. Arendse

University of the Western Cape

November 2022

DECLARATION

I, the undersigned, declare that the dissertation which is hereby submitted to the Department of Physics and Astronomy, Faculty of Natural Sciences, University of the Western Cape, for a degree of Doctor of Philosophy is my work except for the citations and it has not been submitted by me elsewhere to another University.

Name: **Sandrine Kamdoum Noukelag**

Signature:

Date: 17-03-2023

DEDICATION

This thesis dissertation is dedicated to God Almighty, to whom I belong and abide.

This journey would not have been possible without His Amazing Grace!

May His Holy Name be praised forever and ever!

ACKNOWLEDGMENTS

KEYWORDS

Bimetallic

Immiscible

Alloy

Nanoparticles

$AgFeO_2$

$ZnFe_2O_4$

Green

Rosemary leaves extract

Gamma radiolysis

Dose and dose rate

Annealing temperature

pH

Volume ratio

Phase diagrams

Crystallinity

Structural

Morphological

Optical

Magnetic behavior

Antimicrobial

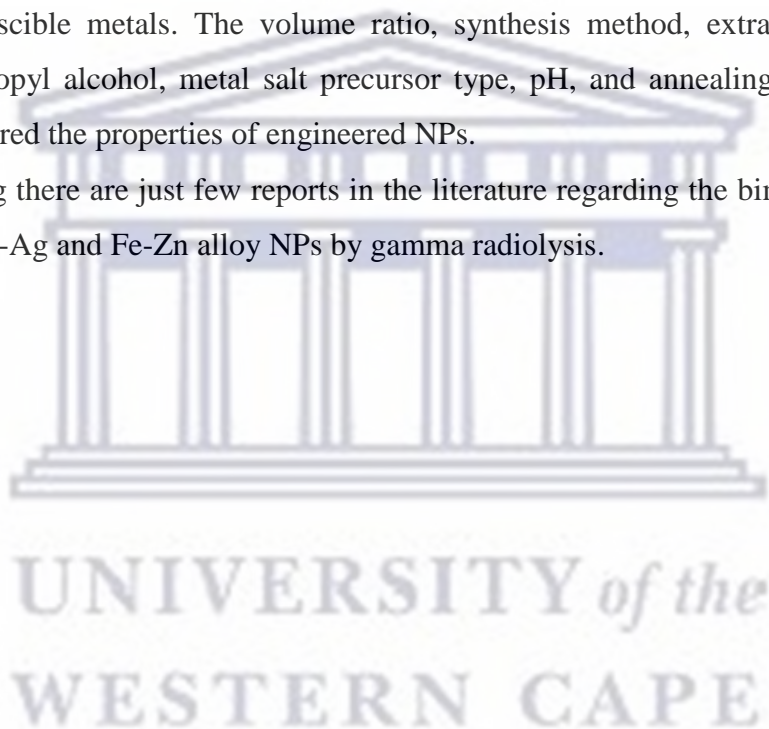Electrochemical

Environmental remediation

ABSTRACT

The synthesis of bimetallic immiscible alloy nanoparticles (NPs) using versatile routes, is a major concern since physio-chemical methods are not environmentally benign. Breaking down the immiscibility would generate NPs with remarkable properties and consequently more applications. As a result, it urges the development of one-step, eco-friendly, efficient, and reliable methods for getting more metastable bimetallic alloys from immiscible metals. To that aim, unconventional approaches such as green and gamma radiolysis were considered as the paths forward in this thesis. The wide immiscibility gaps of iron-silver (Fe-Ag), and iron-zinc (Fe-Zn) led to their selection. From preliminary works completed for both methods, no bimetallic NPs were formed at 25 kGy dose for the gamma radiolysis technique, confirming the literature on this crucial parameter of dose in the synthesis of NPs. Similarly, no bimetallic NPs were produced for the green process at 6 and 5 g of rosemary leaves (RL) in 100 mL of distilled water. The immiscibility was overcome as proof of the concept with green paramagnetic $ZnO/ZnFe_2O_4$ NPs synthesized from the metal salt precursors $ZnCl_2$ and $FeCl_2.4H_2O$ in a basic medium, Fe-Zn [1:2] volume ratio, 2 g of RL extract, annealed under air at 800 °C for 2 hrs 30 min; green paramagnetic $ZnFe_2O_4$ NPs synthesized from $ZnCl_2$ and $FeCl_3.6H_2O$ in an acidic medium, Fe-Zn [2:3] volume ratio, 2 g of RL extract, annealed under air at 800 °C for 2 hrs 30 min; and gamma irradiated superparamagnetic $AgFeO_2$ NPs synthesized from $AgNO_3$ and $Fe(NO_3)_3.9H_2O$ in a basic medium, Fe-Ag [1:7] volume ratio, 10 mL of isopropyl alcohol, at 50 kGy dose. Silver-zinc (Ag-Zn) was introduced as two partially miscible liquids to investigate the potential percentage in which the phase separation may occur. The findings revealed green Ag/ZnO NPs engineered from $AgNO_3$ and $ZnCl_2$ in a basic medium, Ag-Zn [1:9] volume ratio, 2 g of RL extract, annealed under air at 500 °C for 2 hrs, whereas no gamma irradiated Ag/ZnO NPs were engineered at 25 and 50 kGy doses. No magnetic behavior in any Ag-Zn samples by green and gamma radiolysis approaches was perceived as well. Green Ag/ZnO NPs' photocatalytic activities demonstrated their ability to degrade an industrial dye from a clothing company for 100 min. The gamma radiolysis technique did not follow the same protocol since pure Ag/ZnO NPs were not generated.

Gamma irradiated $AgFeO_2$ NPs revealed unique electrochemical properties, which can be utilized to enhance energy storage in devices such as batteries and supercapacitors. In spite of varying different parameters to find out the miscibility, neither green bimetallic alloy Fe-Ag NPs nor gamma irradiated bimetallic alloy Fe-Zn NPs were fabricated. However, green

superparamagnetic Ag/Fe_2O_3 NPs synthesized from $AgNO_3$ and $FeCl_3.6H_2O$ in a basic medium, Fe-Ag [3:1] volume ratio, 2 g of RL extract, annealed under air at 800 °C for 2 hrs, and gamma irradiated ferromagnetic FeO/ZnO NPs synthesized from $FeSO_4.7H_2O$ and $Zn(NO_3)_2.6H_2O$ in an acidic medium, Fe-Zn [1:4] volume ratio, 5 mL of isopropyl alcohol, at 50 kGy dose, both exhibited better antimicrobial activities against spoilage microorganisms *Candida guilliermondii*, *Zygosaccharomyces fermentati*, *Zygosaccharomyces florentinus*, *Penicillium expansum*, *Botrytis cinerea*, and *Alternaria alstroemeria*, whereas green paramagnetic ZnO/Fe_2O_3, $ZnO/ZnFe_2O_4$, and $ZnFe_2O_4$ NPs did not show any antimicrobial activity at all.

Overall, green and gamma radiolysis approaches are versatile for generating bimetallic alloy NPs from immiscible metals. The volume ratio, synthesis method, extract concentration, volume of isopropyl alcohol, metal salt precursor type, pH, and annealing temperature, all considerably altered the properties of engineered NPs.

It is worth noting there are just few reports in the literature regarding the bimetallic synthesis of immiscible Fe-Ag and Fe-Zn alloy NPs by gamma radiolysis.

TABLE OF CONTENTS

x

ABBREVIATIONS

Ag	Silver
ZnO	Zinc oxide
Fe_2O_3	Hematite iron oxide
Fe_3O_4	Magnetite iron oxide
$AgFeO_2$	Silver ferrite
$ZnFe_2O_4$	Zinc ferrite
NPs	Nanoparticles
MNPs	Monometallic nanoparticles
BMNPs	Bimetallic nanoparticles
LET	Linear energy transfer
XRD	X-ray diffraction
FESEM	Field emission scanning electron microscopy
EDS	Energy dispersive X-ray spectroscopy
HRTEM	High resolution transmission electron microscopy
SAED	Selected area electron diffraction
ATR-FTIR	Attenuated total reflection-Fourier transform infra-red
UV-Vis	Ultraviolet Visible
PL	Photoluminescence
VSM	Vibrating sample magnetometer
CV	Cyclic voltammetry
SWV	Square wave voltammetry
EIS	Electrochemical impedance spectroscopy
Rct	Charge transfer resistance
VZI	Volume zone inhibition
CSM	Contaminated solidified media
ACU	Antimicrobial compound used.
RL	Rosemary leaves
DW	Distilled Water
TE	Textile effluent
λ	Wavelength
D	Average crystal size

nm   Nanometer

kGy   Kilogray

Eg   Energy bandgap

CB   Conduction Band

VB   Valence Band

d   Interplanar spacing

θ   Bragg Angle

FWHM   Full Width Half Maximum

FIGURES

TABLES

INTRODUCTION

1.1. Background and Rationale

Environmental remediation pertains to the removal of pollutants or hazardous materials into the environment which is a precious asset to preserve and protect all living organisms for sustainability [1.1]. To ensure the elimination of all sources of pollutants, suitable technologies are required in the biotechnology, nanotechnology and, nanobiotechnology fields.

On the other hand, nanotechnology is evolving at several levels, including materials, devices, and systems. The level of nanomaterials is currently the most advanced, in terms of both scientific knowledge and commercial applications [1.2], because they generate new systems known as nanoparticles (NPs) which are the base of nanotechnology in the nanoworld [1.3]. Those NPs are synthesized via diverse routes for many applications comprising the remediation of harmful wastes, inhibition of spoilage microorganisms' growth, energy storage, and so on.

NPs are defined as objects or materials ranging in size from 1–100 nm with unique properties such as optical, dielectric, electronic, etc., which could not be achievable with the same materials at the macroscopic or bulk level [1.4]. These properties are an open door for innumerable applications in our daily life encompassing energy, healthcare, environment, solar cells, electrochemistry, photocatalysis, agriculture, and so on. Nonetheless, such properties strongly depend on parameters including size, shape, morphology, composition, and surface [1.5]. As a result, it is important to control those parameters using versatile synthesis routes which could boost their properties.

Different types of NPs exist and are categorized as monometallic, inorganic, metal oxides, magnetic, homogeneous or heterogeneous bimetallic, polymer-based or a combination of materials [1.6].

It is noticeable that heterogeneous bimetallic NPs with greater surface area, and an extra degree of freedom, are more fascinating due to novel multifunctional nanomaterials with controlled and desired properties, and applications in different fields arising with synergistic effects between the two metals, which could not be performed with monometallic NPs [1.7, 1.8].

Iron (Fe), nickel (Ni), cobalt (Co) and their corresponding oxides are well-known ferromagnetic NPs which have large surface areas, high thermal stability, and strong mechanical strength. They can be regulated by a magnetic field and are nontoxic [1.9]. Their small diameter in comparison to bulk values, develop novel properties and a broad range of applications in magnetic fluids, catalysis, biotechnology, magnetic resonance imaging, data storage, medicine, and environmental remediation [1.10]. Their magnetic moments during the measurements at room temperature might or might not match up with the applied field. Due to the oxidation state of Fe, magnetic iron and its oxides in particular possess peculiar physiochemical properties, and attractive magnetic features due to their bold magnetic responsiveness. Due to their considerable aggregation, iron oxide NPs such as hematite (α-Fe_2O_3), maghemite (γ-Fe_2O_3), and magnetite (Fe_3O_4) are mostly used [1.10].

Bimetallic NPs based noble metals such as silver (Ag), gold (Au), platinum (Pt), palladium (Pd), and copper (Cu) possess peculiar properties including high melting point, high ionization energy, resistance to corrosion and oxidation, non-reactiveness and miscellaneous applications in various sectors including drug delivery, environmental remediation, antimicrobial activities, water purification, catalysis, which drew the attention of scientific community [1.11, 1.12]. Especially, the size, structure, crystallinity, and morphology of bimetallic NPs constituted of Pt, Ag, and Cu with plasmonic properties, changed during their interactions with visible light which significantly govern their physiochemical properties [1.13].

Ag is most commonly used noble metal due to its high light absorption, excellent electrical conductivity, and uses in catalysis, medicine, and optoelectronics [1.14, 1.15]. Due to their synergistic optical and magnetic properties, plasmonic-magneto materials such as Cu-Fe [1.16], Au-Fe [1.17], and Fe-Ag [1.18], are efficient in therapeutic applications, including thermal treatments (hyperthermia) and drug delivery, imaging diagnostic techniques. On the other hand, the properties of Fe-Ag bimetallic NPs make them excellent candidates for enhancing such applications [1.19, 1.20].

Semiconducting metal oxides like ZnO, CuO, WO_3, SnO_2, NiO, TiO_2, Bi_2O_3, and CeO_2, are of great concern due to their electrical, magnetic, optical, and catalytic properties [1.21]. At the nanoscale level, pure ZnO presents feeble optical characteristics because of defect spots such as oxygen vacancies or interstitial Zn [1.22, 1.23]. Its combination with noble or magnetic NPs engineered bimetallic BMNPs with new optical and magnetic properties and potential uses in photocatalysis, biomedicine and tissue-specific targeting, sensors, energy storage, heavy metal

2

removal, environmental remediation, nanofluids, and so on [1.24, 1.25]. In the semiconductor host, silver or iron is known to be a fast-diffusing compound that alters the lattice structure and thereby affects the related physical properties [1.26].

1.2. Problem Statement

Bimetallic immiscible alloy NPs synthesis is a great concern since the protocol used for their generation does influence their properties, and consequently their applications in multiple domains [1.27]. It is worth noting that conventional methods such as physiochemical are limited when compared to unconventional methods due to the adverse effects presented, such as poor control of particle size and morphology, because the small size of NPs synthesized using eco-friendly techniques, enhances the new and unique properties [1.28]. Additional limitations of conventional routes include high material costs, long synthesis times, poor production rates, high energy demands, defective surface formation, and the need for a vacuum process to evacuate hazardous byproducts [1.29, 1.30].

It upsurges, therefore, a swift need for versatile routes to synthesize bimetallic alloy NPs from immiscible metals in one-step, in-situ, cheap, rapid, reliable, cost-effective, safe, and environmentally friendly without the use of any additional surfactants and/or templates employed with regulated and desired characteristics to properly address the environmental remediation due to pollution caused by harmful wastes derived from residual chemical products.

1.3. Significance of the Research

There are few reports in the literature on the unconventional synthesis of bimetallic alloy NPs from immiscible metals while there are miscelleaneous from miscible metals [1.27]. The bottom-up (green) and top-down (gamma radiolysis) approaches are devised in this thesis to the synthesis of bimetallic alloy NPs from immiscible metals. Both methods are regarded as versatile, one-step, in-situ, clean, and safe.

Green methods based on plant extracts may have an edge over microorganisms because they contain various bioactive compounds that can function as both chelating/reducing and capping agents without the use of additional surfactants. They are ubiquitous, and do not require the

3

technique of creating and sustaining cell cultures. The manufactured particles are shielded from subsequent reactions and aggregation, increasing their stability, longevity, and ease of scale-up [1.31–1.33].

It is easier to control the size, shape, and morphology of NPs in radiolytic methods by optimizing the parameters such as pH, temperature, and dose rate because they influence the properties of final NPs generated due to variations in the nucleation, growth, and aggregation processes during the formation [1.34]. However, the paramount factor is the dose rate [1.35]. Gamma radiolysis is mainly responsible for the metal ions reduction to stable zerovalent metal particles without the use of reducing chemicals [1.36]. The gamma radiation from gamma cells is the best source of ionizing radiation. On the other hand, the results of γ-irradiation reactions are greatly influenced by the irradiation conditions, material type, and irradiation medium.

1.4. Aims and Objectives

The aims of this thesis tend on the one-step synthesis and characterization of bimetallic immiscible alloy NPs with controlled and desired features using versatile methods namely green and gamma radiolysis. The potential applications of resultant NPs encompass the removal of environmental contaminants from nature.

To achieve this target, the specific objectives are defined as follows:

1. Identify suitable conditions to overcome the immiscibility of Fe-Ag and Fe-Zn, and the partial miscibility of Ag-Zn by varying synthesis parameters such as concentration of plant, type of metal salt precursor, volume of isopropyl alcohol, volume ratio, dose and dose rate, pH, and annealing temperature.

2. Assess the magnetic properties and if possible, the mechanism of formation of bimetallic NPs obtained with the bioactive compounds of rosemary leaves extract for the green and isopropyl alcohol for the gamma radiolysis.

3. Interrogate the efficiency of the process in antimicrobial or electrochemical performance to find out whether the green or the gamma radiolysis approach is more suitable for the bimetallic synthesis of immiscible alloy NPs.

4

1.5. Structure of the Work

Chapter One focuses on the general introduction; the problem statement of bimetallic immiscible alloy nanoparticles synthesis; the significance of the research; and the aims and objectives of this thesis.

Chapter Two summarizes the advantages of bimetallic nanoparticles over monometallic nanoparticles; the development of one-step, reliable, cheap, safe, and efficient methods to break down the limitations of traditional approaches; and the importance of green and gamma radiolysis as two versatile methods for generating bimetallic alloy nanoparticles from immiscible metals.

Chapter Three provides the general information on binary phase diagrams and miscibility gaps of Fe-Ag, Ag-Zn, and Fe-Zn based on the literature.

Chapter Four describes the characterization techniques used in this thesis and presents a sneak peek of the different types of magnetic behavior.

Chapter Five exhibits the physical, magnetic, and antimicrobial properties of Fe-Zn and Fe-Ag nanoparticles fabricated via distilled water, green process, and gamma radiolysis routes.

Chapter Six highlights the photocatalytic activities of green Ag-doped ZnO nanoparticles.

Chapter Seven portrays the main physical, magnetic, and electrochemical properties of $AgFeO_2$ nanoparticles obtained by the gamma radiolysis approach at 50 kGy dose.

Chapter Eight depicts the main physical and magnetic properties of biosynthesized ZnO/Fe_2O_3, $ZnO/ZnFe_2O_4$, and $ZnFe_2O_4$ nanoparticles.

Chapter Nine illustrates the antimicrobial performance of gamma irradiated Fe-Zn nanoparticles and the physical properties of gamma irradiated Ag-Zn nanoparticles.

Chapter Ten summarizes the research findings and suggests an open door for further work.

Appendix 1 contains additional information from the preliminary works mentioned in Chapter Nine.

1.6. References

[1.1] R.K. Ibrahim, M. Hayyan, M.A. AlSaadi, A. Hayyan, & S. Ibrahim, Environmental application of nanotechnology: air, soil, and water. Environmental Science and Pollution Research 23 (14), pp. 13754–13788 (2016).

[1.2] H.N. Abdelhamid, Delafossite Nanoparticle as New Functional Materials: Advances in Energy, Nanomedicine and Environmental Applications. Mater. Sci. Forum 832, pp. 28–53 (2015).

[1.3] L. An-Hui, E.L. Salabas, and F. Schüth, Magnetic Nanoparticles: Synthesis, Protection, Functionalization, and Application. Angew. Chem. Int. Ed. 46, pp. 1222–1244 (2007).

[1.4] S. Hasan, A Review on Nanoparticles: Their Synthesis and Types. Research Journal of Recent Sciences 4, pp. 1–3 (2015).

[1.5] G. Sharma, A. Kumar, S. Sharma, M. Naushad, R.P. Dwivedi, Z. Othman, G.T. Mola, Novel development of nanoparticles to bimetallic nanoparticles and their composites: A review. Journal of King Saud University – Science (2017).

[1.6] E. Bosco, P. Rizzi, M. Baricco, Rapid solidification of immiscible alloys. Journal of Magnetism and Magnetic Materials 262, pp. 64–68 (2003).

[1.7] T. Hyeon, "Chemical synthesis of magnetic nanoparticles." Chemical Communications 9 (8), pp. 927– 934 (2003).

[1.8] P. Laokul, V. Amornkitbamrung, S. Seraphin, S. Maensiri, Characterization and magnetic properties of nanocrystalline $CuFe_2O_4$, $NiFe_2O_4$, $ZnFe_2O_4$ powders prepared by the Aloe vera extract solution. Current Applied Physics 11, pp. 101–108 (2011).

[1.9] A. Figuerola, R. Di Corato, L. Manna, T. Pellegrino, From iron oxide nanoparticles towards advanced iron-based inorganic materials designed for biomedical applications. Pharmacol. Res. 62, pp. 126–143 (2010).

[1.10] R.D. Shannon, D.B. Rogers, C.T. Prewitt, Chemistry of Noble Metal Oxides. II. Crystal Structures of $PtCoO_2$, $PdCoO_2$, $CuFeO_2$, and $AgFeO_2$. Inorganic Chemistry 10, pp. 719–723 (1971).

[1.11] J.F. Hund, M.F. Bertino, G. Zhang, C.S. Levantis, N. Lewantis, A.T. Tokuhiro, J. Farmer, Formation and entrapment of noble metal clusters in silica monoliths by gamma radiolysis. J. Phys. Chem. B 107, pp. 465–469 (2003).

[1.12] H.P. Singh, N. Gupta, S.K. Sharma, and R.K. Sharma, "Synthesis of bimetallic Pt–Cu nanoparticles and their application in the reduction of rhodamine B". Colloids and Surfaces A: Physicochemical Engineering Aspects 416, pp. 43– 50 (2013).

[1.13] M.K. Temgire, J. Bellare, and S.S. Joshi, Gamma Radiolytic Formation of Alloyed Ag-Pt Nanocolloids. Advances in Physical Chemistry 2011, 249097, pp. 1–9 (2011).

[1.14] S.I. Thakore, P.S. Nagar, R.N. Jadeja, M. Thounaojam, R.V. Devkar, P.S. Rathore, Sapota fruit latex mediated synthesis of Ag, Cu mono and bimetallic nanoparticles and their in vitro toxicity studies. Arabian Journal of Chemistry (2015).

[1.15] J.L.G. Torresdey, E. Gomez, J.R.P. Videa, J.G. Parsons, H. Troiani, M.J. Yacaman, Alfalfa Sprouts: A Natural Source for the Synthesis of Silver Nanoparticles. Langmuir. 19, pp. 1357–1361 (2003).

[1.16] Z. Han, Y. Dong, S. Dong, Copper- iron bimetal modifies PAN fiber complexes as novel heterogeneous Fenton catalyst for the degradation of organic dye under visible light irradiation. J. Hazard. Mater. 189, pp. 241–248 (2011).

[1.17] Y. Zhai, L. Jin, P. Wang & S. Dong, Dual-Functional Au-Fe$_3$O$_4$ Dumbbell Nanoparticles for Sensitive and Selective Turn-on Fluorescent Detection of Cyanide Based on the Inner Filter Effect. Chemical Communications 47 (29), pp. 8268–8270 (2011).

[1.18] A. Elsukova, L. Zi-An, C. Moller, M. Spasova, M. Acet, M. Farle, M. Kawasaki, P. Ercius, T. Duden, Structure, morphology and aging of Ag–Fe dumbbell nanoparticles. Physica Status Solidi A 208 (10), pp. 2437–2442 (2011).

[1.19] K. Sridharan, T. Endo, C. Sang-Geun, K. Jongryoul, T.J. Park, R. Philip, Single step synthesis and optical limiting properties of Ni–Ag and Fe–Ag bimetallic nanoparticles. Optical Materials 35, pp. 860–867 (2013).

[1.20] K.J. Carroll, D.M. Hudgins, S. Spurgeon, K.M. Kemner, B. Mishra, M. I. Boyanov, L.W. Brown III, M.L. Taheri, and E.E. Carpenter, One-Pot Aqueous Synthesis of Fe and Ag Core/Shell Nanoparticles, Chem. Mater. 22, pp. 6291–6296 (2010).

[1.21] L. Vayssieres, "On the design of advanced metal oxide nanomaterials". International Journal of Nanotechnology 1(1), pp. 1–41 (2004).

[1.22] A. Koli, Biological Synthesis of Stable Zinc Oxide Nanoparticles and its Role as Anti-Diabetic and Anti- Microbial Agents. Int. J. Acad. Res. 2, pp. 139–143 (2015).

[1.23] S. Hameed, J. Iqbal, M. Ali, A.T. Khalil, B.A. Abbasi, M. Numan and Z.K. Shinwari, Green synthesis of zinc nanoparticles through plant extracts: establishing a novel era in cancer theranostics. Mater. Res. Express 6, 102005 (2019).

[1.24] M. Ahmad, J. Zhao, J. Iqbal, W. Miao, L. Xie, R. Mo, J. Zhu, Conductivity enhancement by slight indium doping in ZnO nanowires for optoelectronic applications. Journal of Physics D: Applied Physics 42 (16), pp. 165406-7 (2009).

[1.25] Y. Yan, M.M. Al-Jassim, W. Su-Huai, Doping of ZnO by group-IB elements. Applied Physics Letters 89 (18), 181912 (2006).

[1.26] S. Hosseini, I.A. Sarsari, P. Kameli, H. Salamati, Effect of Ag doping on structural, optical, and photocatalytic properties of ZnO nanoparticles. J. Alloy. Compd. 640, pp. 408–415 (2015).

[1.27] Y.B. Jeong, S.H. Hong, H.J. Park, Y.S. Kim, J.T. Kim, H.D. Lee, Y.J. Hwang, Y.H. Lee, K.B. Kim, Investigation of color change in Cu-Zn alloys by reflectivity and color difference analysis. Korean Journal of Metals and Materials 56 (3), pp. 171–176 (2018).

[1.28] A. Ruíz-Baltazar, R. Esparza, R. Pérez and G. Rosas, Structural Characterization of Fe-Ag Bimetallic Nanoparticles Synthesized by Chemical Reduction. International Research Journal of Pure & Applied Chemistry 4 (3), pp. 263–269 (2014).

[1.29] M. Abbas, B.P. Rao, M.O. Abdel-Hamed, C. Kim, Modified polyol route for synthesis of Fe_3O_4/Ag and α-Fe/Ag nanocomposite. Journal of Alloys and Compounds 615, pp. 308–312 (2014).

[1.30] T. Zargar, A. Kermanpur, Effects of hydrothermal process parameters on the physical, magnetic, and thermal properties of $Zn_{0.3} Fe_{2.7}O_4$ nanoparticles for magnetic hyperthermia applications. Ceramics International 43 (7), pp. 5794–5804 (2017).

[1.31] S. Baker and S. Satish, Endophytes: Toward a Vision in Synthesis of Nanoparticle for Future Therapeutic Agents. Int. J. Bio-Inorg. Hybd. Nanomat. 1 (2), pp. 67–77 (2012).

[1.32] N. Medina-Córdova, R. López-Aguilar, A.I. Campa-Córdova, C. Angulo, Biocontrol activity of the marine yeast Debaryomyces hanseni against phytopathogenic fungi and its ability to inhibit mycotoxins production in maize grain (Zea mays L.) Biol. Control. 97, pp.70–79 (2016).

[1.33] K.S. Kavitha, S. Baker, D. Rakshith, H.U. Kavitha, R.H.C. Yashwantha, B.P. Harini and S. Satish, Plants as Green Source towards Synthesis of Nanoparticles, Int. Res. J. Biol. Sci. 2 (6), pp. 66–76, (2013).

[1.34] D.K. Chmielewska, U. Gryczka, & W. Migdal, Recent patents on creative ionizing radiation in nanotechnology. Recent patents on nanotechnology 2 (3), pp. 201–207 (2008).

[1.35] A. Abedini, F. Larki, E. Saion, A. Zakaria, M. Z. Hussein. Influence of dose and ion concentration on formation of binary Al-Ni alloy nanoclusters. Radiat. Phys. Chem. 81, pp. 1653–1658 (2012).

[1.36] J. Belloni, J. Marignier, M. Mostafavi, Mechanisms of Metal Nanoparticles Nucleation and Growth Studied by Radiolysis. Radiation Physics and Chemistry 169, 107952 (2018).

CHAPTER TWO

LITERATURE REVIEW

2.1. Nanotechnology and Nanoparticles

2.1.1. History and Definition

Nanotechnology is a multifaceted domain because it combines knowledge from various disciplines such as chemistry, physics, and biology. It is referring to a promoting area of nanoscience that includes the synthesis and development of miscellaneous materials from bulk to nanoscale level using convenient techniques [2.1, 2.2].

The basic concept of nanotechnology was introduced by an American physicist and Nobel laureate, Richard P. Feynman, on 29 December 1959, during a yearly meeting presentation of the American Physical Society entitled "There is plenty of space at the bottom". The pioneer of nanotechnology Feynman deciphered how diverse methods transform a specific form of bulk atoms or molecules into a miniature scale (smaller) using different sets of tools, creating nanomaterials atom (molecule) by atom (molecule) to fit in a pamphlet [2.3]. The term "nanotechnology" was coined in 1974 by Norio Taniguchi, a professor at Tokyo Science University, who defined it as "the separation, consolidation, and deformation of materials by a single atom or molecule." His interest in nanotechnology significantly grew up with the published book written by Eric Drexler entitled ''Engines of creation'' wherein he highlighted nanotechnology to the nanometric scale [2.4]. The prefix nano is derived from the Greek word 'nanos', which means "dwarf," and refers to objects of extremely small size, and nanotechnology is defined as the application of controlling the characteristics of the material at the nanoscale level [2.5].

The nanoparticles (NPs) form the basis of nanotechnology and are used in different forms depending on the type of application. NPs are nanometer-sized particles between $1-100nm$ with novel or superior properties unachievable using their conventional bulk materials in different fields and materials engineered at atomic or molecular scale [2.6]. In theory, NPs are formed by the combination of millions of atoms or molecules that can be of the same types or not, amorphous, or crystalline, and their surfaces can act as a carrier for liquid droplets or gases with different properties [2.7].

9

2.1.2. Properties of nanoparticles

Nanotechnology gives a comprehensive sneak peek of the fundamental properties of objects at the atomic, molecular, and supramolecular levels. Because of the predefined superstructures, it is essential in many technological fields by facilitating the manipulation of atoms or molecules and transformation into structures with desired geometry and properties [2.8]. The physiochemical properties of NPs are mainly governed by parameters such as size, shape, surface area, or morphology.

The effect of size on NPs may alter the crystalline structure of the atoms or molecules and change the thermodynamic, electronic, and magnetic properties without changing the composition which is completely different from their bulk counterparts [2.9].

The size reduction also results in an increment in surface area to volume ratio, giving rise to the surface atoms in comparison to those inside. Thereby, smaller particles have more surface area per unit mass than larger particles [2.10]. NPs with high specific surface area, and mechanical strength, are likely to have high surface energy and surface chemistry which is completely different from their bulk form because of the reduction of crystal defects and alteration of thermal, mechanical, electronic, and magnetic properties of NPs. The strength, stiffness, and ductility of nanometer-scale metallic NPs are extraordinarily high, relative to bulk materials which also show favorable functional properties [2.11].

2.1.2.1. Optical properties

As the size of NPs decreases, depending on the type of metal and particle size, NPs absorb the light with a particular wavelength and the interaction of electromagnetic radiation and the electrons in the conduction band (Surface Plasmon Resonance). Different colors are transmitted by NPs [2.12]. Studies on optical spectrum shifts by quantitative and qualitative analyses are possible to perform for more details to describe the phenomenon [2.13].

2.1.2.2. Structural properties

An important feature of NPs is the large specific surface area related to reactivity, solubility, as well as mass, and heat transfer between the particles and their surroundings. More so, the crystal structure of NPs may change with the particle size in diverse instances due to the compressive force exerted on the NPs as a result of the surface tension of the particle itself. Depending on

the nature of the material, the critical particle size of the crystal structure and the size effect could vary significantly [2.14].

2.1.2.3. Thermal properties

Because the atoms and molecules situated at the surface of particles become important in NPs, the melting point of the material is less than the bulk as NPs move more easily at a lower temperature. One of the unique properties of NPs is the reduction of the melting point of ultrafine particles due to the aggregation and grain growth of NPs or enhancement of ceramic material sintering performance. As a result of their free surface and size, nanomaterials' melting points are different from their corresponding bulks [2.15].

2.1.2.4. Mechanical properties

By micronizing the structure of the metal and ceramic material or combining them at the nanoscale level, the hardness of crystalline materials rises with crystalline size reduction, and the mechanical strength of the materials greatly increases [2.16].

2.1.2.5. Electromagnetic properties

Electromagnetic forces prevail once materials are reduced to NPs. The mass of NPs is smaller, and the gravity becomes negligible at such a point that the electromagnetic forces are more predominant than the gravitational force. Electromagnetic properties are important for increasing product performance. The reduction in particle size required to maintain ferroelectric properties is determined by the type and composition of the materials [2.17].

Ferromagnetic fine particles contain a single magnetic domain structure as they become smaller (less than 1 μm approximately) and exhibit superparamagnetic properties. The time it takes for magnetization to disappear depends on particle size, as the magnetization of the material responds to the external magnetic field as a paramagnetic when the particles are smaller. However, it steadily decreases as the particle size grows larger [2.18].

2.1.3. Applications of nanoparticles

NPs have a wide functional diversity and are used in different forms depending on the type of applications [2.19].

2.1.3.1. Human health

Nowadays, nanotechnology is being employed to explore the darkest avenues of medical sciences through numerous pathways such as imaging, sensing, and drug delivery. Thus, organic, and inorganic NPs are drawing great attention in medical applications due to their skill to be biologically functionalized [2.20]. Based on its efficacy, the new generation of drugs is NPs made of polymers, metals, or ceramics that can fight diseases such as cancer [2.21] as well as human pathogens such as bacteria, yeasts, and fungi [2.22, 2.23].

2.1.3.2. Food industries

New applications of nanotechnology have emerged in the food industry such as the use of NPs as micelles, nanoemulsions, cubosomes, liposomes, and the expansion of nanosensors with the target of providing safe food for consumers [2.24]. Furthermore, NPs can selectively bind and detoxify from pathogenic agents in food as well as hazardous chemicals [2.25].

2.1.3.3. Environment

Nanotechnology is useful in the removal of pollutants and germs for water purification. Toxic substances such as heavy metals, nutrients, cyanide, organics, microorganisms, parasites, and antibiotics are detected and removed using nanomaterials. Metal-containing NPs, carbonaceous nanomaterials, zeolites, and dendrimers are being assessed as functional materials for water purification due to their large surface area (surface/volume ratio) [2.26].

2.1.3.4. Energy

Due to the increased need for fossil-fuel-free energy, it is critical to producing solar fuels efficiently. Spencer et al., 2010 created nanocells for fuel generation by grafting light-harvesting molecules to the surface of NPs [2.27]. Nanofluids enhance heat transfer performance. However, due to their large surface area that allows heat transfer, the solid NPs conduct it better than liquid NPs. The smaller the nano-additives such as NPs and nanopowder, the better they can transport heat from solar collectors to storage tanks. By managing charge diffusion and oxidation state, nanomaterials improve power density and durability [2.28].

2.2. Classification of nanoparticles (NPs)

2.2.1. Sources

2.2.1.1. Natural NPs

They are ubiquitous in the environment and are natural resources such as viruses, proteins, antibodies, and so on that can be found in aquatic surface and ground waters [2.29, 2.30]; to natural chemical cyclic systems within the environment manifested by volcanic eruptions, forest fires, dust, storms, meteoritic deterioration, air currents [2.31] involved in solute and trace metal transportation, with chemical groups such as aquatic humic substances (HS) and metal oxides [2.32]; to human activities like quarry materials to exhaust gas, thermal power or cement plant stacks, engine jets or fireworks [2.33, 2.34].

2.2.1.2. Manufactured or Artificial NPs

They hold a great nudge because of the thin size of NPs which fosters an increased specific surface area, leading to excellent properties related to the dominance of quantum effects which change the optical, magnetic, or electrical properties of bulk material that are responsible for the main causes of change in NP behavior [2.35]. They are unintentionally produced as byproducts through mechanical grinding, engine exhaust and smoke, mostly from combustion processes such as diesel engine exhausts and coal-fired power stations [2.35]. They are intentionally engineered through physiochemical or biosynthesis methods in such a way that many different types of structures of NPs are highly produced and predicted to be worth 1.5 trillion US dollars by 2015 [2.36].

2.2.2. Dimensionality

Dimensionally, NPs are classified as zero, one, two or three based on the movement of electrons along the dimension in the NPs [2.37].

2.2.2.1. No dimension (O-D)

The zero-dimensional or no dimension (0-D) NPs have their length, height and breadth fixed at a point 0D, with their electrons in all three directions of space vectors captured in a space that is movable along the x-axis. They are nanorods, nanowires, nanotubes, nanoribbons, quantum dots, nanodots, nanospheres, and nanomaterials whereby most of them are spherical or may be cubic, polygonal or clusters [2.38].

2.2.2.2. One dimension (1-D)

One-dimensional (1-D) NPs exist outside of the nanoscale range, but two spatial vectors are connected to the crucial length scale and the increment is only allowed in the third direction. Their electrons can move along the x-axis. They are typically long but possess a small diameter. For instance, nanowires, nanorods, nanotubes and, nanoribbons [2.39].

2.2.2.3. Two dimensions (2-D)

Two-dimensional (2-D) NPs have two nanostructure dimensions outside the nanometer range and only one vector is connected to the critical length scale, allowing for growth in two spatial directions. They exhibit low dimensional characteristics in comparison with their larger counterparts and possess length and breadth parameters with a unique shape-dependent characteristic movement along the x and y axes. They are nanofilms, nanosheets and, nanowalls [2.34].

2.2.2.4. Three dimensions (3-D)

Three-dimensional (3-D) NPs have three dimensions that are all outside the nanoscale range. Fullerene is an example of bulk material. The electron movement is on the x, y, and z-axes. They are nanoballs (dendritic structures), nanocoils, nanocones, nanopillers and nanoflowers [2.37].
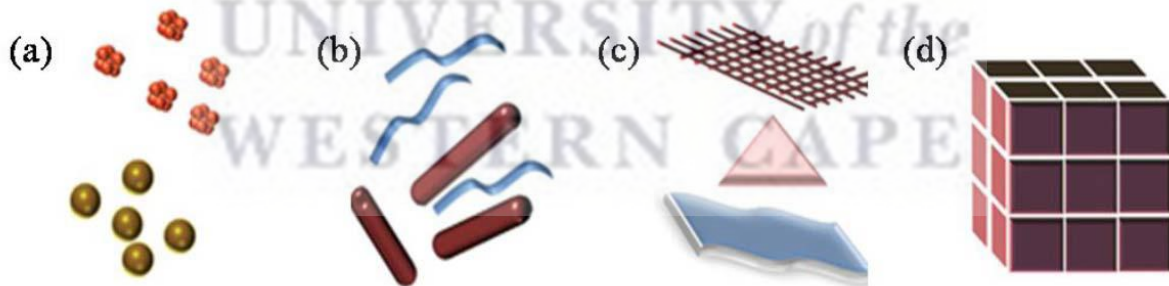
Figure 2.1: (a) 0-D spheres and clusters, (b) 1-D nanofibers, wires, and rods, (c) 2-D films, plates, and networks, (d) 3D nanoparticles [https://nccr.iitm.ac.in/2011.pdf]

2.2.3. Types of nanoparticles (NPs)

2.2.3.1. Monometallic nanoparticles (MNPs)

2.2.3.1.1. Definition and properties

Because of their unique chemical and physical properties, which differ from their materials at the macroscopic level, MNPs have been widely studied. They consist of only single metal existing in different types depending on the metal atom present such as magnetic, metallic, transition metal, metal oxide, and so on [2.40].

Metal and their oxides are very tiny in size. This feature enhances their unique optical and physiochemical properties which can be tuned depending on the subsequent application through different concentrations of salt precursor and the conditions of the reaction [2.41]. The synthesis requires the addition of oxidizing or reducing agents with numeral applications in different areas.

The properties of three metals and their oxides investigated in this thesis, are described in the following sections.

2.2.3.1.2. Iron and iron oxides

The chemical element iron comes from the Latin word *ferrum*, with the symbol Fe, the atomic number 26, and the electronic configuration [Ar] $3d^6\ 4s^2$. It is the most frequent ferromagnetic material, and its properties can be altered by alloying it with other metals and non-metals, particularly carbon and silicon, to form steels [2.42].

Iron oxide is a mineral compound ubiquitous in nature, possessing different structural and magnetic properties [2.43, 2.44]. Eight iron oxides are known, including hematite (α-Fe_2O_3), magnetite (Fe_3O_4), and maghemite (γ-Fe_2O_3) which are the most promising and popular candidates due to their polymorphism including temperature-induced phase transition. Each type has its own set of characteristics and applications [2.45–2.47].

Under ambient conditions, the most stable iron oxide is hematite (α-Fe_2O_3), with a rhombohedral structure and a variety of colors. For instance, black to steel-grey, or brown to red [2.45].

Due to its ferrimagnetic and oxygen stability features with cubic or tetragonal structure, maghemite (γ-Fe_2O_3), the second most stable polymorph of iron oxide, has recently piqued

scientific interest. It is mainly used in the biomedical field due to its magnetism, biocompatibility, and nontoxicity to humans [2.46].

Magnetite (Fe_3O_4) belongs to the spinel ferrite group and is a ferrimagnetic mineral. At high temperatures, it transforms into the alpha phase. Fe_3O_4 is a mixture of one-part FeO and one-part Fe_2O_3, with cubic inverse spinel structure Fe^{3+} ions at A sites (tetrahedral coordination) and Fe^{2+}, Fe^{3+} ions at B sites (octahedral coordination) [2.47].
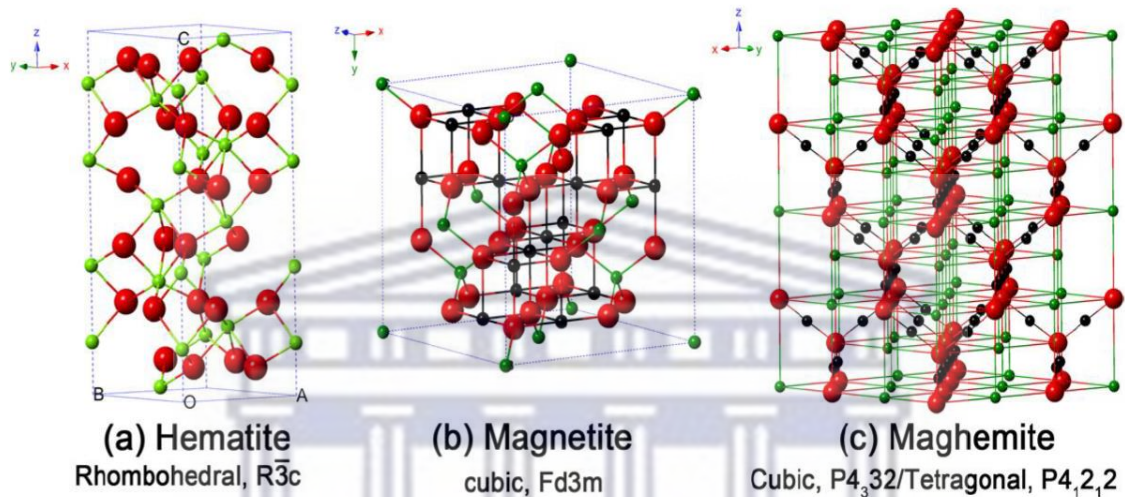
Figure 2.2: Crystal structure of (a) Hematite (α-Fe_2O_3), (b) Magnetite (Fe_3O_4), (c) Maghemite (γ-Fe_2O_3). (The black ball is Fe^{2+}, the green ball is Fe^{3+} and the red ball is O^{2-}) [2.48]

2.2.3.1.3. Silver and silver oxides

Silver (Ag), a gleaming white metallic element that is exceedingly ductile and malleable but is somewhat harder than gold. It is one of the best renowned and most valuable metals on the globe [2.49]. Ag is a durable transition metal because of its rarity (67th in abundance among the elements), and the atomic number of 47, located in the 5th period with an electronic configuration [Kr] $4d^{10}5 s^1$. Naturally, Ag exists as a native element, and as an alloy combined with other metals [2.50].

Silver oxides are AgO, Ag_2O, Ag_2O_3, Ag_3O_4, Ag_4O_3, and Ag_4O_4. As shown in Figure 2.3, AgO is the most thermodynamically stable of them all, with a basic cubic structure at room temperature [2.51].

16
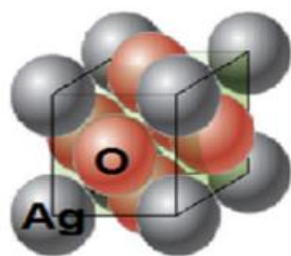
Figure 2.3: Representation of AgO unit cell [2.51]

2.2.3.1.4. Zinc and zinc oxides

Zinc is one of the fifty most abundant elements in the terrestrial crust, accounting for 224 trillion (2.24×10^{14}) metric tons under the dry land, with a concentration of approximately 75 parts per million (ppm) or 0.007 percent [2.52]. It is a transition metal from the fourth period, generally divalent and can donate two outer electrons to form an electrovalent compound, with the electronic configuration [Ar] $3d^{10}4s^2$ [2.53].

In Ancient Greece, ZnO was named *kadmeia* and in Rome *cadmea* nix alba which because of its snow-like appearance. It is a non-toxic semiconductor in the II-VI group with a wide direct band gap energy of 3.37 eV, a broad excitonic binding energy of 60 MeV at room temperature, and the most promising and environmentally friendly material [2.54]. ZnO crystallizes in two major forms, namely hexagonally coordinated wurtzite and tetragonal zinc blende structure. At ambient conditions, wurtzite is the most frequent and thermodynamically stable ZnO structure as depicted in Figure 2.4 [2.55]. The fascinating properties are easily tuned by changing the morphology and applications including polymers, solar cells, ceramics, water purification, cosmetics, biomedical, dielectrics, and electronic materials [2.56].
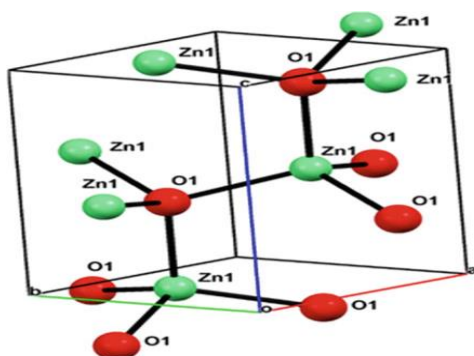
Figure 2.4: Crystal structures of ZnO where red spheres represent oxygen (O) atoms and green spheres represent zinc (Zn) atoms [2.55]

17

2.2.3.2. Bimetallic nanoparticles (BMNPs)

2.2.3.2.1. Definition and properties

As the name implies, BMNPs are two identical or different components. The incorporation of a second metal into the nanoparticle structure alters the size and properties of BMNPs with interesting new properties and a combination of multiple functions far better than pure MNPs due to the synergistic effects [2.57]. BMNPs emerge as a new class of materials and can be improved to great extent unachievable using MNPs [2.58].

2.2.3.2.2. Different structures of BMNPs

Based on structure, BMNPs can be broadly divided into two categories of structures namely mixed and segregated. Segregated structures such as subcluster, core-shell, or a metal core coated by another metal are made up of two independent components with a shared interface whereas mixed structures are achieved through multi-step reactions in which the second metal is introduced after the first metal has developed a structure [2.59].

In terms of atomic ordering, BMNPs can be further divided into four well-defined architectures namely alloys, intermetallic, subclusters, and core-shells, which have drawn impressive regard because of their multiple functionalities and remarkable properties [2.60–2.63] as denoted in Figure 2.5. The electronic effect, which describes charge transfer in bimetallic, is important. An extra degree of freedom is introduced when MNPs are converted to BMNPs [2.64].
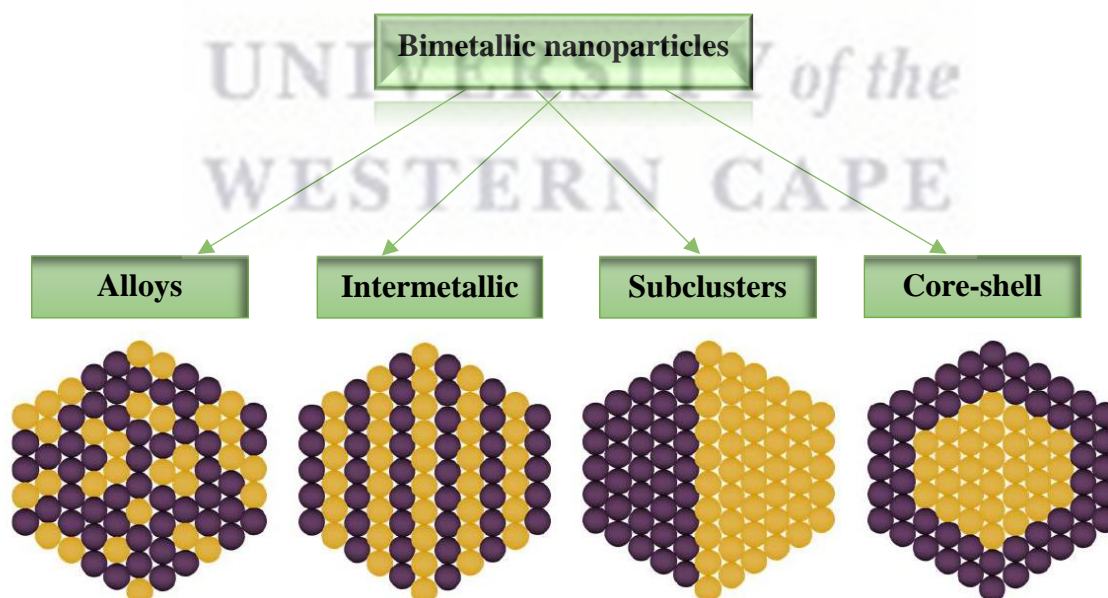
Figure 2.5: Different structures of bimetallic nanoparticles (BMNPs) Yellow and purple spheres represent two different kinds of metal atoms [2.59]

18

Most of the publications concern the synthesis of bimetallic alloy NPs derived from bulk miscible metals (e.g., Pt-Pd, Cu-Pd) whereas study on alloy NPs derived from bulk immiscible metals (e.g., Au-Ni, Ag-Co, Ag-Fe, Ag-Ni, Fe-Cu, Al-Bi, Al-Ni, Fe-Zn) is sparse [2.65]. They are generated when two distinct metal atoms with heterogeneous distributions are randomly arranged in a single particle [2.66].

New alloys in thermodynamic immiscible systems offer outstanding chemical, optical, catalytic, magnetic, mechanical, and tribological properties for material study as well as broad range of applications. Because of their intriguing synergistic properties that cannot be achieved in phase-segregated mixtures, accessing composites within the miscibility gaps is crucial [2.67].

2.3. Methods of synthesis of BMNPs

Figure 2.6 depicted the top-down and bottom-up approaches, commonly explored for the synthesis of BMNPs [2.68]. In top-down (etching, laser ablation, sputtering, thermal decomposition, gamma radiolysis) the bulk materials are broken down into particles at the nanoscale level. However, in the bottom-up (pyrolysis, sol-gel, hydrothermal, sonochemical, co-precipitation, chemical vapor deposition, green process) the fabrication starts from the atomic or molecular level via crystal growth of ions or atoms which are combined to form the bulk material [2.69]. Notably, the bottom-up is more convenient than the top-down because, in the latter, the chances of contamination are enough [2.70].
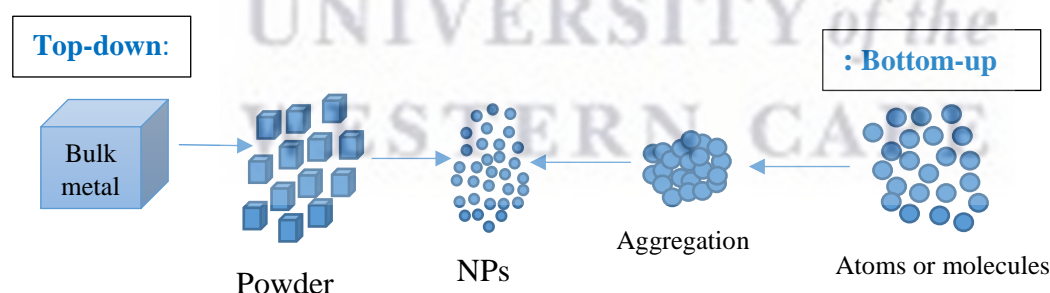
Figure 2.6: Schematic protocol of the synthesis of NPs by top-down and bottom-up approaches

2.3.1. Limits of conventional methods

The method of synthesis may affect the surface morphology, and consequently the properties of BMNPs. Conventional or physiochemical methods are not frequently carried out [2.71, 2.72] because they contain a certain degree of complexity and require high vacuum conditions, costly

19

equipment, high energy, low material conversion, and generate harmful waste from chemical products used during the manufacturing process [2.73].

This thesis develops green and gamma radiolysis approaches to address such issues.

2.3.2. One-Step synthesis reliable and eco-friendly

2.3.2.1. Green synthesis

Nowadays, the green method is an excellent alternative to traditional BMNPs preparation methods. It is an emerging and bright area of research in the scientific world due to its eco-friendliness, reliability, efficacy, benignity, economic prospects, feasibility, and numerous applications [2.74, 2.75].

Plants and microorganisms are primarily employed, and three main steps are involved such as the choice of the solvent, and an eco-friendly benign reducing/capping agent for the stability of BMNPs [2.76, 2.77].

Employing medicinal plants in the preparation of BMNPs, have a burgeoning interest than microorganisms due to the elaboration process time such as intracellular synthesis, consuming process of employing microorganisms and maintaining cell cultures and several purification steps can be omitted [2.78]. They contain a variety of therapeutic compounds including enzymes, proteins, peptides, and polysaccharides that have been utilized in traditional medicine since ancient times and can act as chelating/reducing as well as capping agents in the fabrication, stability, and longevity of BMNPs in large scale production without the use of high temperatures, pressures, energy, toxic chemicals, or non-aseptic environments [2.79].

2.3.2.1.1. Capping agents

They are amphiphilic molecules with a polar head group and a non-polar hydrocarbon tail that confer functionality and improve compatibility with another phase. The non-polar tail interacts with the surrounding medium, whereas the polar head interacts with the nanosystem's metal atom [2.80].

The usage of agricultural wastes or different parts of plants has emerged as their extracts provide natural capping agents free of toxic chemicals via a large range of available phytochemical biomolecules such as alkaloids, terpenoids, phenols, flavonoids, tannins, quinines, carbohydrates, proteins, and coenzyme, among others [2.81]. Those capping agents prevent

20

aggregation during the growth of BMNPs as stabilizers. They enhance the physiochemical properties in a specific way [2.82]. They significantly alter biological activities and environmental perspectives by stabilizing the surface and interface where NPs interact with their medium of preparation [2.83].

2.3.2.1.2. Parameters affecting the process

The production of NPs with desired properties and regulated size, shape, and morphology is dependent on parameters such as plant extract concentration, solvent concentration, metal salt precursor type, concentration, temperature, pressure, pH medium (acidic, basic, or neutral), and contact time [2.84].

Temperature is one of the most significant factors which influences the shape, size, stability, and properties of anisotropic NPs synthesized via a green process. Temperature <100 °C or ambient temperature enhances the nucleation rate and improves the reaction rate with the decrease in size, allowing the use of NPs in diverse fields of applications [2.85, 2.86].

The generation of NPs is governed by pH and molar ratios as well. The size and crystallinity of NPs grow as they increase in the reaction mixture [2.87, 2.88].

Time is another significant factor affecting the fabrication of NPs. According to the reaction mixture, as time advances, a large number of NPs are produced in the medium [2.89]. Besides that, the concentration of plant material, metal salt precursor type, or solvent influences the synthesis of NPs [2.90].

2.3.2.1.3. Plant extracts

Plant parts such as the leaf, root, fruit, flower, seed, latex, pulp, peel, bark, and stem have received great attention as a suitable alternative to traditional synthesis (physical and chemical) because their various extracts can stack many heavy metals into their diverse parts and are constantly explored due to their numerous applications [2.91].

Different parts of plants do not contain the same concentration levels of phytochemicals. The composition of the leaves possesses more phytochemicals than other parts of plants. They are an excellent, benign source for NPs synthesis, and are intensively used for their various applications [2.92, 2.93].

In comparison to fungi and bacteria, which require longer incubation times, the main phytochemicals flavones, terpenoids, sugars, ketones, aldehydes, ascorbic acids, carboxylic acids, and amides within the plant leaf extracts possess an uncanny potential to swiftly reduce metal ions to more stable NPs in a single-step green synthetic method [2.94, 2.95].

The benefits of green synthesis are summarized in Figure 2.7.
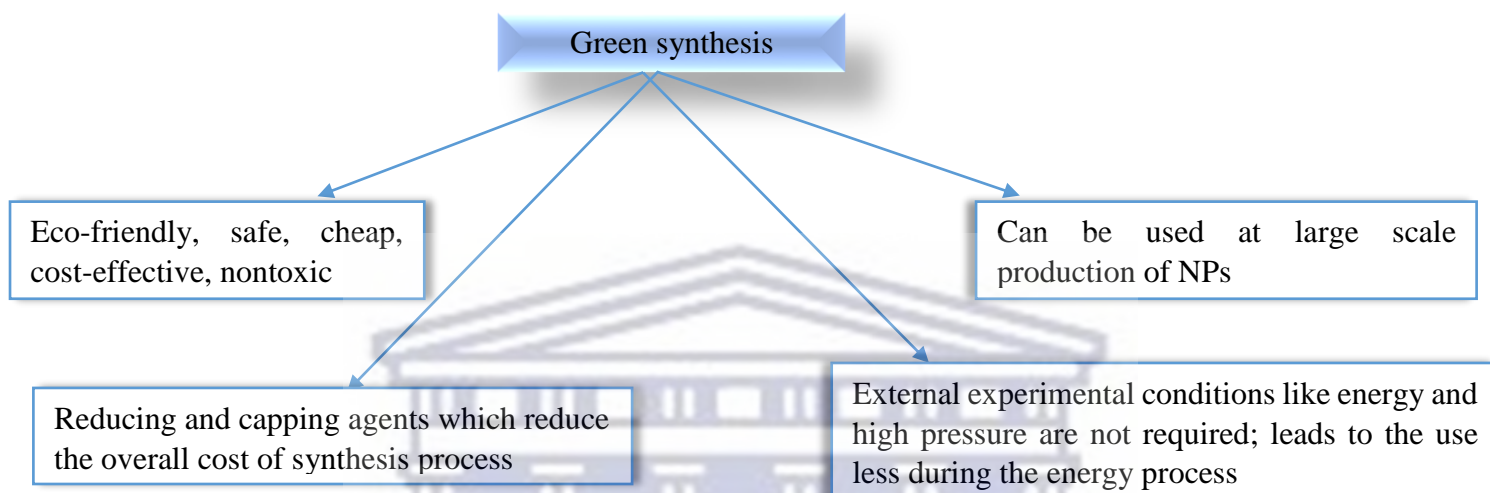
Figure 2.7: Key merits of green synthesis method

Preliminary works have been done in the literature. For instance, Navinchandra et al., 2018 [2.96] and Kulkarni et al., 2017 [2.97] synthesized Ag-Fe$_2$O$_3$ NPs using *Alstonia Scholaris* and *Adathoda vasica* extracts for antibacterial, and antimicrobial/anticancer applications, respectively. Sajjadi et al., 2017 [2.98] synthesized Ag-Fe$_3$O$_4$ NPs using Euphorbia *peplus Linn.* leaf for catalytic activity and Zahra et al., 2022 [2.99] synthesized Ag-Fe$_3$O$_4$ nanocomposite using *Eryngium planum L.* leaf extract for potential applications in the medicine.

In the same line, Hameed et al., 2019 [2.100] and Gurgur et al., 2020 [2.101] synthesized Ag-ZnO NPs using *Valeriana officinalis L.* root, and *Bridelia ferruginea* extracts for biomedical, and biotemplate applications, respectively. Ghosh et al., 2022 [2.102] synthesized ZnO-Ag nanocomposites using *Azadirachta indica* leaf extract for antibacterial activities and photocatalytic effects.

To conclude, Abbas et al., 2020 [2.103] synthesized ZnO/Fe$_2$O$_3$ NPs for antimicrobial activity using *Creeper Blepharis maderaspatensis* extract. Korotkova et al., 2019 [2.104] synthesized ZnO/ZnFe$_2$O$_4$ NPs for environmental remediation using *Petroselinum crispum* extract. Roy et al., 2022 [2.105] synthesized green ZnO@Fe$_3$O$_4$ chitosan-alginate nanocomposite using

22

Camellia sinensis extract for removal of acid violet 7 dye. Madhukara et al., 2019 [2.106] synthesized $ZnFe_2O_4$ NPs using *Limonia acidissima juice* for photocatalytic and antibacterial applications. Sriramulu et al., 2018 [2.107] synthesized $ZnFe_2O_4$ NPs using *Aegle marmelos* leaves for antibacterial activity and drug delivery applications. And Surendra et al., 2019 [2.108] synthesized $ZnFe_2O_4$ NPs using Jatropha extracts for electrochemical sensor, UV photocatalyst and antibacterial activity.

There is no report in the literature so far on the synthesis of Fe-Ag, Ag-Zn, and Fe-Zn NPs using an aqueous extract of *Rosmarinus officinalis* L., commonly known as rosemary [2.109].

An example of green synthesis using plant extract is delineated in Figure 2.8 below.
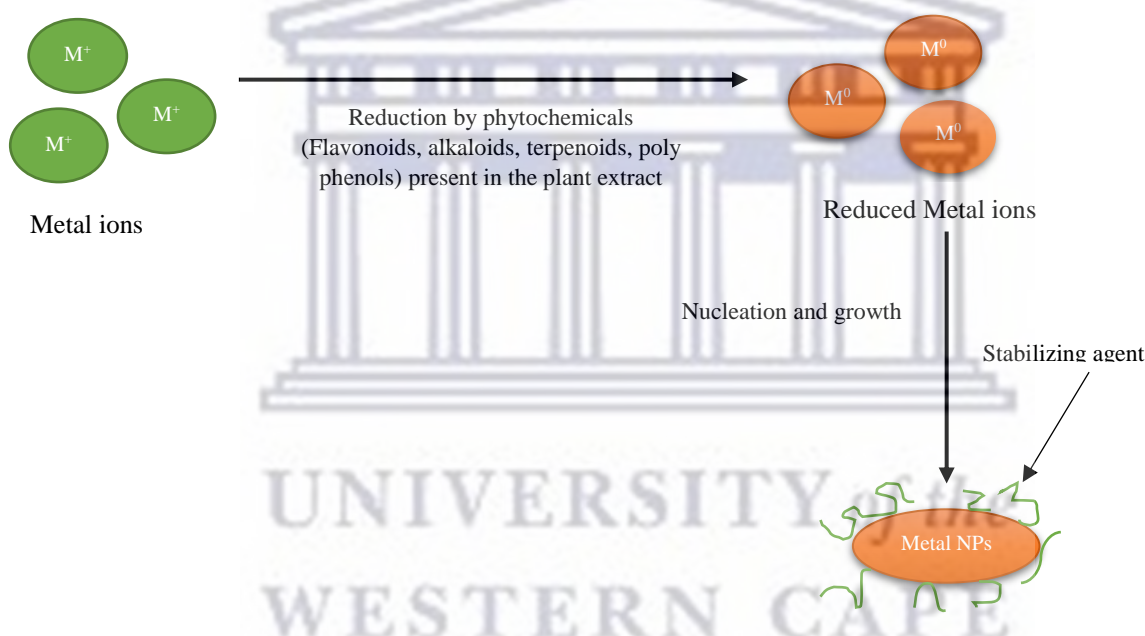
Figure 2.8: Mechanism of NPs formation via bioactive compounds of plant extract [2.110]

2.3.2.1.3.1. *Rosmarinus Officinalis* (rosemary)

2.3.2.1.3.1.1. Origin

The word rosemary comes from the Latin ros-roris (dew) and marinus (sea), which means 'sea dew'. The genus *Rosmarinus* is related to the Greek rhops myrinos, meaning aromatic brush [2.111]. It is made up of three sundry species (*Rosmarinus officinalis*, *Rosmarinus eryocalix*, and *Rosmarinus tomentosus*), all of which are majorly found in the western Mediterranean region, with enclaves on islands in the Aegean Sea and the south of Turkey [2.112].

23

Rosemary is from Labiatae or Lamiaceae family. It is a perennial aromatic brush, medicinal, ubiquitous, and culinary plant with hairy stems and spherical glands that grows all over the world [2.113].

The rosemary plant has a lax inflorescence in axillary or cymose verticillasters with 5–15 flowers, a height of up to two meters, and branches full of green leaves that exude a distinctive fragrance. These leaves are mere, linear to lanceolate, downward curved and entire, with a hairless or tomentose rough surface [2.114].

Figure 2.9: Rosemary leaves

2.3.2.1.3.1.2. Composition

The nutrient composition of rosemary reveals a great number of vitamins and minerals. Carnosic acid, carnosol, caffeic acid, chlorogenic acid, monomeric acid, oleanolic acid, rosmarinic acid, ursolic acid, alpha-pinene, camphor, carnosol, eucalyptol, rosmadial, rosmanol, rosmaquinones A and B, secohinokio, and derivatives of eugenol and luteolin are the most studied [2.115]. Phenolics and carotenoids are bioactive components found in rosemary that can abet to boost its outstanding antimutagenic, antibacterial, and chemopreventive properties [2.116]. The important phenolic compounds found are rosmarinic acid, caffeic acid, carnosic acid, and carnosol whereas the main carotenoids found are β-carotene and lutein in rosemary [2.117]. Many factors influence bioactive compound levels including diversity, plant part, edafoclimatic conditions, extraction, and analysis procedures [2.118].

2.3.2.1.3.1.3. Biological properties

Because of the interference between the plant's molecules and the organic systems, medicinal plants such as rosemary have played an important role as the origin of pharmacologically active substances. Besides, the cosmetic and food industries, are endowed by their chemical composition with beneficial properties that meet society's growing demand for natural products

24

[2.119]. Rosemary can be used in cooking as a spice and flavoring, as a natural preservative in the food industry and food packaging, as an ornamental plant, and in the cosmetic industry [2.120]. Its biological properties such as antibacterial [2.121], antifungal [2.122], insecticidal [2.123], anticancer [2.124], anti-spasmolytic [2.125], anti-inflammatory, antinociceptive [2.126], and antioxidant properties [2.127] have made it a potential new therapeutic agent in the prevention and treatment of several diseases such as diabetes, cancer, attenuate asthma, atherosclerosis, cataract, renal colic, hepatotoxicity, peptic ulcer, inflammatory, hypercholesterolemia, oxidative stress, mental fatigue, myocardial blood pressure, ulcer, lipid peroxidation in heart and brain, atherosclerosis, cancer, glycemia, cutaneous allergy, depressive behavior, ischemic heart and cardiovascular [2.128, 2.129] due to its protein, fiber, vitamins, and minerals [2.130, 2.131]. Major phytochemical compounds in rosemary extract are presented in Figure 2.10.
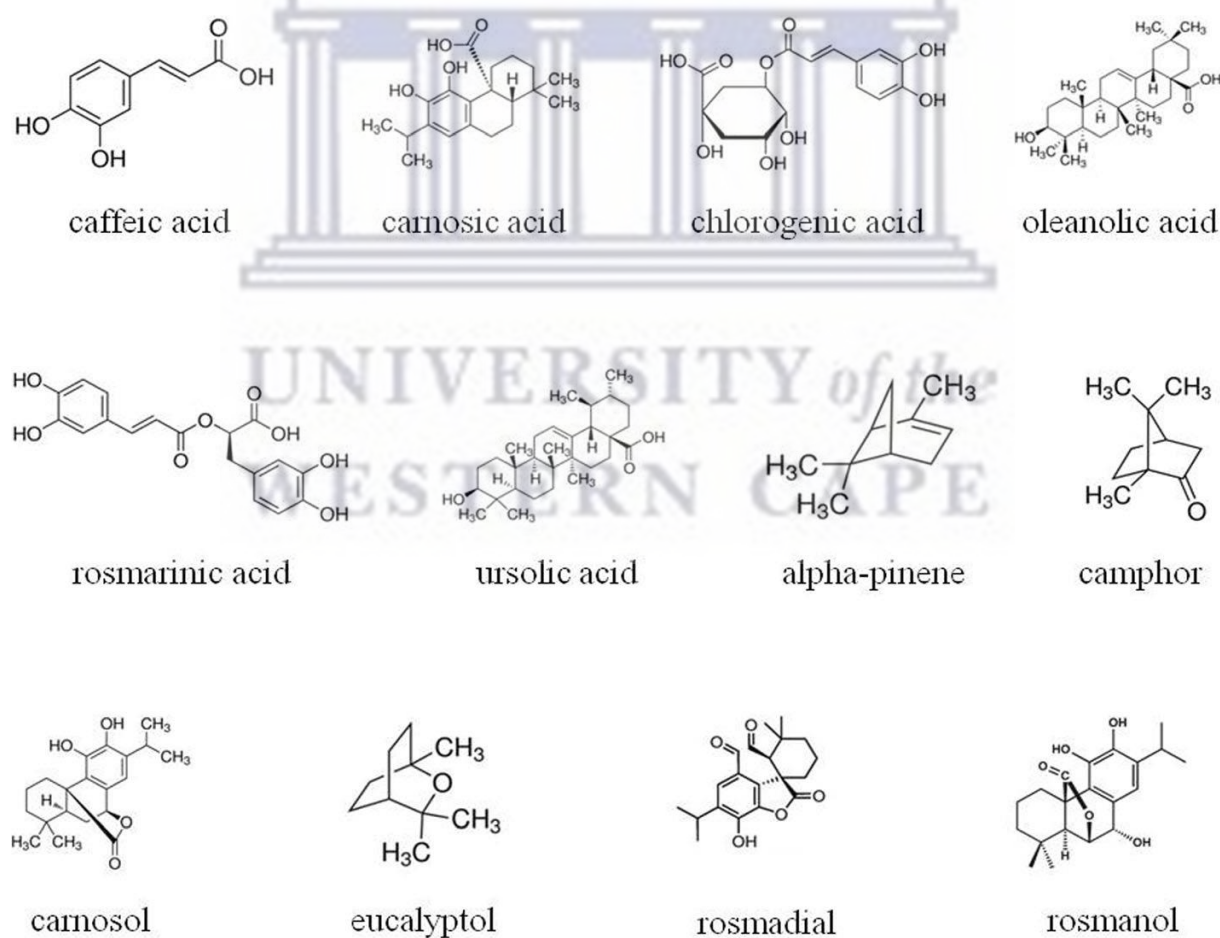
Figure 2.10: Phytochemical compounds present in R. *Officinalis* L. [2.132]

2.3.2.2. Gamma Radiolysis

2.3.2.2.1. Properties, principle, and advantages

Gamma (γ)- radiolysis is primarily responsible for the metal ions reduction to stable zerovalent metal particles without the use of reducing/stabilizing agents of the resulting NPs [2.133]. It is a versatile, one-step, in-situ, clean, low-cost, and efficient technique with a higher yield of BMNPs and less time consumption. Therefore, the process of drying, storage, transportation and, redispersion of NPs are avoided [2.134].

The radiation-induced generation is often performed in an aqueous solution, near room temperature, whereby the reducing radicals generated during the radiolysis of the solvent are used to reduce metal ions. The bombardment of ions with high energy can induce structures not strictly governed by the redox potential of elements [2.135].

A gamma cell irradiation is depicted in Figure 2.11.
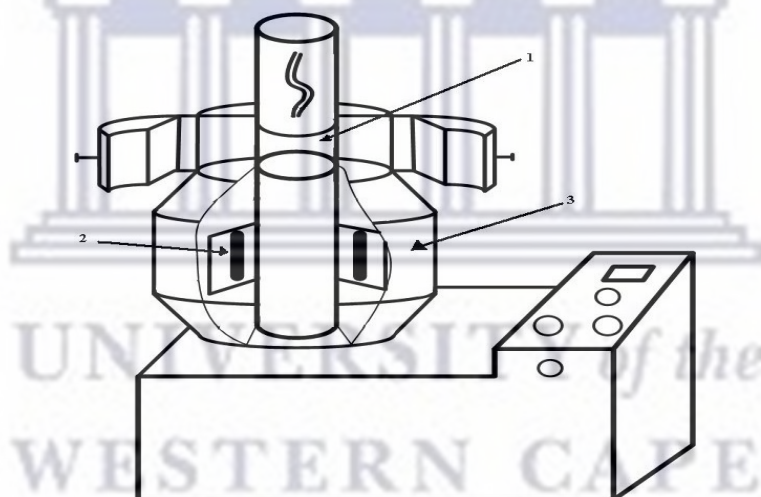
(1): Irradiation room; (2): Rood of ^{60}Co; (3): Surrounding shields of lead

Figure 2.11: Gamma cell irradiation facility type 220 Canadian made [2.136]

There are several advantages to the gamma radiolysis approach for the controlled reduction of metal ions such as (1) no excess reducing agent or undesired oxidation products from the chemical reductant, (2) a well-known reaction's rate because the number of reducing equivalents generated by radiation is well defined and fully determined by the dose deposited in the sample, (3) absorption of the radiation's energy by the solvent (or matrix) without interaction from light-absorbing molecules, (4) quasi-instantaneous (-100 ns) formation of a

26

uniform distribution of the reducing agent in the solution, and (5) large-scale manufacturing potential that can be advantageously set up with satisfying clean production process criteria [2.136].

Table 2.1 portrays electromagnetic radiation including a diverse set of phenomena with TV (television), radio, microwaves, infrared radiation, light, ultraviolet radiation, X-rays, and gamma rays.

Table 2.1: Non-ionizing and ionizing radiations [2.137]

Non-Ionizing (No Electron Removal)	Ionizing (Electron Removal)	
Electromagnetic	Electromagnetic	Particulate
Microwaves	Gamma	Alpha
Infrared	X-ray	Beta
Radar		Neutron
TV		
Radio		

Although there is an energy overlap between gamma and X-ray radiation sources, gamma (γ)-rays are sources of high-frequency electromagnetic radiation with short wavelength, high-energy charged particles, emitted during atomic nucleus deexcitation. Moreover, γ-radiolysis provides the unique opportunity to explore novel materials that are not thermodynamically favorable, and therefore do not form during lower energy synthesis techniques [2.138].

2.3.2.2.2. Linear Energy Transfer (LET)

It is a crucial factor to consider when accounting for NPs synthesized through radiolysis. Irradiation sources are classified based on their LET, which rules the radiolytic yield of reducing species formation and radiation penetration. Low-LET electromagnetic radiation (gamma radiation, UV, accelerated electron beams, and high-energy X-rays) deposits energy discretely along particle paths, whereas high-LET electromagnetic radiation (heavy ions, alpha particles, and neutrons) deposits it densely [2.139].

Another advantage of radiolysis-based NP synthesis is its scalability. Gamma(γ) rays and electrons have low-LET, or energy loss per unit length of the particle path, allowing for larger volumes of material with uniform energy delivered that varies with distance from the source to be irradiated, and thus larger scale synthesis [2.140].

2.3.2.2.3. Different types of sources used for gamma rays

After the 1950s, there was a pressing need to develop nuclear reactors enabling more and more clean radioactive sources among cesium 137 (^{137}Cs), and cobalt 60 (^{60}Co) because they are highly penetrating, pure energy with no mass. Gamma rays from either ^{60}Co or ^{137}Cs are used for the irradiation of high-density and large-volume materials [2.141]. Notably, high-energy gamma-rays ^{60}Co irradiation emitting photons of 1.17 and 1.33 MeV, is considered as an effective method for the synthesis and modification of nanomaterials because γ-irradiation occurs via decay, it is a suitable radiolysis approach that does not require any additional equipment other than those used for shielding [2.142].

Besides, gamma irradiators with ^{60}Co, isotopes produced in nuclear reactors are used as radiation sources and high-energy electrons are produced by accelerators. Furthermore, because ^{60}Co gamma irradiation is highly uniform, the dose and dose rate can be easily controlled and maintained by positioning samples at specific distances from the source when the source is designed as a long cylinder of the appropriate dimensions [2.143].

2.3.2.2.4. Mechanism of formation of NPs via gamma radiolysis

The gamma rays interact with matter in three ways which are photoelectric absorption, Compton scattering, and pair generation, during the formation of nanoparticles using the gamma radiation method [2.144].

Understanding and designing optimal NP reaction conditions that lead to the growth and nucleation of NPs requires research into the mechanism of formation during radiolysis.

The H• and OH• radicals formed by the radiolysis of water molecules indirectly form additional polymer radicals at very high irradiation doses [2.145]. As shown in equation 1, the interaction of ionizing radiation produces secondary electrons in an aqueous solution, forming hydrated electrons (e^-_{aq}), hydroxyl radicals (OH•), and hydrogen radicals (H•) capable of reducing metal cations dissolved in the solution.

$$H_2O \xrightarrow{\text{γ-radiation}} e^-_{aq}, H_3O^+, H^\bullet, H_2, OH^\bullet, H_2O_2 \qquad \text{(Radiolysis of water)} \qquad (1)$$

Solvated electrons (e⁻_aq) are strong reducing agents that can reduce metal ions into their lower state, as shown in equation 2.

$$M^+ + e^- \rightarrow M^0 \qquad \text{(Reduction and nucleation)} \qquad (2a)$$

$$M^{n+} + ne^- \rightarrow M^0 \qquad \text{(Reduction and nucleation)} \qquad (2b)$$

The most frequently used hydroxyl radical scavenger isopropanol, scavenges hydrogen and hydroxyl radicals, producing a secondary radical with high negative potential.

According to equations 3, 4, and 5, the new radical can considerably contribute to more metal ions reduction into their zero-valent state.

$$OH^\bullet + CH_3\text{-}CH(OH)\text{-}CH_3 \rightarrow H_2O + H_3C\text{-}C^\bullet(OH)\text{-}CH_3 \qquad \text{(Radical association)} \qquad (3)$$

$$H^\bullet + CH_3\text{-}CH(OH)\text{-}CH_3 \rightarrow H_2 + H_3C\text{-}C^\bullet(OH)\text{-}CH_3 \qquad \text{(Radical association)} \qquad (4)$$

Thus formed 2-propanol radical can additionally reduce the metal ions:

$$M^0 + M^0 + 2H^\bullet + 2[CH_3\text{-}CH(OH)\text{-}CH_3] \rightarrow 2[H_3C\text{-}C^\bullet(OH)\text{-}CH_3] + M\text{-}M + 2H_2 \qquad \text{(Reduction}$$

and nucleation) $\qquad (5)$
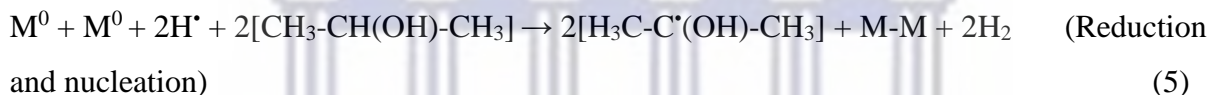
A summary of the formation of NPs and allots is summarized in Figure 2.12 below.
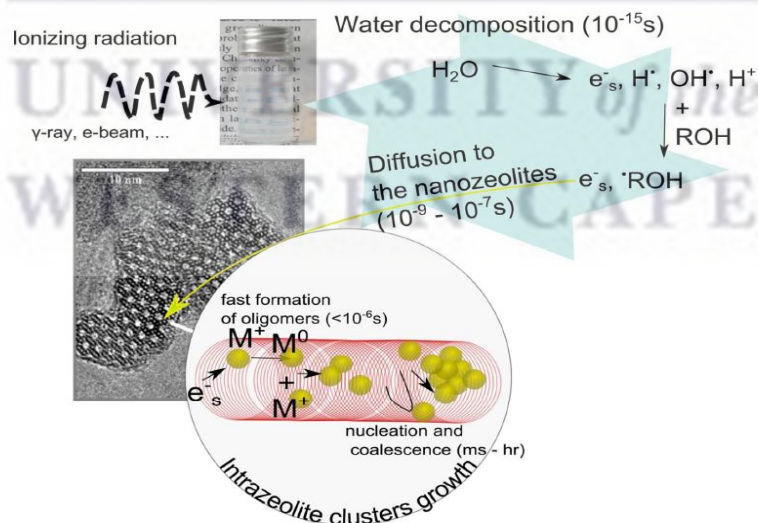
Figure 2.12: Elementary processes and timescales governing the formation of metal and alloy nanoparticles in colloidal suspensions of zeolite nanocrystals [2.146]

2.3.2.2.5. Parameters affecting the process

The results of γ-irradiation reaction highly depend on irradiation conditions namely dose and dose rate, irradiation medium, material type, concentration, metal salt precursors used, solvent type, which significantly influence the composition, crystalline structure, particle size, size distribution, and morphology due to the variation in the nucleation, growth, and aggregation processes in the formation of NPs [2.147, 2.148].

For instance, Wang et al., 2014 [2.149] worked on gamma-ray irradiated $AgFeO_2$ nanoparticles with enhanced gas sensor properties; Abedini et al., 2017 [2.150] developed a two-step process for the synthesis of core-shell ZnO/Ag at 30, 50, and 100 kGy doses; Hammam Abdurabu et al., 2021 [2.151] worked on the synthesis and thermoluminescence characteristics and structural and optical studies of ZnO/Ag/ZnO system for dosimetric applications; Santosh et al., 2020 [2.152] investigated the structural and electrical properties of $ZnFe_2O_4$ prepared by sol-gel combustion technique and irradiated by a gamma-ray source (^{60}Co) to evaluate the modifications on structural and electrical properties.

Overall, there are few reports in the literature on bimetallic Fe-Ag, Fe-Zn, and Ag-Zn NPs regarding the gamma radiolysis approach.

It is well-established that the dose rate is a crucial parameter governing the complex nucleation-growth reactions of NPs [2.153]. Because the reduction is abrupt and faster than any possible inter-metal electron transfer, a high dose rate promotes the formation of numerous nucleation centers and small NPs in a solution with a narrow particle size distribution. At a low dose rate, larger NPs are usually obtained. The structure, size, and shape of these NPs result from an equilibrium between the radiolytic reduction and the electron transfer reaction [2.154]. The design of engineered NPs makes gamma radiolysis relevant for synthesis research and promising applications. The main features of the radiolysis technique are condensed in Table 2.2 below.

Table 2.2: γ-irradiation approach [2.155]

γ-irradiation sources
No harsh reducing agents
Aqueous environment
Room temperature, atmospheric pressure

Control size and morphology by mild scavengers
Specific dose rates
Non-thermodynamically favored NPs
Large scale synthesis

2.3.2.2.6. Possible applications

Gamma radiolysis is an economically viable avenue for developing novel materials and advanced products for different sectors of industry due to the ease of producing NPs on a reasonaby large scale [2.156]. The ability to directly synthesize onto such a large diversity of supports gives a glimpse of the versatility of this technique in designing applications [2.157]. Areas of interest for radiolysis-induced NPs formation include a continuous focus on catalysts by designing alloys with better selectivity for sensors or improved catalytic properties. It may be spread to the areas of medicine and energy as well [2.158].
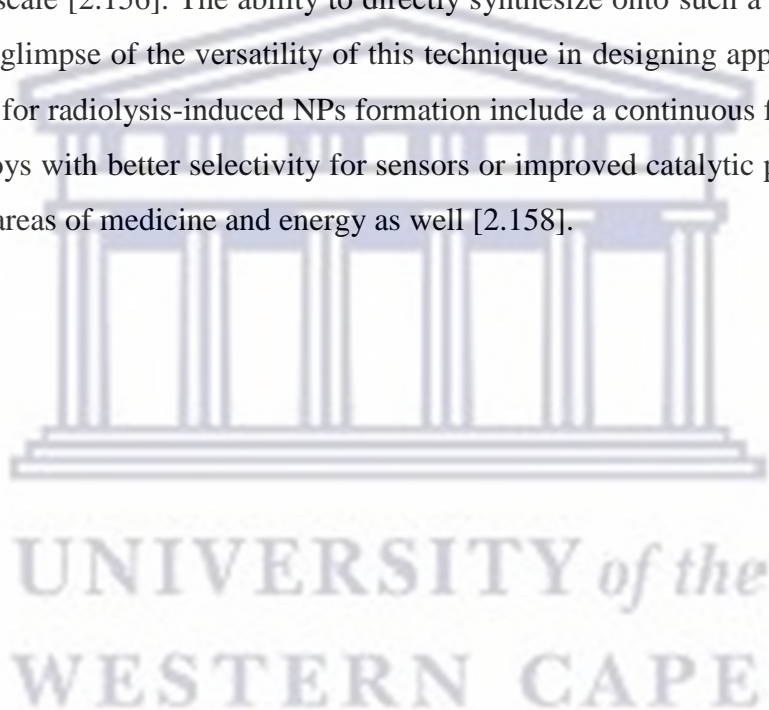
2.4. References

[2.1] M. Nasrollahzadeh, S.M. Sajadi, M. Sajjadi, & Z. Issaabadi, Chapter 1 – An introduction to green nanotechnology. Interface Science and Technology 28, pp. 1–27 (2019).

[2.2] D.T. Dan, Nanotechnology, Nanoparticles and Nanoscience: A New Approach in Chemistry and Life Sciences. Soft Nanoscience Letters 10 (2), pp. 17–26 (2020).

[2.3] M.F. Hochella, There's plenty of room at the bottom: Nanoscience in geochemistry. Geochimica and Cosmochimica Acta 66 (5), pp. 735–743 (2002).

[2.4] M.F. Hochella, M.G. Spencer, & K.L Jones, Nanotechnology: nature's gift or scientists' brainchild? Environmental Science: Nano 2 (2), pp. 114–119 (2015).

[2.5] R. Kumar K. Gupta, N. Bordoloi, Chapter 4 – Nanotechnology: an emerging strategy for combating air pollution. Environmental Sustainability and Industries, pp. 117–128 (2022).

[2.6] A.E. Kestell, & G.T. DeLorey, Nanoparticles: properties, classification, characterization, and fabrication. Hauppauge, New York: Nova Science (2009).

[2.7] M. Auffan, J. Rose, J.Y. Bottero, G.V. Lowry, J.P. Jolivet, and M.R. Wiesner, Towards a definition of inorganic nanoparticles from an environmental, health and safety perspective. Nature Nanotechnology 4 (10), pp. 634–641(2009).

[2.8] T.T.P. O'Brien & N.L. Pickett, Nanocrystalline semiconductors: Synthesis, Properties, and Perspectives. Chem. Mater. 13 (11), pp. 3843–3858 (2001).

[2.9] J. Jellinek, Nanoalloys: tuning properties and characteristics through size and composition. Faraday Discuss. 138, pp. 11–35 (2008).

[2.10] M.A. Neouze, & U. Schubert, Surface modification and functionalization of metal and metal oxide nanoparticles by organic ligands. Monatshefte Für Chemie 139 (3), pp. 183–195 (2008).

[2.11] M. Singh, M. Goyal, K. Devlal, Size and shape effects on the band gap of semiconductor compound nanomaterials. J. Taibah Univ. Sci. 12 (4), pp. 470–475 (2018).

[2.12] P. Mulvaney, Surface Plasmon Spectroscopy of Nanosized Metal Particles. American Chemical Society 12 (3), pp. 788–800 (1996).

[2.13] P. Do-Hyung, S. Kim, The effects of consumer knowledge on message processing of electronic word-of-mouth via online consumer reviews. Electronic Commerce Research and Applications 7 (4), pp. 399–410 (2008).

[2.14] A.A. Khan, M. Javed, A.R. Khan, Y. Iqbal, A. Majeed, S.Z. Hussain, S.K. Durrani, Influence of preparation method on structural, optical and magnetic properties of nickel ferrite nanoparticles. Mater. Sci. Pol. 35 (1), pp. 58–65 (2017).

[2.15] D.S. Srivastava, The role of conservation in expanding biodiversity research. OIKOS 98 (2), pp. 351–360 (2002).

[2.16] T. Hasan, Mechanical properties of nanomaterials: a review. International Journal of Advance Research and Innovative Ideas in Education 2 (4), pp. 1131–1138 (2016).

[2.17] A. Akbarzadeh, M. Samiei and S., Davaran, Magnetic nanoparticles: preparation, physical properties, and applications in biomedicine. Nanoscale Research Letters 7 (1), 144 (2012).

[2.18] T. Matsui, A. Raya, Y. Kawakami, C. Callol-Massot, J. Capdevila, C. Rodriguez-Esteban, B.J.C. Izpisúa, Noncanonical Wnt signaling regulates midline convergence of organ primordia during zebrafish development. Genes Dev. 19 (1), pp. 164–175 (2005).

[2.19] P. Heera, & S. Shanmugam, Nanoparticle characterization and application: an overview. International Journal of Current Microbiology and Applied Science 4 (8), pp. 379–386 (2015).

[2.20] A. Vaseashta & D. Dimova-Malinovska, Nanostructured and nanoscale devices, sensors and detectors. Science and Technology of Advanced Materials. International Conference on Nanotechnology in Environmental Protection and Pollution 6 (3–4), pp. 312–318 (2005).

[2.21] Y. Xu, A. Malhotra, M. Ren, M. Schlame, The enzymatic function of tafazzin. J. Biol. Chem. 281 (51), pp. 39217–39224 (2006).

[2.22] P.K. Stoimenov, R.L. Klinger, G.L. Marchin, and K.J. Klabunde, Metal Oxide Nanoparticles as Bactericidal Agents. American Chemical Society 18 (17), pp. 6679–6686 (2002).

[2.23] A. Panacek, L. Kvítek, R. Prucek, M. Kolar, R. Vecerova, N. Pizúrova, V.K. Sharma, T. Nevecna, R. Zboril, Silver colloid nanoparticles: synthesis, characterization, and their antibacterial activity. J. Phys. Chem B. 110 (33), pp. 16248–16253 (2006).

[2.24] N. Nasongkla, E. Bey, J. Ren, H. Ai, C. Khemtong, J.S. Guthi, S.F. Chin, A.D. Sherry, D.A. Boothman, J. Gao, Multifunctional polymeric micelles as cancer-targeted, MRI-ultrasensitive drug delivery systems. Nano Letters 6 (11), pp. 2427–2430 (2006).

[2.25] M. Esposito, P. Coulthard, P. Thomsen, H.V. Worthington, The role of implant surface modifications, shape and material on the success of osseointegrated dental implants. A Cochrane systematic review. The European journal of prosthodontics and restorative dentistry 13 (1), pp. 15–31 (2005).

[2.26] M. Tiwari, V.K. Bajpai, A.A. Sahasrabuddhe, A. Kumar, R.A. Sinha, S. Behari and M.M. Godbole, Inhibition of N-(4-hydroxyphenyl) retinamide-induced autophagy at a lower dose enhances cell death in malignant glioma cells. Carcinogenesis 29 (3), pp. 600–609 (2008).

[2.27] M.S. Spencer, J. Chen, G.C. Gee, C.G. Fabian, and D.T. Takeuchi, Discrimination and Mental Health–Related Service Use in a National Study of Asian Americans. American Journal of Public Health 100 (12), pp. 2410–2417 (2010).

[2.28] J. Wan, T. Song, C. Flox, J. Yang, Y. Quan-Hong, and X. Han, Advanced Nanomaterials for Energy-Related Applications. Journal of Nanomaterials 2015, Article 564097 (2015).

[2.29] J.R. Lead, D. Muirhead, and C.T. Gibson, Characterization of Freshwater Natural Aquatic Colloids by Atomic Force Microscopy (AFM). Environmental Science & Technology 39 (18), pp. 6930–6936 (2005).

[2.30] J.R. Lead, and K.J. Wilkinson, Aquatic Colloids and Nanoparticles: Current Knowledge and Future Trends. Environmental Chemistry 3 (3), pp. 159–171 (2006).

[2.31] M.F Hochella, D. Mogk, K. Maher. The new earth and environmental nanoscience and technology centers sponsored by NSF. Elements 12 (1), pp. 77–78 (2016).

[2.32] J.R. Lead, J. Hamilton-Taylor, W. Davison, and M. Harper, Trace metal sorption by natural particles and coarse colloids. Geochimica et Cosmochimica Acta 63 (11–12), pp. 1661–1670 (1999).

[2.33] N. Strambeanu, L. Demetrovici, D. Dragos, M. Lungu, Chapter 1. Nanoparticles: definition, classification, general physical properties. In: 'Nanoparticles' Promises and Risks: characterization, manipulation, and potential hazards to humanity and the environment. Cham, pp 3–5 (2015).

[2.34] J. Jeevanandam, A. Barhoum, Y.S. Chan, A. Dufresne, & M.K. Danquah, Review on nanoparticles and nanostructured materials: history, sources, toxicity and regulations. Beilstein Journal of Nanotechnology 9, pp. 1050–1074 (2018).

[2.35] D. Lin, X. Tian, F. Wu, B. Xing, Fate and Transport of Engineered Nanomaterials in the Environment. Journal of Environmental Quality 39 (6), pp. 1896–1908 (2010).

[2.36] R.J. Aitken, M.Q. Chaudhry, A.B.A. Boxall, M. Hull, Manufacture and use of nanomaterials: current status in the UK and global trends. Occupational Medicine 56 (5), pp. 300–306 (2006).

[2.37] I. Khan, K. Saeed, & I. Khan, Nanoparticles: properties, applications and toxicities. Arabian Journal of Chemistry 12 (7), pp. 908–931 (2019).

[2.38] A.N.S. Ealias, & M.P. Saravanakumar, A review on the classification, characterisation, synthesis of nanoparticles and their application. IOP Conference Series: Materials Science and Engineering 263 (3), Article 032019 (2017).

[2.39] S.L. Pal, U. Jana, P.K. Manna, G.P. Mohanta, R. Manavalan, Nanoparticle: An overview of preparation and characterization. Journal of Applied Pharmaceutical Science 01 (06), pp. 228–234 (2011).

[2.40] P. Kuppusamy, M.M. Yusoff, G.P. Maniam, & N. Govindan, Biosynthesis of metallic nanoparticles using plant derivatives and their new avenues in pharmacological applications-An updated report. Saudi Pharmaceutical Journal 24 (4), pp. 473–484 (2016).

[2.41] J. Singh, T. Dutta, K. Ki-Hyun, M. Rawat, P. Samddar and P. Kumar, 'Green' synthesis of metals and their oxide nanoparticles: applications for environmental remediation. J. Nanobiotechnol. 16, 84 (2018).

[2.42] B. Marsalek, D. Jancula, E. Marsalkova, M. Mashlan, K. Safarova, J. Tucek, R. Zboril, Multimodal action and selective toxicity of zerovalent iron nanoparticles against cyanobacteria. Environ. Sci. Technol. 46 (4), pp. 2316–2323 (2012).

[2.43] R.M. Cornell, U. Schwertmann, The Iron Oxides: Structure, Properties, Reactions, Occurrences and Uses. 2nd Edition, Wiley-VCH, Weinheim (2003).

[2.44] H. Guo, & A.S. Barnard, Naturally occurring iron oxide nanoparticles: morphology, surface chemistry and environmental stability. Journal of Material Chemistry A. Materials for Energy and Sustainability 1 (1), pp. 27–42 (2013).

[2.45] L. Machala, J. Tuček, and R. Zbořil, Polymorphous Transformations of Nanometric Iron (III) Oxide: A Review. Chem. Mater. 23 (14), pp. 3255–3272 (2011).

[2.46] P. Katikaneani, A.K. Vaddepally, R.N. Tippana, R. Banavath, & S. Kommu, Phase transformation of iron oxide nanoparticles from hematite to maghemite in presence of polyethylene glycol: application as corrosion resistant nanoparticle paints. Journal of Nanoscience 2016, Article 1328463 (2016).

[2.47] S.M. Abdollah, F. Fereshteh, N. Farhadyar, Synthesis and modification of iron oxide nanoparticles (magnetite) for biomedical applications. Res. J. Biotech. 12 (9), pp. 87–95 (2017).

[2.48] W. Wu, Z. Wu, T. Yu, C. Jiang, K. Woo-Sik, Recent progress on magnetic iron oxide nanoparticles: Synthesis, surface functional strategies and biomedical applications. Science and Technology of Advanced Materials 16 (2), Article 023501 (2015).

[2.49] M.S. Seehra and A.D. Bristow, Introductory Chapter: Overview of the Properties and Applications of Noble and Precious Metals. Noble and Precious Metals – Properties, Nanoscale Effects and Applications. IntechOpen (2018).

[2.50] B. Khodashenas, H.R. Ghorban, Synthesis of silver nanoparticles with different shapes. Arab. J. Chem. 12 (8), pp. 1823–1838 (2015).

[2.51] E.S. Hassan, A.K. Elttayef, S.H. Mostafa, M.H. Salim, S.S. Chiad, Silver oxides nanoparticle in gas sensors applications. Journal of Materials Science: Materials in Electronics 30 (17), pp. 15943–15951 (2019).

[2.52] N. Roohani, R. Hurrell, R. Kelishadi, R. Schulin, Zinc and its importance for human health: An integrative review. J. Res. Med. Sci. 18 (2), pp. 144–157 (2013).

[2.53] K. Kaur, R. Gupta, S.A. Saraf, & S.K. Saraf, Zinc: the metal of life. Comprehensive Reviews in Food Science and Food Safety 13 (4), pp. 358–376 (2014).

[2.54] A. Kołodziejczak-Radzimska, & T. Jesionowski, Zinc oxide–from synthesis to application: A Review. Materials 7 (4), pp. 2833–2881 (2014).

[2.55] P.R.F. Marcelino, M.B. Moreira, T.M. Lacerda and S.S. da Silva, Zinc and Silver Nanoparticles: Properties, Applications and Impact to the Aquatic Environment. Nanomaterials: Ecotoxicity, Safety, and Public Perception. Cham, pp. 167–190 (2018).

[2.56] C. Mayrinck, E. Raphael, J.L. Ferrari, M.A. Schiavon, Síntese, propriedades e aplicações de óxido de zinco nanoestruturado. Revista Virtual de Química 6 (5), pp. 1185–1204 (2014).

[2.57] N. Toshima, T. Yonezawa, Bimetallic Nanoparticles-Novel Materials for Chemical and Physical Applications. New J. Chem. 22, pp. 1179–1201 (1998).

[2.58] Y. Wang, H. Zhao, G. Zhao, Iron-copper bimetallic nanoparticles embedded within ordered mesoporous carbon as effective and stable heterogeneous Fenton catalyst for the degradation of organic contaminants. Appl. Catal. B: Environ. 164, pp. 396–406 (2015).

[2.59] J. Sopoušek, J. Pinkas, P. Brož, J. Buršík, V. Vykoukal, D. Škoda, A. Stýskalík, O. Zobač, J. Vešál, A. Hrdlička, and J. Šimbera, Ag–Cu colloid synthesis: Bimetallic nanoparticle characterization and thermal treatment. J. Nanomater. 2014, Article 638964 (2014).

[2.60] A. Zaleska-Medynska, M. Marchelek, M. Diak, E. Grabowska, Noble Metal-Based Bimetallic Nanoparticles: The Effect of the Structure on the Optical, Catalytic and Photocatalytic Properties. Advances in colloid and interface science 229, pp. 80–107 (2016).

[2.61] J. Gao, X. Ren, D. Chen, F. Tang, J. Ren, Bimetallic Ag-Pt Hollow Nanoparticles: Synthesis and Tunable Surface Plasmon Resonance. Scripta Mater. 57 (8), pp. 687–690 (2007).

[2.62] H. Abdollah, H. Mansor, R. Ebrahimi-Kahrizsangi, M.M. Taghi, Effect of milling atmosphere on structural and magnetic properties of Ni-Zn ferrite nanocrystalline. Chin. Phys. B 24 (4), 048102 (2015).

[2.63] Y. Benguedouar, N. Keghouche, J. Belloni, Structural and magnetic properties of Ni-Pt nanoalloys supported on silica. Mater. Sci. Eng. B 177 (1), pp. 27–33 (2012).

[2.64] Z. Ban, Y.A. Barnakov, F. Li, V.O. Golub, C.J. O'Connor, The synthesis of core–shell iron@gold nanoparticles and their characterization. J. Mater. Chem. 15 (43), pp. 4660–4662 (2005).

[2.65] C. Yang, B.H. Ko, S. Hwang, Z. Liu, Y. Yao, W. Luc, M. Cui, A.S. Malkani, T. Li, X. Wang, J. Dai, B. Xu, G. Wang, D. Su, F. Jiao, L. Hu, Overcoming immiscibility toward bimetallic catalyst library. Sciences Advances 6 (17): eaaz6844 (2020).

[2.66] Z. Swiatkowska-Warkocka, A. Pyatenko, F. Krok, B.R. Jany & M. Marszalek, Synthesis of new metastable nanoalloys of immiscible metals with a pulse laser technique. Scientific reports 5, 9849 (2015).

[2.67] E. Ma, Alloys created between immiscible elements. Progress in Materials Science 50 (4), pp. 413–509 (2005).

[2.68] J.K. Patra & K.H. Baek, Green nanobiotechnology: Factors affecting synthesis and characterization techniques. Journal of Nanomaterials 2014, Article 417305 (2014).

[2.69] M. Brady, A. Walsh, Setting strategic direction: A top down or bottom up process? Business Strategy Series 9 (1), pp. 5–11 (2007).

[2.70] K.M.A. Haque, M.S. Hussain, Synthesis of Nano-sized Nickel Particles by a Bottom-up Approach in the Presence of an Anionic Surfactant and a Cationic Polymer. J. Sci. Res. 2 (2), pp. 313–321 (2010).

[2.71] S. Kumar, S. Dhankhar, V.P. Priya, S. Yadav and J. P. Yadav, Antimicrobial activity of Salvadora oleoides Decne against some microorganisms. Journal of Medicinal Plants Research, 6 (14), pp. 2754–2760 (2012).

[2.72] A. Chaudhary, D. Gustafson, & A. Mathys, Multi-indicator sustainability assessment of global food systems. Nat. Commun. 9 (1), 848 (2018).

[2.73] M. Sorbiun, E.S. Mehr, A. Ramazani, & A.M. Malekzadeh, 'Biosynthesis of metallic nanoparticles using plant extracts and evaluation of their antibacterial properties'. Nanochemistry Research 3 (1), pp. 1–16 (2018).

[2.74] K.S. Kavitha, S. Baker, D. Rakshith, H.U. Kavitha, R.H.C. Yashwantha, B.P. Harini and S. Satish, Plants as Green Source towards Synthesis of Nanoparticles. International Research Journal of Biological Sciences 2 (6), pp. 66–76 (2013).

[2.75] X. Li, H. Xu, Z.S. Chen, G. Chen, Biosynthesis of nanoparticles by microorganisms and their applications. J. Nanomater. 2011, Article 270974 (2011).

[2.76] A. Husen, M. Iqbal, Nanomaterials and Plant Potential: An Overview. Nanomaterials and Plant Potential. Cham. pp. 3–29 (2019).

[2.77] Z. Vaseghi, A. Nematollahzadeh and O. Tavakoli, Green methods for the synthesis of metal nanoparticles using biogenic reducing agents: a review. Reviews in Chemical Engineering 34 (4), pp. 529–559 (2018).

[2.78] R.K. Das, V.L. Pachapur, L. Lonappan, M. Naghdi, R. Pulicharla, S. Maiti, M. Cledón, L.M.A. Dalila, S.J. Sarma & S.K. Brar, Biological synthesis of metallic nanoparticles: plants, animals and microbial aspects. Nanotechnology for Environmental Engineering 2 (1), pp.1–21 (2017).

[2.79] J.S. Valli & B. Vaseeharan, Biosynthesis of silver nanoparticles by *Cissus quadrangularis* extracts. Materials Letters 82, pp. 171–173 (2012).

[2.80] S. Gulati, M. Sachdeva, K.K. Bhasin, Capping agents in nanoparticle synthesis: surfactant and solvent system. AIP Conf. Proc. 1953 (1), Article 030214 (2018).

[2.81] R. Javed, M. Zia, S. Naz, S.O. Aisida, N.U. Ain and Q. Ao, Role of capping agents in the application of nanoparticles in biomedicine and environmental remediation: recent trends and future prospects. J. Nanobiotechnol. 18 (1), Article 172 (2020).

[2.82] S. Baker, D. Rakshith, K.S. Kavitha, P. Santosh, H.U. Kavitha, Y. Rao and S. Satish, "Plants: Emerging as Nanofactories towards Facile Route in Synthesis of Nanoparticles". Bioimpacts 3 (3), pp. 111–117 (2013).

[2.83] M.H. Siddiqui, M.H. Al-Whaibi, M. Firoz, M.Y. Al-Khaishany, Role of Nanoparticles in Plants. Nanotechnology and Plant Sciences. Cham. pp. 19–35 (2015).

[2.84] J.S.G. Christopher, B. Saswati and P.S. Ezilrani, Optimization of Parameters for Biosynthesis of Silver Nanoparticles Using Leaf Extract of Aegle marmelos. Brazilian Archives of Biology and Technology 58 (5), pp. 702–710 (2015).

[2.85] M. Mohammadlou, H. Maghsoudi, and H. Jafarizadeh-Malmiri, A review on green silver nanoparticles based on plants: Synthesis, potential applications and eco-friendly approach. International Food Research Journal 23 (2), pp. 446–463 (2016).

[2.86] H. Liu, H. Zhang, J. Wang, J. Wei, Effect of temperature on the size of biosynthesized silver nanoparticle: Deep insight into microscopic kinetics analysis. Arabian Journal of Chemistry 13 (1), pp. 1011–1019 (2020).

[2.87] C. D'Antonio, S.L. Flory, Long-term dynamics and impacts of plant invasions, Journal of Ecology 105 (6), pp. 1459–1461 (2017).

[2.88] S. Lhimr, Effect of Molar Ratio on Structural and Size of ZnO/C Nanocomposite Synthesized Using a Colloidal Method at Low Temperature. Indonesian Journal of Chemistry 19 (2), pp. 422–429 (2019).

[2.89] A.M.E. Shafey, Green synthesis of metal and metal oxide nanoparticles from plant leaf extracts and their applications: A review. Green Processing and Synthesis 9 (1), pp. 304–339 (2020).

[2.90] P.S. Pimprikar, S.S. Joshi, A.R. Kumar, S.S. Zinjarde, S.K. Kulkarni, Influence of biomass and gold salt concentration on nanoparticle synthesis by the tropical marine yeast Yarrowia lipolytica NCIM 3589. Colloids Surf. B Biointerfaces 74 (1), pp. 309–316 (2009).

[2.91] A.V. Pethkar, R.P. Gaikaiwari and K.M. Paknikar, Biosorptive removal of contaminating heavy metals from plant extracts of medicinal value. JSTOR 80 (9), pp. 1216–1219 (2001).

[2.92] B. Sadeghi, M. Mohammadzadeh, & B. Babakhan, Green synthesis of gold nanoparticles using *Stevia rebaudiana* leaf extracts: Characterization and their stability. Journal of Photochemistry and Photobiology B: Biology 148, pp. 101–106 (2015).

[2.93] S. Mondal, N. Roy, R.A. Laskar, I. Sk, S. Basu, D. Mandal, N.A. Begum, "Biogenic synthesis of Ag, Au and bimetallic Au/Ag alloy nanoparticles using aqueous extract of mahogany (Swietenia mahogani JACQ.) leaves". Colloids and Surfaces B Biointerfaces 82 (2), pp. 497–504 (2011).

[2.94] S. Sahu, D. Rawat, D. Singh, "Antimicrobial Activity of *Trachyspermum ammi* Leaves Mediated Silver Nanoparticles: Green Approach". International Journal of Research in Engineering and Technology 4 (9), pp. 34–38 (2015).

[2.95] S. Rajeshkumar, & L.V. Bharath, Mechanism of plant-mediated synthesis of silver nanoparticles – A review on biomolecules involved, characterisation and antibacterial activity. Chemico-Biological Interactions 273, pp. 219–227 (2017).

[2.96] N.G. Shimpi, M. Khan, S. Shirole, and S. Sonawane, Process Optimization for the Synthesis of Silver (AgNPs), Iron Oxide (α-Fe_2O_3 NPs) and Core-Shell (Ag-Fe_2O_3 NPs) Nanoparticles Using the Aqueous Extract of Alstonia Scholaris: A Greener Approach. The Open Materials Science Journal 12 (1), pp. 29–39 (2018).

[2.97] S. Kulkarni, M. Jadhav, P. Raikar, D.A. Barretto, S.K. Vootlac and U.S. Raikar, Green synthesized multifunctional Ag@Fe_2O_3 nanocomposites for effective antibacterial, antifungal and anticancer properties. New J. Chem. 41, pp. 9513–9520 (2017).

[2.98] M. Sajjadi, M. Nasrollahzadeh, S. Mohammad Sajadi, Green synthesis of Ag/Fe_3O_4 nanocomposite using Euphorbia *peplus Linn* leaf extract and evaluation of its catalytic activity. Journal of Colloid and Interface Science 497, pp. 1–13 (2017).

[2.99] D. Zahra, R. Mojtaba, G. Mostafa, K. Fatemeh, Green synthesis of Ag-Fe_3O_4 nanocomposite utilizing *Eryngium planum L.* leaf extract and its potential applications in medicine. J. Drug Deliv. Sci. Technol. 67, Article 102941 (2022).

[2.100] S. Hameed, A.T. Khalil, M. Ali, M. Numan, S. Khamlich, Z.K. Shinwari, & M. Maaza, Greener synthesis of ZnO and Ag–ZnO nanoparticles using *Silybum marianum* for diverse biomedical applications. Nanomedicine 14 (6), pp. 655–673 (2019).

[2.101] E. Gurgur, S.S. Oluyamo, A.O. Adetuyi, O.I. Omotunde, A.E. Okoronkwo, Green synthesis of zinc oxide nanoparticles and zinc oxide–silver, zinc oxide–copper nanocomposites using *Bridelia ferruginea* as biotemplate. SN Applied Sciences 2, 911 (2020).

[2.102] T. Ghosh, A. Chattopadhyay, S. Pramanik, A. Das, S. Mukherjee, S. Das, A.C. Mandal, D. Dhak, P.K. Kuiri, Role of Ag Nanoparticles on Photoluminescence Emissions, Antibacterial Activities, and Photocatalytic Effects in ZnO-Ag Nanocomposites Synthesized via Low Temperature Green Synthesis Method Using *Azadirachta Indica* Leaf Extract. Mater. Technol. (2022).

[2.103] H.S. Abbas, A. Krishnan, and M. kotakonda, Fabrication of Iron Oxide/Zinc Oxide Nanocomposite Using Creeper *Blepharis maderaspatensis* Extract and Their Antimicrobial Activity. Frontiers in bioengineering and biotechnology 8, Article 595161 (2020).

[2.104] A.M. Korotkova, O. B. Polivanova, I. A. Gavrish, E. N. Baranova, S. V. Lebedev, Green synthesis of zinc based nanoparticles zinc ferrite by *Petroselinum crispum*. IOP Conference Series: Earth and Environmental Science 341 (1), Article 012175 (2019).

[2.105] N. Roy, S.A. Alex, N. Chandrasekaran, K. Kannabiran, A. Mukherjee, Studies on the removal of acid violet 7 dye from aqueous solutions by green ZnO@Fe$_3$O$_4$ chitosan-alginate nanocomposite synthesized using *Camellia sinensis* extract. Journal of environmental management 303, Article 114128 (2022).

[2.106] M.M. Naik, H.S.B. Naik, G. Nagaraju, M. Vinuth, H.R. Naika, K. Vinu, Green synthesis of zinc ferrite nanoparticles in *Limonia acidissima* juice: Characterization and their application as photocatalytic and antibacterial activities. Microchemical Journal 146, pp. 1227–1235 (2019).

[2.107] M. Sriramulu, D. Shukla and S. Sumathi, *Aegle marmelos* leaves extract mediated synthesis of zinc ferrite: Antibacterial activity and drug delivery. Mater. Res. Express 5 (11), Article 115404 (2018).

[2.108] B.S. Surendra, H.P. Nagaswarupa, M.U. Hemashree, J. Khanum, *Jatropha* extract mediated synthesis of ZnFe$_2$O$_4$ nanopowder: Excellent performance as an electrochemical sensor, UV photocatalyst and an antibacterial activity. Chemical Physics Letters 739 (12), Article 136980 (2020).

[2.109] V.G. Kontogianni, G. Tomic, I. Nikolic, A.A. Nerantzaki, N. Sayyad, S. Stosic-Grujicic, I. Stojanovic, I.P. Gerothanassis, A.G. Tzakos, Phytochemical profile of *Rosmarinus*

officinalis and *Salvia officinalis* extracts and correlation to their antioxidant and anti-proliferative activity. Food Chem. 136 (1), pp. 120–129 (2013).

[2.110] V.V. Makarov, A.J. Love, O.V. Sinitsyna, S.S. Makarova, I..V. Yaminsky, M.E. Taliansky, and N.O. Kalinina, Green nanotechnologies: synthesis of metal nanoparticles using plants. Acta Naturae 6 (1), pp. 35–44 (2014).

[2.111] G. Pintore, M. Usai, P. Bradesi, C. Juliano, G. Boatto, F. Tomi, M. Chessa, R. Cerri, & J. Casanova, Chemical composition and antimicrobial activity of *Rosmarinus officinalis L.* oils from Sardinia and Corsica. Flavour and Fragrance Journal 17 (1), pp. 15–19 (2002).

[2.112] A. Begum, S. Sandhya, S.S. Ali, K.R. Vinod, S. Reddy, & D. Banji, An in-depth review on the medicinal flora *Rosmarinus officinalis* (Lamiaceae). Acta Sci. Pol. Technol. Aliment 12 (1), pp. 61–73 (2013).

[2.113] B. Sasikumar, Rosemary. Handbook of Herbs and Spices, 2nd Ed., Cambridge: Woodhead, pp. 452–468 (2012).

[2.114] N. Erkan, G. Ayranci, and E. Ayranci, Antioxidant activities of rosemary (*Rosmarinus officinalis L.*) extract, blackseed (*Nigella sativa L.*) essential oil, carnosic acid, rosmarinic acid and sesamol. Food Chemistry 110 (1), pp. 76–82 (2008).

[2.115] Z.J. Yassin, T.M. Zaida, Impact of Rosemary Leave extracts on Triacylglycerol levels in Human Serum Albumin. Biomed. J. Sci & Tech. Res. 23 (4), pp. 17511–17515 (2019).

[2.116] E. Horváthová, D. Slameňová, J. Navarová, Administration of rosemary essential oil enhances resistance of rat hepatocytes against DNA-damaging oxidative agents. Food Chemistry 123 (1), pp. 151–156 (2010).

[2.117] T. Kayashima, K. Matsubara, Antiangiogenic effect of carnosic acid and carnosol, neuroprotective compounds in rosemary leaves. Biosci. Biotechnol. Biochem. 76 (1), pp.115–119 (2012).

[2.118] L. Hongyu, H. Zhang, J. Wang, J. Wei, Effect of temperature on the size of biosynthesized silver nanoparticle: Deep insight into microscopic kinetic analysis. Arabian Journal of Chemistry 13 (1), pp. 1011–1019 (2017).

[2.119] T. Bakirel, U. Bakirel, O.U. Keleş, S.G. Ulgen, & H. Yardibi, In vivo assessment of antidiabetic and antioxidant activities of rosemary (*Rosmarinus officinalis*) in alloxan-diabetic rabbits. Journal of Ethnopharmacology 116 (1), pp. 64–73 (2008).

[2.120] C.L. Hsieh, C.H. Peng, C.C. Chyau, Y.C. Lin, H.E. Wang, R.Y. Peng, Low-density lipoprotein, collagen, and thrombin models reveal that *Rosemarinus officinalis* L. exhibits potent antiglycative effects. J. Agric. Food Chem. 55, pp. 2884–2891 (2007).

[2.121] A. Al-Mariri, M. Safi, The antibacterial activity of selected labiatae (Lamiaceae) essential oils against Brucella melitensis. Iran. J. Med. Sci. 38 (1), pp. 44–50 (2013).

[2.122] S. Carvalhinho, A.M. Costa, A. Coelho, M. Eugénio, Susceptibilities of Candida albicans Mouth Isolates to Antifungal Agents, Essentials Oils and Mouth Rinses. Mycopathologia 174 (1), pp. 69–76 (2012).

[2.123] S. Zoubiri and A. Baaliouamer, Potentiality of plants as source of insecticide principles. Journal of Saudi Chemical Society 18 (6), pp. 925–938 (2011).

[2.124] R.A.A. Mothana, S.S. Hasson, W. Schultze, A. Mowitz, U. Lindequist, Phytochemical composition and in vitro antimicrobial and antioxidant activities of essential oils of three endemic Soqotraen Boswellia species. Food Chemistry 126 (3), pp. 1149–1154 (2011).

[2.125] R. Ventura-Martínez, O. Rivero-Osorno, C. Gomez, M.E. González-Trujano, Spasmolytic activity of *Rosmarinus officinalis* L. involves calcium channels in the guinea pig ileum. Journal of Ethnopharmacology 137 (3), pp. 1528–1532. (2011).

[2.126] I. Takaki, L.E. Bersani-Amado, A. Vendruscolo, S.M. Sartoretto, S.P. Diniz, C.A. Bersani-Amado, R.K. Cuman. Anti-inflammatory and antinociceptive effects of *Rosmarinus officinalis* L. essential oil in experimental animal models. J. Med. Food 11 (4), pp.741–746 (2008).

[2.127] L. Menghini, S. Genovese, F. Epifano, B. Tirillini, C. Ferrante, L. Leporini, Antiproliferative, protective and antioxidant effects of artichoke, dandelion, turmeric and rosemary extracts and their formulation. Int. J. Immunopathol. Pharmacol. 23 (2), pp. 601–610 (2010).

[2.128] A.I. Hussain, F. Anwar, S.A.S. Chatha, A. Jabbar, S. Mahboob & P.S. Nigam, *Rosmarinus officinalis* essential oil: antiproliferative, antioxidant and antibacterial activities. Brazilian Journal of Microbiology 41 (4), pp. 1070–1078 (2010).

[2.129] M.S. Afonso, A.M de O Silva, E.B. Carvalho, D.P. Rivelli, S.B. Barros, M.M. Rogero, A.M. Lottenberg, R.P. Torres, & J. Mancini-Filho, Phenolic compounds from rosemary (*Rosmarinus officinalis* L.) attenuate oxidative stress and reduce blood cholesterol concentrations in diet-induced hypercholesterolemic rats. Nutrition & Metabolism 10 (1), 19 (2013).

[2.130] B. Teixeira, A. Marques, C. Ramos, N.R. Neng, J.M. Nogueira, J.A. Saraiva, M.L. Nunes, Chemical composition and antibacterial and antioxidant properties of commercial essential oils. Industrial Crops and Products 43, pp. 587–595 (2013).

[2.131] E. Arranz, S. Santayo, L. Jaime, T. Fornari, G. Reglero, A. Guri, M. Corredig, Improved bioavailability of Supercritical Rosemary Extract Through Encapsulation in Different Delivery Systems After In Vitro Digestion. Food Dig. Res. Curr. Opin. 6 (1), pp. 30–37 (2015).

[2.132] R.S. Borges, B.L.S. Ortiz, A.C.M. Pereira, H. Keita, J.C.T. Carvalho, *Rosmarinus officinalis* essential oil: A review of its phytochemistry, anti-inflammatory activity, and mechanisms of action involved. J. Ethnopharmacol. 229, pp. 29–45 (2019).

[2.133] E. Gharibshahi, E. Saion, A. Ashraf, L. Gharibshahi, Size-Controlled and Optical Properties of Platinum Nanoparticles by Gamma Radiolytic Synthesis. Appl. Radiat. Isot. 130, pp. 211–217 (2017).

[2.134] J. Belloni, M. Mostafavi, H. Remita, J.I. Marignier, M.O. Delcourt, Radiation induced synthesis of mono- and multi-metallic clusters and nanocolloids. New J. Chem. 22 (11), pp. 1239–1255 (1998).

[2.135] N. Misra, J. Biswal, V. P. Dhamgaye, G. S. Lodha, S. Sabharwal, A comparative study of gamma, electron beam, and synchrotron X-ray irradiation method for synthesis of silver nanoparticles in PVP. Adv. Mat. Lett. 4 (6), pp. 458–463 (2013).

[2.136] Atomic Energy of Canada, "Certification 42 of measurement gamma cell 220 No.200", John Wiley & Sons, Ltd., Toronto, 1984.

[2.137] S.S. Gasaymeh, S. Radiman, L.Y. Heng, E. Saion, G.H.M. Saeed, Synthesis and characterization of silver/polyvinilpirrolidone (Ag/PVP) nanoparticles using gamma irradiation techniques. Am. J. Appl. Sci. 7 (7), pp. 892–901 (2010).

[2.138] D.N. Ngoc, P.D. Van, A.Q. Le, Q.N. Quoc, Electron beam/γ-ray irradiation synthesis of gold nanoparticles and investigation of antioxidant activity. Advances in Natural Sciences : Nanoscience and Nanotechnology 5 (4), Article 045002 (2014).

[2.139] O.N. Vassiliev, On calculation of the average linear energy transfer for radiobiological modelling. Biomed. Phys. Eng. Express 7(1), Article 015001 (2021).

[2.140] B. Akar, K.S. Pushpavanam, E. Narayanan, K. Rege, J. Heys, Mechanistic investigation of radiolysis induced gold nanoparticle formation for radiation dose prediction. Biomed. Phys. Eng. Express 4 (6), Article 065011 (2018).

[2.141] H. Erramli and J.E. Asri, Gamma Rays: Applications in Environmental Gamma Dosimetry and Determination Samples Gamma- Activities Induced by Neutrons. In book: Use of Gamma Radiation Techniques in Peaceful Applications (2019).

[2.142] H. Remita, I. Lampre, M. Mostafavi, E. Balanzat, S. Bouffard, Comparative study of metal clusters induced in aqueous solutions by γ-rays, electron or C_6^+ ion beam irradiation. Rad. Phys. Chem. 72 (5), pp. 575–586 (2005).

[2.143] Y. Gerasimov, Radiation methods in nanotechnology. J. Eng. Phys. Thermophys. 84 (4), pp. 947–963 (2011).

[2.144] B. Munoz-Flores, B.I. Kharisov, V.M. Jimenez-Perez, P.E. Martinez, S.T. Lopez, Recent Advances in the Synthesis and Main Applications of Metallic Nanoalloys. Ind. Eng. Chem. Res. 50 (13), pp. 7705–7721 (2011).

[2.145] Y. Rao, D. Banerjee, A. Datta, S. Das, R. Guin, A. Saha, Gamma irradiation route to synthesis of highly re-dispersible natural polymer capped silver nanoparticles. Radiat. Phys. Chem. 79 (12), pp. 1240–1246 (2010).

[2.146] J. Belloni, Nucleation, growth and properties of nanoclusters studied by radiation chemistry Application to catalysis. Catal. Today 113 (3–4), pp. 141–156 (2006).

[2.147] A. Abedini, F. Larki, E. Saion, A. Zakaria, M.Z. Hussein, Influence of dose and ion concentration on formation of binary Al-Ni alloy nanoclusters. Radiat. Phys. Chem. 81, pp. 1653–1658 (2012).

[2.148] H. Shehla, F.T. Thema, A. Ishaq, N.Z. Ali, I. Javed, D. Wan, and M. Maaza: γ-Rays Irradiation Induced Structural and Morphological Changes in Copper Nanowires, Hindawi Publishing Corporation, Journal of Nanomaterials 2016, Article 6134801 (2016).

[2.149] X. Wang, Z. Shi, S. Yao, F. Liao, J. Ding, M. Shao, Gamma ray irradiated $AgFeO_2$ nanoparticles with enhanced gas sensor properties, J. Solid State Chem. 219, pp. 228–231 (2014).

[2.150] A. Abedini, M. Saraji, A.A.A. Bakar, P.S. Menon, S. Shaari, Gamma-Radiation-assisted synthesis of luminescent ZnO/Ag heterostructure core-shell nanocomposites. Plasmonics 13 (3), pp. 771–778 (2018).

[2.151] H.A. Thabit, N.A. Kabir, N.M. Ahmed, Synthesis and thermoluminescence characteristics and structural and optical studies of ZnO/Ag/ZnO system for dosimetric applications. Journal of Luminescence 236, Article 118097 (2021).

[2.152] S. Kalunge, A.V. Humbe, M.V. Khedkar, S.D. More, A.P. Keche, and A.A. Pandit, Investigation on synthesis, structural and electrical properties of zinc ferrite on gamma irradiation. Journal of physics conference series 1644 (1), Article 012017 (2020).

[2.153] H. Remita, A. Etcheberry, J. Belloni, Dose Rate Effect on Bimetallic Gold—Palladium Cluster Structure. J. Phys. Chem. B 107 (1), pp. 31–36 (2003).

[2.154] K. Sehested, "The Fricke Dosimeter". Manual on Radiation Dosimetry. New York, pp. 313–317 (1970).

[2.155] J. Grand, S.R. Ferreira, V. de Waele, S. Mintova and T.M. Nenoff, Nanoparticle Alloy Formation by Radiolysis. J. Phys. Chem. C 122 (24), pp. 12573–12588 (2018).

[2.156] A. Zaleska-Medynska, M. Marchelek, M. Diak, E. Grabowska, Noble metal-based bimetallic nanoparticles: the effect of the structure on the optical, catalytic and photocatalytic properties. Adv. Colloid. Interf. Sci. 229, pp. 80–107 (2016).

[2.157] B.M. Muñoz-Flores, B.I. Kharisov, V.M. Jiménez-Pérez, P.E. Martinez, S.T. López, Recent Advances in the Synthesis and Main Applications of Metallic Nanoalloys. Ind. Eng. Chem. Res. 50 (13), pp. 7705–7721 (2011).

[2.158] J.F. Wishart, Tools for radiolysis studies. In: M. Spotheim-Maurizot, M. Mostafavi, T. Douki, J. Belloni (eds) In Radiation Chemistry: From Basics to Applications in Material and Life Sciences. EDP Sciences, Paris, pp. 17–33 (2008).

BINARY PHASE DIAGRAMS AND MISCIBILITY GAP

3.1. Introduction

The term *phase* is based on the work of the American mathematician Josiah Willard Gibbs who first introduced the term in describing the thermodynamics of heterogeneous solids [3.1].

A phase is a physically homogeneous state of matter with specific chemical composition and atomic arrangement. The phase diagram delineates the existence regions of various phases, referred to as microstructural level equilibrium of elements with varying composition, i.e., phase and defect distribution in a material, and the relationships between temperature and compositions at constant pressure [3.2].

Binary phase diagrams are very useful to predict the phase transformations and resulting microstructures, which can be either equilibrium or non-equilibrium i.e., the number and types of phases (thermochemistry of the liquid, metal solution, and the compounds in a binary system), the weight percentage (wt%) of each phase, for a given temperature, each binary composition of the system [3.2, 3.3].

The formulas in a binary system can be used to convert between weight percentage (wt %) and atomic percentage (at. %):

$$wt \, \% \, A = \frac{at.\% \, A \times at.wt \, of \, A}{(at.\% \, A \times at.wt \, of \, A) + (at.\% \, B \times at.wt \, of \, B)} \times 100 \qquad (3.1)$$

and

$$at.\% \, A = \frac{wt \, \% \, A/at.wt \, of \, A}{(at.\% \, A/at.wt \, of \, A) + (wt \, \% \, B/at.wt \, of \, B)} \times 100 \qquad (3.2)$$

3.2. The Gibbs Phase Rule for binary phase diagrams

3.2.1. Number of phases P present in an equilibrium

The Gibbs phase rule is a set of thermodynamic rules that greatly simplifies the construction of phase diagrams. It is determined by controllable parameters independently variable namely

46

degrees of freedom (F), number of chemical components (C), and number of phases (P) present in an equilibrium of the system [3.4] via a simple equation:

$$P = C - F + 2 \tag{3.3}$$

In a binary alloy (C = 2), both composition and temperature could be variable during the equilibrium, so F = 2. In this case, the greatest number of heterogeneous phase equilibria would be:

$$P = 2 - 2 + 1 = 1 \tag{3.4}$$

If both composition and temperature could vary while the system remains in equilibrium, only one homogeneous phase would be possible. However, if equilibrium in a binary alloy can be maintained while either composition or temperature keeps constant (F = 1), then two heterogeneous phases can exist in equilibrium:

$$P = 2 - 1 + 1 = 2 \tag{3.5}$$

This possibility of two phases coexisting in a binary system depicts phase areas such as the mushy zone (liquid + solid phases) or a two-phase mixture in a solid [3.5].

Binary alloy phase diagrams can contain an invariant point as well (F = 0), where equilibrium conditions are set by a specific (constant) composition and temperature. In this case, the invariant point of a binary alloy has three coexisting equilibrium phases [3.2]:

$$P = 2 - 0 + 1 = 3 \tag{3.6}$$

3.2.2. Gibbs free energy

The Gibbs free energy G from the composition at a given temperature T of the binary alloy is defined as the sum of the components A and B plus the energy of mixing ΔG_{mix} [3.6]:

$$G = X_A G_A + X_B G_B + \Delta G_{mix} \tag{3.7}$$

This energy of mixing is constituted of the enthalpy of mixing associated with the A–B bonds ΔH_{mix}, and entropy of mixing ΔS_{mix} associated with the random mixing of A and B atoms. Thus, the following equation is generated:

$$\Delta G_{mix} = \Delta H_{mix} - T\Delta S_{mix} \tag{3.8}$$

47

3.3. Miscibility gap

Bimetallic alloys from immiscible metals are characterized by the miscibility gap in the phase diagram and the positive heat of mixing enthalpy ΔH [3.3].

The origin of the miscibility gap in the liquid state may be described as follows: at a given temperature and constant pressure of one atmosphere, the molar Gibbs free energy of a system consisting of two immiscible liquid components is assessed by thermodynamic calculations [3.5, 3.7]. Accessing composites within the miscibility gaps is critical because such phases possess intriguing synergistic properties not perceived with phase-segregated mixtures [3.8].

A phase diagram of a miscibility gap in the liquid state can be divided into three regions defined by the phases that exist over the temperature and composition range delimited by the boundary lines. They are namely stable (miscibility gap in the equilibrium liquid state), metastable (miscibility gap in the metastable undercooled liquid state), and unstable region (miscibility gap in the unstable undercooled liquid state) [3.9]. Considering the liquidus line separates the liquid phase region from the solid + liquid mixture region, the miscibility gap above the liquidus line is stable, whereas the miscibility gap below the liquidus line is metastable [3.10, 3.11]. The liquid inside the spinodal line is unstable because any feeble fluctuation in composition that results in the A-rich and B-rich regions for a binary alloy A-B system causes a decrease in free energy, inducing L-L phase separation to swiftly occur without any energy barrier [3.12]. Therefore, the phase separation into two liquids occurs through nucleation and growth, as well as by overcoming energy barriers [3.13].

3.4. Binary phase diagrams

Direct alloying from immiscible metals is extremely difficult due to the absence of a thermodynamic driving force at equilibrium [3.5]. Numerous experimental and theoretical works are being performed over the world to explore the miscibility gap of immiscible alloys which is critical in nanotechnology since it gives freedom to design and fabricate immiscible alloys because of their stunning properties and potential applications in a variety of fields [3.4, 3.7–3.11].

According to binary phase diagrams, Fe is thermodynamically immiscible with other metals such as Ag, Cu, Pt, Zn, Au, and so on [3.1, 3.4, 3.6]. Fe-Ag (Iron-Silver), and Fe-Zn (Iron-Zinc) binary systems possess a wide immiscibility gap whereas Ag-Zn (Silver-Zinc) system is composed of two liquids that are partially miscible.

48

3.4.1. Fe-Ag phase diagram

Binary Fe-Ag alloy is an immiscible alloy with a liquid miscibility gap and positive heat of mixing. Its phase diagram (Figure 3.1) depicts five distinct equilibrium phases: the liquid field (L), the solid solution (S) based on the low-temperature base-centered cubic (bcc) phase of Fe (α), the solid solution (S) based on the high-temperature bcc phase of Fe (δ), the solid solution (S) based on the face-centered cubic (fcc) phase of Fe (γ), and the solid solution (S) based on the face-centered cubic phase (fcc) of Ag [3.1, 3.14].

Fe and Ag are completely miscible in the liquid state. At a temperature (T) of 1806 K, two liquids L_1 and L_2 with different chemical compositions coexist in equilibrium [3.15].

The syntectic reaction occurs:

$$L_1 + L_2 \rightarrow S \qquad (3.9)$$

At T=1671K, the monotectic reaction occurs:

$$L_1 \rightarrow \delta\text{-}Fe + L_2 \qquad (3.10)$$

At T= 1234 K, the peritectic reaction occurs:

$$\delta\text{-}Fe + L_2 \rightarrow \gamma\text{-}Fe \qquad (3.11)$$
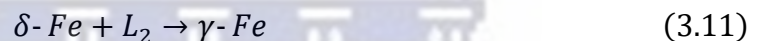
At T= 1184.5 K, L_2 solidifies through the eutectic reaction:

$$L_2 \rightarrow \gamma\text{-}Fe + Ag \qquad (3.12)$$

The eutectoid reaction occurs below the temperature of 1184.5 K:

$$\gamma\text{-}Fe \rightarrow \alpha\text{-}Fe + Ag \qquad (3.13)$$

The phase decomposition of the mixed liquid (L) into Fe-rich liquid (L_1) and Ag-rich liquid (L_2) took place by nucleation and growth. Therefore, an energy barrier was overcome at the metastable miscibility gap [3.16].
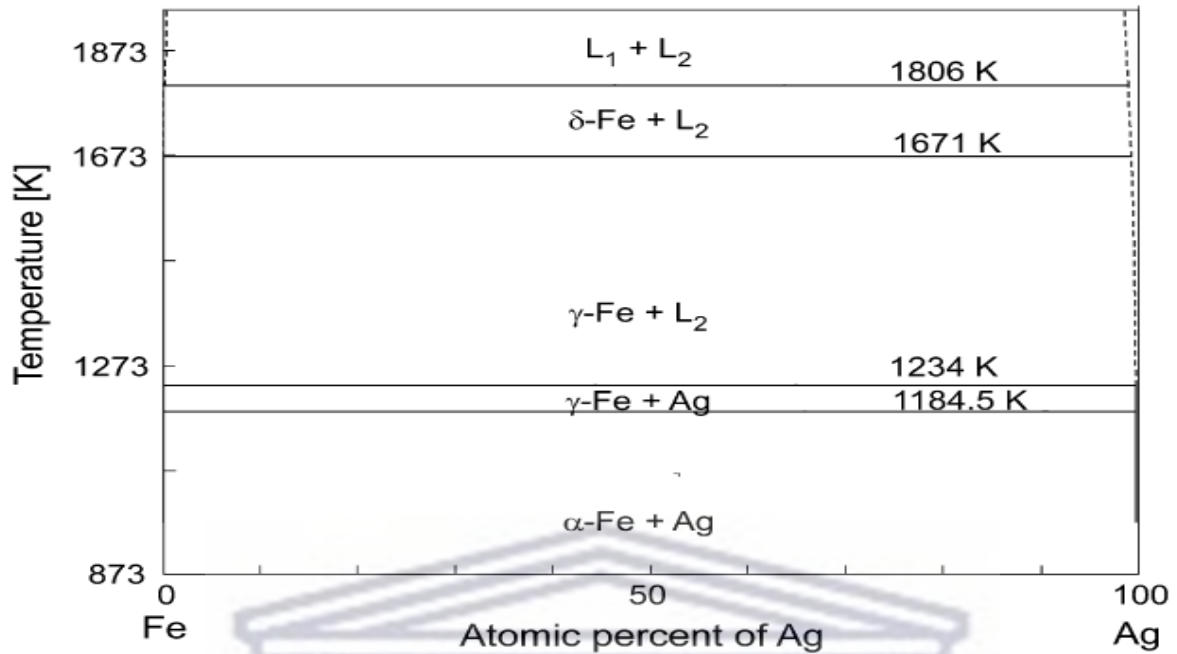
Figure 3.1: Binary phase diagram of Fe-Ag alloy system [3.15]

3.4.2. Ag-Zn phase diagram

The Ag-Zn binary system contains six phases, terminal solid solutions between silver-rich (α or (Ag)-phase) and zinc-rich (or η (Zn)-phase). In the phase diagram, the intermediate solid solutions are as follows : β-phase, corresponding to Ag-Zn - the equiatomic composition and stability at higher temperatures; ζ-phase, corresponding to Ag-Zn stable at lower temperatures; and phases γ and ε, corresponding to intermetallic compounds [3.10].

The upper layer of the so-called η-phase is made up of almost entirely pure metal and is formed by simple solidification of the metal melt. Metal crystallizes in the system and has relatively high toughness and low hardness at common temperatures [3.12].

Nonetheless, it should be made clear that the intermediate phases in this system exist over wide concentration ranges around the stoichiometric compositions. The position of the chosen Ag–Zn mixtures is shown in Figure 3.2 [3.17].
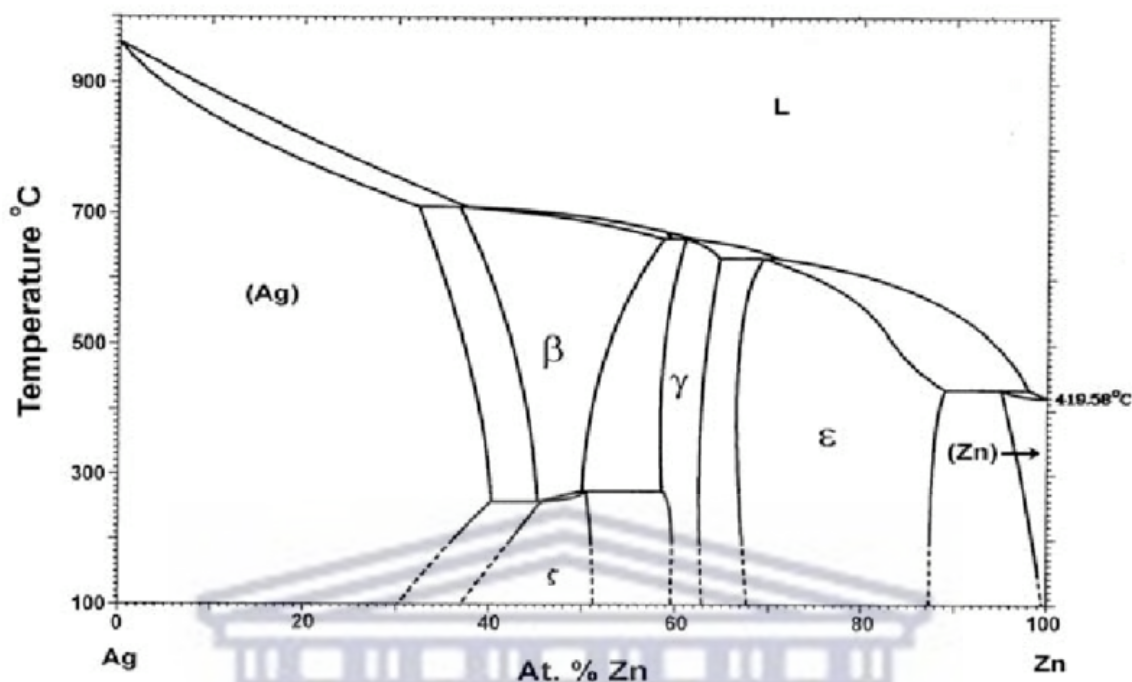
Figure 3.2: Binary phase diagram of Ag-Zn system [3.17]

3.4.3. Fe-Zn phase diagram

Among the immiscible alloys with liquid-phase separation, Fe-Zn alloy has been the subject of study for a long time. The liquid-phase separation phenomenon is generally observed in the alloy having the combination that the mixing enthalpy (ΔH_{mix}) between constituent elements shows a large positive value ($\Delta H_{mix} > 0$) [3.6].

The Fe-Zn system contains eight phases namely the liquid phase, Ѓ, Ѓ1, δ, and ζ intermetallic phases, and three-terminal solid solutions of α-Fe base-centered cubic (bcc), γ-Fe face-centered cubic (fcc), and Zn hexagonal close-packed (hcp) [3.4, 3.18].

The Fe-Zn phase diagram revealed a large α-Fe solubility area, a closed γ loop, and three compounds in the Zn-rich region marked by Ѓ, δ, and ζ phases [3.19].

A peritectic reaction (3.14) between delta phase (δ) and zinc melt (L) at 530 ± 10 °C, produces the intermetallic zeta (ζ) phase. It crystallizes in the coating in a base-centered monoclinic system with the space group C2/m [3.6].

51

$$\delta + L \rightarrow \zeta \tag{3.14}$$

The structure of the phase δ1k (or δ) is much larger than the phase δ1p (or δ1). In general, both phases are sparked by a peritectic reaction (3.15) between gamma phase (Γ) and zinc melt (L) around 665 °C with the space group P6$_3$/ mcm [3.20].

$$Γ́ + L \rightarrow δ1k/δ1p \tag{3.15}$$
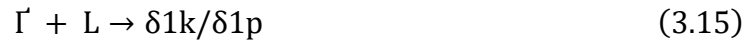
Unlike previous phases, this phase is formed by the mutual reaction of two intermetallic phases, namely gamma (Γ) and delta (δ) at a temperature of 550 ± 10 °C (peritectic reaction).

The reaction's path is represented by equation (3.16) in which the Γ́$_1$ phase forms a continuous transition between (δ) and gamma (Γ) phases [3.21].

$$Γ́ + δ \rightarrow Γ́_1 \tag{3.16}$$

The Γ phase depicts the existence of intermetallic with a higher ratio of atoms in the structure. It is formed by the peritectic reaction of bimetallic at 782 °C using the equation (3.17) [3.22]

$$M \text{ (metal)} + L \rightarrow Γ́ \tag{3.17}$$

The experimental results of the solidus of the (αFe) solution in equilibrium with the Γ́ phase were reported by the works of Okamato et al., 2014 [3.20], showing consistency among different measurements.

Two groups of authors newly proposed a Fe-Zn binary phase diagram that clearly defined the phase boundaries of the liquid and intermetallic phases, allowing for more specific thermodynamic modelling of the Fe-Zn binary system [3.18, 3.23].

The phase decomposition of the mixed liquid (L) took place through nucleation and growth. Therefore, an energy barrier was overcome at the metastable miscibility gap.
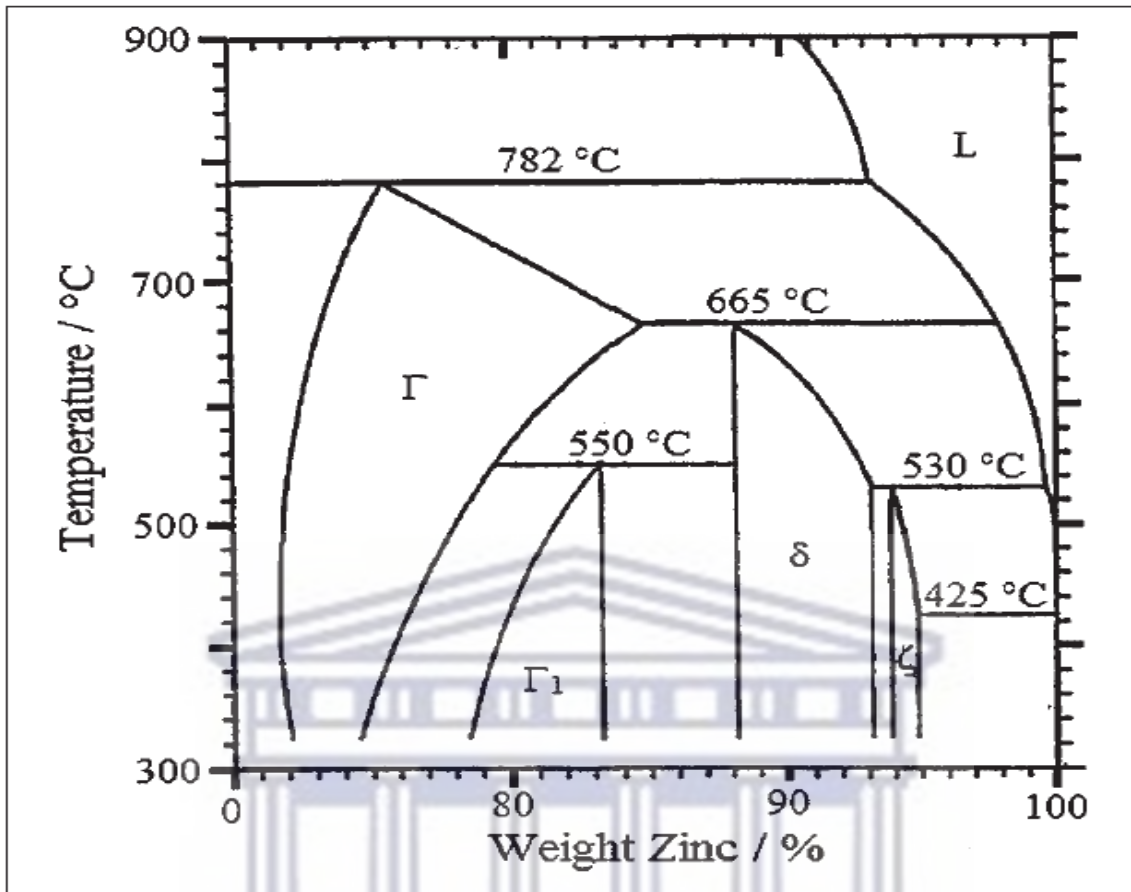
Figure 3.3: Section of the phase diagram of Fe-Zn alloy with high zinc ratio [3.18]

3.5. References

[3.1] L.J. Swartzendruber, The Ag−Fe (Silver-Iron) system. Bulletin of Alloy Phase Diagrams 5, pp. 560–564 (1984).

[3.2] H. Okamoto, Phase Diagrams of Binary Alloys. ASM International, Ohio, 2010.

[3.3] D. Jinlong, H. Yuan, L. Jiwen, L. Yongchang, W. Zumin, Irradiation damage alloying for immiscible alloy systems and its thermodynamic origin. Materials & Design 170, 107699 (2019).

[3.4] A. Kobayashi, K. Nagayama, Microstructure and solidification process of Fe-Cu immiscible alloy by using containerless process. Journal of the Japan Institute of Metals 81 (5), pp. 251–256 (2017).

[3.5] T. Zheng, Y.B. Zhong, Z.S. Lei, W.L. Ren, X. Li, F. Debray, E. Beaugnon, Y. Fautrelle, Effects of high static magnetic field on distribution of solid particles in BiZn immiscible alloys with metastable miscibility gap. Journal of Alloys and Compounds 623, pp. 36–41 (2015).

[3.6] B.P. Burton, P. Perrot, Phase Diagrams of Binary Iron Alloys. ed. By H. Okamoto. ASM International, Materials Park, OH, pp. 459–466 (1993).

[3.7] Y. Shubin, P. Plyusnin, M. Sharafutdinov, E. Makotchenko, S. Korenev, Successful synthesis and thermal stability of immiscible metal Au–Rh, Au–Ir and Au–Ir–Rh nanoalloys. Nanotechnology 28 (20), Article 205302 (2017).

[3.8] C. Yang, B.H. Ko, S. Hwang, Z. Liu, Y. Yao, W. Luc, M. Cui, A.S. Malkani, T. Li, X. Wang, J. Dai, B. Xu, G. Wang, D. Su, F. Jiao, L. Hu, Overcoming immiscibility toward bimetallic catalyst library. Sciences Advances 6 (17): eaaz6844 (2020).

[3.9] S. Masuda, K. Mori, T. Sano, K. Miyawaki, C. Wei-Hung, H. Yamashita, Simple Route for the Synthesis of Highly Active Bimetallic Nanoparticle Catalysts with Immiscible Ru and Ni Combination by Utilizing TiO_2 Support. ChemCatChem, The European Society Journal for Catalysis 10 (16), pp. 3526–3531 (2018).

[3.10] T.B. Massalski, H.W. King, The lattice spacing relationships in H.C.P. ϵ and η phases in the systems Cu-Zn, Ag-Zn; Au-Zn and Ag-Cd. Acta Metallurgica, 10 (12), pp. 1171–1181 (1962).

[3.11] J. Zhao, T. Ahmed, H. Jiang, J. He, Q. Sun, Solidification of immiscible alloy. A Review. Acta Metallurgica Sinica, 30 (1), pp. 1–28 (2017).

[3.12] T. Gomez-Acebo, Thermodynamic assessment of the Ag-Zn system. Calphad 22 (2), pp. 203–220 (1998).

[3.13] Y. Xia, X. Xia, H.C. Peng, Shape-Controlled Synthesis of Colloidal Metal Nanocrystals: Thermodynamic versus Kinetic Products. J. Am. Chem. Soc. 137, pp. 7947–7966 (2015).

[3.14] A. Paul, The Kirkendall effect in solid state diffusion, Eindhoven: Technische Universiteit Eindhoven (2004).

[3.15] T. Nagase, M. Suzuki, T. Tanaka, Amorphous phase formation in Fe–Ag-based immiscible alloys. Journal of Alloys and Compounds 619, pp. 311–318 (2015).

[3.16] B.X. Liu, F. Pan, & K. Tao, A Cubic Phase Formed in Immiscible Fe/Ag (Cu) System S by Ion Mixing. MRS Online Proceedings Library 316, pp. 289–294 (1993).

[3.17] H. Okamoto, Ag-Zn (Silver-Zinc). Journal of Phase Equilibria 23 (5), pp. 454–454 (2002).

[3.18] S. Budurov, P. Kovatchev, N. Stoj£ev, Z. Kamenova, Z. Metallkd. 63, pp. 348–350 (1972).

[3.19] P.J. Gellings, E.W.D. Bree, G. Gierman, Synthesis and Characterization of Homogeneous Intermetallic Fe-Zn Compounds, Part 2. International Journal of Materials Research 70 (5), pp. 315–317 (1979).

[3.20] N. L. Okamoto, A. Yasuhara, H. Inui, Order-disorder structure of the δ1k phase in the Fe – Zn system determined by scanning transmission electron microscopy. Acta Materialia 81, pp. 345–357 (2014).

[3.21] A.R. Marder, The metallurgy of zinc–coated steel. Progress in Materials Science 45, pp. 91–271 (2000).

[3.22] J.C. de Lima, E.C. Borba, C. Paduani, V.H.F.D. Santos, T.A. Grandi, H.R. Rechenberg, I. Denicoló, M. Elmassalami, A.F. Barbosa, Mechanical alloying of Fe and Zn: phase analysis and Mössbauer studies. Journal of Alloys and Compounds 234, pp. 43–47 (1996).

[3.23] T. Takayama, S. Shinohara, K. Ishida, T. Nishizawa, J. Phase Equilib. 16, pp. 390–395 (1995).

CHAPTER FOUR

CHARACTERIZATION TECHNIQUES

4.1. Surface characterization techniques

4.1.1. Scanning electron microscopy (SEM)

Electron microscopes are scientific instruments that use a beam of energetic electrons to investigate objects at the nanoscale level. A Zeiss Auriga field emission SEM was used to examine electrons' interaction with the atoms in the sample which produce the signals with high-energy electrons beam in a raster scan pattern and information regarding the surface morphology, size, and shape of NPs [4.1].
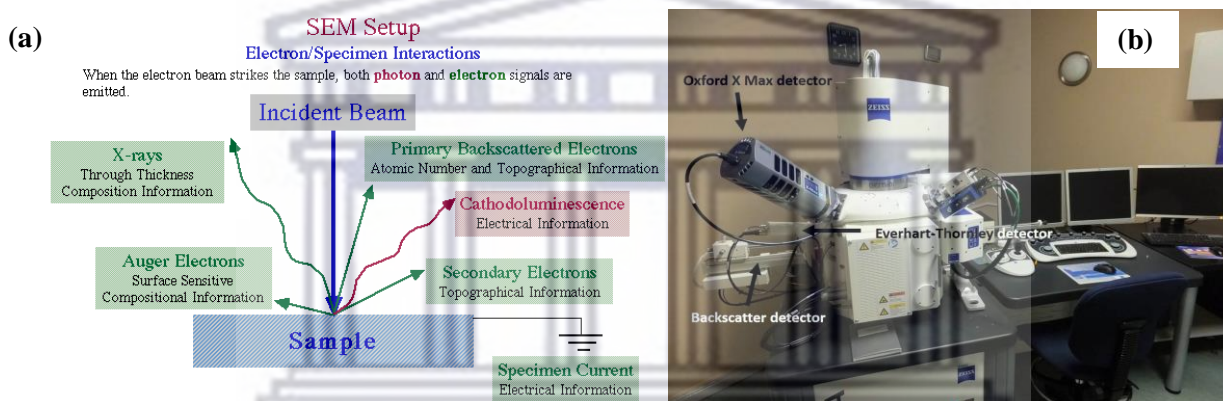
Figure 4.1: (a) Set up, **(b)** Equipment of a Zeiss Auriga FESEM hosted at the University of the Western Cape; the major detectors used are as indicated [4.1, 4.2]

Secondary electrons from the sample once in contact with the electron beam, back-scattered electrons, characteristic X-rays, light (cathodoluminescence), specimen current, and transmitted electrons are examples of signals produced by SEM micrographs which possess a large depth of field because of the thinner electron beam, resulting in a distinctive three-dimensional appearance useful for understanding the surface structure of a sample [4.2].

4.1.2. Transmission electron microscopy (TEM)

TEM was developed by scientists Max Knoll and Ernst Ruska in 1931 in Germany. It is largely used in the characterization of NPs for analyzing agglomeration, annealing effects, dispersion in a matrix, and the internal structure, size, and shape [4.3].

56

The magnification of the TEM is determined by the distances between the specimen and the image plane of the objective lens. Analytical TEM may provide elemental analysis, maps and line scans using auxiliary detectors. TEM can focus an electron beam on a single particle, to get information from individual particles [4.4].

The technique involves (i) irradiation of a very thin sample by a high-energy electron beam, which is diffracted by the lattices of a crystalline or semi-crystalline material and propagated along with different directions, (ii) imaging and angular distribution analysis of the forward-scattered electrons (unlike SEM where backscattered electrons are detected), and (iii) energy analysis of the emitted X-rays [4.5].
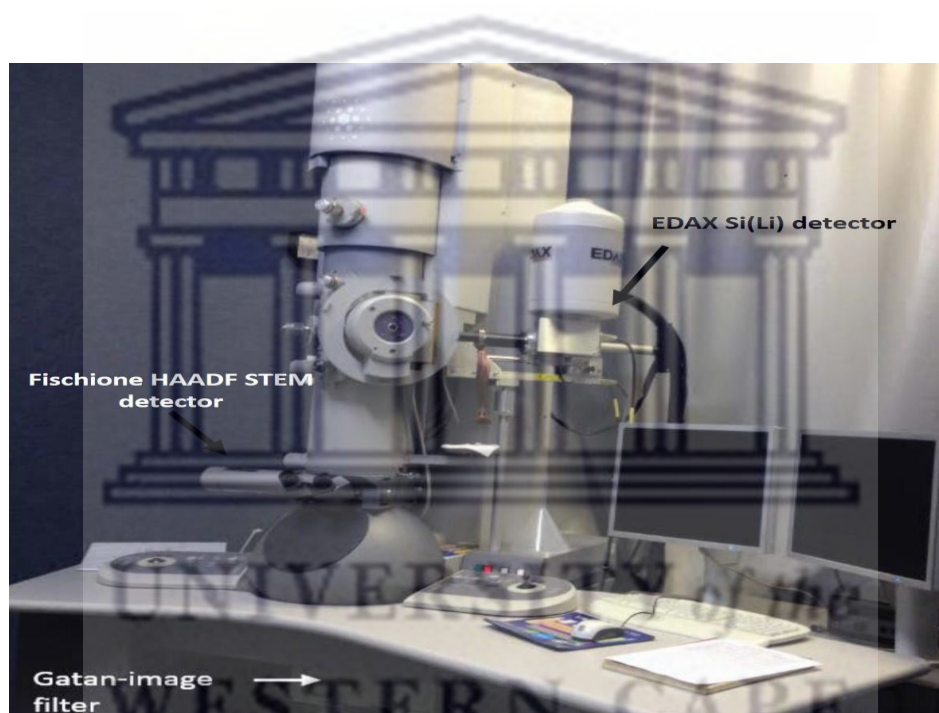
Figure 4.2: A pictorial representation of the Tecnai G220 field-emission gun TEM hosted at the University of the Western Cape [4.2]

4.1.3. X-ray diffraction (XRD)

XRD is a complementary method used to determine and identify the phase purity, crystal structure, geometry, particle size, degree of crystallinity and unit cell parameters of NPs [4.6]. All the prepared samples in this work were characterized by X-ray diffraction using a Bruker D8 Advance diffractometer with Cu Kα radiation (λ= 1.540598 Å) located at iThemba LABS, Cape Town which is presented in Figure 4.3.

57
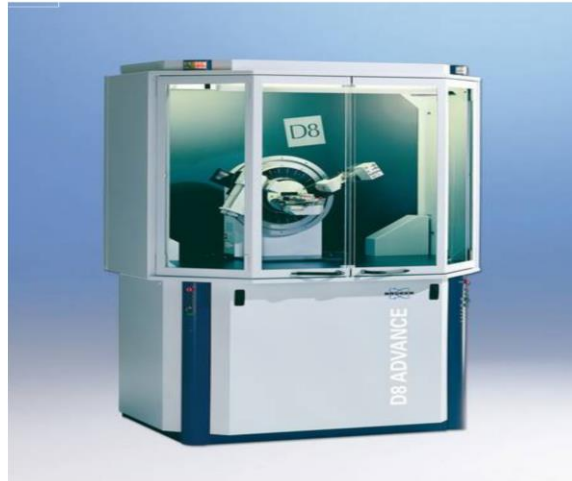
Figure 4.3: Bruker D8 Advance powder diffractometer [4.7]

Electromagnetic waves of wavelength comparable to crystal lattice spacing are highly diffracted by a crystal. Bragg's equation relates the distance (d) between two (hkl) planes and the angle of diffraction (2θ) is defined as:

$$2d \sin \theta = n \lambda \qquad (4.1)$$

Here d is the inter-planar spacing, θ is the angle of diffraction, λ is the wavelength of X-rays, the order of diffraction is represented by the integer n, and h, k and l represent Miller indices of the respective planes [4.8].

In a typical set-up, a collimated beam of X-rays is incident on the sample. The intensity of the diffracted X-rays is proportional to the diffracted angle 2θ as portrayed in Figure 4.4**.** The atomic arrangement is revealed by the intensities of the diffracted beams. The sharpness and shape of the reflections are related to the crystal's perfection [4.6].
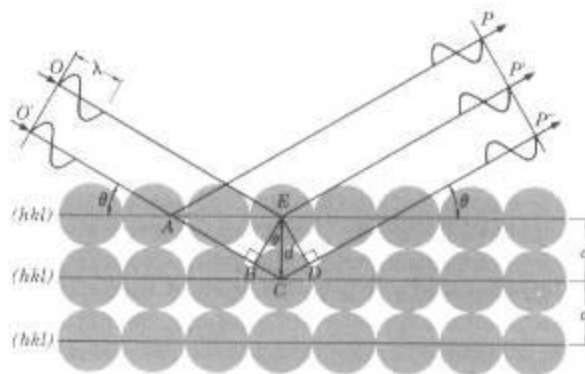
Figure 4.4: Diffraction of X-rays by crystal planes [4.8]

58

The mean crystallite size (D) is calculated using Scherrer's formula:

$$D = \frac{K\lambda}{\beta Cos\theta}$$ (4.2)

where θ is the diffraction angle of the highest intensity peak, β is the full width at half maximum (FWHM) of the highest-intensity peak, k is the Scherrer constant, and λ is the wavelength of the incident X-rays.

4.1.4. Energy dispersive X-ray spectroscopy (EDS)

EDS is a complementary technique utilized to analyze a sample's elemental composition or chemical characterization [4.9]. It is an accessory of electron microscopy instruments associated with either TEM or SEM devices with high resolution to determine the structure, and chemical composition of the elements present on the sample's surface [4.10].

Nonetheless, EDS is most associated with SEM. It is based on the study of a sample via interactions between electromagnetic radiation or particles and matter [4.11].

4.1.5. Selected area electron diffraction (SAED)

SAED is an accessory of electron microscopy instruments using a TEM device. It is used to characterize the crystalline nature of NPs from areas as small as microns or tens of nanometers via electron diffraction patterns [4.12]. Regarding a single crystal, the diffraction pattern is determined by the specimen's orientation and the structure of the sample illuminated by the electron beam [4.3]. The image depicts the space group symmetries in the NPs as well as their orientation to the beam path as illustrated in Figure 4.5.

Figure 4.5: SAED pattern of a single particle

4.2. Spectroscopic techniques

4.2.1. Attenuated total reflection Fourier transform infrared (ATR-FTIR)

ATR-FTIR is a spectroscopy technique that allows the direct measurement of samples previously pressed in a mortar using KBr (potassium bromide) powder as a matrix (holder). One of the primary benefits of ATR-FTIR imaging is very thin sample preparation before the spectral measurements due to the deep penetration of IR light into the sample regardless of thickness [4.13]. ATR-FTIR deals with the vibration of chemical bonds in a molecule at various frequencies depending on the elements and bond types range from 4000 to 400 cm^{-1} in the mid-infrared region of the electromagnetic spectrum [4.14].

The energy corresponding to absorption frequencies which represent excitations of vibrations of the chemical bonds, corresponds to the infrared region of the electromagnetic spectrum, specific to the type of bond, functional groups, chemical structure, and possible biomolecules responsible for efficient stabilization and surface modification of NPs in the detecting samples [4.15].

4.2.2. UV-Visible spectroscopy

It is an essential optical technique for the identification and characterization of electronic transitions between orbitals or bands of atoms, ions, or molecules in ranges of 200–800 nm, for measuring the change between the incident and backscattered light intensity related to the ground to excited states (absorption) and from the excited to ground states (scattering process) [4.16].

The spectrometer is composed of basic components including a light source, focusing devices, a wavelength monochromator, a photodetector, and a display instrument. The light's absorption varies, depending on the type and density of the sample and other parts of the radiant energy are transmitted to the detector and registered in the readout device [4.17].

Surface plasmons are the name given to the resonances which occur only for NPs and not for bulk metallic particles [4.18]. The shift in the surface plasmon resonance bands depends on the size, shape, and interaction of the particles with the solvent used. The optical bandgap 'Eg' is calculated using the following well-known Tauc's relation $(\alpha h\nu) = A [h\nu - Eg]^n$ where A denotes a constant, α denotes the absorption coefficient, and n denotes a constant for a given transition which is equal to 1/2 for direct bandgap and 2 for indirect bandgap. Extrapolating the linear portion of the plotted graph to the energy axis at $\alpha = 0$, yielded 'Eg 'as illustrated in

Figure 4.6. Thus, UV-Visible spectroscopy can be used to investigate the unique optical properties of NPs [4.19].
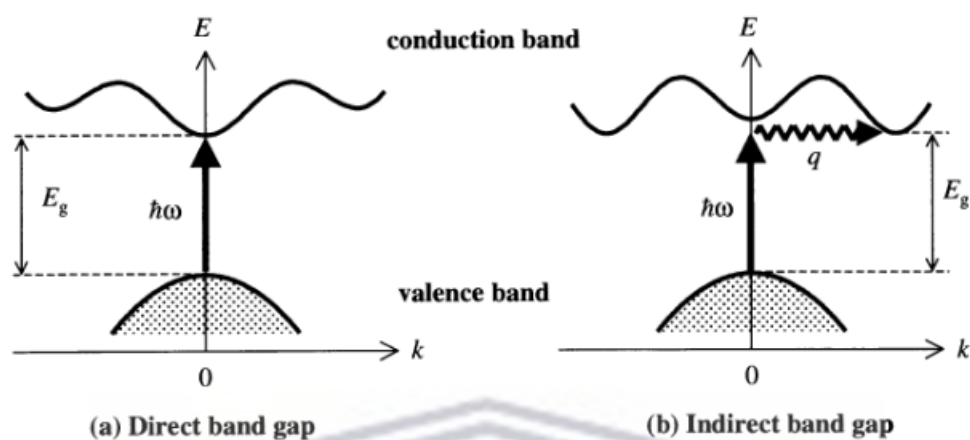
Figure 4.6: Interband transitions in (a) direct band gap and (b) indirect band gap materials [4.19]

4.2.3. Photoluminescence spectroscopy (PL)

PL is a nondestructive method for the characterization of the optical energy bands and electronic properties of molecules, for measurement of structure-induced trapping within the bandgap of semiconductors, for identification of energy levels, surface states, interface, impurities, oxygen vacancies and structure-induced trapping states present within the NPs. PL phenomenon is characterized by an excitation to an upper energy state followed by a return to a lower energy state, accompanied by the emission of a photon (electromagnetic radiation) [4.20].

Light is directed onto a sample, where it is absorbed and imparted excess energy into photoexcitation is a process that causes electrons within a material to move into permissible excited states. These excited electrons return to their equilibrium states by releasing the excess energy in the form of photons, a process known as light emission or luminescence. They are either radiative or non-radiative processes. Based on the nature of the excited state, PL is formally classified as either fluorescence or phosphorescence. [4.21]. Figure 4.7 shows a schematic diagram of PL emission.

61
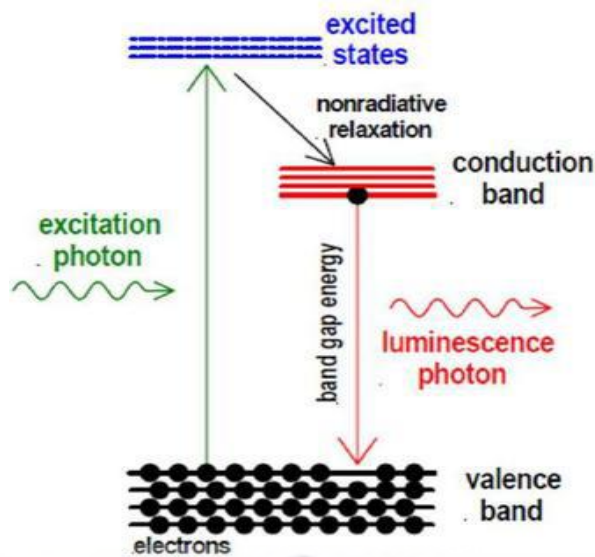
Figure 4.7: Schematic diagram of PL emission [4.22]

4.3. Magnetism

4.3.1. Magnetic nanoparticles (NPs)

They are magnetized from a magnetic field gradient which produces lines of force that penetrate the medium where the field is applied. Their notable properties are due to the numerous surface-to-volume ratios that result from the uncompensated magnetic spins assigned to the atoms' surface becoming more important and potentially causing net magnetization [4.23].

The magnetic behavior of NPs is typically characterized by a vibrating sample magnetometer (VSM) and the following are assessed: coercivity (H_c), remanent magnetization (M_r), saturation magnetization (M_s), and magneto crystalline anisotropy constant (K). The magnetic moment per unit volume defined as magnetization (M) is usually measured as a function of temperature (T) and applied magnetic field (H) [4.24].

The magnetic flux density B is given by:

$$B = \mu_0(H + M) \tag{4.3}$$

where μ_0 is the permeability of free space, $4\pi \times 10^{-7}$ H m^{-1}; H is the symbol for henry; μ_0H is the induction generated by the field alone, and μ_0M is the additional induction contributed by the sample.

Typically, the magnetic susceptibility χ is used to discuss magnetization:

62

$$\chi = \frac{M}{H} \tag{4.4}$$

The interplay of an applied field and thermal randomization leads to temperature dependence described by the Curie Law:

$$\chi = \frac{C}{T} \tag{4.5}$$

where C is a constant called the Curie constant, and T is in Kelvin.

4.3.2. Different types of magnetic behavior

The nature of interaction with a magnetic phenomenon allows the classification according to their magnetic behavior. A magnetic domain is a region of uniform magnetization. Depending on the sign and the value of θ of the Curie-Weiss law, magnetic materials are divided into three types. If θ = 0 the material is classified as an ideal paramagnet, if θ > 0 the material may be classified as an enhanced paramagnet or could be ferromagnetic for a much larger θ, if θ < 0 the material is antiferromagnetic or ferromagnetic [4.25]. A magnetization hysteresis loop is depicted in Figure 4.8.
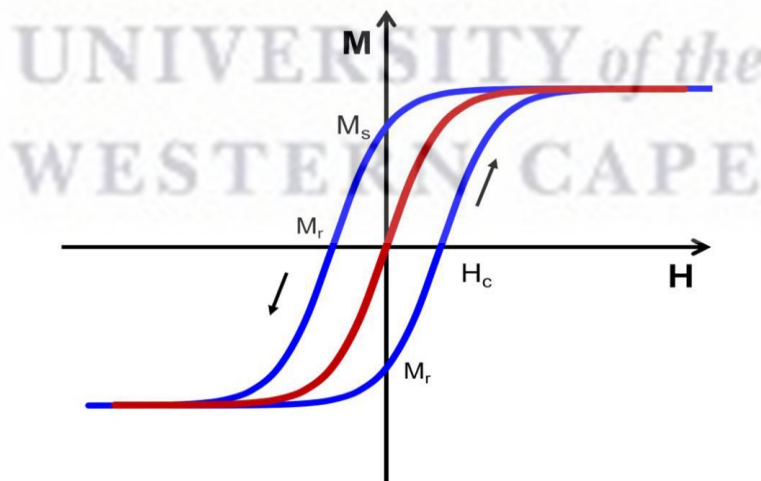
Figure 4.8: Schematic illustration of a magnetization hysteresis loop (blue) which shows the change in magnetization as a function of an applied magnetic field. A non-hysteretic magnetic curve (red) is representative of superparamagnetic behavior [4.25]

63

4.3.2.1. Superparamagnetic

Below the Curie temperature, all spins are coupled together and cooperate to yield a large moment which is firmly bound to the NPs by one or more of the variety of anisotropies K. With the reduction of particle size, the bond energy decreases as well until the thermal energy can disrupt the bonding of the total moment to the NPs [4.26]. Prior to the reverse of the magnetization process, a sufficiently large magnetic field in the opposite direction must be applied because of the magnetic moment which rapidly flips at certain temperatures and exhibits a superparamagnetic behavior which leads to a zero net magnetic moment. The size of NPs becomes smaller than their bulk [4.25].

4.3.2.2. Ferromagnetic

Above the Curie point, the Curie-Weiss Law governs susceptibility which states that $1/\chi$ rises from zero at the Curie point and increases linearly with temperature. θ is positive and typically close to the Curie temperature T_C. In contrast to paramagnetic behavior, the atomic moments post up stronger interactions caused by the electronic exchange, resulting in atomic moment alignments that are parallel or antiparallel [4.27].

Because of the strong positive interaction between the neighboring spins, the spins are aligned parallel to one another. Thermal energy disrupts the spin arrangement as the temperature rises, thus resulting in the temperature dependence of spontaneous magnetization [4.28]. Before the magnetization process can be reversed, a sufficiently large magnetic field in the opposite direction must be applied as observed in superparamagnetic. The Curie-Weiss Law becomes

$$\chi = \frac{C}{T - T_C} \tag{4.6}$$

where T_C is the Curie Temperature.

4.3.2.3. Antiferromagnetic

It seems paramagnetic at the bulk level. Antiferromagnetic NPs present a feeble and positive value of χ at the onset of cooperative behavior because the magnetic moments are discarded [4.29]. The elementary magnetic moments are linked due to an antiferromagnetic behavior characterized by an antiparallel arrangement of the spins moments resulting from interactions between neighboring atoms, called negative exchange interactions to produce a strong magnetic effect with a net moment equal to zero in the absence of a magnetic field [4.30].

64

The Curie Law becomes

$$\chi = \frac{C}{T + T_N} \tag{4.7}$$

where T_N is the Néel temperature.

4.3.2.4. Ferrimagnetic

It is like antiferromagnetic when two sublattices exist that couple through a superexchange mechanism to create an antiparallel alignment. However, the magnetic moments on the ions of the sublattices are not equal and a finite difference remains to leave a net magnetization in contrast to antiferromagnetic where it is cancelled. Magnetic ordering occurs due to the crystal structure. Ions on the octahedral sites interact with those on the tetrahedral sites with each other and spins align parallel and many atoms with unequal and spontaneous opposing magnetic moments [4.31].

4.3.2.5. Diamagnetic

Diamagnetic NPs generated an induced magnetic field in the reverse direction of an applied magnetic field, stimulating repulsion between them and lowering flux density. The Law of Lenz states that when a conducting loop is acted upon by an applied magnetic field, a current is induced in the loop that counteracts the change in the field. The atoms do not present any magnetic moments meaning that all the orbital shells are filled, and all electrons are paired [4.32].

4.3.2.6. Paramagnetic

When the atomic, ionic, or molecular constituents possess a nonzero magnetic moment, and can freely change directions, paramagnetic behavior is observed because of unpaired electrons in partly field orbitals, and some of the atoms or ions within the material possess a net magnetic moment. They cease to be ferromagnetic and become paramagnetic when the temperature is quite sensitive, above the Curie temperature and the flux density is increasing [4.33].

The spins can form permanent magnets exhibiting high magnetic permeability, characteristic saturation point, and magnetic hysteresis to obey the Curie-Weiss law [4.34]:

$$\chi_m = \frac{C}{T - \theta} \tag{4.8}$$

65

where χ_m is the molar magnetic susceptibility, C = Curie constant, and θ = Weiss constant.

The various categories of magnetic behavior are summarized in Figure 4.9 below.
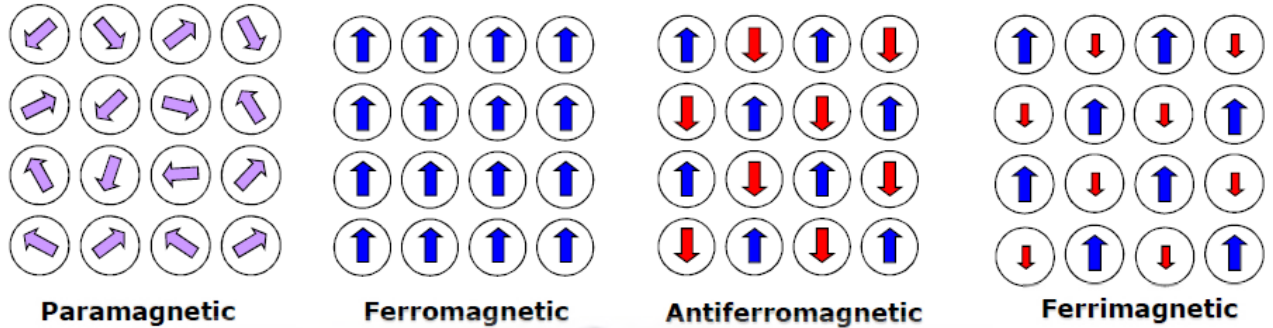
Figure 4.9: Different categories of magnetic behavior [4.33]

4.4. References

[4.1] R.F. Egerton, The Scanning Electron Microscope. In: Physical Principles of Electron Microscopy. pp. 125–153 (2005).

[4.2] M.B. Ladan, Application of Vertically Aligned Arrays of Metal-Oxide Nanowires in Heterojunction Photovoltaics, PhD Thesis, University of the Western Cape (2020).

[4.3] H.H. Rose, "Optics of high-performance electron Microscopes", Science and Technology of Advanced Materials 9 (1), pp. 14107–14130 (2008).

[4.4] S.L. Pal, U. Jana, P.K. Manna, G.P. Mohanta, R. Manavalan, Nanoparticle: an overview of preparation and characterization. Journal of Applied Pharmaceutical Science 1 (6), pp. 228–234 (2011).

[4.5] V.J.R. Fryer, The Chemical Applications of Transmission Electron Microscopy. Academic Press 92 (2), pp. 145–145 (1980).

[4.6] N.M. Zali, C.S. Mahmood, S.M. Mohamad, C.T. Foo & J.A. Murshidi, X-ray diffraction study of crystalline barium titanate ceramics. AIP Conference Proceedings 1584, pp. 160–163 (2014).

[4.7] A.K.H. Bashir, Transport and thermodynamic properties of rare earth compounds and alloys, PhD Thesis, University of the Western Cape (2017).

[4.8] W. H. Bragg, and W. L. Bragg, "The Reflection of X-Rays by Crystals." Proceedings of the Royal Society of London. Series A, Containing Papers of a Mathematical and Physical Character 88 (605), pp. 428–438 (1913).

[4.9] E. Suzuki, "High-resolution scanning electron microscopy of immunogold-labelled cells by the use of thin plasma coating of osmium". Journal of Microscopy 208 (3), pp. 153–157 (2002).

[4.10] K.K. Harish, V. Nagasamy, B. Himangshu, & K. Anuttam, Metallic Nanoparticle: A Review. Biomedical Journal of Science and Technical Research, 4 (2), pp. 3765–3775 (2018).

[4.11] R. Touroude, P. Girard, G. Maire, J. Kizling, M. Boutonnet-Kizling and P. Stenius, Preparation of colloidal platinum/palladium alloy particles from non-ionic microemulsions: Characterization and catalytic behaviour. Colloids and Surfaces 67, pp. 9–19 (1992).

[4.12] J.J. Bang, E.A. Trillo, L.E. Murr, Utilization of Selected Area Electron Diffraction (SAED) patterns for characterization of air submicron particulate matter collected by a thermophoretic precipitator. Journal of the Air & Waste Management Association 53 (2), pp. 227–236 (2003).

[4.13] P. Heera, & S. Shanmugam, Nanoparticle characterization and application: an overview. International Journal of Current Microbiology and Applied Science 4 (8), pp. 379–386 (2015).

[4.14] W. Yuan-Yuan, L. Jie-Qing, L. Hong-Gao, and W. Yuan-Zhong, Attenuated Total Reflection Spectroscopy (ATR-FTIR) Combined with Chemometrics Methods for the Classification of Lingzhi species. Molecules 24 (12), Article 2210 (2019).

[4.15] C.N. Banwell and E.M. McCash, "Fundamentals of Molecular Spectroscopy". McGraw-Hill, 4th ed., New Delhi, England (1994).

[4.16] S. Mourdikoudis, R.M. Pallares, & N.T.K. Thanh, Characterization techniques for nanoparticles: comparison and complementarity upon studying nanoparticle properties. Nanoscale 10 (27), pp. 12871–12934 (2018).

[4.17] M. Faraday, The Bakerian Lecture: Experimental Relations of Gold (and Other Metals) to Light. Philosophical Transactions of the Royal Society of London 147, pp. 145–181 (1857).

[4.18] G.C. Papavassiliou, "Optical Properties of Small Inorganic and Organic Metal Particles". Progress in Solid State Chemistry 12 (3–4), pp.185–271 (1979).

[4.19] L. Jing, L. Tianbao, Z. Yaxin, W. Peng, D. Xihua, Z. Yongcai, Solvothermal Synthesis of Visible-light Driven S,N Co-doped Titanium Dioxide Photocatalyst and Photocatalytic Reduction of Aqueous Cr(VI). Materials Reports 34 (21), pp. 21045–21051 (2020).

[4.20] M. Sadeghi, E. Babaeian, M. Tuller, S.B. Jones, The optical trapezoid model: A novel approach to remote sensing of soil moisture applied to Sentinel-2 and Landsat-8 observations. Remote Sensing of Environment 190, pp. 52–68 (2017).

[4.21] T. Chitradevi, A.J. Lenus, and N.V. Jaya, Structure, morphology, and luminescence properties of sol-gel method synthesized pure and Ag-doped ZnO nanoparticles. Mater. Res. Express 7 (1), Article 015011 (2020).

[4.22] A.D. McNaught, A. Wilkinson, & International Union of Pure and Applied Chemistry, IUPAC Compendium of Chemical Terminology: the gold book, 2nd Ed. (1997).

[4.23] D. Yoo, L. Jae-Hyun, S. Tae-Hyun, and J. Cheon, Theranostic Magnetic Nanoparticles. Acc. Chem. Res. 44 (10), pp. 863–874 (2011).

[4.24] S. Mørup, C. Frandsen, & M.F. Hansen, Magnetic Properties of Nanoparticles. The Oxford Handbook of Nanoscience and Technology, 2, pp. 713–744 (2010).

[4.25] P. Farinha, J.M.P. Coelho, C.P. Reis, M.M. Gaspar, A Comprehensive Updated Review on Magnetic Nanoparticles in Diagnostics. Nanomaterials (Basel), 11 (12), 3432 (2021).

[4.26] S. Kralj, & D. Makovec, Magnetic assembly of superparamagnetic Iron Oxides Nanoparticles Clusters into Nanochains and Nanobundles. ACS Nano 9 (10), pp. 9700–9707 (2015).

[4.27] J. Townsend, R. Burtovyy, Y. Galabura, & I. Luzinov, Flexible Chains of Ferromagnetic Nanoparticles. ACS Nano 8 (7), pp. 6970–6978 (2014).

[4.28] A.H. Morrish. The physical principles of Magnetism. John Wiley & Sons, New York (1965).

[4.29] M.S. Suzuki, I.S. Suzuki, Lecture Note on Antiferromagnet Solid State Physics. Department of Physics, State University of New York at Binghamton (2012).

[4.30] A.G. Kolhatkar, A.G. Jamison, D. Litvinov, R.C. Willson, T.R. Lee, Tuning the Magnetic Properties of Nanoparticles. International Journal of Molecular Sciences 14 (8), pp. 15977–16009 (2013).

[4.31] C. Tsun-Hsu, Ferrite Materials and Applications. In Electromagnetic Materials and Devices, IntechOpen (2019).

[4.32] E.C. Sklute, M. Eguchi, C.N. Henderson, M.S. Angelone, H.P. Yennawar, & T.E. Mallouk, Orientation of Diamagnetic Layered Transitional Metal Oxide Particles in 1-Tesla Magnetic Fields. Journal of the American Chemical Society 133 (6), pp. 1824–1831 (2011).

[4.33] S. Zanzoni, M. Pedroni, M. D'Onofrio, A. Speghini, & M. Assfalg, Paramagnetic Nanoparticles Leave Their Mark on Nuclear Spins of Transiently Adsorbed Proteins. Journal of the American Chemical Society 138 (1), pp. 72–75 (2016).

[4.34] S.A.M.K. Ansari, E. Ficiarà, F.A. Ruffinatti, I. Stura, M. Argenziano, O. Abollino, R. Carvalli, C. Guiot, and F. D'Agata, Magnetic Iron Oxide Nanoparticles: Synthesis, Characterization and Functionalization for Biomedical Applications in the Central Nervous System. Materials 12 (3), 465 (2019).

[4.35] A. Akbarzadeh, M. Samiei and S. Davaran, Magnetic nanoparticles: preparation, physical properties, and applications in biomedicine. Nanoscale Research Letters, 7 (1), 144, (2012).

CHAPTER FIVE

INFLUENCE OF SYNTHESIS METHOD ON STRUCTURAL, MORPHOLOGICAL, MAGNETIC, AND ANTIMICROBIAL PROPERTIES OF Fe-Ag AND Fe-Zn NANOPARTICLES

Abstract

This contribution reports on the development of three versatile and efficient methods, namely the green, gamma radiolysis, and distilled water for the synthesis and characterization of Fe-Ag and Fe-Zn nanoparticles (NPs), and further their growth inhibition potential on some spoilage microorganisms. Green Ag/Fe_2O_3 NPs were obtained at Fe-Ag [3:1], the annealing temperature of 800 °C for 2h; gamma irradiated Ag/Fe_3O_4 NPs at Fe-Ag [7:1], a 50 kGy dose; green ZnO/Fe_2O_3 NPs at Fe-Zn [1:1], the annealing temperature of 500 °C for 2h; and $ZnSO_4/Zn(SO_4)(H_2O)/Fe_2O_3$ NPs at Fe-Zn [2:3] synthesized from distilled water. The polycrystallinity nature of NPs observed from X-ray diffraction (XRD) was in accordance with the selected area electron diffraction (SAED). The vibrational properties confirmed the presence of bimetallic Fe-Ag and Fe-Zn NPs with the depiction of chemical bonds Fe-O, Zn-O, and Ag-O from attenuated total reflection-Fourier transform infrared spectroscopy (ATR-FTIR) analyses, and elements Ag, Fe, Zn, O from energy-dispersive X-ray spectroscopy (EDS). Photoluminescence (PL) indicated the existence of surface defects and oxygen vacancies. The magnetic properties carried out using a vibrating sample magnetometer (VSM) suggested a superparamagnetic behavior for Ag/Fe_2O_3 NPs and a weak ferromagnetic behavior for Ag/Fe_3O_4 NPs, ZnO/Fe_2O_3 NPs, and $ZnSO_4/Zn(SO_4)(H_2O)/Fe_2O_3$ NPs. Overall, the green Ag/Fe_2O_3 NPs successfully inhibited the growth of spoilage yeasts *Candida guilliermondii*, *Zygosaccharomyces fermentati*, *Zygosaccharomyces florentinus*, and spoilage molds *Botrytis cinerea, Penicillium expansum, Alternaria alstroemeriae*.

5.1. Introduction

Yeasts have traditionally been employed to manufacture alcoholic beverages, biomass, and other value-added chemicals and food products. They have numerous applications in food and beverage production such as sausage, cheese, bakery products, and other fermented foods production [5.1]. However, spoilage yeasts contaminate these foods that have been processed and packaged, resulting in a significant impact on the agri-food industry. This is largely due to

the poor handling, and processing including transportation facilities available to producers [5.2]. Some scholars reported that the yeasts *Dekkera bruxellensis*, *Dekkera anomala*, *Zygosaccharomyces bailii*, *Hanseniaspora uvarum*, *Candida guilliermondii*, *Zygosaccharomyces fermentati*, *Schizosaccharomyces pombe*, *Debaryomyces hansenii*, *Saccharomyces cerevisiae*, and *Zygosaccharomyces florentinus* are responsible for final product spoilage, and are sources of foodborne diseases [5.3–5.7]. This culminates in economic losses noticeable in populated countries such as China, India, USA, Russia, and Nigeria.

Molds and fungi are distinguishable from other organisms by the formation of hyphae (a mass of branching, tangled filaments) that result in colony development (known as a mycelium). They grow on the food's surface and proliferate in beverages under conditions whereby there is sufficient dissolved oxygen and a suitable pH [5.8]. These species, i.e., *Botrytis, Rhizopus*, *Colletotrichum*, *Alternaria*, *Fusarium*, *Penicillium*, *Aspergillus* and *Monilinia,* sp., are commonly responsible for fruit, vegetable, beverage, and food spoilage [5.9–5.11]. *Botrytis* sp. are the primary spoilage microorganisms of many agriculturally important crops, including grape berries, tomato fruits, bulb flowers, and ornamental crops among others. If ingested, they inculcate negative clinical outcomes in humans [5.12]. According to the World Health Organization (WHO), 600 million diseases and 420,000 deaths are annually reported worldwide due to these spoilage microorganisms [5.13]. As this is a concern, alternative solutions to such a problem are needed, as chemical preservatives have also been determined to be detrimental to human health [5.14]. It was also proven that the use of antibiotics against spoilage microorganisms is inefficient, and they have effects on the human body associated with severe clinical risks [5.15]. As such, some researchers found that the problem could be remediated by using nanoparticles (NPs), particularly Ag and Zn based NPs, as antimicrobial agents in food decontamination and as deactivator of toxins [5.15, 5.16]. They do assist in the generation of reactive oxygen species (ROS), which damage the spoilage organism's cell membranes via lysis, cytoplasmic contents deactivation, and disruption of cellular homeostasis, culminating in the preservation of edible goods, thus safe food, fruit, and beverages for consumers [5.17]. NPs with a combined Fe-Ag (iron-silver) or Fe-Zn (iron-zinc) crystalline matrix can enhance their appeal for application in the food industry as they can largely be recovered, i.e., due to the Fe components in their atomic structure, to minimize ingestion with Fe-Ag or Fe-Zn decontaminated food, fruit, and beverages [5.18–5.20]. Similarly, other properties such as recoverability due to magnetism have resulted in researchers conducting studies with bimetallic NPs consisting of Fe atoms [5.21, 5.22]. Such NPs are hypothesized to possess higher efficacy in their intended application, and potential recovery or reuse, due to their synergistic effects and

71

distinct properties, including their unique surface chemistry, small size, magnetism, and composition [5.18]. Therefore, bimetallic Fe-Ag and Fe-Zn NPs have been considered as suitable for reducing food contamination, and deactivation of toxins due to their perceived antimicrobial activity against many microorganisms (bacteria, yeasts, fungi, viruses). This is due to their ability to generate ROS, the bandgap, stability, novel physicochemical, biological, and magnetic properties, all of which are imparted by characteristics associated with the induction of oxygen vacancies, crystalline transformation, and light scattering pattern alterations that make them different from their counterparts albeit with inherent oxidation vulnerabilities [5.20, 5.23–5.25]. The conventional synthesis methods employed to generate such NPs present some limitations, such as the overall synthesis cost, efficacy, high-temperature usage thus high energy consumption, particularly when high vacuum systems are used to decontaminate harmful by-products during synthesis [5.21, 5.22, 5.26, 5.27]. Residual waste generated from such a synthesis process contributes to environmental problems associated with their disposal. To palliate such drawbacks, the interest has been focused on the development of one-pot, less harmful, facile, cheap, reliable, and eco-friendly synthesis protocols by using nontoxic solvents and reagents under mild conditions [5.15, 5.24]. The aim is to largely produce the desired NPs whereby the size, shape, and morphology can be controlled, with supplementary attributes such as the inhibition of spoilage microorganisms for human health concerns [5.17]. Notably, for such synthesis, high-energy gamma Co^{60} ray irradiation is considered as an effective method for the synthesis and modification of nanomaterials due to several benefits such as (1) the reduction of metal ions to zero-valent metal particles under ambient conditions with minimized use of reducing agents; (2) the ability to control the rate of reduction reaction; (3) large-scale production potential that can be favorably set up with satisfactory requirements of a clean production process [5.28–5.30]. Furthermore, producing NPs with a green synthesis method using plant extracts whereby the approach is performed without the use of chemicals (acid or base, surfactants, and solvents), generating a limited amount of waste with few by-products, further characteristics can be imparted onto the NPs due to residues of the biomolecules or organic elements in the plant extracts being embedded, i.e., additional properties associated with the enhanced immune system and blood circulation, the memory including cognitive stimulation, etc., in the final NPs [5.31, 5.32]. This is the case with NPs synthesis using some plant extracts such as *Argemonemexicana* [5.20], *Blepharis maderaspatensis* [5.23], *Passiflora edulis* [5.24], *Jatropa* [5.25], *Amaranthus blitum* [5.32], *Eryngium planum* [5.33], *Alstonia Scholaris* [5.34], *Crataegus pinnatifida* [5.35], *Euphorbia peplus* [5.36], *Vitis labrusa* [5.37], *Adotha vasica* [5.38], *Aegle marmelos* [5.39]. To

the best of our knowledge, there is no finding thus regarding the synthesis of bimetallic Fe-Ag and Fe-Zn using *Rosmarinus officinalis* (rosemary) plant extract [5.40–5.42]. This study aims to report for the first time the different properties exhibited by Fe-Ag and Fe-Zn NPs synthesized by green, gamma radiolysis and distilled water approaches, and their efficacy in inhibiting *Candida guilliermondii*, *Zygosaccharomyces fermentati*, Zygosaccharomyces *florentinus*, *Botrytis cinerea*, *Penicillium expansum* and *Alternaria alstroemeriae*, i.e., organisms associated with fruit, vegetable, beverage, and food spoilage.

5.2. Materials and Methods

5.2.1. Materials

Rosemary leaves (RL) were purchased from Western Cape Province-South Africa. Silver nitrate ($AgNO_3$), iron (III) chloride hexahydrate ($FeCl_3.6H_2O$), ferrous sulphate ($FeSO_4.7H_2O$), zinc sulphate heptahydrate ($ZnSO_4.7H_2O$), isopropyl alcohol ($CH_3CHOHCH_3$), and sodium hydroxide (NaOH) were purchased as analytical grade reagents (Sigma Aldrich, Modderfontein, Johannesburg, South Africa), and used without any further purification.

5.2.2. Methods

5.2.2.1. Preliminary works

From research performed in a basic medium, no bimetallic Fe-Ag NPs were obtained at volume ratios [1:1], [2:1], [2:3], and [4:1]; annealing temperatures of 500 and 800 °C; including 4 and 2 g of RL, using the green synthesis method. Similarly, for the gamma radiolysis approach performed at 50 kGy doses for all samples, no bimetallic Fe-Ag NPs were obtained as well at volume ratios [1:1], [2:1], [3:1], [4:1], [5:1], and [6:1].

5.2.2.2. Synthesis of Fe-Zn [2:3] with distilled water, i.e., Fe-Zn [2:3] DW

A mass of $FeCl_3.6H_2O$ (2 g) and a mass of $ZnSO_4.7H_2O$ (3 g), were added respectively into a beaker with 100 mL of boiled DW and stirred for 1 hr at 60 °C on a hot plate. The resultant beige solution was dried in an oven at 100 °C. After 4 hrs, a light-yellow powder was obtained and thereafter annealed in a ceramic crucible at 600 °C in an open-air furnace for 2 hrs, leading to a change of color from light yellow to red.

5.2.2.3. Synthesis of Fe-Zn [1:1] with an aqueous extract of RL, i.e., Fe-Zn [1:1] RL

A mass of RL (2 g) was weighed and washed with DW at ambient temperature. Subsequently, it was immersed into a beaker with 100 mL of boiled DW and stirred for 2 hrs at 80 °C on a hot plate. The extract solution was filtered twice with a Whatman paper (N°5) to eliminate residual solids. Thereafter, a mass of $FeCl_2$ (0.5 g) and a mass of $ZnCl_2$ (0.5 g) in addition to a mass of polyvinyl pyrrolidone (2 mg), were added respectively into another beaker with 100 mL of filtered RL extract and stirred for 1 hr at 60 °C on a hot plate. The pH of the resultant extract was found to be 3.35 with a dark green color. This extract was dried in an oven at 100 °C. After 6 hrs, a black powder was obtained and thereafter annealed in a ceramic crucible at 500 °C in an open-air furnace for 2 hrs without change of color.

5.2.2.4. Synthesis of Fe-Ag [3:1] with an aqueous extract of RL, i.e., Fe-Ag [3:1] RL

A mass of RL (2 g) was weighed and washed with DW at ambient temperature. Subsequently, it was immersed into a beaker with 100 mL of boiled DW and stirred for 2 hrs at 80 °C on a hot plate. The extract solution was filtered twice with a Whatman paper (N°5) to eliminate residual solids. Thereafter, a mass of $AgNO_3$ (50 mg) and a mass of $FeCl_3.6H_2O$ (150 mg), were added respectively into another beaker with 100 mL of filtered RL extract and stirred for 1 hr at 60 °C on a hot plate. The pH of the resultant extract was found to be 1.75 with a dark brown color. A mass of NaOH (2 g) was added dropwise into the mixture for a basic medium. The pH of the resultant extract was found to be 11.20 without a change of color. This extract was dried in an oven at 100 °C. After 4 hrs, a black powder was obtained and thereafter annealed in a ceramic crucible at 800 °C in an open-air furnace for 2 hrs, leading to a change of color from black to red.

5.2.2.5. Synthesis of Fe-Ag [7:1] by gamma radiolysis using Co^{60} as source, i.e., Fe-Ag [7:1] Gamma

A mass of $FeSO_4.7H_2O$ (700 mg) and a mass of $AgNO_3$ (100 mg), were immersed respectively into a beaker with 25 mL of boiled DW and stirred for 30 min at 50 °C on a hot plate. The pH of the resultant solution was found to be 4.53 with an orange color. Thereafter, 10 mL of $CH_3CHOHCH_3$ was added as a scavenger of OH radicals, and a mass of NaOH (75 mg) was added dropwise into the mixture for a basic medium, followed by another 30 min of stirring on a hot plate at 50 °C. The pH of the resultant solution was found to be 10. Two distinct phases were observed (at the top grey color and the bottom black color). The mixture solution was transferred into a test tube for the irradiation process, which was performed after one week. It

was exposed to a 50 kGy dose at a dose rate of 50 kGy/min using Co^{60} as the source at ambient temperature. After the irradiation process, the two distinct phases were still observed. The final solution was centrifuged thrice at 4000 rpm for 20 min with DW and ethanol. Thereafter, it was dried in an oven at 60 °C for 4 hrs. A black powder was obtained as the final color.

5.2.3. Analytical techniques

High-resolution transmission electron microscopy (HRTEM) measurements were performed using a Joel JEM 4000 EX electron microscope at an accelerating voltage of 200 kV equipped with selected area electron diffraction (SAED). Field emission scanning electron microscopy (FESEM) measurements were performed using a Zeiss Ultra 55 scanning electron microscope, equipped with energy-dispersive X-ray spectroscopy (EDS). EDS spectrum was collected with an EDS Oxford instrument with an X-Max solid-state silicon drift detector operated at 20 kV. An X-ray diffractometer (model Bruker AXS D8 Advance) with an irradiation line Kα1 of copper (λCuKα1=1.5406 Å) operating at a voltage of 40 kV and a current of 35 mA, in the angular range of 20 to 90°, was used to study the crystalline nature and structure of the NPs. An attenuated total reflection-Fourier transform infrared (ATR-FTIR) absorption spectrometer (Thermo Nicolet 8700 FTIR spectrometer) was used in the spectral range 400–4000 cm^{-1} to ascertain the surface coating and chemical bonding. Photoluminescence (PL) spectroscopy was recorded from 200 to 800 nm using a Varian Cary Eclipse Fluorescence Spectrophotometer at an excitation wavelength of 372 nm. The magnetic properties were measured at room temperature using a vibrating sample magnetometer (VSM), (Cryogenic Ltd., UK). Gamma-ray with a Co^{60} source type GIK-9-4, S/N 08398 and 56 TBq was used.

5.2.4. Antimicrobial activities

5.2.4.1. Microorganisms' origin, culture condition, and inoculum preparation

The spoilage organisms used for the study were obtained from the Agricultural Research Council (ARC) Infruitec-Nietvoorbij culture collection (The Fruit, Vine and Wine Institute of the Agricultural Research Council, Stellenbosch, South Africa). From the culture collection, the spoilage yeasts were streaked out on Yeast Malt Peptone Agar (YMA), Glucose (10 g/L), Malt extract (3 g/L), agar bacteriological (20 g/L), Peptone (5 g/L) and incubated at 28 °C until sufficient growth was obtained from the fully-grown plates containing pure colonies of *Candida guilliermondii*, *Zygosaccharomyces fermentati*, and *Zygosaccharomyces florentinus*. The yeast cultures were further prepared by transferring a wire loop full colony of each yeast into a volume of 5 mL of Yeast Malt broth (YMB) (Sigma Aldrich, SA), and were incubated at 28 °C

75

for 48 hrs. From each yeast culture broth, the cell concentration was determined by direct count using a Neubauer counting chamber under a microscope at 400x magnification. As described in the method developed by Mewa-Ngongang et al., 2017 [5.3], a seeding concentration of 10^6 cells/mL in white grape juice agar was used for each of the spoilage yeasts in three replicates. Fruit spoilage molds, *Botrytis cinerea*, *Penicillium expansum* and *Alternaria alstroemeriae*, were cultured for 7 to 14 days at 25 °C on potato dextrose agar (PDA, Merck, South Africa). The spore solutions were prepared by lightly scrapping off the surface of the agar with sterile distilled rinsing water. The scrapping off process was done three times to achieve a 100 mL mother spore solution in 250 mL Scott bottles for each mold. A 400x microscopic magnification was used to count the spores from the mother solution, which will allow a preparation of a 10^5 spores/mL solution to be used as inoculum during the growth inhibition assay [5.9, 5.10].

5.2.4.2. Growth inhibition assay and activity quantification

The growth inhibition method used in this work was adopted from Mewa-Ngongang et al., 2017 [5.3], using grape pomace extract (GPE) agar as a test medium. A mass of 0.2 g of the annealed powders of Fe-Zn [2:3] DW, Fe-Zn [1:1] RL, Fe-Ag [3:1] RL, and Fe-Ag [7:1] Gamma, were immobilized in a 100 µL volume of sterile distilled water and were tested against selected spoilage yeasts. From the resulting mixtures, a volume of 10 µL was spotted in 5 mm diameter and 1.7 mm depth wells created on the test agar plates using an agar driller [5.4, 5.39]. Before plate inspection for the presence of inhibition zones around the wells, the seeded plates were incubated for 72 hrs at a temperature of 22 °C. Each sample was tested in three replicates and the average diameter of the zone of inhibition was used for the quantification of growth inhibition activity.

The growth inhibition effect of the best performing (n=2) NP solutions on mold spore germination was carried out following the aforementioned approach. In three replicates per treatment, the GPE test agar medium was seeded with the corresponding mold spores at the concentration of 10^5 spores/mL. The plates were incubated at 20 °C until a clear zone of inhibition was observed around the 5 mm wells, in which a volume of 10 µL was spotted.

The concept of the volumetric zone of inhibition (VZI) [5.4] was used to quantify the growth inhibition activity of Fe-Zn [2:3] DW; Fe-Zn [1:1] RL; Fe-Ag [3:1] RL; and Fe-Ag [7:1] Gamma solutions against common beverage and fruit spoilage organisms identified, i.e. *C. guilliermondii*, *Z. fermentati*, *Z. florentinus*, *B. cinerea*, *P. expansum*, and *A. alstroemeriae*. The VZI concept expressed in a liter of contaminated solidified media per milliliter of antimicrobial compounds/agents used, i.e., L CSM/mL ACU, is interpreted as the volume of the contaminated

medium at a specific cell or spore concentration per milliliter growth-inhibiting solution of the Fe-Zn [2:3] DW; Fe-Zn [1:1] RL; Fe-Ag [3:1] RL; and Fe-Ag [7:1] Gamma. This method was developed to estimate the number of NPs or antimicrobial agents required to control spoilage organisms and remove the targeted microbial contamination.

5.3. Results and Discussion
5.3.1. Crystallography analyses

The determination of the crystal structure and purity phase of Fe-Ag and Fe-Zn NPs were investigated by X-ray diffraction (XRD) analyses as illustrated in Figure 5.1.

XRD of Fe-Zn [2:3] DW in Figure 5.1 (a) generated a $ZnSO_4$/$Zn(SO_4)(H_2O)$/Fe_2O_3 diffraction peaks, i.e. zinc sulphate ($ZnSO_4$), zinc sulphate hydrate ($Zn(SO_4)(H_2O)$), and hematite (Fe_2O_3), with their maxima centered at 2θ (°) = 18.73, 21.37, 25.12, 26.37, 33.86, 36.63, 45.79, 51.34, 54.12, 59.11, 63.83, and 67.29 corresponded with the reflections planes of (110), (020), (121), (111), (104), (004), (024), (034), (116), (051), (300), and (060), consistent with the JCPDS pattern numbers 01-080-2210 for $ZnSO_4$, 01-081-0022 for $Zn(SO_4)(H_2O)$, and 033-0664 for Fe_2O_3. From the findings, it is noticeable that the metal salt precursor was not able to reduce $ZnSO_4$/$Zn(SO_4)(H_2O)$ to ZnO. This was attributed to non-existent reducing or capping agents in distilled water. By fitting the values to the Scherrer equation, the average particle size was found to be 28.47 nm.

XRD of Fe-Zn [1:1] RL in Figure 5.1 (b) denoted a ZnO/Fe_2O_3 structure with intensive peaks only being obtained with Fe_2O_3, revealing a poor ZnO crystallinity with very feeble peaks. Their maxima centered at 2θ (°) = 23.96, 30.28, 33.06, 35.48, 40.87, 49.41, 54.06, 57.40, 62.23, 63.91, and 69.10 matched with the reflection's planes of (012), (100), (104), (110), (113), (024), (116), (122), (214), (300), and (201), consistent with the JCPDS pattern numbers 036-1451 for zinc oxide (ZnO) and 033-0664 for (Fe_2O_3). The obtained peaks are in line with the works of Noukelag et al., 2020 [5.41, 5.42] on the synthesis of ZnO and Fe_2O_3 using RL extract, respectively. By fitting the values to the Scherrer equation, the average particle size was found to be 37.97 nm.

XRD of Fe-Ag [3:1] RL in Figure 5.1 (c), displayed an Ag/Fe_2O_3 NP profile. The presence of intense and well-defined diffraction peaks of silver (Ag) and hematite (Fe_2O_3) with their

maxima centered at 2θ (°) = 24.33, 33.05, 35.45, 38.07, 44.17, 49.19, 53.98, 62.28, 64.46, and 77.32 matched to the reflections planes of (012), (104), (110), (111), (200), (024), (116), (214), (220), and (311), indicating the highly crystalline nature of face-centered cubic Ag/Fe_2O_3, consistent with the JCPDS pattern numbers 004-0783 for Ag and 033-0664 for Fe_2O_3 These results are in accordance with the works of Shimpi et al., 2018 [5.34] who synthesized Ag/Fe_2O_3 NPs using an aqueous extract of *Alstonia scholaris*. By fitting the values to the Scherrer equation, the average particle size was found to be 39.59 nm.

XRD of Fe-Ag [7:1] Gamma in Figure 5.1 (d), portrayed an Ag/Fe_3O_4 NP profile. The presence of intense and well-defined diffraction peaks of silver (Ag) and (Fe_3O_4) with their maxima centered at 2θ (°) =30.03, 35.47, 38.08, 42.92, 44.53, 57.21, 62.84, 64.65, and 74.31 corresponded to the reflections planes of (220), (311), (111), (400), (200), (511), (440), (220), and (533), showing the highly crystalline nature of the rhombohedral $Ag-Fe_3O_4$, consistent with the JCPDS pattern numbers 004-0783 for Ag and 019-0629 for Fe_3O_4. The results corroborate with the works of Liu et al., 2017 [5.26] who evaluated the anticancer properties of $Ag@Fe_3O_4$ NPs. By fitting the values to the Scherrer equation, the average particle size was found to be 28.57 nm.
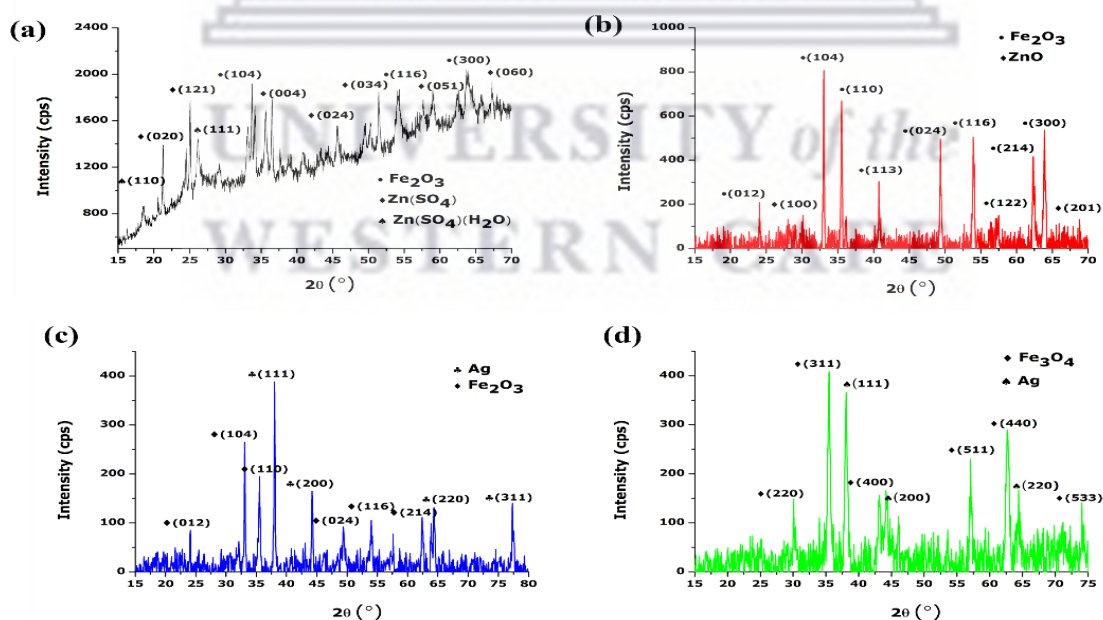
Figure 5.1: XRD results of **(a)** Fe-Zn [2:3] DW, **(b)** Fe-Zn [1:1] RL, **(c)** Fe-Ag [3:1] RL, and **(d)** Fe-Ag [7:1] Gamma

Table 5.1 illustrates major XRD characteristics of the various Bragg diffraction peaks of the annealed samples of Fe-Zn and Fe-Ag using the Scherrer equation.

Table 5.1: Major XRD characteristics of the various Bragg diffraction peaks of Fe-Zn [2:3] DW, Fe-Zn [1:1] RL, Fe-Ag [3:1] RL, and Fe-Ag [7:1] Gamma

NPs	(hkl)	2θ(degree)	FWHM (degree)	Crystalline size (Å)	Average Crystalline size (nm)
$Zn(SO_4)(H_2O)$	(110)	18.73	0.8087	99.56	28.47
$ZnSO_4$	(020)	21.37	0.1331	607.40	
$ZnSO_4$	(121)	25.12	0.1808	450.17	
$Zn(SO_4)(H_2O)$	(111)	26.37	0.4183	195.06	
Fe_2O_3	(104)	33.86	0.1905	453.92	
$ZnSO_4$	(004)	36.63	0.2053	407.61	
$ZnSO_4$	(024)	45.79	0.7948	108.50	
$ZnSO_4$	(034)	51.34	0.6429	137.10	
Fe_2O_3	(116)	54.12	0.7351	121.35	
Fe_2O_3	(012)	23.96	0.2378	341.51	37.97
Fe_2O_3	(104)	33.06	0.4181	198.20	
Fe_2O_3	(110)	35.48	0.4916	169.67	
Fe_2O_3	(113)	40.87	0.1178	719.80	
Fe_2O_3	(024)	49.41	0.1573	555.92	
Fe_2O_3	(116)	54.06	0.3143	283.75	
Fe_2O_3	(214)	62.23	0.2009	461.89	
Fe_2O_3	(300)	63.91	0.3048	307.19	
Fe_2O_3	(012)	24.33	0.1306	622.27	39.59
Fe_2O_3	(104)	33.05	0.1506	550.24	
Fe_2O_3	(110)	35.45	0.2881	289.49	
Ag	(111)	38.07	0.1742	482.42	

Ag	(200)	44.17	0.3562	240.69	
Fe_2O_3	(024)	49.19	0.3355	260.42	
Ag	(311)	77.32	0.3118	326.30	
Fe_3O_4	(220)	30.03	0.3497	591.75	28.57
Fe_3O_4	(311)	35.47	0.3842	217.09	
Ag	(111)	38.08	0.3995	210.36	
Fe_3O_4	(400)	42.92	0.3497	216.27	
Fe_3O_4	(440)	62.84	0.4822	193.06	

5.3.2. Microscopic observations

Figure 5.2 portrays the shape, size, internal structure, and crystallinity of Fe-Ag NPs from FESEM (Field emission scanning electron microscopy) and HRTEM (High-resolution transmission electron microscopy) micrographs.

Well assembled, agglomerated, and crystalline NPs were showcased with a face-centered cubic structure, spherical shape for Fe-Zn [1:1] RL and Fe-Ag [3:1] RL; rhombohedral structure, cubic shape for Fe-Ag [7:1] Gamma. No specific form is observed with Fe-Zn [2:3] DW that could be explained by the lack of reducing/capping agents. Energy-dispersive X-ray spectroscopy (EDS) spectra confirmed the presence of elements Fe, Ag, Zn, and O with some contaminating elements. Selected area electron diffraction (SAED) exhibited multiple diffraction rings with clear diffraction spots demonstrating its polycrystallinity as observed in XRD analyses. The observations concurred with XRD and FESEM results.

By fitting the histogram data with a Gaussian distribution, the average particle size extracted from the HRTEM micrographs was found to be 23.20 ± 0.51 nm for Fe-Zn [2:3] DW, 26.60 ± 0.35 nm for Fe-Zn [1:1] RL, 20.00 ± 0.63 nm for Fe-Ag [3:1] RL and 15.37 ± 0.55 nm for Fe-Ag [7:1] Gamma, respectively.
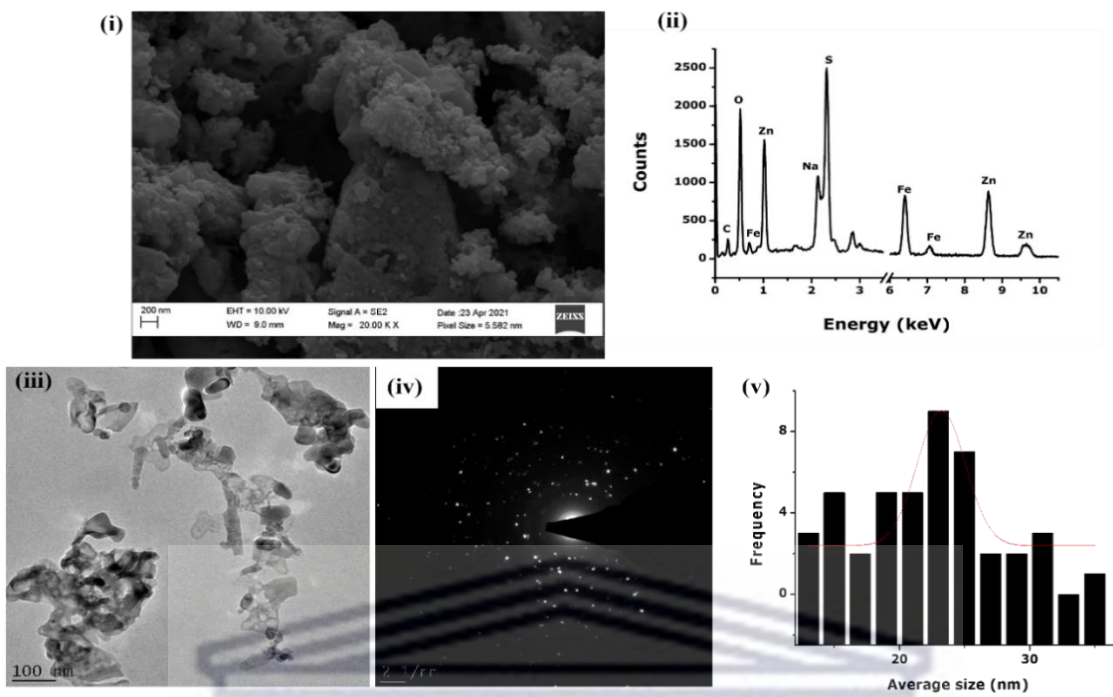
Figure 5.2 (a): (i) FESEM, **(ii)** EDS, **(iii)** HRTEM, **(iv)** SAED, and **(v)** Average size distribution of Fe-Zn [2:3] DW
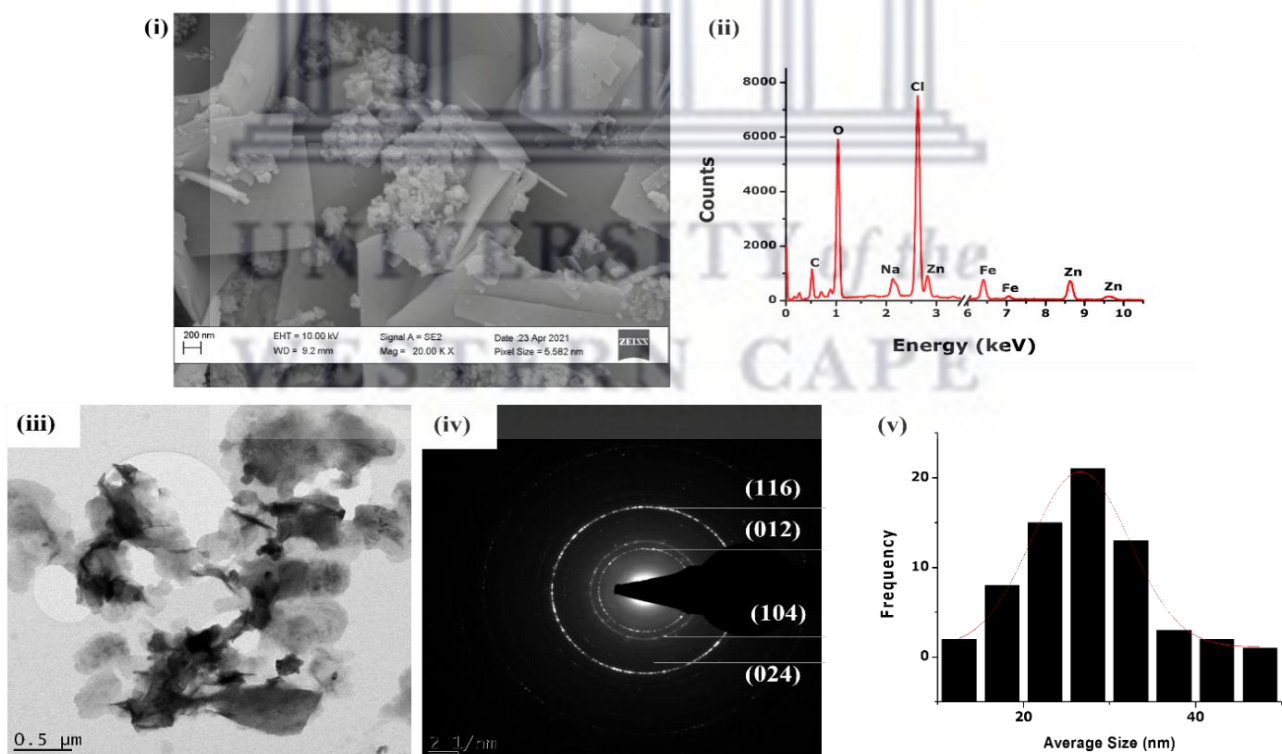
Figure 5.2 (b): (i) FESEM, **(ii)** EDS, **(iii)** HRTEM, **(iv)** SAED, and **(v)** Average size distribution of Fe-Zn [1:1] RL

81
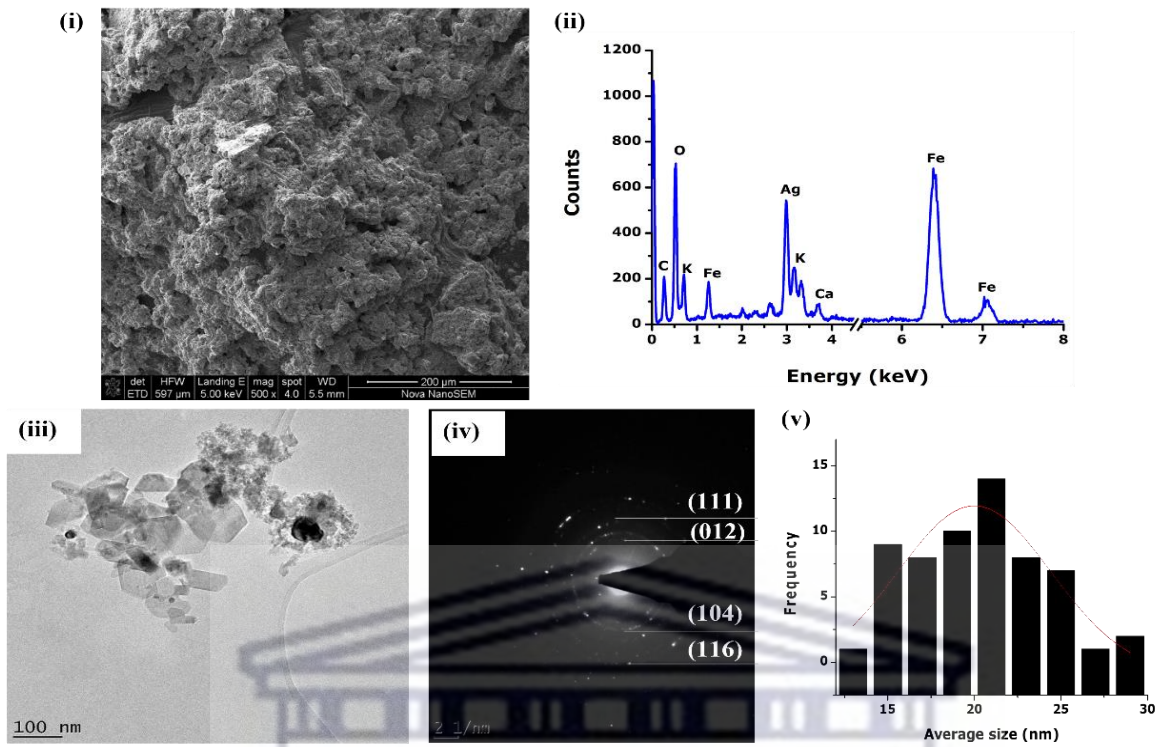
Figure 5.2 (c): **(i)** FESEM, **(ii)** EDS, **(iii)** HRTEM, **(iv)** SAED, and **(v)** Average size distribution of Fe-Ag [3:1] RL
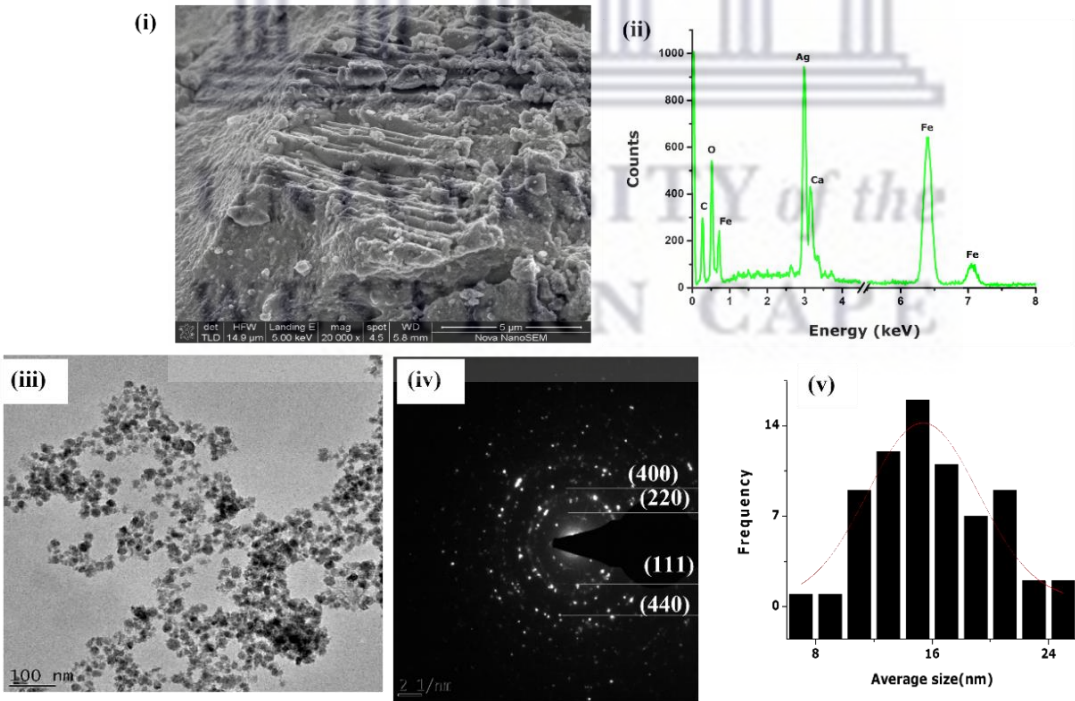
Figure 5.2 (d): **(i)** FESEM, **(ii)** EDS, **(iii)** HRTEM, **(iv)** SAED, and **(v)** Average size distribution of Fe-Ag [7:1] Gamma

5.3.3. Vibrational properties

To validate and confirm the purity of Fe-Zn [2:3] DW, Fe-Zn [1:1] RL, Fe-Ag [3:1] RL, and Fe-Ag [7:1] Gamma, attenuated total reflection-Fourier transform infrared spectroscopy (ATR-FTIR) studies were carried out to identify the possible molecules involved in the synthesis as presented in Figure 5.3.

The peaks that appear around 400 and 500 cm^{-1}, are from the skeleton of iron oxide (–O–Fe), and (-O-Zn)/(-O-Ag) stretching vibration mode, respectively, which indicate the presence of Fe-Zn and Fe-Ag NPs [5.24, 5.32]. The prominent peaks around 800 cm^{-1}, are ascribed to the FeOOH group [5.42]. Additionally, the absorption bands around 1000 cm^{-1} are assigned to the C-N of aliphatic amines or alcohols/phenols [5.21] with absorption bands located around 1300 and 1600 cm^{-1} representing the symmetric and asymmetric bending modes of C=O bonds of amino acid and esters, respectively [5.33, 5.38]. Finally, the broad peaks centred approximately around 2000, and 3400 cm^{-1} are associated respectively with standard H_2O bending modes and OH stretching [5.39, 5.41]. Overall, the results reveal that Fe-Zn [2:3] DW was not pure due to non-identified peaks.
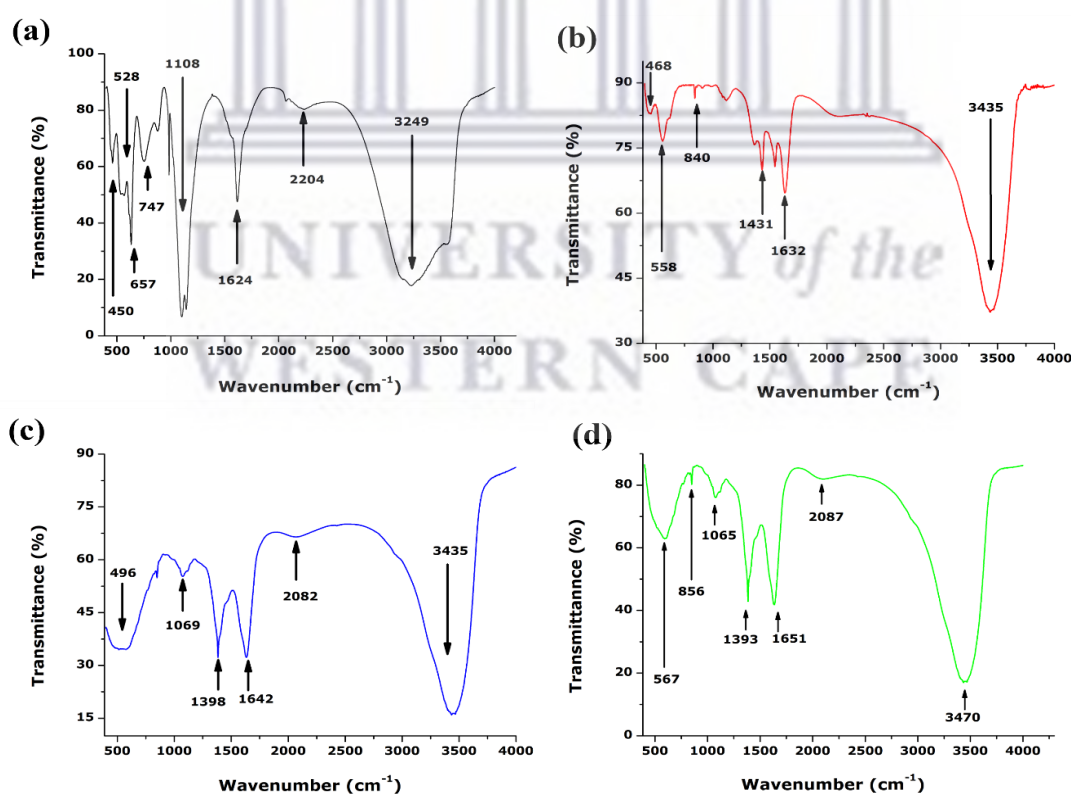
Figure 5.3: ATR-FTIR results of **(a)** Fe-Zn [2:3] DW, **(b)** Fe-Zn [1:1] RL, **(c)** Fe-Ag [3:1] RL, and **(d)** Fe-Ag [7:1] Gamma

83

5.3.4. Photoluminescence (PL)

It is a vital phenomenon to detect the optical properties of NPs in which the emission of light takes place from the material under optical excitation, and useful indicator for determining the recombination rate and life span of photogenerated charge carriers according to the fluorescence intensity [5.17, 5.34]. Figure 5.4 showcases PL of Fe-Zn [2:3] DW, Fe-Zn [1:1] RL, Fe-Ag [3:1] RL, and Fe-Ag [7:1] Gamma. In the entire PL spectra, there were four clear peaks at 427, 431, 502, and 587 nm, corresponding to visible emissions.

At 427 and 431 nm, very strong blue-green emission peaks were observed, which are similar to the electronic transitions between the conduction band edges to the deep level acceptors. These emission peaks are induced by band edge emission, which is caused by the recombination of electrons and holes of free excitons [5.22, 5.32]. The green emission observed at 502 nm may be ascribed to the oxygen vacancy, which is associated with the radiative recombination process, and it is a radiative transition of an electron from a deep donor level to an acceptor level. The peak obtained at 587 nm corresponds to a yellow emission associated with the interstitial defects of zinc or oxygen vacancies [5.39]. The appearance of these visible emissions in the visible spectrum suggested that the NPs had a high surface-to-volume ratio with multiple surface-states and native defects (vacancies and interstitials) which generate the trap levels responsible for the observed emissions. Besides, the method of synthesis and experimental conditions may affect various factors such as oxygen deficiency, surface roughness including chemistry, and impurity centers [5.32].
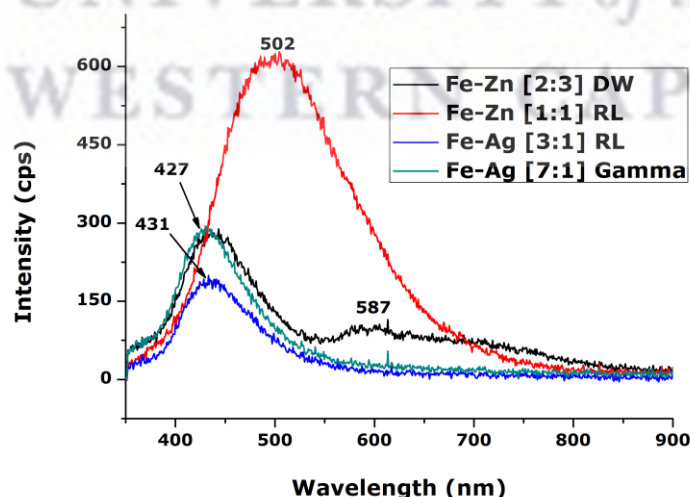
Figure 5.4: PL results of Fe-Zn [2:3] DW, Fe-Zn [1:1] RL, Fe-Ag [3:1] RL, and Fe-Ag [7:1] Gamma

5.3.5. Magnetic properties

Figure 5.5 exhibits the different magnetic properties of Fe-Zn [2:3] DW, Fe-Zn [1:1] RL, Fe-Ag [3:1] RL, and Fe-Ag [7:1] Gamma, assessed via a vibrating sample magnetometer (VSM) where the moments in comparison to applied magnetic field are presented. The temperature of the samples was kept constant at 300 K during the measurement. The applied magnetic field, from the superconducting magnet, varied from -3 T to +3 T, while the vibrating amplitude and frequency of the sample holder were set at 0.2 Hz and 20 Hz, respectively. These NPs can be tuned from superparamagnetic to paramagnetic by modifying the proportion between the Fe and Zn/Ag constituents; albeit this is dependent on other parameters including the synthesis method, average size, amount, and distribution of cations, annealing temperature, dose rate, and oxygen ion occupancy [5.18, 5.43].

5.3.5.1. Ferromagnetic behavior

The magnetic hysteresis loops (M-H) suggested a weak ferromagnetic behavior of Fe-Zn [2:3] DW/Fe-Zn [1:1] RL, and Fe-Ag [7:1] Gamma. The low value of saturation magnetization (M_s = 0.0018 and 0.0024 emu/g) compared to bulk values of Fe (218 emu/g), Fe_2O_3 (74 emu/g), and Fe_3O_4 (93 emu/g), confirmed the existence of doping elements as demonstrated by XRD and ATR-FTIR analyses. It could be explained by a higher number of defects such as oxygen vacancies at the sample's surface [5.44]; a decrease in superexchange interaction between iron cations in the tetrahedral and octahedral sites resulting in three important factors such as impurity phases, cationic distribution, surface morphology or size of NPs [5.16].

5.3.5.2. Superparamagnetic behavior

The magnetic hysteresis loops (M-H) of Fe-Ag [3:1] RL, i.e., Ag/Fe_2O_3 NPs, presents a very low coercivity (H_c = 0.015 T) close to zero, a very low magnetic remanence (M_r = 0.0012 emu/g) and saturation magnetization (M_s = 0.0026 emu/g). The drop in the saturation magnetization value of the Ag/Fe_2O_3 NPs may be interpreted as evidence of the effective incorporation of silver metal onto the iron oxide NPs [5.45]. The magnetic measurements suggested a superparamagnetic behavior of Ag/Fe_2O_3 NPs owing to the reduced coordination symmetry between oxygen atoms at the surface of the NPs, disordered surface spins [5.22], to crystallinity, particle size and concentration of the plant extract. The magnetic behavior observed is in line with the works of Mohamed et al., 2001 [5.27] who assessed the magnetic properties of α-Fe/Ag nanocomposites synthesized by a modified polyol route.

85

Overall, the low coercivity (H_c) accounts for the small value of the magnetocrystalline anisotropy constant (K), which was calculated from the following equation:

$$H_c = \frac{0.98\,K}{M_s} \tag{5.1}$$

Furthermore, the value of the squareness (M_r/M_s) was calculated and reported in Table 5.2. Ag/Fe$_2$O$_3$ NPs showed the interaction of NPs by magnetostatic interactions as the squareness < 0.5 [5.16].
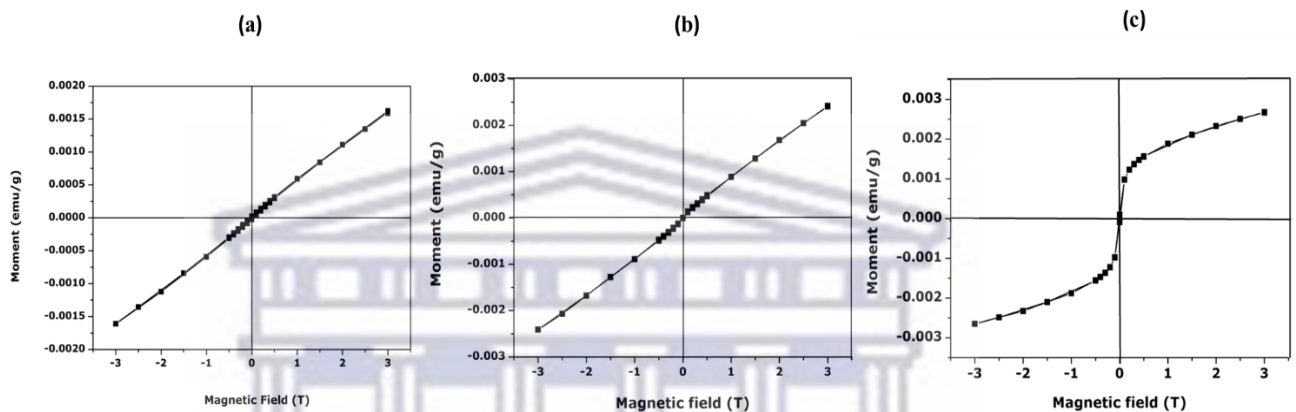
Figure 5.5: Magnetic moments of **(a)** Fe-Zn [2:3] DW/Fe-Zn [1:1] RL, **(b)** Fe-Ag [7:1] Gamma, and **(c)** Fe-Ag [3:1] RL, i.e., Ag/Fe$_2$O$_3$

Table 5.2: Magnetic parameters of Ag/Fe$_2$O$_3$ NPs

Magnetic parameters	H_c (T)	M_s (emu/g)	M_r (emu/g)	Squareness (M_r/M_s)	Magnetocrystalline anisotropy constant K (erg/T) x 10^{-5}	Behavior
Ag/Fe$_2$O$_3$	0.015	0.0012	0.0026	0.461	3.979	Superparamagnetic

5.3.6. Antimicrobial properties

The growth inhibition potential of 20 % (m/v) of Fe-Zn [2:3] DW, Fe-Zn [1:1] RL, Fe-Ag [3:1] RL, and Fe-Ag [7:1] Gamma, against common beverage and food spoilage yeasts *Z. fermentati*, *C. guilliermondii*, *Z. florentinus* (see Figure 5.6), and spoilage fruit spoilage molds *B. cinerea*, *P. expansum*, and *A. alstroemeriae*, was assessed and the results showed the different levels of

86

growth inhibition activity (see Figure 5.7). In general, the antimicrobial activity of NPs depends on their concentration, size, contact or penetration into microbes' cells. In Figure 5.6, Fe-Ag [3:1] RL solution was found to exhibit a higher growth inhibition activity than others. The highest VZI of 10.71 L CSM/ mL ACU suggested that a volume of 1 mL at 20 % (m/v) Fe-Ag [3:1] RL solution can suppress the growth of *Z. fermentati* in 10.71 L of contaminated food/beverage at a cell concentration of 10^6 cell/mL. The value of 10.60 is a significant increase in the growth inhibition with a VZI up to x 7.52 higher in comparison with the works of Mewa-Ngongang et al. [5.3] with C. *guilliermondii*. It is noticeable here that the synthesis method determines the antimicrobial properties with the agglomeration of Fe-Ag and Fe-Zn NPs on microbial surfaces, producing degradation of cellular membrane and decrease of permeability. The solution of Fe-Zn [1:1] RL did not present any antimicrobial activity compared to Fe-Zn [2:3] DW. The reasons might be the aggregation of iron and zinc cations without trapping several microorganisms' cells, the formation of a passive FeOOH layer [5.43], the low concentration of Fe and Zn or the resistance to penetrate the cell structure of spoilage yeasts and damage its walls.
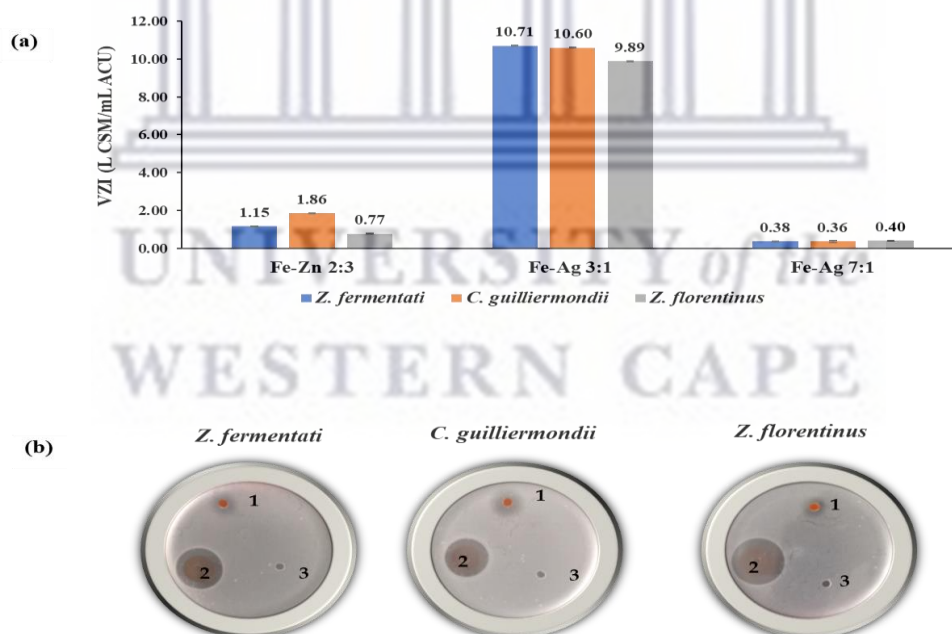
Figure 5.6: (a) The histogram and **(b)** the photograph showing the growth inhibition activity of 20 % (m/v) of Fe-Zn [2:3] DW, Fe-Ag [3:1] RL, Fe-Ag [7:1] Gamma, against *Z. fermentati, C. guilliermondii*, and *Z. florentinus*. VZI in L CSM/mL ACU = Volumetric Zone of Inhibition, expressed in Liter of Contaminated Solidified Media per milliliter of Antimicrobial Compound Used

87

The strong growth inhibition activity exhibited by Fe-Ag [3:1] RL and Fe-Zn [2:3] DW against spoilage yeasts were selected for further growth inhibition tests against fruit spoilage molds i.e., *B. cinerea*, *P. expansum*, and *A. alstroemeriae*. The highest VZI are observed with Fe-Ag [3:1] RL. The results extended the broad-spectrum of growth inhibition potential, match with the findings of Sameer et al., 2017 [5.38] who reported on better antimicrobial activity of green synthesized Ag@Fe$_2$O$_3$ nanocomposites from leaf extract of *Adathoda Vasica*.
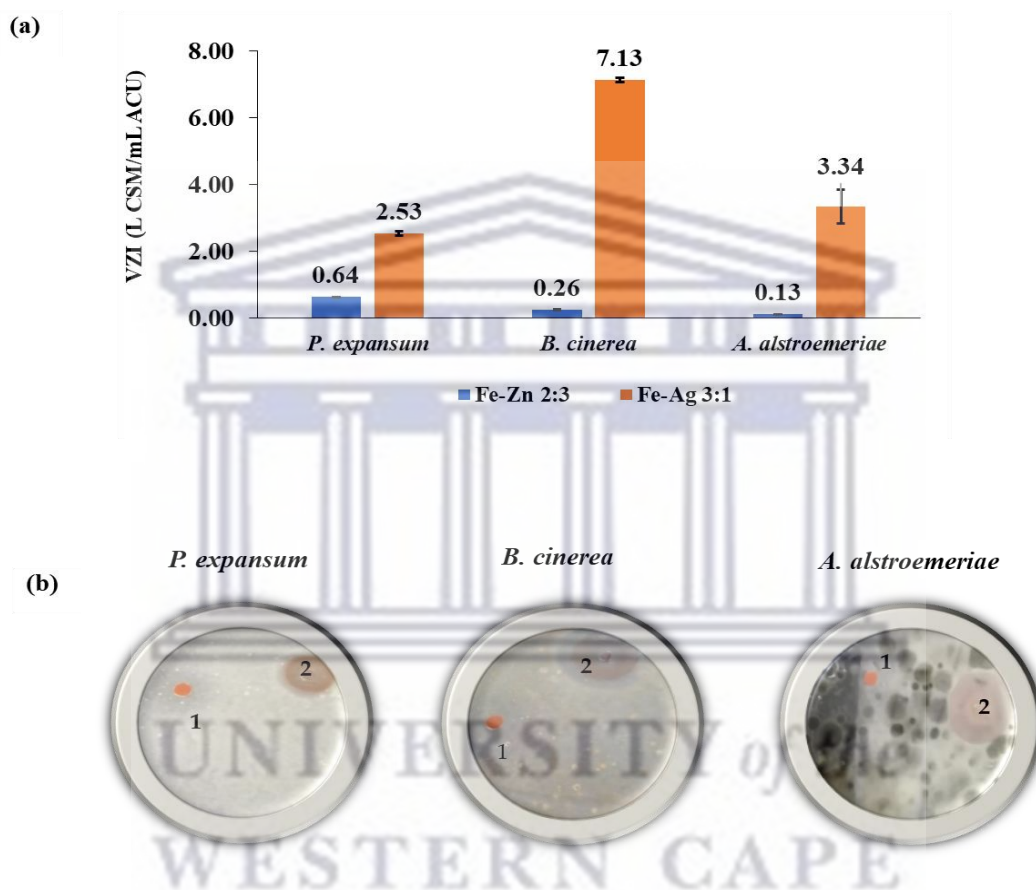
Figure 5.7: (a) The histogram and **(b)** the photograph showing the growth inhibition activity of 20 % (m/v) of Fe-Zn [2:3] DW (1), Fe-Ag [3:1] RL (2), against *P. expansum*, *B. cinerea*, and *A. alstromeriae*. VZI in L CSM/mL ACU = Volumetric Zone of Inhibition, expressed in Liter of Contaminated Solidified Media per milliliter of Antimicrobial Compound Used

These findings report for the first-time using growth inhibition potential test of 20 % (m/v) through the VZI concept, successfully quantifying the biocidal effect of Ag/Fe$_2$O$_3$ NPs on the germination of yeast and mold spores expressed in L CSM/mL ACU.

88

The lowest or inexistent antimicrobial activity observed with other samples could be due to its inability to generate enough reactive oxygen species (ROS) which are responsible for growth inhibition of spoilage microorganisms compared to Ag/Fe_2O_3 NPs which portrayed the highest antimicrobial activity with large VZI values. This efficacy might be due to the phenolic compounds prevalent in RL extract which possess excellent antimicrobial properties [5.46–5.51], to its shape, size, and composition.

The plausible mechanism is as follows: Ag/Fe_2O_3 NPs and free ions penetrate the microbial surfaces of spoilage yeasts and molds by secreting toxic elements via direct absorption onto biomolecules and generate ROS responsible for oxidative destruction of biological macromolecules including cellular membranes and deoxyribonucleic acid, leading to the capture, degradation, decrease of permeability, and consequently to the death due to the increase of superoxide radicals under visible light exposure [5.17].

5.4. Conclusions

For the first time, the synthesis and growth inhibition potential of 20 % (m/v) of Fe-Ag and Fe-Zn NPs by environmentally salubrious and safe methods, are reported. The characterization techniques revealed different properties from XRD, HRTEM, FESEM and VSM analyses. The antimicrobial properties portrayed that Fe-Ag [3:1] RL (Ag/Fe_2O_3 NPs) was more practical than NPs produced using other methods, confirming the synthesis method significantly influences the properties of Fe-Ag and Fe-Zn NPs. This work paves the way to further develop the growth inhibition potential of RL extract-NPs interactions against food and beverage spoilage microorganisms for a broad range of applications in the food and beverage industry, food preservation, to satisfy customers' standards, and multiply innovative food and fruit packaging systems. More so, the efficacy against a large variety of pathogens of rosemary synthesized NPs could be further investigated in subsequent studies for biomedical applications such as antiviral, antioxidant, or anticancer.

5.5. References

[5.1] C.A. Monteiro, R.B. Levy, R.M. Claro, I.R. Castro, G. Cannon, A new classification of foods based on the extent and purpose of their processing. Cad Saude Publica 26 (11), pp. 2039–2049 (2010).

[5.2] J.M. Zuehlke, B. Petrova, C.G. Edwards, Advances in the control of wine spoilage by *Zygosaccharomyces* and *Dekkera/Brettamoyces*. Annu. Rev. Food Sci. Technol. 4, pp. 57–58 (2013).

[5.3] M. Mewa-Ngongang, H.W du Plessis, U.F. Hutchinson, L. Mekuto, S.K.O Ntwampe, Kinetic modelling and optimization of antimicrobial compound production by *Candida pyralidae* KU736785 for control of *Candida guilliermondii*. Food Sci. Technol. Inter. 23 (4), pp. 1–13 (2017).

[5.4] M. Mewa-Ngongang, H.W du Plessis, E. Hlangwani, S.K.O Ntwampe, B.S. Chidi, U.F. Hutchinson, and P.N. Neil, Activity Interactions of Crude Biopreservatives against Spoilage Yeast Consortia. Fermentation 5 (3), 53 (2019).

[5.5] S. Droby, V. Vinokur, B. Weiss, L. Cohen, A. Daus, E.E. Goldschmidt, R. Porat, Induction of resistance to *Penicilium digitatum* in grapefruit by the yeast biocontrol agent *Candida oleophila*. Phytopathology 92, pp. 393–399 (2002).

[5.6] F. Comitini, N.D. Pietro, L. Zacchi, I. Mannazzu, & M. Ciani, *Kluyveromyces phaffii* killer toxin active against wine spoilage yeasts: purification and characterization. Microbiology 150 (8), pp. 2535–2541 (2004).

[5.7] N.N. Mehlomakulu, M.E. Setati, & B. Divol, Characterization of novel killer toxins secreted by wine-related non-Saccharomyces yeasts and their action on Brettanomyces spp. Inter. J. of Food Microbiology 188, pp. 83–91 (2014).

[5.8] N. Medina-Córdova, R. López-Aguilar, A.I. Campa-Córdova, C. Angulo, Biocontrol activity of the marine yeast Debaryomyces hanseni against phytopathogenic fungi and its ability to inhibit mycotoxins production in maize grain (*Zea mays* L.). Biology Control 97, pp. 70–79 (2016).

[5.9] C.J. Moir, Spoilage of processed foods: Causes and diagnosis. The Food Microbiology Group of the Australian Institute of Food Science and Technology Inc., Waterloo, NSW (2001).

[5.10] R.R. Sharma, D. Singh, R. Singh, Biological control of postharvest diseases of fruits and vegetables by microbial antagonists: A review. Biological Control 50 (3), pp. 205–221 (2009).

[5.11] J.I. Pitt & A.D. Hocking, Fungi and food spoilage. 3rd Edition, Springer Dordrecht Heidelberg London New York Cambridge, pp. 357–382 (2009).

[5.12] B. Williamson, B. Tudzynski, P. Tudzynski, & J.A.V. Kan, Botrytis cinerea: the cause of grey mould disease. Molecular Plant Pathology 8 (5), pp. 561–580 (2007).

[5.13] M.D. Kirk, S.M. Pires, R.E. Black, M. Caipo, J.A. Crump, B. Devleesschauwer, D. Döpfer, A. Fazil, C.L. Fischer-Walker, T. Hald, A.J. Hall, K.H. Keddy, R.J. Lake, C.F. Lanata, P.R. Torgerson, A.H. Havelaar, F.J. Angulo, World Health Organization Estimates of the Global and Regional Disease Burden of 22 Foodborne Bacterial, Protozoal, and Viral Diseases, 2010: A Data Synthesis. PLoS Med. 12 (12), e1001921 (2015).

[5.14] R.K. Yadav, R. Gupta, Impact of chemical food preservatives through local product on human health- A review. High Technol. Lett. 27 (6), 767–773 (2021).

[5.15] G. Sharma, N.D. Jasuja, M. Kumar, M.I. Ali, "Biological Synthesis of Silver Nanoparticles by Cell-Free Extract of Spirulina platensis". Journal of Nanotechnology 2015 (4), pp.1–6 (2015).

[5.16] G. Bisht, S. Rayamajhi, B. Kc, S.N. Paudel, D. Karna, and B.G. Shrestha, Synthesis, characterization, and study of in vitro cytotoxicity of $ZnO-Fe_3O_4$ magnetic composite nanoparticles in human breast cancer cell line (MDA-MB-231) and mouse fibroblast (NIH 3T3). Nanoscale Research Letters 11 (1), 537 (2016).

[5.17] Y. Li, W. Zhang, J. Niu, and Y. Chen, Mechanism of photogenerated reactive oxygen species and correlation with the antibacterial properties of engineered metal-oxide nanoparticles. ACS Nano 6 (6), pp. 5164–5173 (2012).

[5.18] A. Akbarzadeh, M. Samiei, and S. Davaran, Magnetic nanoparticles: preparation, physical properties, and applications in biomedicine. Nanoscale Research Letters 7 (1), 144 (2012).

[5.19] L.Y. Wang, J. Luo, S.Y. Shan, E. Crew, J. Yin, C.J. Zhong, B. Wallek, S.S.S. Wong, Bacterial inactivation using silver-coated magnetic nanoparticles as functional antimicrobial agents. Anal. Chem. 83, pp. 8688–8695 (2011).

[5.20] S. Arokiyaraj, M. Saravanan, N.K.U. Prakash, A.M. Valan, B. Vijayakumar, S. Vincent, Enhanced antibacterial activity of iron oxide magnetic nanoparticles treated with *Argemonemexicana* L. leaf extract: an in vitro study. Mater. Res. Bull. 48 (9), pp. 3323–3327 (2013).

[5.21] P. Lu, T. Jing, & C.Y. Hong, Synthesis of Fe_3O_4, Fe_2O_3, Ag/Fe_3O_4 and Ag/Fe_2O_3 nanoparticles and their electrocatalytic properties. Sci. China Chem. 56 (3), pp. 362–369 (2013).

[5.22] R. Peña-Garcia, Y. Guerra, R. Milani, D.M. Oliveira, A.R. Rodrigues, E. Padrón-Hernández, The role of Y on the structural, magnetic and optical properties of Fe-doped ZnO

91

nanoparticles synthesized by sol gel method. Journal of Magnetism and Magnetic Materials 498, Article 166085 (2020).

[5.23] H.S. Abbas, A. Krishnan, and M. kotakonda, Fabrication of Iron Oxide/Zinc Oxide Nanocomposite Using Creeper *Blepharis maderaspatensis* Extract and Their Antimicrobial Activity. Frontiers in bioengineering and biotechnology 8, Article 595161 (2020).

[5.24] R. Sandupatla, A. Dongamanti, R. Koyyati, Antimicrobial and antioxidant activities of phytosynthesized Ag, Fe and bimetallic Fe-Ag nanoparticles using *Passiflora edulis*: A comparative study. Mater. Today: Proceed. 44 (1), pp. 2665–2673 (2021).

[5.25] B.S. Surendra, H.P. Nagaswarupa, M.U. Hemashree, J. Khanum, *Jatropha* extract mediated synthesis of $ZnFe_2O_4$ nanopowder: Excellent performance as an electrochemical sensor, UV photocatalyst and an antibacterial activity. Chemical Physics Letters 739, Article 136980 (2020).

[5.26] B. Liu, J. Zhou, B. Zhang, and J. Qu, Synthesis of $Ag@Fe_3O_4$ Nanoparticles for Photothermal Treatment of Ovarian Cancer. J. Nanomater. 2019, Article 6457968 (2019).

[5.27] A. Mohamed, R.B. Parvatheeswara, M.O. Abdel-Hamed, K. CheolGi, Modified polyol route for synthesis of Fe_3O_4/Ag and α-Fe/Ag nanocomposite. Journal of Alloys and Compounds 615, pp. 308–312 (2014).

[5.28] D.K. Chmielewska, U. Gryczka, & W. Migdal, Recent patents on creative ionizing radiation in nanotechnology. Recent patents on nanotechnology 2 (3), pp. 201–207 (2008).

[5.29] J.F. Hund, M.F. Bertino, G. Zhang, C.S. Levantis, N. Lewantis, A.T. Tokuhiro, J. Farmer, Formation and entrapment of noble metal clusters in silica monoliths by gamma radiolysis. J. Phys. Chem. B 107, pp. 465–469 (2003).

[5.30] S. Kalunge, A.V. Humbe, M.V. Khedkar, S.D. More, A.P. Keche, and A.A. Pandit, Investigation on synthesis, structural and electrical properties of zinc ferrite on gamma irradiation. J. Phys. Conf. series 1644 (1), Article 012017 (2020).

[5.31] S. Ying, Z. Guan, P.C. Ofoegbu, P. Clubb, C. Rico, F. He, J. Hong, Green synthesis of nanoparticles: Current developments and limitations. Environmental Technology & Innovation 26, Article 102336 (2022).

[5.32] H. Muthukumar, S.K. Palanirajan, M.K. Shanmugam, S.N. Gummadi, Plant extract mediated synthesis enhanced the functional properties of silver ferrite nanoparticles over chemical mediated synthesis. Biotechnology 26, Article e00469 (2020).

[5.33] D. Zahra, R. Mojtaba, G. Mostafa, K. Fatemeh, Green synthesis of $Ag-Fe_3O_4$ nanocomposite utilizing *Eryngium planum* L. leaf extract and its potential applications in medicine. J. Drug Deliv. Sci. Technol. 67, Article 102941 (2022).

[5.34] N.G. Shimpi, M. Khan, S. Shirole, and S. Sonawane, Process Optimization for the Synthesis of Silver (AgNPs), Iron Oxide (α-Fe$_2$O$_3$ NPs) and Core-Shell (Ag-Fe$_2$O$_3$ NPs) Nanoparticles Using the Aqueous Extract of *Alstonia Scholaris*: A Greener Approach. The Open Materials Science Journal 12 (1), pp. 29–39 (2018).

[5.35] L. Wei-Hong, and N. Yang, Green and facile synthesis of Ag-Fe$_3$O$_4$ nanocomposites using the aqueous extract of *Crataegus pinnatifida* leaves and their antibacterial performance. Mater. Lett. 162, pp. 157–160 (2016).

[5.36] M. Sajjadi, M. Nasrollahzadeh, S.M. Sajadi, Green synthesis of Ag/Fe$_3$O$_4$ nanocomposite using *Euphorbia peplus* Linn leaf extract and evaluation of its catalytic activity. J. Colloid Interf. Sci. 497, 1–13 (2017).

[5.37] S.R. Batakurki, V. Adimule, M.M. Pai, E. Ahmed & P. Kendrekar, Synthesis of Cs-Ag/Fe$_2$O$_3$ Nanoparticles Using *Vitis labrusa* Rachis Extract as Green Hybrid Nanocatalyst for the Reduction of Arylnitro Compounds. Topics in Catal. (2022).

[5.38] K. Sameer, M. Jadhav, P. Raikar, D.A. Barretto, S.K. Vootlac, and U.S. Raikar, Green synthesized multifunctional Ag@Fe$_2$O$_3$ nanocomposites for effective antibacterial, antifungal, and anticancer properties. New J. Chem. 41, pp. 9513–9520 (2017).

[5.39] S. Mohana, S. Dhananjay, and S. Shanmugam, *Aegle marmelos* leaves extract mediated synthesis of zinc ferrite: Antibacterial activity and drug delivery. Mater. Res. Express 5 (11), Article 115404 (2018).

[5.40] J.R. de Oliveira, S.E.A. Camargo, and L.D. de Oliveira, *Rosmarinus officinalis* L. (rosemary) as therapeutic and prophylactic agent. Journal of Biomedical Science 26 (1), 5 (2019).

[5.41] S.K. Noukelag, H.E.A. Mohamed, B. Moussa, L.C. Razanamahandry, S.K.O. Ntwampe, C.J. Arendse & M. Maaza, Investigation of structural and optical properties of biosynthesized Zincite (ZnO) nanoparticles (NPs) via an aqueous extract of *Rosmarinus officinalis* (rosemary) leaves. MRS Advances 5 (45), pp. 2349–2358 (2020).

[5.42] S.K. Noukelag, C.J. Arendse, M. Maaza, Biosynthesis of hematite phase α-Fe$_2$O$_3$ nanoparticles using an aqueous extract of *Rosmarinus officinalis* leaves. Material Today: Proceedings 43, pp. 3679–3683 (2021).

[5.43] L. Fang, X. Zu, C. Liu, Z. Li, G. Peleckis, S. Zhu, L. Hua-Kun, L. Wang, Microstructure and magnetic properties of Sn$_{1-x}$Fe$_x$O$_2$ (x = 0.01, 0.05, 0.10) nanoparticles synthesized by hydrothermal method. Journal of Alloys and Compounds 491 (1–2), pp. 679–683 (2010).

[5.44] M. Hoffmann, V.N. Antonov, L.V. Bekenov, K. Kokko, W. Hergert, A. Ernst, Variation of magnetic properties of Sr_2FeMoO_6 due to oxygen vacancies. J. Phys.: Condens. Matter 30 (30), Article 305801 (2018).

[5.45] R.M. Khafagy. Synthesis, characterization, magnetic and electrical properties of the novel conductive and magnetic polyaniline/$MgFe_2O_4$ nanocomposite having the core–shell structure. J. Alloys Compd. 509 (41), pp. 9849–9857 (2011).

[5.46] M. Mewa-Ngongang, H. W. du Plessis, S.K.O. Ntwampe, B.S. Chidi, U.F. Hutchinson, L. Mekuto, P.J. Neil, Grape Pomace Extracts as Fermentation Medium for the Production of Potential Biopreservation Compounds. Foods 8 (2), 51 (2019).

[5.47] A.A. Mostafa, A.A. Al-Askar, K.S. Almaary, T.M. Dawoud, E.N. Sholkamy, M.M. Bakri, Antimicrobial activity of some plant extracts against bacterial strains causing food poisoning diseases. Saudi J. Biol. Sci. 25, pp. 361–366 (2018).

[5.48] Y. Fu, Y. Zu, L. Chen, X. Shi, Z. Wang, S. Sun, T. Efferth, Antimicrobial activity of clove and rosemary essential oils alone and in combination. Phytother. Res. 21, pp. 989–994 (2007).

[5.49] M. Ghaedi, M. Yousefinejad, M. Safarpoor, H.Z. Khafri, M.K. Purkait, *Rosmarinus officinalis* leaf extract mediated green synthesis of silver nanoparticles and investigation of its antimicrobial properties. J. Ind. Eng. Chem. 31, pp. 167–172 (2015).

[5.50] S. Moreno, T. Scheyer, C.S. Romano & A.A. Vojnov, Antioxidant and antimicrobial activities of rosemary extracts linked to their polyphenol composition. Free Radical Res. 40 (2), pp. 223–231 (2006).

[5.51] E. Lorenzetti, J.R. Stangarlin and O.J. Kuhn, Antifungal activity of rosemary extract on Macrophomina phaseolina and charcoal rot control in soybean. J. Plant Pathol. 99 (3), pp. 783–786 (2017).

INDUSTRIAL DYE REMOVAL USING BIOSYNTHESIZED Ag-DOPED ZnO NANOPARTICLES

Abstract

This contribution reports on the bioremediation of the industrial textile effluent by the valorization of agro-waste extracts of *Rosmarinus officinalis* (rosemary) leaves using biosynthesized Ag-doped ZnO nanoparticles (NPs), as photocatalysts. Characterization of the NPs was carried out using field emission scanning electron microscopy (FESEM), X-ray diffraction (XRD), energy-dispersive X-ray spectroscopy (EDS), attenuated total reflection-Fourier transform infrared spectroscopy (ATR-FTIR), UV-Visible, photoluminescence (PL), and efficacy in the photocatalytic degradation of dyes in non-synthetic industrial textile effluent. FESEM and XRD results depicted the hexagonal structure of the Ag-doped ZnO NPs with the average particle size of 21.655 ± 0.250 nm for FESEM, in the range of 7.450–38.611 nm from the Scherrer equation and 28.946 ± 0.002 nm from the Williamson-Hall plot for XRD. EDS indicated Ag (3.94%), Zn (41.01%), and O (30.52%) atoms in the sample, and the carbon (24.53%) attributed to the phenolic compounds in the plant extract, while ATR-FTIR identified stretching vibration mode of Ag-O and Zn-O at 476 and 840 cm^{-1}, respectively. From UV-Vis-NIR, the energy bandgap amounted to 3.23 eV and the photoluminescence emission spectrum indicated the existence of surface defects and oxygen vacancies. Synthesized NPs were used for the treatment of the industrial textile effluent (TE) by assessing the pH and temperature, total suspended solids (TSS), biochemical oxygen demand after 5 days (BOD), and chemical oxygen demand (COD). The mineralization and thus decontamination of the TE has been confirmed with 63 % degradation of the dye being observed after 100 min visible light exposure. The analyses reported herein indicated that this plant extract synthesized nanoparticles can play an important role in the bioremediation of textile industry wastewater.

6.1. Introduction

Water is a scarce natural resource, a basic human need, and a precious national asset thus its use needs to be appropriately planned and managed. Global water challenges are associated with worldwide population growth and climate change effects which necessitates novel innovative water-usage technologies to ensure an adequate supply of clean drinking water and

to reduce its pollution [6.1, 6.2]. A major group of pollutants for freshwater resources include synthetic dyes [6.3–6.5].

Dyes are used mostly in the textile (fabric used in clothing) and paper industries. These industries have shown a significant increase in the use of synthetic complex organic dyes as the coloring agent for the material. The annual world production in the textile industry is about 30 million tons which requires 700,000 tons of different dyes. About 15% of the total world production of dyes is lost during the dyeing process [6.3] and is released into the environment in wastewater which causes considerable environmental pollution problems [6.6]. These dyes create severe environmental pollution outcomes as they are classified as toxic and potentially carcinogenic substances. The accumulation of these toxic pollutants can affect human life and sustainable development in countries with limited water resources [6.5]. They are intensively used in the textile industry because of their large variety of color shades, high wet profiles, stability, and ease of application. However, due to their synthetic nature, they are the least ecologically benign compounds because some are classified as hazardous [6.1, 6.3, 6.4, 6.5] producing strongly colored and brine containing wastewater. Some contain functionalized organic groups with toxicant attributes thus they impose a serious challenge to the receiving environment. Some of them are methyl violet, methylene orange, malachite green, rhodamine B, methylene blue, brilliant blue, reactive blue, Eriochrome Black T, and crystal violet [6.7–6.13]. Therefore, the removal of such dyes in wastewater is a major focus for wastewater remediation.

The conventional methods used to treat dyes, such as precipitation, adsorption activated carbon, air stripping, coagulation, reverse osmosis, and membrane ultrafiltration are mostly ineffective to destroy dyes. To achieve this, photocatalytic degradation techniques are recommended [6.14] albeit this depends on the efficacy of absorption of high-energy photons by a suitable photocatalyst that can effectively promote electrons to the conduction band (CB) leaving holes in the valance band (VB).

The hydroxyl and superoxide radicals can attack organic pollutants and break them into smaller fragments and convert finally them to H_2O/CO_2 [6.15]. Nevertheless, the major problem of heterogeneous photocatalysis is the recombination of photogenerated electron-hole pairs which significantly reduces the generation of hydroxyl radicals and hence the degradation efficiency [6.16, 6.17]. The use of natural sunlight can offer a promising treatment strategy due to its energy-efficient and environmentally friendly operation for textile dyehouse effluents [6.18]. Even the processes associated with photodegradation need to be environmentally benign, thus

the use of bionanotechnology for the development of effective photocatalytic systems synthesis of nanomaterials used as photocatalysts, is of paramount importance.

Bionanotechnology is an emerging and rapidly growing field used to synthesize new materials at the nanoscale. Different semiconductor metal oxide photocatalysts such as TiO_2, CuO, NiO, CeO_2, ZrO_2, ZnO, MgO, etc. have gained significant popularity for the development of new and effective strategies in wastewater treatment [6.19, 6.8, 6.20, 6.21, 6.22, 6.9]. Their interface can be bio-conjugated to provide novel and advanced properties for multi-functional applications in photocatalysis. Titanium dioxide (TiO_2) is generally considered to be the best photocatalyst and can detoxify water from several organic pollutants [6.23]. However, despite its advantages, the main drawback of TiO_2 in photocatalysis relates to the large bandgap (3.2eV) for its anatase crystalline phase which restricts its utilization to ultraviolet (UV) irradiation ($\lambda <$ 387 nm), the light absorption capability in the visible region is still relatively low [6.24]. Besides, the poor adsorption, low surface area, absorption of only a small fraction of sunlight (2-3%), rapid recombination of electron-hole pair, and difficulty of separation from solution properties lead to great limitations in exploiting the TiO_2 to the best of its photoefficiency [6.25]. ZnO was reported that it is more efficient than TiO_2 in UV light photocatalytic degradation of some organic compounds in an aqueous solution [6.26, 6.27]. ZnO nanoparticles (NPs) have previously been used in dye photodegradation [6.8] due to their wide bandgap (3.37 eV) and high excitation energy (60 meV) characteristics [6.20], making them the most exploited n-type semiconducting metal oxide nanoparticles due to their multifunctional morphological, photonic, and optical properties; therefore, a growing interest in the bionanotechnology synthesis of ZnO NPs [6.26]. To further enhance the properties of such NPs, noble metals such as gold (Au), silver (Ag), platinum (Pt), etc., in their combinational analogs with NPs, have been attractive due to their furtherance of properties of the primary NPs, thus their miscellaneous applications [6.28]. Overall, Ag is the most widely investigated doping agent in NP because it has great absorption of visible light capabilities. NP analogs such as Ag-ZnO, are associated with the induction of oxygen vacancies, crystalline transformation, alteration, and intensification of light scattering patterns [6.29, 6.10]. The coupling of two semiconductors with different bandgap energies creates a new heterostructure system that separates charge carriers which effectively minimizes electron-hole recombination and enhances photocatalytic degradation [6.30].

To synthesize such analogs, several physical and chemical methods can be used. Among many, laser-induced deposition, solvothermal, mechanochemical, thermal decomposition, photosynthesis, hydrothermal, microwave-plasma assisted growth, sonochemical, sol-gel, and

97

pulse radiation can be used [6.29, 6.10, 6.31–6.35, 6.11, 6.36, 6.12]. However, most of these techniques have a certain degree of complexity and require either high vacuum conditions or generate harmful waste. To mitigate these challenges, greener methods of synthesis are being researched. Among the various biosynthetic approaches used to prepare metal oxides in their nano-scaled form, the use of plant extracts is advocated for [6.37, 6.38].

Plant extracts have the potential to produce desired nanoparticles with a specific size, shape, and composition. The synthesis process is eco-friendly, clean, easy, safe, cost-effective, and it is not necessary to use high pressure, and most instances, the process will have low energy requirements whereby synthesis can occur at ambient temperature [6.38, 6.39]. This approach has the merit to generate a minimum quantity of waste with minimal by-products as it is carried out without chemical (acid or base, surfactants, and solvents) supplementation, with the biomolecules or organic constituents in the plant extracts being embedded in the final NPs [6.40, 6.20–6.22]. Several plants [6.5, 6.29, 6.39, 6.40–6.42] have been used as capping, reducing, chelating, stabilizing agents, and viable sources for NP analog synthesis of Ag-doped ZnO NPs except for leaf extracts of *Rosmarinus officinalis* (rosemary) to the best of our knowledge.

Rosemary is an aromatic medicinal and condiment plant that belongs to the family Labiate. It can be cultivated around the world due to its hardiness. The medicinal uses of rosemary are well documented, and it is mostly used in the treatment of jaundice, hepatitis, circulatory, and cardiovascular diseases [6.43, 6.44]. It has also shown antidiabetic and neuroprotective activities, among others [6.45]. These biological properties have made rosemary a potential new therapeutic agent in the treatment of many diseases. Recent studies have displayed rosemary extracts' strong antibacterial, antifungal, and antioxidant activity, all of which combine to make the plant a very effective inhibitor of food pathogens [6.46, 6.47]. Many compounds have been isolated from rosemary, including flavones, diterpenes, steroids, and triterpenes. Of these, the antioxidant activity of rosemary extracts has been primarily related to two phenolic diterpenes: carnosic acid and carnosol [6.48]. The main compounds responsible for the antimicrobial activity are α-pinene, bornyl acetate, camphor, and 1,8-cineole [6.49, 6.50]. Phenolic compounds are considered as a major group of antioxidant molecules that contribute to the antioxidant activities of plants because of their ability to scavenge free radicals under the presence of hydroxyl groups, they generate greater control in the growth of nanoparticles as they are nontoxic, economic, simple [6.51, 6.52]. Bioactive components in rosemary extracts including phenolic compounds and other constituents (Table 6.1) can play a critical role in the capping and stabilization of NP analogs. Thus, the proposal is to synthesize Ag-ZnO NPs using

the plants' extracts for the effective chemical breakdown of non-synthetic industrial textile effluent under visible light irradiation. This would result in the bioremediation of effluent which can be assessed for reuse by the textile facility whereby the sample was obtained to reduce the facilities' potable water usage.

Table 6.1: Major compounds of agro-waste extracts of rosemary leaves [6.44]

Compounds	Chemical composition
Flavonoids	Pelargonidin-3,5-Diglucoside (I); Cyanidin-3,5-Diglucoside (II); Kaempherol (III)
Monoterpenoids	α- Pinene (IV); 1,8-Cineole; Camphor
Phenolic acids	Rosmarinic acid; Caffein acid
Diterpenoids	Carnosol; Methyl Carnosate; 12-Methoxycarnosic acid; Epi- and Iso-Rosmanol

6.2. Experimental details

6.2.1. Industrial textile effluent characteristics

Industrial textile effluent from the Colorite Dyers Company (Cape Town, South Africa) a clothing dyeing company, was used in this study. The wastewater was characterized by physico-chemical parameters using methods M60 for ammonia (NH_3-N), M6 for pH and temperature, M8 for total suspended solids (TSS), M16 for Zinc (Zn), Cadmium (Cd), Arsenic (As), M72 for orthophosphate (P), M16 for lead (Pb), M55 for cyanide (CN-), M41 for mercury (Hg), M46 for biochemical oxygen demand after 5 days (BOD), M2 for chemical oxygen demand (COD) [6.53]. Each parameter measured indicated the type of analysis performed, assessing the accuracy and stability of the method, including the performance and reliability of the methods for the measured constituents, i.e., metals (Zn, Cd, As, P, Pb, Hg), anions (CN-), and sum parameters (NH_3-N, pH, temperature, TSS, BOD, COD) [6.53].

6.2.2. Preparation of agro-waste extracts of rosemary leaves

Rosemary leaves were purchased from a nursery in the Western Cape Province-South Africa. Silver nitrate ($AgNO_3$), zinc (II) chloride ($ZnCl_2$), and sodium hydroxide (NaOH) were purchased as an analytical grade reagent (Sigma Aldrich, Modderfontein, South Africa) and used without any further purification.

6.2.3. Valorization of agro-waste extracts of rosemary leaves

A mass (2 grams) of Rosemary leaves was immersed in 100 milliliters of boiled deionized water at 80 °C for 2 h. The resultant extracts' pH was found to be 3.65. The extract solution was filtered twice with Whatman paper (Nº5) to eliminate residual solids. Thereafter, 50 milligrams of silver nitrate and 450 milligrams of zinc (II) chloride were mixed homogenously in 100millileters of the rosemary extract, at 60 °C for 1hr. After homogenization, 2 grams of sodium hydroxide was added to the resultant solution with a final pH of 10.58. The dark green solution was dried in the oven at 100 °C for 4h. Subsequently, the dried dark green powder was annealed at 500 °C in an open-air furnace for 2h leading to the formation of grey Ag-ZnO NPs [6.20–6.22].

6.2.4. Ag-doped ZnO nanoparticles characterization

Field emission capable Zeiss Ultra 55 Scanning Electron Microscope (FESEM) was used to study the morphology and shape of the synthesized NPs with X-ray diffraction (XRD) measurements being conducted using a Bruker AXS D8 diffractometer with an irradiation line Kα1 of copper (λCuKα1=1.5406 Å) operating at a voltage of 40 kV and a current of 35 mA, in the angular range of 20 to 90°. Energy-dispersive X-ray spectroscopy (EDS) spectrum was collected with an EDS Oxford instrument X-Max solid-state silicon drift detector operated at 20 kV. Furthermore, a Thermo Nicolet 8700 FTIR spectrometer was used to measure the ATR-FTIR absorption spectrum in the spectral range of 400 to 4000 cm^{-1}. UV-VIS-NIR experiment was also conducted using a Nicolette Evolution 100 Spectrophotometer to analyze the optical properties in the spectral range of 200 to 800 nm. The photoluminescence (PL) spectrum was recorded from 200 to 800 nm using a Varian Cary Eclipse Fluorescence Spectrophotometer at an excitation wavelength of 372 nm. These methods have been previously determined to be suitable for the biosynthesized NP analogs [6.20–6.22].

6.2.5. Bioremediation of industrial textile effluent and experimental setup

The photocatalytic activity was studied with non-systemic wastewater from an industrial textile facility under visible light irradiation. A UV lamp (20 W), served as the UV light source for photocatalysis. A mass (50 milligrams) of Ag-doped ZnO NPs was added to the agitated 50 milliliters of textile effluent (TE) and was exposed to visible light irradiation. Before contact time with visible light, the mixtures were stirred for 30 minutes under darkness to reach the adsorption-desorption equilibrium. Thereafter, the mixture was exposed to visible light irradiation under constant stirring (120 rpm) and room temperature (25 °C). Subsequently, the residual TE concentration was determined by a UV–vis spectrophotometer. At the start of the experiment (t0), the absorbance measurement of the TE was determined at a wavelength range of 200 to 800 nm and the maximum wavelength has been found at 541 nm. The initial absorbance (A0) of TE wastewater was measured before the dye degradation process. TE aliquots (5 milliliters) were taken every 25 min for 100 min. The photocatalytic activity test has been done in Figure 6.1 according to [6.36].
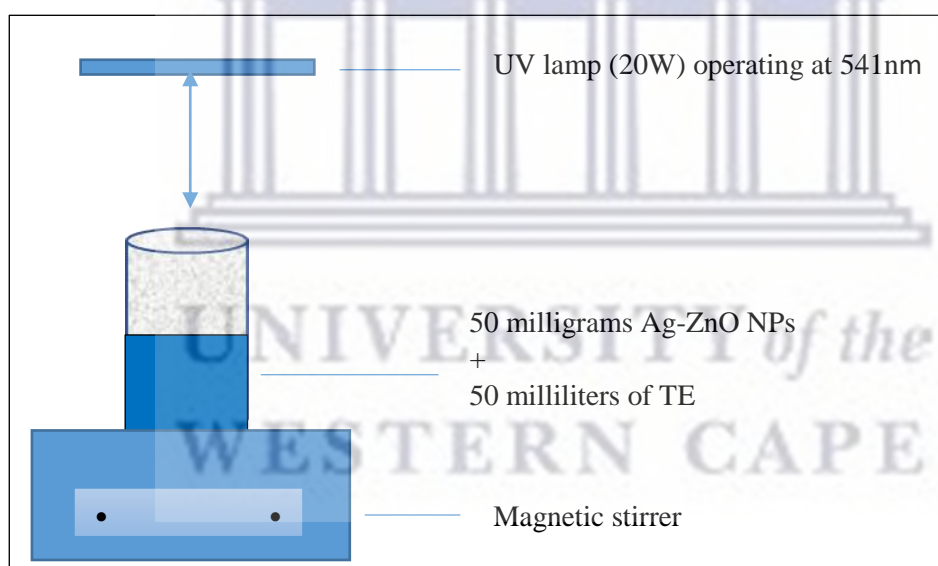
Figure 6.1: Photocatalytic reactor of Ag-doped ZnO NPs

6.2.6. TE Removal rates and kinetics

The photodegradation of the TE was calculated by taking the absorbance values recorded at λmax before and after photocatalytic degradation using the following equations (6.1), (6.2), and (6.3) [6.54, 6.55].

$$Degradation\ percentage = \frac{(A_0 - A_t)}{A_0} \times 100 \qquad (6.1)$$

where A_0 = initial absorbance of pollutant before exposure to visible light irradiation; A_t = absorbance of the pollutant at a given time of exposure.

Pseudo-first-order kinetics Langmür-Hinshelwood of the dye removal in the TE was calculated by using equations (6.2) and (6.3).

$$r = -\frac{dc}{dt} = k'\theta = k'\frac{KC}{1 + KC} \qquad (6.2)$$

In this system, the rate (r) varies proportionally with the coverage (θ), r (mgL^{-1} min), K (Lmg^{-1}), and C (mg L^{-1}). By multiplying equation (2) by ln, we got equation (3)

$$\ln\left(\frac{C_0}{C_t}\right) = k'Kt = kt \qquad (6.3)$$

whereby k is the constant rate of the TE degradation.

The removal rate constant (Kapp) will be calculated from the slope of the plot $ln\left(\frac{A_0}{A_t}\right)$ versus irradiation time.

6.3. Results and Discussion

6.3.1. Wastewater characteristics

The TE characteristic (Table 6.2) indicated high pollution when compared to numerous internationally recognized water standards.

It was observed that NH_3-N, BOD, and COD were above the ISO, European Union, and United States standards. These values confirmed that industrial wastewater is highly polluted; henceforth, the necessity to degrade the hazardous elements to a set minimum standard. Therefore, photocatalytic degradation had to be done and presented in a subsequent sub-section 3.6.

Table 6.2: Summary statistics on the elemental composition of the industrial textile wastewater (TE) [6.53, 6.56].

Parameters	Method	Unit	Value	Limits progressive	ISO	European standard	United States
NH$_3$-N	M60	mg/L	25.0	1.0	ISO 11732, ISO 7150	EN ISO 11732	US EPA 350.1, APA 4500 NH$_3$-N
Ph	M6	/	5.28	6-9	ISO 10523	EN ISO 10523	US EPA 150.1
Temperature	M6	°C	25	Max.30	No standard	No standard	US EPA 17.01
TSS	M8	mg/L	< 2.00	15.0	ISO 11923	ISO 11923	US EPA 160.2, APHA 2540 D
Zn	M16	mg/L	< 0.05	1.0	ISO 11885	EN ISO 11885	US EPA 200.7, US EPA 200.8, US EPA 6010c, US EPA 6020a
Cd	M16	µg/L	<3.00	5.0	ISO 11885	EN ISO 11885	US EPA 200.7, US EPA 200.8, US EPA 6010c, US EPA 6020a
As	M16	µg/L	<10.0	10.0	ISO 11885	EN ISO 11885	US EPA 200.7, US EPA 200.8, US EPA 6010c, US EPA 6020a
P	M72	mg/L	0.08	0.50	ISO 11885, ISO 6878	EN ISO 11885	US EPA 365.4, APHA 4500P-J
Pb	M16	µg/L	<10.0	50.0	ISO 11885	EN ISO 11885	US EPA 200.7, US EPA 200.8, US EPA 6010c, US EPA 6020a
CN-	M55	µg/L	12.1	100	ISO 6703-1,-2,-3, ISO 14403-1,-2	ISO 6703-1,-2,-3, ISO 14403-1,-2	US EPA 335.2, APHA 4500-CN
Hg	M41	µg/L	<6.00	5.00	ISO 12846 or ISO 17852	EN ISO 18412 or ISO 17852	US EPA 200.7, US EPA 200.8, US EPA 6010c, US EPA 6020a
BOD	M46	mg/L	74.1	15	ISO 5815-1, -2 (5days)	EN 1899-1 (5days)	US EPA 405.1 (5 days), APHA 5210B (5 days)
COD	M2	mg/L	5155	80	ISO 6060**	ISO 6060**	US EPA 410.4, APHA 5220 D**

6.3.2. Ag-doped ZnO NPs microscopic observations

The morphology, size distribution, and composition of the Ag-doped ZnO NPs annealed at 500 °C for 2h were investigated using FESEM and EDS as presented in Figure 6.2.

103

The surface morphology exhibited quasi-hexagonal Ag-ZnO NPs that had a high degree of agglomeration with a Wurtzite structure. By fitting the histogram data with a Gaussian distribution, the average particle size was 21.65 ± 0.25 nm. Similar micrographs were obtained by [6.29] who synthesized Ag-ZnO NPs with 2.0 % of the dopant of silver by green chemistry using *P. cerasifera* fruits extract with an average NP size of 72.11–128.06 nm. Similarly, [6.42] who synthesized Ag-ZnO NPs with different dopant concentrations of silver nitrate (1, 3, 5, 7 mol) by phytochemical water splitting method produced NP size of 20-30 nm, which concurred with the results reported herein which revealed that the surface morphology of the Ag-ZnO NPs was influenced by the embedded Ag in the ZnO lattice and the concentration of the silver dopant, which increased the particle size of the NPs albeit, with a good particle size distribution as observed in a previously published paper on ZnO whereby the particle size was 15.62 ± 0.22 nm [6.20].

Furthermore, the elemental composition, as observed via the EDS, was used to obtain the profile of the annealed Ag-ZnO nanoparticles at 500 °C for 2h. The presence of silver (3.94 %), zinc (41.01 %), and oxygen (30.52 %) atoms in the sample are confirmed. The carbon (24.53 %) was attributed to the phenolic compounds (biomolecules) present in the rosemary leaves extract which encapsulated the surface of the nanoparticles [6.11]. With a mass ratio of Ag-ZnO almost [1:10], that is close to [1:9]. The slight difference is due to the experimental uncertainties. The same observations have been seen in the works of [6.57]. The EDS spectrum further revealed that the Ag was successfully incorporated into the ZnO matrix, an assertion concurring with the FESEM results.
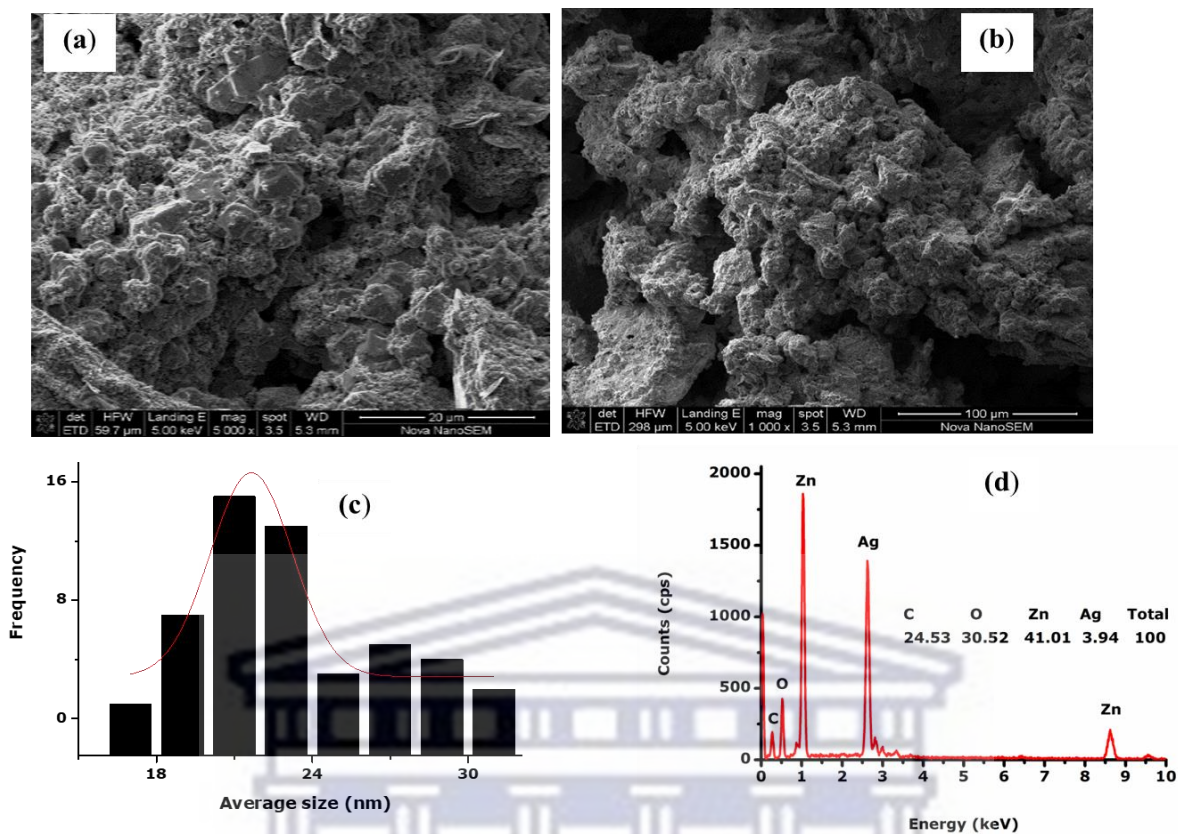
Figure 6.2: (a) FESEM of Ag-ZnO NPs at 500°C for 2h, **(b)** FESEM of Ag-ZnO NPs at 500 °C for 2 h, **(c)** the average size distribution, and **(d)** EDX spectrum

6.3.3. Crystallinity and structural analysis

XRD of the Ag-doped ZnO nanoparticles was employed to study their structural properties for the final annealed particles at 500 °C for 2 h. As elucidated in Figure 6.3 and Table 6.3, the presence of intense and well-defined diffraction peaks are observed at maxima centered at 2θ(°) = 31.770; 34.422; 36.253; 38.117; 44.278; 47.539; 56.603; 62.864; 64.427; 67.963; 69.100 and 77.475, which are assigned to the reflections planes of ZnO (100); (002); (101); Ag (111); (200); ZnO (102); (110); (103); Ag (220); ZnO (112); (201); and Ag (311), respectively. This is consistent with the JCPDS patterns No.036-1451 and No. 004-0783 for ZnO and Ag, respectively. Similar observations have been done by [6.58, 6.59] who synthesized Ag/ZnO NPs by the simple wet chemical sol-gel method.

The XRD pattern of the Ag-ZnO nanoparticles corresponded to a hexagonal wurtzite crystalline structure, with the crystallographic reflections of ZnO having standard lattice parameters of a = 3.2498 Å and c = 5.20661 Å. The peaks associated with Ag are weakly presented due perhaps to the low content of Ag in the final analog product; albeit the sharper and narrower peaks in

105

the XRD spectrum indicated the highly crystalline nature of the Ag-ZnO NPs. Similar results were obtained by [6.34] who synthesized Ag-ZnO NPs with a 1:10 volume ratio, by a facile wet chemical method. [6.60] synthesized Ag-ZnO NPs with different dopant concentrations of silver nitrate ranging between 2 and 7% by a facile chemical method, which was comparable to results obtained by [6.42] in a study whereby the synthesized Ag-ZnO NPs were done using different dopant concentrations of silver nitrate (1, 3, 5, 7 mol) by phytochemical water splitting method [6.34]. In comparison with XRD of ZnO NPs [6.20], the intensity of peaks of Ag-ZnO NPs was higher and broader, which can be deduced as a good degree of comparable crystallinity to the NPs synthesized using chemical methods, an indication that the biosynthesized NPs can be used in a wide range of applications. Besides, the substitution of Ag into the ZnO lattice produced oxygen vacancies in the lattice of ZnO to maintain charge neutrality. Similar behaviors have also been observed in other transitional metal doping systems [6.61, 6.62].

Additionally, by using the Debye-Scherrer formula, the calculated average crystalline size (D) of the annealed Ag-ZnO nanoparticles was found in the range of 7.450−38.611 nm which demonstrated that the embedment of Ag onto ZnO lattice, significantly affected the average size of NPs synthesized. In a previous study on ZnO synthesis using rosemary leaves, the NPs average size was found in the range of 8.894-20.852 nm [6.20]; an indication of the influence of the Ag on the final NPs that could result in reduced total surface area for photocatalytic applications. By fitting the values by the Williamson-Hall plot [6.63], the slope ε is found at 0.0013 and the average size at 28.946 ± 0.002 nm. The d-spacing for each plane and its comparison to the bulk value and the corresponding crystal size obtained from the Scherrer approximation are reported (Table 6.3).
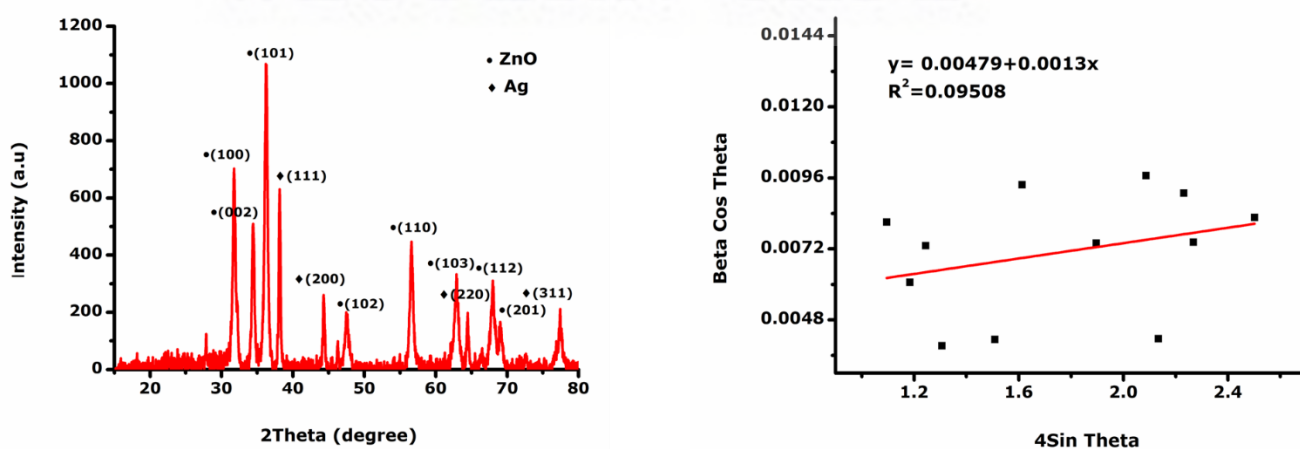
Figure 6.3: XRD of Ag-ZnO NPs at 500 °C for 2 h and Williamson-Hall Plot

106

Table 6.3: XRD values and crystalline size of Ag-ZnO NPs annealed at 500 °C for 2 h

hkl	2θ (⁰)	θ (rad)	d_{bulk}(Å)	d_{exp}(Å)	Δd/d_{bulk}	FWHM (rad)	⟨∅⟩ (nm)
(100)	31.770	0.277	2.8143	2.8144	0.0035	0.0081	19.775
(002)	34.422	0.300	2.6033	2.6033	0.0000	0.0113	14.272
(101)	36.253	0.316	2.4759	2.4760	0.0040	0.0169	09.592
(111)	38.117	0.332	2.3592	2.3590	0.0000	0.0038	38.611
(200)	44.278	0.386	2.0431	2.0440	0.0004	0.0074	20.228
(102)	47.539	0.414	1.9111	1.9111	0.0000	0.0114	14.766
(110)	56.603	0.494	1.6247	1.6250	0.0180	0.0136	12.838
(103)	62.864	0.548	1.4771	1.4772	0.0067	0.0203	08.894
(220)	64.427	0.562	1.4446	1.4450	0.0002	0.0022	07.450
(112)	67.963	0.593	1.3782	1.3784	0.0145	0.0158	11.697
(201)	69.100	0.603	1.3582	1.3585	0.0220	0.0089	20.852
(311)	77.475	0.676	1.2320	1.2310	0.0008	0.0061	29.140

6.3.4. Ag-doped ZnO NPs biomolecules composition

To validate the purity of the NPs produced, further spectroscopy analyses were conducted, i.e., ATR-FTIR analyses were carried out to identify residual biomolecules in the form of functional embedded in the biosynthesized Ag-doped ZnO NPs as elucidated in Figure 6.4. Functional groups found in the final NPs can impart certain advantageous attributes as reported elsewhere [6.20].

The important bands at 476 and 840 cm^{-1} were attributed to Ag-O and Zn-O stretching vibration modes as observed elsewhere [6.58, 6.14] while bands located at 1432 cm^{-1} were associated with the symmetric C-N stretch and were assigned to aromatic amine groups; and 1605 cm^{-1} represented the asymmetric bending modes of N-H bonds of the amino acid [6.33, 6.40]. As observed in other studies [6.29], the absorption bands at 1083 cm^{-1} were attributed to C-N of aliphatic amines [6.20–6.23]. Furthermore, the two broad bands centered approximately at 2137 were associated with the C-H stretch bond and were assigned to alkanes [6.35]; while 3419 cm^{-1} was associated with standard H$_2$O bending modes and OH stretching and was assigned to alcohols/phenolic groups in rosemary leaves extract [6.42, 6.20–6.22]. The shift in the position of the band toward lower frequencies can be associated with changes in bond length due to the partial substitution of Ag^{+} ions in the ZnO lattice. Therefore, the active phenolic compounds from the leaves as evidenced by the FTIR spectrum could be responsible for the reduction and stabilization of the biosynthesized NPs.
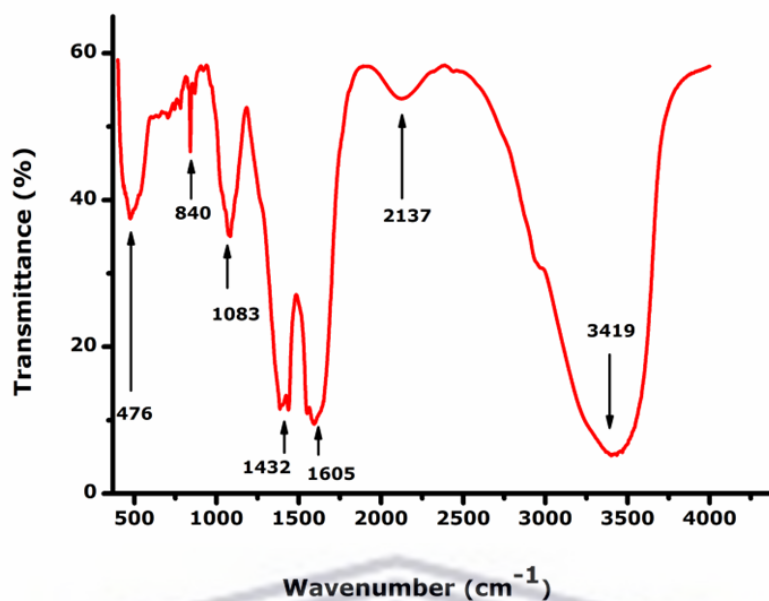
Figure 6.4: ATR-FTIR of Ag-ZnO NPs annealed at 500 °C for 2 h

6.3.5. Ag-doped ZnO NPs optical properties

6.3.5.1. UV-Visible

The absorbance of Ag-doped ZnO NPs annealed at 500 °C for 2 h is carried out to ratify their presence depicted in Figure 6.5 (a). The strong UV absorption shifted to 346 nm is attributed to the presence of silver as it is well known that ZnO has an electronic bandgap of 3.37 eV [6.20]. The silver is inserted into the ZnO lattice, and a rearrangement of the neighboring atoms occurred to ensure the charge balance, resulting in the lattice deformation which affects the electronic structure of the ZnO crystalline lattice, thus leading to the change in the optical absorption of ZnO [6.64].

The optical bandgap 'Eg' was calculated using the following well-known Tauc's relation $(\alpha h v) = A [h v - Eg]^n$ where A is a constant, α is the absorption coefficient, and n is a constant for a given transition which is equal to 1/2 for direct bandgap. 'Eg' was determined by extrapolating the linear portion of the plotted graph to the energy axis at $\alpha = 0$ (Figure 6.5 (b)) and was found to be equal to 3.23 eV. Similar results have been obtained by [6.10] who synthesized Ag-doped ZnO by co-precipitation method with silver doping at 4%.
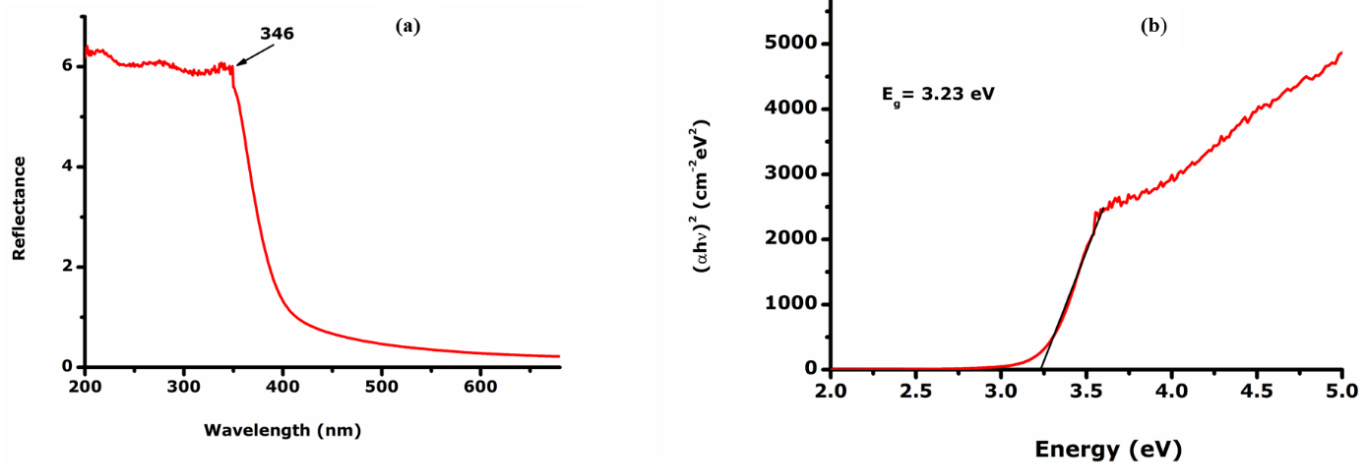
Figure 6.5: (a) UV-Visible and **(b)** Tauc Plot of Ag-doped ZnO NPs annealed at 500 °C for 2 h

6.3.5.2. Photoluminescence

The photoluminescence (PL) spectrum of the Ag-doped ZnO NPs annealed at 500 °C for 2 h as illustrated in Figure 6.5 (c), was performed to verify the crystal quality and possible effects of Ag on the ZnO lattice. Generally, there are two emission bands in the PL spectra of ZnO NPs with the initial peak being due to the near band edge emission through the collision between a pair of an excitonic peak in the UV region (352 nm), while the other was attributed to the recombination of the electron-hole pair caused by the intrinsic and surface point defects in the visible region (428 nm). This was previously observed elsewhere for ZnO NPs [6.20]. The blue shift emission at 441 nm instead of 428 nm was ascribed to the insertion of Ag ions into the ZnO lattice, as the average size increased when XRD and FESEM analyses were compared. The cause of this shift was associated with the surface-to-volume ratio with numerous surface states and native defects of the ZnO (vacancies and interstitials) lattice, which create trap levels responsible for the emissions observed [6.39, 6.42]. The blue shift emission at 441 nm instead of 428 nm resulted in the inhibition of e-/h+ recombination that must cause to increase in its photocatalytic activity [6.65]. Therefore, the appearance of this blue shift emission observed in the PL spectrum indicated the orbital hybridization between the dopant and the host lattice and suggested that Ag-doped ZnO NPs are accountable and increased the luminescence characteristics of ZnO NPs [6.7, 6.35].
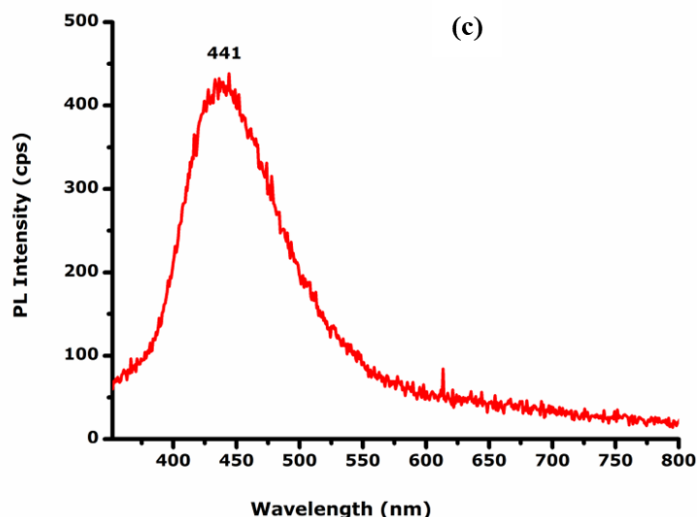
Figure 6.5: (c) PL spectrum of Ag-ZnO NPs annealed at 500 °C for 2 h

6.3.6. Dye removal rate

Ag-doped ZnO NPs are photocatalysts that can interact with organic pollutants under visible light irradiation thus their suitability for photodegradation of industrial textile effluent (TE). When photocatalytic processes occur when light radiation is imposed on semiconducting materials, accelerated chemical reactions can occur [6.31, 6.32]. This process when used effectively, results in the efficient generation of free radical species which may react with organic components, resulting in their mineralization and eventual subsequent degradation [6.30]. This is due to the promotion of electrons from their valence band to the conduction band, which consequently creates and facilitates the separation of a photo-induced charge [6.29, 6.34, 6.66–6.68] presented in Figure 6.6.

When ZnO is used as a semiconductor material in a photocatalytic application, the absorption of visible light energy will either be equivalent to or higher than its bandgap energy thus leading to the excitation of electrons from the valence band (VB) to the conduction band (CB). As a result, a vacancy will be created at the valence band while the electron is excited to the conduction band. An electron-hole pair (e^-, h^+) will thus be generated, a stage classified as the photo-excitation stage. The vacancies (holes) react with water to form hydroxyl radicals ($OH^•$). Simultaneously, electrons will therefore react with oxygen to form a series of reactive oxidizing species such as superoxide anions, hydrogen peroxide, and hydroxyl radicals. The possible mechanism of dye degradation according to previous studies [6.60, 6.11, 6.37] was proposed as shown in the following equations.

110

$$Ag\text{-}ZnO + h\nu \longrightarrow e^- (CB\ Ag\text{-}ZnO) + h^+ (VB\ Ag\text{-}ZnO) \tag{1.1}$$

$$e^- (CB\ Ag\text{-}ZnO) + O_2 \longrightarrow O_2^- + H^+ \longrightarrow HO_2^+ \tag{1.2}$$

$$HO_2^+ + O_2^- + H^+ \longrightarrow H_2O_2 + O_2 \tag{1.3}$$

$$HO_2^+ + e^- (CB\ Ag\text{-}ZnO) \longrightarrow OH^- + H^\bullet \tag{1.4}$$

$$H_2O_2 + h\nu \longrightarrow 2\ OH^- \tag{1.5}$$

$$h^+ (VB\ Ag\text{-}ZnO) + H_2O \longrightarrow H^+ + OH^\bullet \tag{1.6}$$

$$h^+ (VB\ Ag\text{-}ZnO) + OH^- \longrightarrow OH^\bullet \tag{1.7}$$

$$OH^\bullet + TE\ molecules \longrightarrow CO_2 + H_2O \tag{1.8}$$
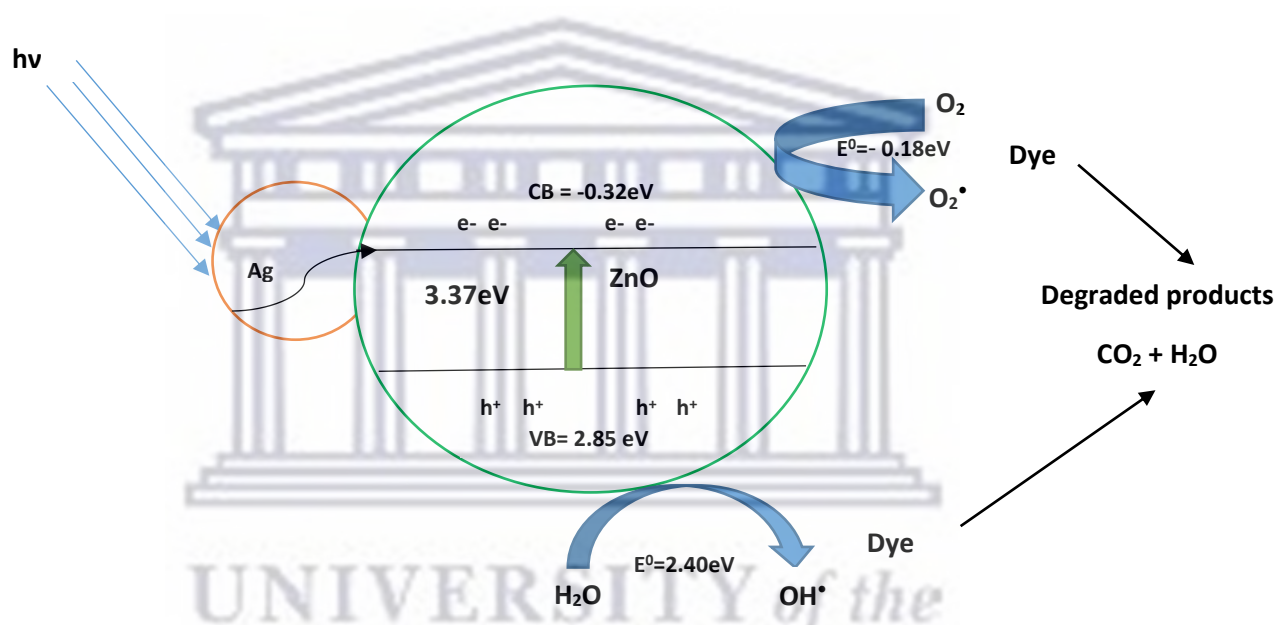
Figure 6.6: Mechanism of degradation of TE in presence of Ag-doped ZnO NPs (photocatalyst)

The degradation of TE was employed and the efficacy of Ag-doped ZnO NPs was evaluated. From the UV–Visible spectrum of TE, the absorbance was measured in the range between 200–800 nm for every sampling time as shown in Figure 6.7. It was observed that the sharp decrease in the absorption peak at 541 nm over time was apparent with prolonged exposure to visible light irradiation. The basic condition of the medium with a pH above 7 eliminates the formation of a positive charge due to the presence of hydronium ions. The positive charge could reduce the performance of the active surface of the Ag-doped ZnO NPs [6.36, 6.12].

111
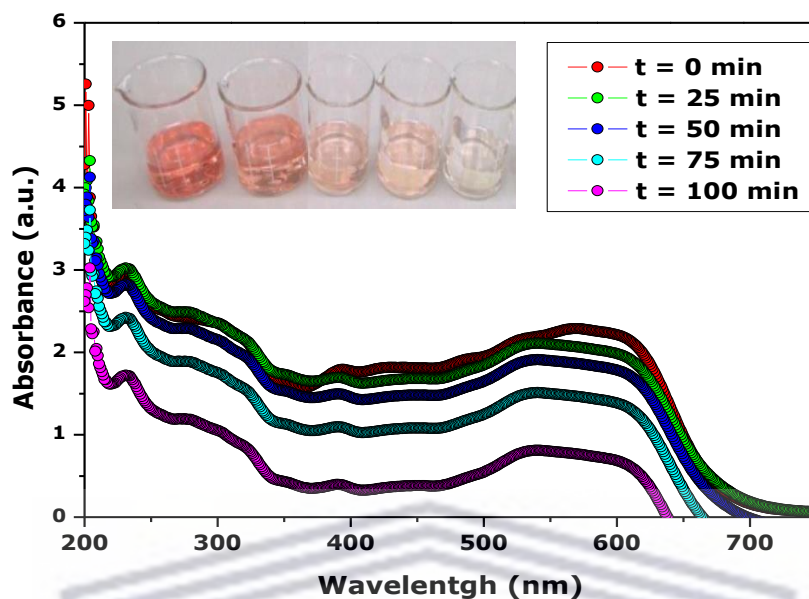
Figure 6.7: Photocatalytic degradation of TE in contact time with Ag-doped ZnO NPs under visible light irradiation

The photocatalytic degradation followed the pseudo-first-order mechanism as presented in Figure 6.8. The relative absorbance changes $ln\left(\frac{A_0}{A_t}\right)$ of TE at 541 nm, as a function of visible light irradiation exposure in the presence of Ag-ZnO NPs, exhibited good photocatalytic activity for TE degradation. In the presence of visible light irradiation only, the percentage of degradation of TE was 0.21 %, and in Ag-ZnO NPs samples, the degradation was significantly higher, i.e., increased to 63 % after 100 min of exposure under visible light irradiation. The results confirmed that exposure time, particle size, surface area, morphology, and defect had a significant impact on the improvement of the photodegradation process. [6.12] reported photocatalytic degradation of reactive blue 21 using Ag-doped ZnO albeit, doping with silver at 3 %, resulting in 83 % degradation efficiency under UV irradiation after 100 min of exposure at pH of 7. The justification for enhanced photocatalytic degradation under neutral and acidic conditions is because, at a pH higher than 8, the surface of ZnO photocatalyst is negatively charged, whereas, at a pH lower than 8, it becomes positively charged. Whereby anionic dyes, i.e., RB21, are to be degraded, a pH less than that corresponding to the zero-point charge is preferred, as adsorption of such dyes is enhanced on the catalyst surface which results in an enhanced degradation. [6.11] assessed structural, optical, and photocatalytic activities of Ag-doped and Mn-doped ZnO NPs, achieving 55 % of degradation of methyl violet after 100 min

112

of exposure under solar light at pH of 7. pH, catalyst, and dye concentration were determined to be influential with [6.37] reporting that biotemplated synthesis of Ag-ZnO nanoparticles/bacterial cellulose nanocomposites for photocatalysis application, was slightly better; albeit, with an increased dopant of silver at 9%. The enhanced photocatalytic degradation was only 60 % under ultraviolet irradiation after 100 min of exposure to degrade methylene blue at a pH of 13. The results confirmed that the photocatalytic activity strongly depends on the concentration of TE molecules adsorbed on the surface of the photocatalyst and the active sites of the catalyst reduced, which is caused by the solution of pH. More light is absorbed by molecules of TE and the excitation of photocatalyst particles by photons is reduced [6.25]. A comparative study on photocatalysis using Ag-doped ZnO NPs is provided in Table 6.4.

The removal rate constant (Kapp) was calculated from the slope of the plot $ln\left(\frac{A_0}{A_t}\right)$ versus irradiation time as Kapp $= 0.0111$ s^{-1} and R$^2 = 0.916$. R^2 refers to the correlation coefficient that provides for the least square fitting to the original data. This confirmed the relevance of the Langmuir-Hinshelwood kinetic model simplified as $ln\left(\frac{A_0}{A_t}\right) = Kapp(t)$ for TE photodegradation where Kapp is the first-order rate kinetic reaction constant.
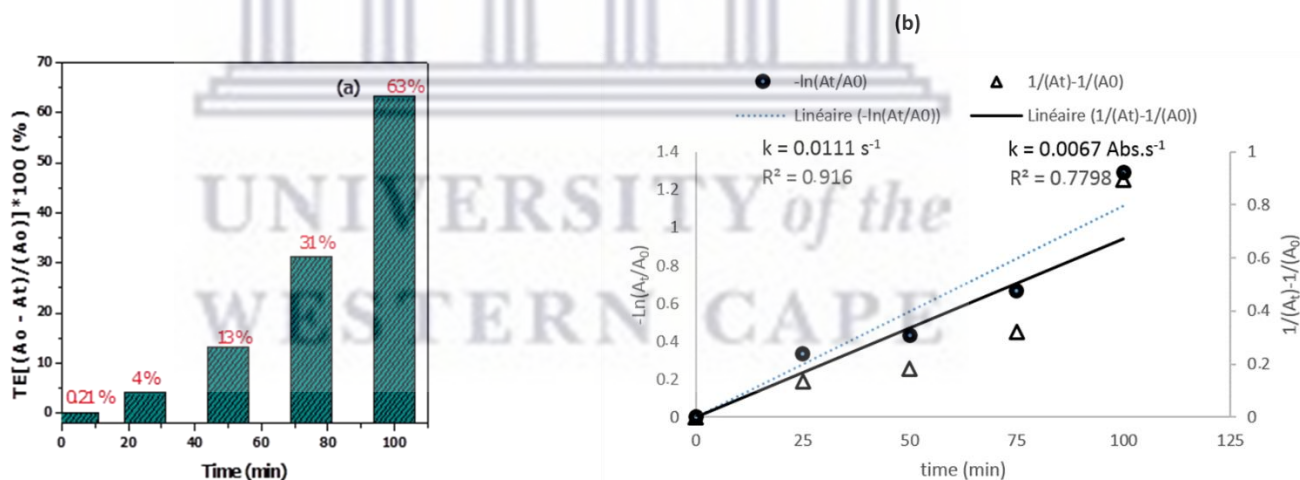
Figure 6.8: Photocatalytic degradation percentage of **(a)** textile industrial effluent (TE) and **(b)** removal kinetics in contact time with Ag-doped ZnO NPs under visible light irradiation

113

Table 6.4: Comparative study on photocatalysis using Ag-doped ZnO NPs

Method	Silver doping (%)	Pollutant	Degradation (%)	Time (min)	pH	Authors
Biotemplated	9	Methylene blue	60	100	13	[6.37]
Ultrasonic deposition	3	Reactive blue 21	83	100	7	[6.12]
Coprecipitation	5	Methyl violet	55	100	7	[6.11]
Biosynthesis	11	Industrial dye	63	100	5.28	This work

6.4. Conclusion

Removal of toxic organic compounds such as dyes from wastewater is a major challenge in environmental and wastewater engineering. Therefore, the detoxification of wastewater is very important to maintain an ecological balance in receiving water bodies to which the treated wastewater is released. To mitigate the pollution of wastewater containing pollutants via photocatalysis, high-quality Ag-doped ZnO NPs were successfully synthesized by an entirely green synthesis process in which extracts of *Rosmarinus officinalis* leaves were used as an effective reducing and capping agent.

The characterizations of the NPs produced confirmed that the samples produced were Ag-doped ZnO NPs. XRD revealed the synthesized particle crystallinity while FESEM elucidated the hexagonal structure and highly agglomerated form of the particles. ATR-FTIR further elucidated their chemical bonds including purity by EDS. Furthermore, PL exhibited a significant population of oxidative oxygen species culminating in a significantly induced photoluminescence. The NPs produced were further assessed for their usability using TE remediation efficacy as a measure of their usefulness, with 63 % degradation of the dye in TE being achieved after 100 min of exposure under visible light irradiation. Hence, this green synthesis pathway has demonstrated the importance of rosemary leaves extracts as cost-effective, cheap, and environmentally benign agents to facilitate the biosynthesis of Ag-doped ZnO NPs to reduce dyes in TE thus minimizing the pollution of freshwater sources by the TE released into the environment. Future research should be focused on the identification of the bioactive constituents within the agro-waste extract of rosemary leaves to better understand the mechanism of reaction with the salt precursor and the use of hydrogen peroxide H_2O_2 as a scavenger to improve the percentage of dye removal. Additionally, this research opens an avenue to investigate the effects of some parameters which encompass the pH, the amount of the catalyst, and the concentration of the pollutants.

6.5. References

[6.1] S. Barclay, C. Buckley, Waste minimization guide for the textile industry, a step towards cleaner production, the pollution research group. University of Natal Durban, South Africa. Water Research Commission 1 (2000).

[6.2] United Nations Environment Programme (UNEP), Groundwater and its susceptibility to degradation: A global assessment of the problem and options for management. UNDP Report, Nairobi, Kenya (2003).

[6.3] INRS, Reactive dyes in the sector of the textile ennoblement: allergic pathology related to their use. Document for the Doctor of Work, N85, 1st quarter (2001).

[6.4] C.G. Da Silva, J.L. Faria, Photochemical and photocatalytic degradation of an azo dye in aqueous solution by UV irradiation. J. Photochem. Photobiol. A: Chem. 155 (1–3), pp. 133–143 (2003).

[6.5] C. Parvathi, U.S. Shoba, C. Prakash, S. Sivamani, Manihot esculenta Peel Powder: Effective adsorbent for removal of various textile dyes from aqueous solutions. Journal of Testing and Evaluation 46 (6), pp. 1–13 (2018).

[6.6] A.M. Talarposhti, T. Donelly, G.K. Anderson, Colour removal from a simulated dye wastewater using a two-phase anaerobic packed bed reactor. Water Res. 35 (2), pp. 425–432 (2001).

[6.7] A.Y. Özlem, E.U. Husnu, and D. Caner, Highly Efficient Room Temperature Synthesis of Silver-Doped Zinc Oxide (ZnO:Ag) Nanoparticles: Structural, Optical, and Photocatalytic Properties. J. Am. Ceram. Soc. 96 (3), pp. 766–773 (2013).

[6.8] E.D. Sherly, J.J. Vijaya, L.J. Kennedy, A. Meenakshisundaram, M. Lavanya, A comparative study of the effects of CuO, NiO, ZrO_2, and CeO_2 coupling on the photocatalytic activity and characteristics of ZnO. Korean J. Chem. Eng. 33 (4), pp. 1431–1440 (2016).

[6.9] L.S.Y. Reddy, K. Lingaraju, K. Manjunath, G.K. Raghu, K.H.S. Kumar, G. Nagaraju, Synergistic effect of MgO nanoparticles for electrochemical sensing, photocatalytic-dye degradation, and antibacterial activity. Mater. Res. Express 4 (2), Article 025028 (2017).

[6.10] R. Singh, P.B. Barman, D. Sharma, Synthesis, structural and optical properties of Ag-doped ZnO nanoparticles with enhanced photocatalytic properties by photo degradation of organic dyes. J. Mater. Sci.: Mater. Electron. 28 (8), pp. 5705–5717 (2017).

[6.11] E.A. Mengstu, M.T. Gebrekidan, Y.N. Gebretinsae, and W.G. Tesfakiros, Structural, optical, and photocatalytic activities of Ag-doped and Mn-doped ZnO Nanoparticles. Journal of Nanomaterials 2018, Article 9425938, pp. 1–9 (2018).

[6.12] A.A. El-Bindary, A. Ismail, E.F. Eladl, Photocatalytic degradation of reactive blue 21 using Ag-doped ZnO nanoparticles. J. Mater. Environ. Sci. 10 (12), pp. 1258–1271 (2019).

[6.13] A.M. Seyyedeh, A. Nezamzadeh-Ejhieh, CdS-Ag$_3$PO$_4$ nano-catalyst: A brief characterization and kinetic study towards methylene blue photodegradation. Material Science in Semiconductor Processing 122 (1), Article 105455 (2021).

[6.14] S.P. Santosh, G.M. Mukund, S.T. Mohaseen, R.P. Deepak, V.K. Milind, Y. Hyun, K. Hayong, S.A. Salem, S.Y. Sam, S.K. Sanjay, B.K. Bharat, Green approach for hierarchical nanostructured Ag-ZnO and their photocatalytic performance under sunlight. Catalysis Today 260, pp. 126–134 (2016).

[6.15] B.A. Ünnü, G. Gündüz, M. Dükkanc, Heterogeneous Fenton-like oxidation of crystal violet using an iron loaded ZSM-5 Zeolite. Des. Water Treat. 57 (25), pp. 11835–11849 (2016).

[6.16] Q. Li, T. Kako, J. Ye, PbS/CdS nanocrystal-sensitized titanate network films: enhanced photocatalytic activities and super-amphiphilicity. J. Mater. Chem. 20 (45), pp. 10187–10192 (2010).

[6.17] H. Derikvandi, A. Nezamzadeh-Ejhieh, Comprehensive study on enhanced photocatalytic activity of heterojunction ZnS-NiS/Zeolite nanoparticles: Experimental design based on response surface methodology (RSM), impedance spectroscopy, and GC-MASS studies. J. Colloid and Inter. Sci. 490, pp. 652–664 (2017).

[6.18] E.C. Meon, D. Petrou, D. Mantzavinos, Photocatalytic treatment of textile dyehouse effluents with simulated and natural solar light. Global NEST journal 15 (1), pp. 21–28 (2013).

[6.19] D.C. Hurum, A.G. Agrios, A.K. Gray, T.T. Rajh, and M.C. Thurnauer, Explaining the enhanced photocatalytic activity of Degussa P25 mixed phase TiO$_2$ using EPR. J. Phys. Chem. B 107 (19), pp. 4545–4549 (2003).

[6.20] S.K. Noukelag, H.E.A. Mohamed, B. Moussa, L.C. Razanamahandry, S.K.O Ntwampe, C.J. Arendse, and M. Maaza, Investigation of structural and optical properties of biosynthesized Zincite (ZnO) nanoparticles (NPs) via an aqueous extract of Rosmarinus officinalis (rosemary) leaves. MRS Advances 5 (45), pp. 2349–2358 (2020).

[6.21] S.K. Noukelag, H.E.A. Mohamed, B. Moussa, L.C. Razanamahandry, S.K.O Ntwampe, C.J. Arendse, Bio-inspired synthesis of PbO nanoparticles (NPs) via an aqueous extract of *Rosmarinus officinalis* (rosemary) leaves. Mater. Today. Proc. 36 (23), pp. 421–426 (2021).

[6.22] S.K. Noukelag, H.E.A. Mohamed, B. Moussa, L.C. Razanamahandry, S.K.O. Ntwampe, C.J. Arendse, Structural and optical investigations of biosynthesized bunsenite NiO nanoparticles (NPs) via an aqueous extract of *Rosmarinus officinalis* (rosemary) leaves. Mater. Today. Proc. 36 (4), pp. 245–250 (2021).

[6.23] A.A. Khodja, T. Sehili, J.F. Pilichowski, P. Boule, Photocatalytic degradation of 2-phenylphenol on TiO$_2$ and ZnO in aqueous suspensions. J. Photochem. Photobiol. A: Chem. 141(2–3), pp. 231–239 (2001).

[6.24] M.R. Prairie, L.R. Evans, B.M. Stange, S.L. Martinez, An investigation of TiO$_2$ photocatalysis for the treatment of water contaminated with metals and organic chemicals Environ. Sci. Techno. 27 (9), pp. 1776–1782 (1993).

[6.25] A. Nezamzadeh-Ejhieh, S. Hushmandrad, Solar photodecolorization of methylene blue by CuO/X Zeolite as a heterogeneous catalyst. Appl. Catal. A: General 388 (1–2), pp. 149–159 (2010).

[6.26] R. Wang, K. Hashimoto, A. Fujishima, M. Chikuni, E. Kojima, A. Kitamura, M. Shimohigoshi, T. Watanabe, Light-induced amphiphilic surfaces. Nature 388 (6641), pp. 431–432 (1997).

[6.27] M. Swati, and R.C. Meena, Photocatalytic degradation of textile dye through an alternative photocatalyst methylene blue immobilized resin dowex 11 in presence of solar light. Arch. Appl. Sci. Res. 4 (1), pp. 472–479 (2012).

[6.28] M. Ghaedi, M. Yousefinejad, M. Safarpoor, H.Z. Khafri, M.K. Purkait, *Rosmarinus officinalis* leaf extract mediated green synthesis of silver nanoparticles and investigation of its antimicrobial properties. J. Ind. Eng. Chem. 31, pp. 167–172 (2015).

[6.29] K.S. Ahmad, S.B. Jaffri, Phytosynthetic Ag-doped ZnO nanoparticles: semiconducting green remediators. Open Chem. (16), pp. 556–570 (2018).

[6.30] M. Rezaei, A. Nezamzadeh-Ejhieha, The ZnO-NiO nano-composite: A brief characterization, kinetic and thermodynamic study and study the Arrhenius model on the sulfasalazine photodegradation. International Journal of Hydrogen Energy 45 (46), pp. 24749–24764 (2020).

[6.31] S. Rajaboopathi, S. Thambidurai, Synthesis of bio-surfactant based Ag/ZnO nanoparticles for better thermal, photocatalytic, and antibacterial activity. Materials Chemistry and Physics 223, pp. 512– 522 (2018).

[6.32] H. Sutanto, S. Wibowo, L. Nurhasanah, E. Hidayanto, and H. Hadiyanto, Ag doped ZnO thin films synthesized by spray coating technique for methylene blue photodegradation under UV Irradiation. Hindawi Publishing Corporation. Int. J. Chem. Eng. 2016, Article 6195326, pp. 1–6 (2016).

[6.33] C. Abinaya, M. Marikkannan, M. Manikandan, J. Mayandi, P. Suresh, V. Shanmugaiah, C. Ekstrum, J.M Pearce, Structural and optical characterization and efficacy of hydrothermal

synthesized Cu and Ag-doped zinc oxide nanoplate bactericides. Mater. Chem. Phys. 184, pp. 172–182 (2016).

[6.34] S. Kuriakose, V. Choudhary, B. Satpati, and S. Mohapatra, Enhanced photocatalytic activity of Ag–ZnO hybrid plasmonic nanostructures prepared by a facile wet chemical method. Beilstein J. Nanotechnol. 5, pp. 639–650 (2014).

[6.35] T. Chitradevi, A.J. Lenus, and N.V. Jaya, Structure, morphology, and luminescence properties of sol-gel method synthesized pure and Ag-doped ZnO nanoparticles, Mater. Res. Express 7 (1), Article 015011 (2020).

[6.36] M.F.A. Messih, M.A. Ahmed, A. Soltan, S.S Anis, Synthesis and characterization of novel Ag/ZnO nanoparticles for photocatalytic degradation of methylene blue under UV and solar irradiation. J. Phys. Chem. Solids 135, Article 109086 (2019).

[6.37] H.F. Aritonang, O.E. Kamea, H. Koleangan, & A.D. Wuntu, Biotemplated synthesis of Ag-ZnO nanoparticles/bacterial cellulose nanocomposites for photocatalysis application. Polymer-Plastics Technology and Materials 59 (12) pp. 1292–1299 (2020).

[6.38] S. Baker, D. Rakshith, K.S. Kavitha, P. Santosh, H.U. Kavitha, Y. Rao, and S.S. Satish, Plants: emerging as nanofactories towards facile route in synthesis of nanoparticles. Bioimpacts 3 (3), pp. 111–117 (2013).

[6.39] A. Yeganeh-Faal, M. Bordbar, N. Negahdar, M. Nasrollahzadeh, Green synthesis of the Ag/ZnO nanocomposite using *Valeriana officinalis* L. root extract: application as a reusable catalyst for the reduction of organic dyes in a very short time. IET Nanobiotechnology 11 (6), pp. 669–676 (2017).

[6.40] S. Hameed, A.T. Khalil, M. Ali, M. Numan, S. Khamlich, Z.K. Shinwari, & M. Maaza, Greener synthesis of ZnO and Ag–ZnO nanoparticles using *Silybum marianum* for diverse biomedical applications. Nanomedicine 14 (6), pp. 655–673 (2019).

[6.41] E. Gurgur, S.S. Oluyamo, A.O. Adetuyi, O.I. Omotunde, A.E. Okoronkwo, Green synthesis of zinc oxide nanoparticles and zinc oxide–silver, zinc oxide–copper nanocomposites using *Bridelia ferruginea* as biotemplate. SN Applied Sciences 2, 911 (2020).

[6.42] L.S.R. Yadav, S. Pratibha, K. Manjunath, M. Shivanna, T. Ramakrishnappa, N. Dhananjaya, G. Nagaraju, Green synthesis of Ag-ZnO nanoparticles: Structural analysis, hydrogen generation, formylation, and biodiesel applications. Journal of Science: Advanced Materials and Devices 4 (3), pp. 425–431 (2019).

[6.43] M.R. Al-Sereiti, K.M. Abu-Amer, P. Sen, Pharmacology of rosemary (*Rosmarinus officinalis* Linn.) and its therapeutic potentials. Indian Journal of Experimental Biology 37 (2), pp. 124–130 (1999).

118

[6.44] J.R. de Oliveira, S.E.A. Camargo, and L.D. de Oliveira, *Rosmarinus officinalis* L. (rosemary) as therapeutic and prophylactic agent. Journal of Biomedical Science 26 (1), 5 (2019).

[6.45] S.K. Tavassoli, S.M. Mousavi, D.Z. Emam, S.H. Razavi, Chemical composition and evaluation of antimicrobial properties of *Rosmarinus officinalis* L. essential oil. African Journal of Biotechnology 10 (63), pp. 13895–13899 (2011).

[6.46] L. Gachkar, D. Yadegari, B. Rezaei, M. Taghizadeh, S.A. Astaneh, Chemical and biological characteristics of Cuminum cyminum and *Rosmarinus officinalis* essential oils. Food Chemistry 102 (3), pp. 898–904 (2007).

[6.47] M.M. Özcan, J.C. Chalchat, Chemical composition and antifungal activity of rosemary (*Rosmarinus officinalis* L.) oil from Turkey. Inter. J. Food Sci. and Nutrition 59 (7–8), pp. 691–698 (2008).

[6.48] E.N. Frankel, S.W. Huang, R. Aeschbach, and E. Prior, Antioxidant activity of a rosemary extract and its constituents, carnosic acid, carnosol, and rosmarinic acid, in bulk oil and oil-in-water emulsion. J. Agri. and Food Chem. 44 (1), pp. 131–135 (1996).

[6.49] G. Pintore, M. Usai, P. Bradesi, C. Juliano, G. Boatto, F. Tomi, M. Chessa, R. Cerri, J. Casanova, Chemical composition and antimicrobial activity of *Rosmarinus officinalis* L. oils from Sardinia and Corsica. Flavour and Fragrance Journal, Sassari/Ajaccio, 17 (1), pp. 15–19 (2002).

[6.50] K.G. Aziza, H. Haiko, S.J. Artur, M. Simone, Rosemary (*Rosmarinus officinalis*) – a study of the composition, antioxidant and antimicrobial activities of extracts obtained with supercritical carbon dioxide. Ciênc. Tecnol. Aliment. Campinas, 28 (2), pp. 463–469 (2008).

[6.51] S. Maqsood, B. Soottawat, A.I. Aisha, and A. Asifa, Phenolic compounds and plant phenolic extracts as natural antioxidants in prevention of lipid oxidation in seafood: A detailed review. Compr. Rev. Food Sci. Food Saf. 13 (6), pp. 1125–1140 (2014).

[6.52] Y.C. Ozlem, N. Pınar, G Aynur, B. Erdal and V.S. Fazilet, Determination of phenolic content and antioxidant activity of extracts obtained from Rosmarinus officinalis'calli. J. Plant Phys. 164 (11), pp. 1536–1542 (2007).

[6.53] Integral Laboratories (Pty) Ltd. No 1 Zandwyk Park, Sandringham Close Paarl, 7646, Certificate of Analysis (2019). Email: westerncape@integrallabs.co.za.

[6.54] A. Nezamzadeh-Ejhieh, K. Mahshid, Photodecolorization of Eriochrome Black T using NiS-P Zeolite as a heterogeneous catalyst. J. Hazard. Mater. 176 (1–3), pp, 629–637 (2010).

[6.55] M. Giahi, D. Pathania, S. Agarwal, G.A.M. Ali, K.F. Chong, V.K. Gupta, Preparation of Mg-doped TiO_2 nanoparticles for photocatalytic degradation of some organic pollutants. Studia Universitatis Babes-Bolyai Chemia 64 (1), pp. 7–18 (2019).

[6.56] ZDHC Wastewater Guidelines Version 1.1, 2019. Ø ZDHC The Roadmap to Zero Programme.

[6.57] S. Kannan, N.P. Subiramaniyam & M. Sathishkumar, A novel green synthesis approach for improved photocatalytic activity and antibacterial properties of zinc sulfide nanoparticles using plant extract of *Acalypha indica* and *Tridax procumbens*. J. Mater. Sci.: Mater. Electro. 31 (12), pp. 9846–9859 (2020).

[6.58] A.H. Shah, E. Manikandan, M.B. Ahmed, and V. Ganesan, Enhanced Bioactivity of Ag/ZnO Nanorods-A Comparative Antibacterial Study. J. Nanomed. Nanotechnol. 4 (3), Article 168 (2013).

[6.59] H. Yawei, H. Huirong, K. Xia, M. Yangmin, Synthesis and Antibacterial Activities of Ag/ZnO Nanoparticles. Key Engineering Materials 697, pp. 714–717 (2016).

[6.60] S.M. Hosseini, I.A. Sarsari, P. Kameli, and H. Salamati, Effect of Ag doping on structural, optical, and photocatalytic properties of ZnO nanoparticles. Journal of Alloys and Compounds 640, pp. 408–415 (2015).

[6.61] Z. Wang, G. Yong, P. Biswas and W.J. Bresser, Processing of iron-doped titania powder in flame aerosol reactors. Powder Technol. 114 (1–3), pp. 197–204 (2001).

[6.62] B. Choudhury, A. Choudhury, A structural, optical, and ferromagnetic properties of Cr doped TiO_2 nanoparticles. Mater. Sci. Eng. B 178 (11), pp. 794–800 (2013).

[6.63] V.D. Mote, Y. Purushotham, and B.N. Dole, Williamson-Hall analysis in estimation of lattice strain in nanometer-sized ZnO particles. J. Theoretical and Appl. Phys. 6, 6 (2012).

[6.64] M. Krayaoui, A. Mhamdi, H.K. Labidi, A. Boukhachem, K. Boubaker, M. Amlouk, R. Choturou, Some physical investigation on silver–ZnO doped sprayed thin films. Mat. Sci. Semicon. Proc. 30, pp. 255–262 (2015).

[6.65] H. Tang, S. Chang, G. Tang, W. Liang, AgBr and g-C_3N_4 co-modified Ag_2CO_3 photocatalyst: A novel multi-heterostructured photocatalyst with enhanced photocatalytic activity. Appl. Surf. Sci. 391, pp. 440–448 (2017).

[6.66] S. Ghattavi, A. Nezamzadeh-Ejhieh, A double-Z-scheme ZnO/AgI/WO_3 photocatalyst with high visible light activity: Experimental design and mechanism pathway in the degradation of methylene blue. J. Mol. Liquids 322 (2), Article 114563 (2021).

[6.67] A. Ziashahabi, M. Prato, Z. Dang, R. Poursalehi & N. Naseri, The effect of silver oxidation of the photocatalytic activity of Ag/ZnO hybrid plasmonic/metal-oxide nanostructures under visible light and in the dark. Sci. Rep. 9, Article 11839 (2019).

[6.68] H. Derikvandi, A. Nezamzadeh-Ejhieh, Increased photocatalytic activity of NiO and ZnO in photodegradation of a model drug aqueous solution: Effect of coupling, supporting, particle size, and calcination on temperature. J. Hazard. Mater. 321, pp. 629–638 (2017).

INVESTIGATION OF PHYSICAL, MAGNETIC, AND ELECTROCHEMICAL PROPERTIES OF SILVER-IRON NANOPARTICLES SYNTHESIZED BY GAMMA RADIOLYSIS

Abstract

The synthesis of silver-iron nanoparticles (NPs) by gamma-ray co[60] at 25 and 50 kGy doses were studied. The radiolytic synthesis method can be used to properly control the nucleation process in a single step process without the need for reducing agents. The dose rate has a significant effect because it facilitates the modification of the physical and chemical properties of the material. X-ray diffraction (XRD) confirmed the formation of AgCl, and $AgFeO_2$ NPs at 25 kGy and 50 kGy doses, respectively. This observation guided us to pursue further analyses on the $AgFeO_2$ NPs obtained at 50 kGy dose. The crystallographic results from XRD, and selected area electron diffraction (SAED), showed the microstructure of the $AgFeO_2$ NPs to be polycrystalline, with an average size of 9.55 nm, extracted from the Scherrer equation. A rhombohedral structure of highly agglomerated $AgFeO_2$ NPs was observed from high resolution transmission electron microscope (HRTEM). The average NP size was estimated to be 18.180 ± 0.571 nm. The energy dispersive X-ray spectroscopy (EDS) and attenuated total reflection-Fourier transform infra-red (ATR-FTIR) confirmed pure silver and iron in the sample. The photoluminescence measurement showed some defects with oxygen vacancies. The magnetic behavior using a vibrating sample magnetometer (VSM) suggested the superparamagnetic behavior of $AgFeO_2$ NPs. Electrochemical properties confirmed pseudo-capacitive behavior of $AgFeO_2$ electrode.

7.1. Introduction

Delafossites named in honor of French mineralogist Gabriel Delafosse, are a promising class of materials with the general formula of ABO_2, that consists of alternating layers of A cations (Cu^+ or Ag^+) and edge-sharing are coordinated by two oxygen ions with the linear O-B-O bonds. Each B cation (typically Ga^{3+}, Fe^{3+}, Cr^{3+}, In^{3+}, and Co^{3+}), located in the slightly distorted oxygen octahedron, is coordinated with six oxygen ions and oriented to the c-axis [7.1, 7.2]. Depending on the order of layer stacking, the delafossite structure can exist in two polytypes,

namely rhombohedral 3R (space group symmetry R-3m) and hexagonal 2H type (space group symmetry P63/mmc) [7.3]. Among different types of delafossites, $AgFeO_2$ is an n-type semiconductor material that possesses a layered structure with one layer as the close-packed monovalent Ag ions and the other as an edge-shared $Fe^{3+}O_6$ octahedron with Fe^{3+} inside [7.3]. $AgFeO_2$ is of interest to researchers mainly due to its tailored bandgap in the range of 1.15–1.7 eV [7.1, 7.4] and, its magnetic properties [7.5, 7.6] that are related to its shape and morphology [7.7]. It, therefore, has a diverse range of applications including photocatalysis [7.3], antimicrobial [7.8], photochemical [7.9], energy storage [7.10], electrocatalysis [7.11], electrochemical [7.12], and gas sensors [7.13].

Several methods have been used to synthesize delafossite $AgFeO_2$ (silver iron oxide) nanoparticles (NPs) as reported by some works elsewhere. Wang et al., 2014 [7.13] synthesized $AgFeO_2$ NPs via the facile hydrothermal method and irradiated them with various doses of gamma-ray for enhancement of gas sensor properties. El-Bassuony and Abdelsalam, 2017 [7.10] synthesized $AgFeO_2$ by double nanometric delafossite to be suitable for energy storage in a solar cell. Moghaddam et al., 2019 [7.11] synthesized $AgFeO_2$ as an electrocatalyst with excellent activity for water reduction and oxidation via carbon paste electrode. Ahmed et al., 2020 [7.9] synthesized $AgFeO_2$ NPs by the modified hydrothermal procedure for photocatalytic performance. Singh et al., 2021 [7.12] synthesized $AgFeO_2$ delafossite by chemical method to assess the electrochemical performance. Muthukumar et al., 2020 [7.14] synthesized $AgFeO_2$ NPs via the precipitation method using leaves extract as a reducing agent for antibacterial, antioxidant and cytotoxicity activities. Rao in 2021 [7.15] synthesized and characterized zinc oxide @ silver ferrite multiferroic nanocomposite by co-precipitation followed by sol-gel technique for assessment of magnetic properties. Zhao et al., 2022 [7.16] synthesized g-C_3N_4/$AgFeO_2$ delafossite by co-precipitation method for photocatalytic performance. However, some methods presented limitations such as long analysis times and the use of expensive chemical modifications which are toxic due to the generation of harmful residues for the environment. To mitigate such drawbacks, ionizing radiations [7.17] can interact with the nanomaterials and cause significant simple point (vacancies and interstitials) and line (dislocation lines) defects in the microstructures of the bombarded material [7.18, 7.19]. Obodo et al., 2020 [7.20, 7.21] demonstrated that ion beam irradiation is a useful tool to enhance or damage the properties of nanostructured materials depending on the dosage's radiation beamed on the material showing that those modifications enhanced the properties of irradiated Co_3O_4-NiO-ZnO/GO especially when it occurs at the nanoscale level for the betterment of humanity. They also reported that low doses of copper ion irradiation enhanced the properties of the

123

nanowires while high doses induced structural defects. Furthermore, the effects of copper ion irradiation were found to change the properties of the nanowires and to increase in irradiation dose that induced extra changes in the nanowires.

Besides, other works showed that the radiolytic reduction method using gamma Co^{60} ray irradiation with short wavelength and high energy is considered as an effective method for the synthesis and modification of nanomaterials due to several benefits such as (1) the reduction reaction of metal ions performed at ambient condition; (2) the rate of reduction reaction can be properly controlled; (3) the reducing agents uniformly distributed in the solution; and (4) large-scale production can be favorably set up and satisfied with requirements of the clean production process [7.13, 7.22–7.25]. No previous report in the literature has been done so far to synthesize AgFeO$_2$ delafossite using the radiolytic reduction by gamma irradiation for electrochemical properties.

For the first time, we report here, the main structural, morphological, magnetic, and electrochemical properties of AgFeO$_2$ NPs synthesized by gamma radiolysis using Co^{60} as the source of irradiation.

7.2. Experimental

7.2.1. Chemicals

All the chemicals namely silver nitrate (AgNO$_3$), ferric nitrate nonahydrate, (Fe(NO$_3$)$_3$.9H$_2$O), iron (III) chloride hexahydrate (FeCl$_3$.6H$_2$O), isopropyl alcohol (CH$_3$CHOHCH$_3$) and sodium hydroxide (NaOH) were purchased as an analytical grade reagent (Sigma Aldrich, Modderfontein, South Africa) and used without any further purification.

7.2.2. Synthesis: irradiation process via gamma-ray Co^{60}

7.2.2.1. Fe-Ag [1:7] at 25 kGy dose

100 mg of FeCl$_3$.6H$_2$O and 700 mg of AgNO$_3$ were dissolved, respectively, in 50 mL of distilled water and stirred for 30 min on a hot plate at 60 °C. The solution was orange, and the pH was equal to 2.35. Thereafter, 10 mL of CH$_3$CHOHCH$_3$ was added as a scavenger of OH radicals to the solution. 75 mg of NaOH was added dropwise into the mixture until its pH reaches 11, followed by another 30 min of stirring on a hot plate at 60 °C. The color changed from orange to black due to the addition of NaOH. The final black solution was irradiated using a Co^{60} gamma irradiation source at 25 kGy dose (dose rate of 25 kGy/min). No change of color was

observed. The black irradiated solution was centrifuged thrice at 4000 rpm with distilled water and ethanol every 20 min and dried in the oven at 80 °C for 2 h.

7.2.2.2. Fe-Ag [1:7] at 50 kGy dose

100 mg of $Fe(NO_3)_3.9H_2O$ and 700 mg of $AgNO_3$ were dissolved in 50 mL of distilled water and stirred for 30 min on a hot plate at 60 °C. The solution was orange, and the pH was equal to 2.35. Thereafter, 10 mL of $CH_3CHOHCH_3$ was added as a scavenger of OH radicals to the solution. 75 mg of NaOH was added dropwise into the mixture until its pH reaches 11.24, followed by another 30 min of stirring on a hot plate at 60 °C. The color changed from orange to black due to the addition of NaOH. The final solution was irradiated using a Co^{60} gamma irradiation source at 50 kGy dose (dose rate of 50 kGy/min). No change of color was observed. The black irradiated solution was centrifuged thrice at 4000 rpm with distilled water and ethanol every 20 min and dried in the oven at 80 °C for 2 h.

7.2.3. Characterizations

High-resolution transmission electron microscopy (HRTEM) measurements were performed using a Joel JEM 4000EX electron microscopy unit with a resolution limit of about 0.12 nm at an accelerating voltage of 200 kV, combined with selected area electron diffraction (SAED). Field emission scanning electron microscopy (FESEM) measurements were performed using Zeiss Ultra 55 scanning electron microscopy. X-ray diffraction (XRD) measurements were performed using a Bruker AXS D8 diffractometer with an irradiation line CuKα1 with a wavelength of $\lambda_{CuK\alpha1}=1.5406$ Å operating at a voltage of 40 kV and a current of 35 mA, in the angular range of 20–90°. Energy dispersive X-ray spectroscopy (EDS) spectrum was collected with an EDS Oxford instrument X-Max solid-state silicon drift detector operated at 20 kV. The ATR-FTIR absorption spectrum was measured using a Thermo Nicolet 8700 FTIR spectrometer in 400 to 4000 cm^{-1} spectral range. At an excitation wavelength of 372 nm, a photoluminescence (PL) spectrum was recorded from 200 to 800 nm using a Varian Cary Eclipse Fluorescence Spectrophotometer. A vibrating sample magnetometer (VSM) was used to measure the magnetic properties at room temperature (Cryogenic Ltd., UK). Gamma-ray with Co^{60} source type GIK-9-4, S/N 08398 and 56 TBq was used.

7.2.4. Electrochemical measurements

A working Glassy carbon electrode (GCE), Ag/AgCl reference electrodes with a 3 M NaCl salt bridge solution, and platinum wire as a counter electrode were purchased from CH Instruments,

USA, performed out in a three-electrode system configuration and conducted on Autolab Potentiostat electrochemical workstation.

A small amount of $AgFeO_2$ NPs was prepared by dissolving in ethanol and 2 µl of 5 % Nafion solution was added. The mixture was ultra-sonicated in a warm water bath for 15 min, before being drop-coated on the cleaned GCE's surface area. To make $GCE/AgFeO_2$ the working electrode for the electrochemical analysis, the coated GCE was dried in an oven at 35 °C for 1 h. The cyclic voltammetry (CV) analysis is used to describe the nature of $GCE/AgFeO_2$, square wave voltammetry (SWV) analysis is used to improve the sensitivity and complete CV, and the electrochemical impedance spectroscopy (EIS) on $GCE/AgFeO_2$ was measured in 0.1 M KOH aqueous solution used as the electrolyte, at a perturbation amplitude of 10 mV within a frequency of 100 kHz-100 mHz to investigate the electrochemical behavior of the electrode.

7.3. Results and Discussion

7.3.1. Crystallographic analysis

The XRD of Fe-Ag [1:7] at 25 kGy dose (AgCl NPs) in Figure 7.1(a) showed the presence of intense and well-defined diffraction peaks. The peaks observed at 2θ degrees of 27.831; 32.244; 46.234; 54.830; 57.480; and 76.736 harmonized to the reflection's planes of AgCl (111); (200); (220); (311); (222); and (420) in line with the reported data JCPDS card number 31–1238, which correspond to face centered cubic crystalline structure with standard lattice parameters of a = 5.549 Å. The sharper peaks in the XRD spectrum indicate the highly crystalline nature of the AgCl NPs. Through these results, it can be concluded at 25 kGy dose, the bimetallic silver-iron NPs expected were not obtained.

The XRD of Fe-Ag [1:7] at 50 kGy dose ($AgFeO_2$ NPs) in Figure 7.1(b) depicted the presence of intense and well-defined diffraction peaks. The sharper peaks observed at 2θ degrees of 28.791; 34.386; 60.919; and 68.751 matched well with the reflection's planes of $AgFeO_2$ (006), (102), (110), and (116) in line with the reported data JCPDS card number 75–2147 of the rhombohedral crystalline structure without any impurity peaks depicted in the XRD spectrum, confirm a highly crystalline phase of $AgFeO_2$ NPs [7.3, 7.26]. XRD results showed the obtention of AgCl and $AgFeO_2$ NPs at 25 and 50 kGy doses, respectively. As the goal of this study aims to evaluate the properties of silver-iron oxide NPs, further analyses were performed at 50 kGy dose only. The findings are consistent with those reported elsewhere [7.27].

126
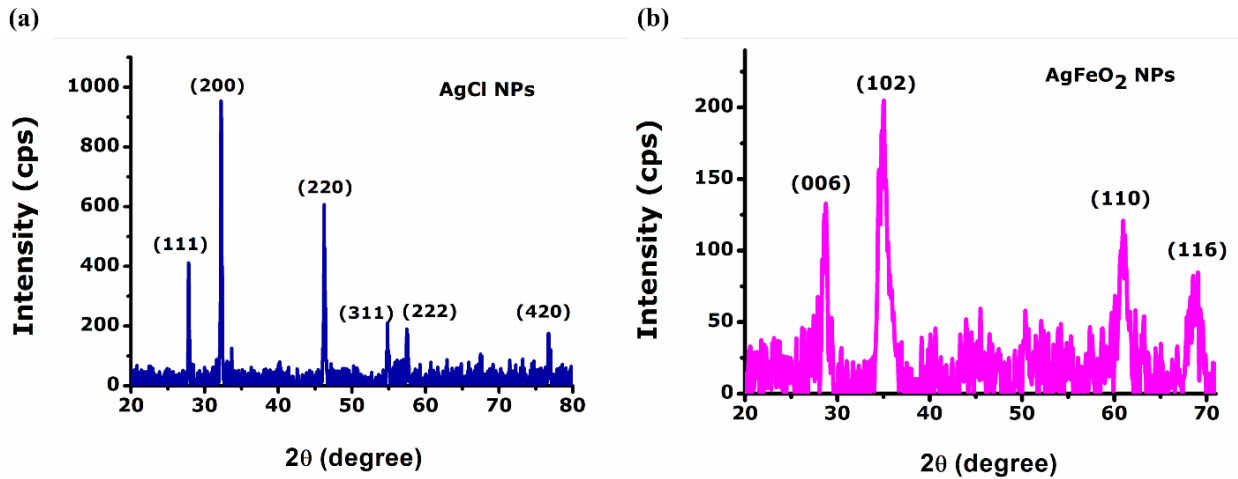
Figure 7.1: XRD results of AgCl NPs irradiated at 25 kGy dose **(a)** and AgFeO₂ NPs irradiated at 50 kGy dose **(b)** in a basic pH

The corresponding crystal size obtained from the Scherrer equation is reported in Table 7.1 by considering the intensive peaks from the XRD spectrum.

From the Scherrer equation, it is well-known that:

$$D = \frac{K\lambda}{\beta Cos\theta}$$ (7.1)

Where D is the average size in nm, λ is the wavelength, β is the full width half maximum, and θ is the peak position in radians.

Table 7.1: Major XRD characteristics of the various Bragg diffraction peaks of AgFeO₂ NPs using the Scherrer equation

(hkl)	2θ (°)	FWHM (°)	R^2	Crystalline size (Å)	Average Crystalline size (nm)	Lattice strain
(006)	28.65	0.8516	0.999	113	9.55	1.440
(102)	34.87	0.9729	0.998	95		1.345
(110)	60.97	1.0030	0.999	100		0.741
(116)	68.58	1.3624	0.998	74		0.870

7.3.2. Microscopic measurements

The morphology, microstructure, and crystallinity of Fe-Ag [1:7] i.e., $AgFeO_2$ NPs irradiated at 50 kGy dose were investigated using HRTEM combined with SAED and FESEM as presented in Figure 7.2. Highly agglomerated, quasi-rhombohedral shaped nanoparticles are depicted from HRTEM and FESEM micrographs whereas SAED exhibits several diffraction rings with clear diffraction spots confirming its polycrystalline nature, with the indexing provided in the figure. This agrees with the XRD spectrum in Figure 7.1(b). By fitting the histogram data with a Gaussian distribution, the average particle size extracted from HRTEM micrographs amounted to 18.180 ± 0.571 nm.

EDS analysis was used to confirm the structure of the pure silver, iron, and oxygen atoms on the sample's surface. The carbon peak in the EDS spectrum is because of the use of carbon tape as grid support to immobilize the $AgFeO_2$ NPs and minimize charging effects. These findings are in line with the previous publications of Abdelhamid et al., 2015 and Wang et al., 2014 [7.2, 7.13]. Hence, it is concluded that the gamma radiolysis method is very effective to prepare delafossite $AgFeO_2$ NPs.
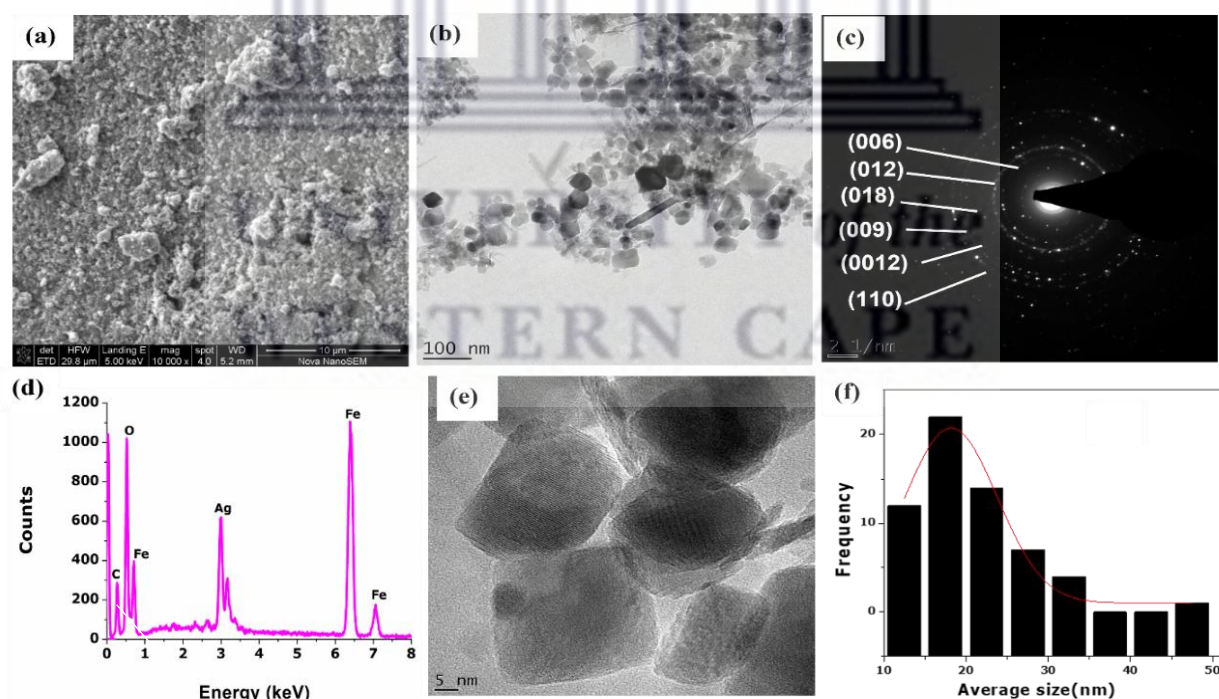
Figure 7.2: (a) FESEM, **(b)** HRTEM, **(c)** SAED, **(d)** EDS spectrum, **(e)** HRTEM, **(f)** Average size distribution of $AgFeO_2$ NPs irradiated at 50 kGy dose in a basic pH

7.3.3. Vibrational properties

To validate and to conclude on the purity of $AgFeO_2$ NPs, attenuated total reflection-Fourier transform infrared spectroscopy (ATR-FTIR) studies were conducted to identify the possible biomolecules involved in the irradiation and presented in Figure 7.3. The peaks centered around 447 and 576 cm^{-1} are from Ag-O and Fe-O, respectively [7.9, 7.10, 7.14], indicating the existence of $AgFeO_2$ NPs. The bands around 1354 cm^{-1} originated from the asymmetric and symmetric stretching of the –C–O–C–. The prominent peaks at 796 and 890 cm^{-1} are attributed to FeOOH [7.11]. The strong and broad band centered around 1560 cm^{-1} could be assigned to the bending modes of interlayer water molecules [7.10]. The broad bands around 2925 and 3766 cm^{-1} are assigned to the hydroxyl groups that originated from moisture content in the sample [7.14].
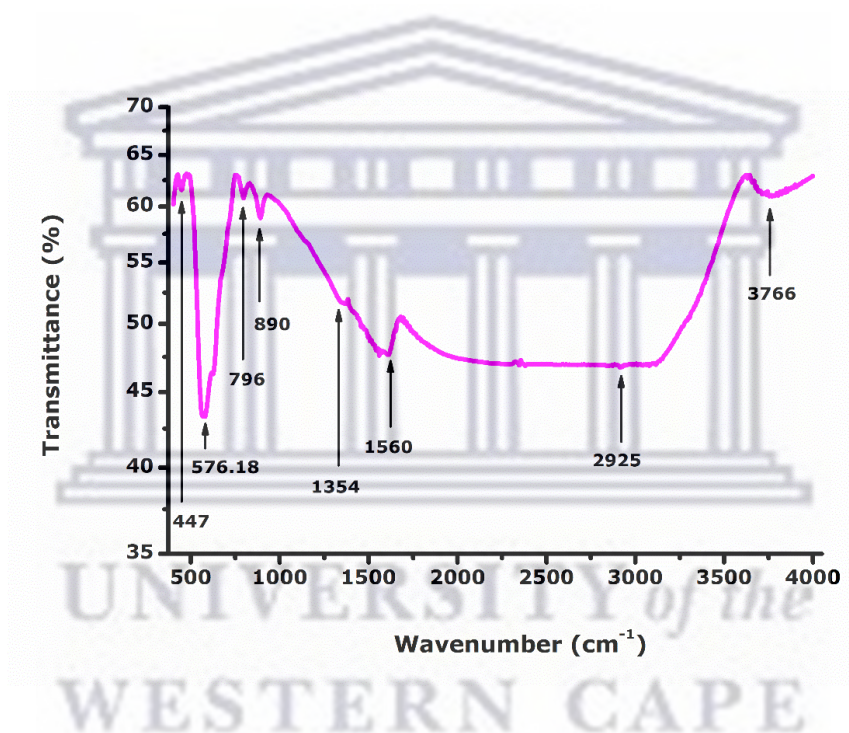
Figure 7.3: ATR-FTIR of $AgFeO_2$ NPs irradiated at 50 kGy dose in a basic pH

7.3.4. Photoluminescence spectroscopy (PL)

PL is a powerful tool to investigate the electronic structure, transfer behavior and recombination rate of photoexcited electron-hole pairs in semiconductors according to the fluorescence intensity [7.3].

Figure 7.4 depicts the photoluminescence (PL) spectrum of the $AgFeO_2$ NPs irradiated at 50 kGy dose. The appearance of blue emission in a visible region centered at 503 nm could be attributed to the defects emission region where emission results from the existence of defects

129

and oxygen vacancies in the $AgFeO_2$ structure [7.10]. Besides, the method of synthesis and experimental conditions may affect various factors such as oxygen deficiency, surface roughness, and impurity centers [7.28, 7.29].
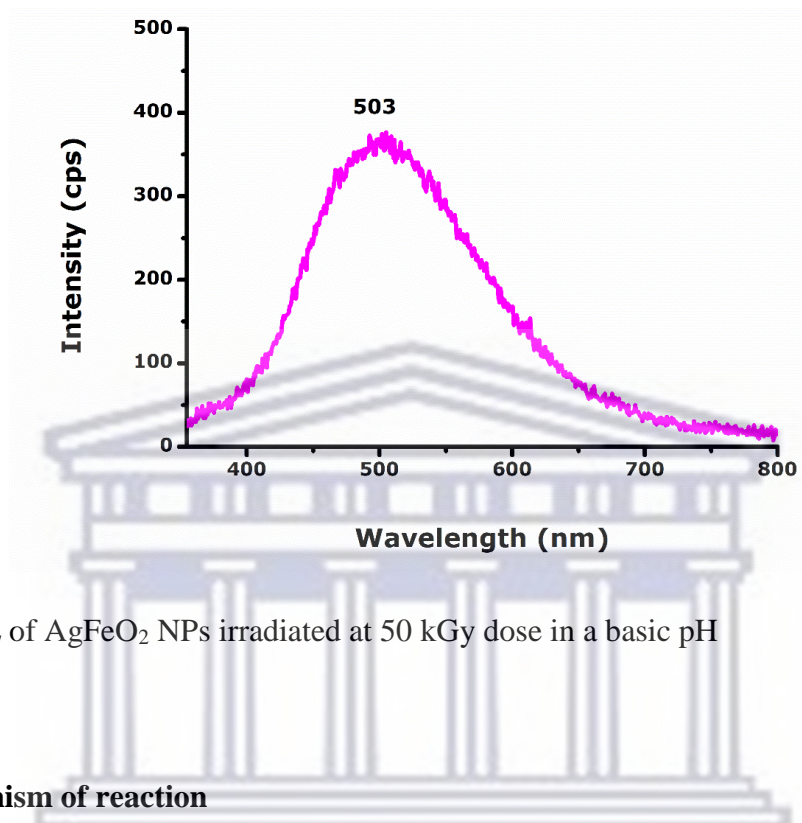
Figure 7.4: PL of $AgFeO_2$ NPs irradiated at 50 kGy dose in a basic pH

7.3.5. Mechanism of reaction

The formation of $AgFeO_2$ nanoparticles during the radiolytic reduction by gamma irradiation is presented [7.30].

The interaction results in the production of secondary electrons in an aqueous solution that forms hydrated electrons (e^-_{aq}), hydroxyl radicals ($OH^\bullet$) and hydrogen radicals ($H^\bullet$) as shown in Eq. 1.

$H_2O \xrightarrow{\gamma\text{-radiation}} e^-_{aq}, H_3O^+, H^\bullet, H_2, OH^\bullet, H_2O_2$ (Radiolysis of water) (1)
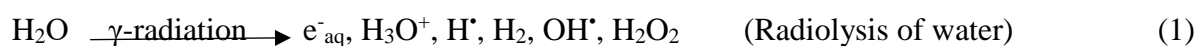
Among these active species, the solvated electrons (e^-_{aq}) are strong reducing agents and can reduce Ag (I) and Fe (III) ions into their lower state as shown in Eq. 2a, b.

$Ag^+ + e^- \rightarrow Ag^0$ (Reduction and nucleation) (2a)

$Fe^{3+} + 3e^- \rightarrow Fe^0$ (Reduction and nucleation) (2b)

Isopropyl alcohol, the most commonly used hydroxyl radical scavenger, scavenges hydrogen and hydroxyl radicals, generating a secondary radical with high negative potential.

According to Eqs. 3, 4 and 5, the new radical can now contribute to the reduction of metal ions into their zero-valent form.

130

$OH^{\bullet} + CH_3\text{-}CH(OH)\text{-}CH_3 \rightarrow H_2O + H_3C\text{-}C^{\bullet}(OH)\text{-}CH_3$ (Radical association)   (3)

$H^{\bullet} + CH_3\text{-}CH(OH)\text{-}CH_3 \rightarrow H_2 + H_3C\text{-}C^{\bullet}(OH)\text{-}CH_3$ (Radical association)   (4)
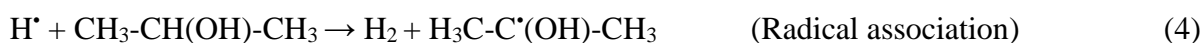
Thus formed 2-propanol radical can additionally reduce the silver (Ag^+) and ferric (Fe^{3+}) ions:

$Ag^0 + Fe^0 + 2OH^{\bullet} + 2[CH_3\text{-}CH(OH)\text{-}CH_3] \rightarrow 2[H_3C\text{-}C^{\bullet}(OH)\text{-}CH_3] + AgFeO_2 + 2H_2$

(Reduction and nucleation)   (5)
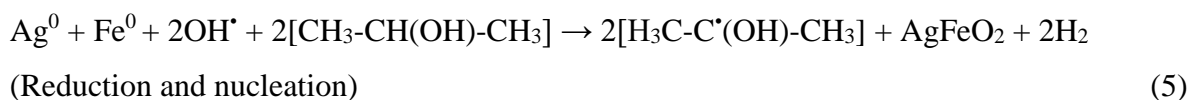
The $AgFeO_2$ nanoparticles formed by gamma irradiation were confirmed by characterization on several analytical techniques as explained in the above sections.

7.3.6. Magnetic properties

The magnetic measurements of $AgFeO_2$ NPs irradiated at 50 kGy dose were performed using VSM at room temperature (300 K) with a maximum of an applied magnetic field range from -3 T to + 3 T as presented in Figure 7.5. It is clearly seen that the magnetization curve increases with the applied magnetic field and the curve shows a magnetic saturation at a high field. Nanoparticles' unique magnetic properties are due to their high surface-to-volume ratios which result in the uncompensated magnetic spins attributed to the surface atoms and may contribute to the net magnetization [7.5]. Another factor that plays a significant role in influencing magnetic behavior is the composition of resultant NPs [7.6, 7.31].

The magnetic hysteresis loops (M-H) of $AgFeO_2$ NPs exhibit a low coercivity ($H_c = 0.002$ T), a low magnetic remanence ($M_r = 0.0145$ emu/g) and saturation magnetization ($M_s = 0.0190$ emu/g). The low value of coercivity (H_c) is due to the low magnetocrystalline anisotropy constant (K) value which was calculated from the following equation [7.7]:

$$H_c = \frac{0.98\,K}{M_s} \tag{7.2}$$

Furthermore, the value of the saturation magnetization (M_s), which is smaller than the bulk value of 55 emu/g is because of the low value of the magnetic dipole moment (η) that was calculated from the following equation [7.10]:

$$\eta = \frac{M_{wt} \times M_s}{5585} \tag{7.3}$$

where M_s is saturation magnetization and M_{wt} is the molecular weight. Also, the value of the squareness (M_r/M_s) was calculated and reported in Table 7.2.

131

The decrease in M_s value of AgFeO$_2$ NPs compared to its bulk value can be attributed to a variety of factors, including the shape of the sample, heat treatment rate, crystallinity, particle sizes, and magnetization direction [7.32, 7.33]. AgFeO$_2$ NPs exhibited the interaction of nanoparticles by exchange coupling when the squareness > 0.5 and by magnetostatic interactions when the squareness < 0.5 [7.10]. The magnetic measurement showed a superparamagnetic behavior of AgFeO$_2$ NPs because of the reduced coordination symmetry between oxygen atoms at the nanoparticles' surface, disordered surface spins, crystallinity, particle size, and irradiation dose [7.34]. Hence, NPs with smaller particle sizes have more spin disorder than those with larger particle sizes. Consequently, the increase in M_s value is usually observed in conjunction with an increase in particle sizes [7.35].
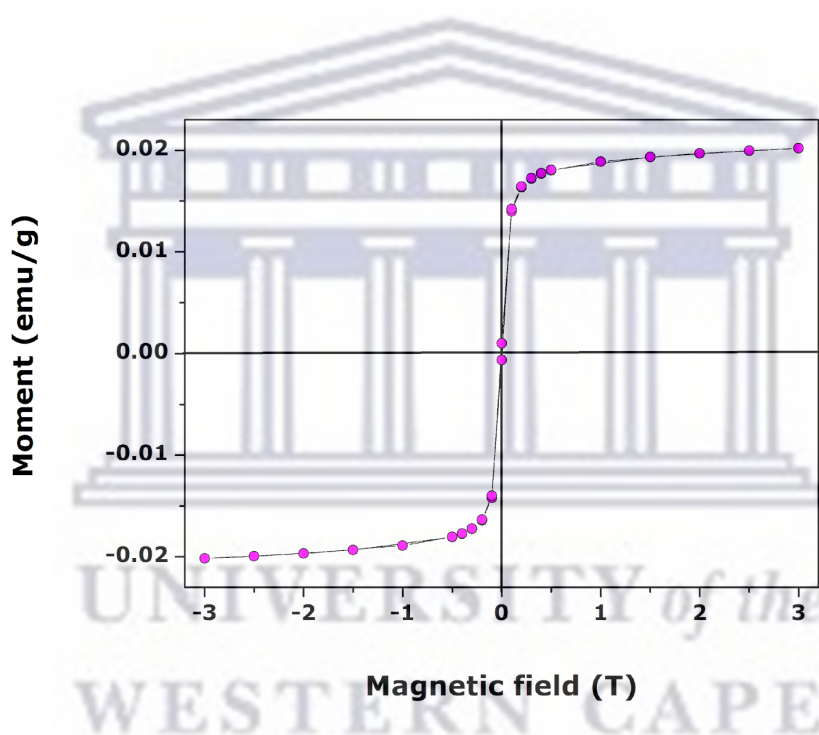
Figure 7.5: Magnetic characterization of AgFeO$_2$ NPs irradiated at 50 kGy dose in a basic pH

Table 7.2: Magnetic parameters of AgFeO$_2$ NPs

Magnetic parameters	H_c(T)	M_s (emu/g)	M_r (emu/g)	Squareness (M_r/M_s)	Magnetocrystalline anisotropy constant K (erg/T) x 10^{-5}	Experimental magnetic moment η (μ_B)	Behavior
AgFeO$_2$	0.002	0.019	0.0145	0.763	3.877	0.066	Superparamagnetic

7.3.7. Electrochemical studies

7.3.7.1. Cyclic Voltammetry (CV) results

To evaluate the charge transfer properties, the unmodified and modified GCE electrodes were conducted in the potential region of - 0.6 V to +0.6 V with the scan rate of 50 mV/s in 0.1 M KOH as presented in Figure 7.6. It is clearly seen that the unmodified electrode GCE does not have a peak, while the modified electrode GCE shows four redox peaks. The oxidation peak in the region of 0.1 V corresponds to the oxidation of Fe to Fe^{3+} and the oxidation peak in the region of 0.5 V corresponds to the oxidation of Ag to Ag^+ at anodic sweep while the reduction peak in the region of - 0.38 V corresponds to the reduction of Fe^{3+} to Fe and the reduction peak in the region of 0.24 V corresponds to the reduction of Ag^+ to Ag at cathodic sweep. These observations reveal the electrochemical characteristics derived from Faradaic redox reactions between the glassy carbon's surface area and alkaline electrolyte [7.36, 7.37].
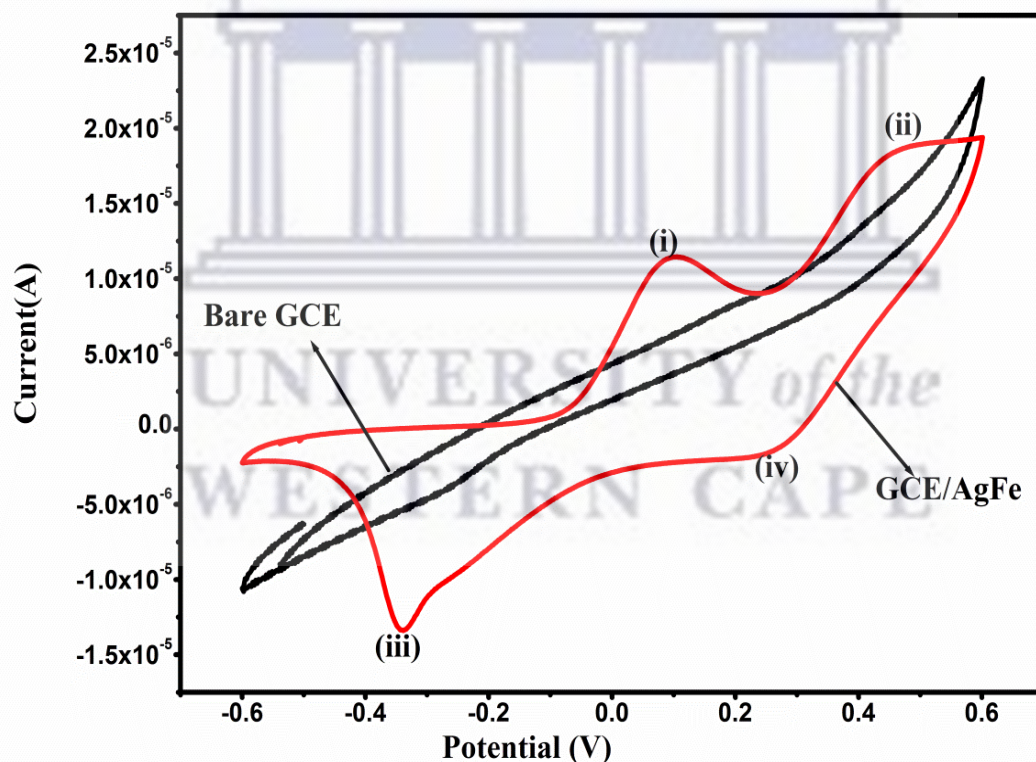
Figure 7.6: (a) Cyclic voltammetry of bare GCE and **(b)** GCE/AgFe NPs at 50 mV/s in 0.1 M KOH

The impact of the scan rate (υ) on the modified $GCE/AgFeO_2$ electrode was measured in scan rates (20–100 mV/s) as presented in Figure 7.7. The electrochemical performance can be evaluated by observing the peak current density in the cathodic and anodic scans. The results show an increase as the scan rates are increased, the high current at the modified $GCE/AgFeO_2$ electrode suggesting a fast diffusion of more molecules in and out of the electrode surface and excellent electrochemical reversible redox reaction [7.12, 7.20]. It is also observed the slight shift of redox peak potentials, and diffusion of electrolyte/analyte solution to the electrode surface limits the surface electrochemistry to more positive potentials.
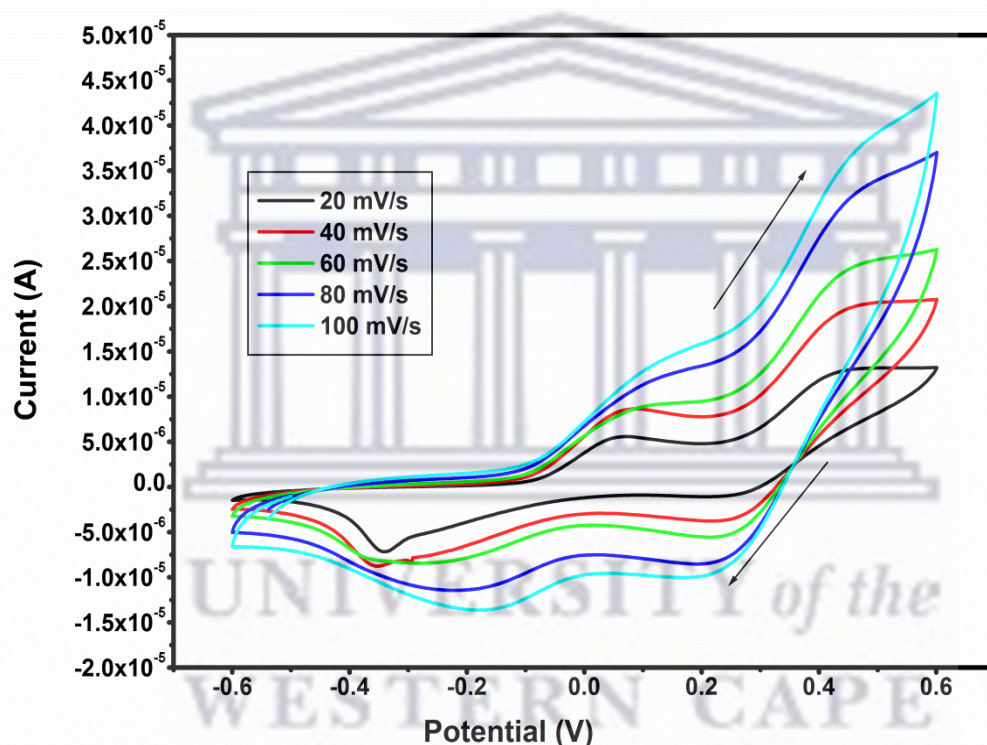
Figure 7.7: Cyclic voltammetry of $GCE/AgFeO_2$ NPs in 0.1 M KOH at different scans rates (20– 100 mV/s)

To improve the sensitivity of the unmodified and modified $GCE/AgFeO_2$ electrode and validate the CV results, typical square wave voltammetry was used and illustrated in Figure 7.8.
The anodic peak is observed only from the modified electrode suggesting that $GCE/AgFeO_2$ electrode possesses good rate capability, good stability of NPs, and electrochemical reversibility which denotes the fast charge transfer kinetics between the electrode and the

134

analyte which can further improve the electrochemistry through the feasible oxidation states and the synergetic effect [7.37, 7.38].
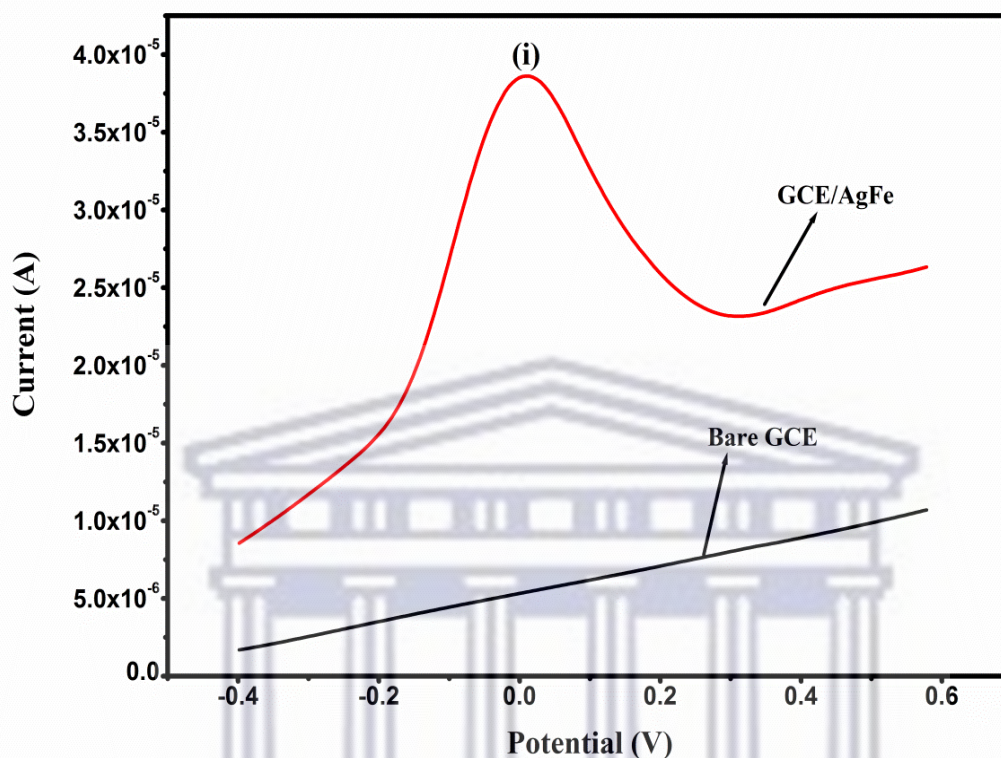
Figure 7.8: Square wave voltammetry of GCE/AgFe NPs in 0.1 M KOH as an electrolyte

7.3.7.2. Electrochemical Impedance Spectroscopy (EIS) results

EIS is used to understand the electrochemical behavior of the modified GCE/AgFeO$_2$ electrode and to give insightful information about the reaction at the electrode-electrolyte interface.

The electron transfer resistance (R_{ct}) of the redox probe at the electrode interface corresponds to a semi-circular portion in the high frequency region, and the Warburg impedance corresponds to a linear portion in the low frequency region from the diffusion limited process as presented in Figure 7.9 (a). The R_{ct} indicates fast charge transfer between the electrolyte and electrode, which suggests excellent electron transfer kinetics and conductivity. The electrochemical process on the electrode's surface is measured by Warburg impedance implying controlled diffusion. Thus, the electrochemical performance is related to the charge transfer process at the interface, and controlled diffusion making AgFeO$_2$ highly suitable for charge transfer applications [7.11, 7.37].

135

Figure 7.9 (b) highlights information on the impedance and the conductivity of materials through phase angle as a function of frequency which measures the phase shift in degree. The maximum phase angles of 70°, close to 90° suggesting a good electrical conductivity of the modified GCE/AgFeO$_2$ electrode [7.38–7.40].
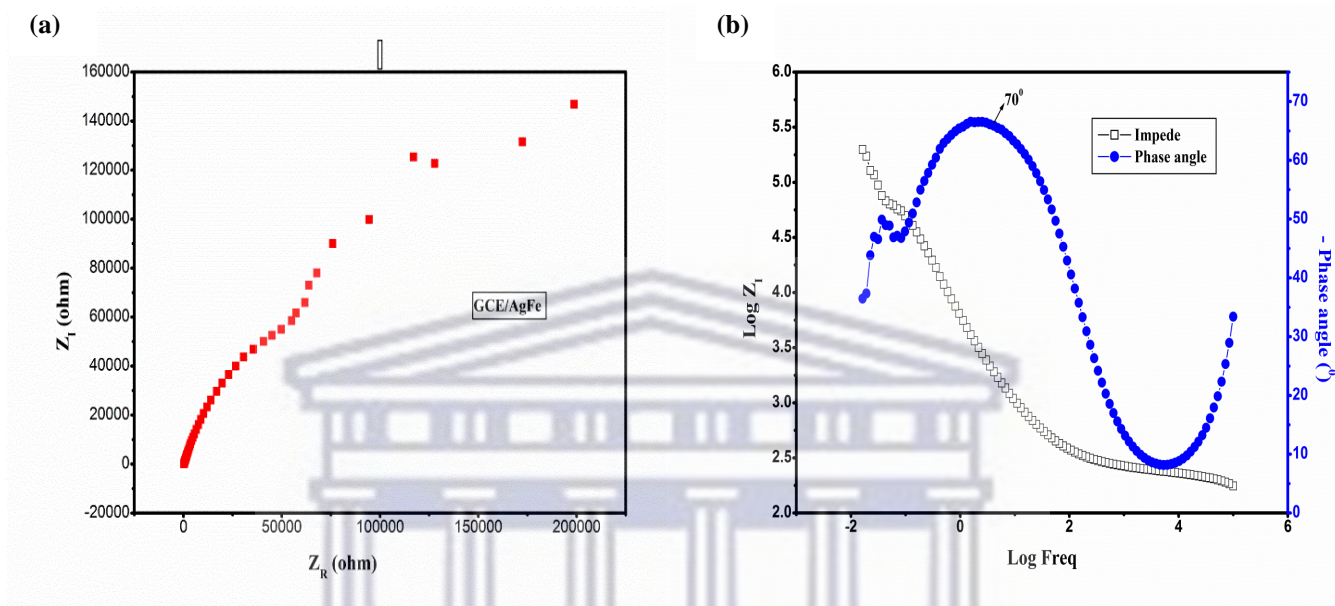
Figure 7.9: **(a)** Nyquist and **(b)** Bode plots

7.4. Conclusion

This research provides a new method for the preparation of silver iron oxide (AgFeO$_2$) nanoparticles (NPs) namely the gamma radiolysis and could be explored for use in the preparation of other delafossites. The crystallographic and microscopic results confirmed the polycrystallinity, self-assembled, highly agglomerated, and rhombohedral structure of AgFeO$_2$ NPs. The average sizes from the Scherrer equation and HRTEM observations were 9.55 and 18.180 ± 0.571 nm, respectively. Vibrational properties confirmed the purity and chemical bonds of the irradiated AgFeO$_2$ NPs. The photoluminescence showed defects with oxygen vacancies. The magnetic properties suggested the superparamagnetic behavior of AgFeO$_2$ NPs. The electrochemical studies exhibited good electrical conductivity of the irradiated AgFeO$_2$ NPs, which makes them suitable for electrochemical applications.

136

7.5. References

[7.1] K.P. Ong, K. Bai, P. Blaha, P. Wu, Electronic structure and optical properties of $AFeO_2$ (A_Ag, Cu) within GGA calculations. Chem. Mater. 19, pp. 634–640 (2007).

[7.2] H.N. Abdelhamid, Delafossite Nanoparticle as New Functional Materials: Advances in Energy. Nanomedicine and Environmental Applications. Mater. Sci. Forum 832, pp. 28–53 (2015).

[7.3] L. Yin, Y. Shi, L. Lu, R. Fang, X. Wan and H. Shi, A Novel Delafossite Structured Visible-Light Sensitive $AgFeO_2$ Photocatalyst: Preparation, Photocatalytic Properties, and Reaction Mechanism. Catalysts, 6, 69 (2016).

[7.4] W.C. Sheets, E.S. Stampler, M.I. Bertoni, M. Sasaki, T.J. Marks, T.O. Mason, and K.R. Poeppelmeier, Silver Delafossite Oxides. Inorg. Chem. 47, pp. 2696–2705 (2008).

[7.5] N. Terada, D.D. Khalyavin. P. Manuel, Y. Tsujimoto, A.A. Belik, Magnetic ordering and ferroelectoicity in multiferroic $2H-AgFeO_2$: Comparsion between hexagonal and rhombohedral polytypes. Phys. Rev. B 91, Article 094434, pp. 1–7 (2015).

[7.6] J. Chakraborty and D. Dasgupta, Electronic, magnetic and ferroelectric properties of rhombohedral $AgFeO_2$: an ab initio study. Cond-mat.mtrl-sci., Article 700032 (2018).

[7.7] Y.L.N. Murthy, T. Kondala Rao, I. K. viswanath, R. Singh, Synthesis and characterization of nano silver ferrite composite. Journal of Magnetism and Magnetic Materials 322, pp. 2071–2074 (2010).

[7.8] A.A. H. El-Bassuony, H. K. Abdelsalam, Synthesis, characterization and antimicrobial activity of $AgFeO_2$ delafossite. Journal of Materials Science: Materials in Electronics 29, pp. 11699–11711 (2018).

[7.9] J. Ahmed, N. Alhokbany, A. Husain, T. Ahmad, M.A.M. Khan & S.A. Alsheri, Synthesis, characterization, and significant photochemical performances of delafossite $AgFeO_2$ nanoparticles. Journal of Sol-Gel Science and Technology 94, pp. 493–503 (2020).

[7.10] A.A.H. El-Bassuony, H.K. Abdelsalam, Modification of $AgFeO_2$ by double nanometric delafossite to be suitable as energy storage in solar cell. Journal of Alloys and Compounds 726, pp. 1106–1118 (2017).

[7.11] S.K. Moghaddam, B. Haghighi, S.M.S. Ahmadian, Z. Rezva, Carbon paste electrode modified with $AgFeO_2$ as an electrocatalyst with excellent activity for water reduction and oxidation. Journal of Electroanalytical Chemistry 836, pp. 158–164 (2019).

[7.12] A.N. Singh, R. Mondal, C. Rath and P. Singh, Electrochemical performance of delafossite, $AgFeO_2$: A pseudo-capacitive electrode in neutral aqueous Na_2SO_4 electrolyte. Journal of The Electrochemical Society 168, Article 120512 (2021).

137

[7.13] X. Wang, Z. Shi, S. Yao, F. Liao, J. Ding, M. Shao, Gamma ray irradiated $AgFeO_2$ nanoparticles with enhanced gas sensor properties. J. Solid State Chem. 219, pp. 228–231 (2014).

[7.14] H. Muthukumar, S.K. Palanirajan, M.K. Shanmugam, S.N. Gummadi, Plant extract mediated synthesis enhanced the functional properties of silver ferrite nanoparticles over chemical mediated synthesis. Biotechnology Reports 26, Article e00469 (2020).

[7.15] T.K. Rao, Synthesis and characterization of zinc oxide @ silver ferrite multiferroic nanocomposite. Materials Today: Proceedings 46, pp. 10747–10751 (2021).

[7.16] Y. Zhao, S. Wang, T. Wei, Y. Ren, T. Luan, Enhanced peroxymonosulfate activation for Orange I degradation by $g\text{-}C_3N_4/AgFeO_2$ composite in water. J. Env. Chem. Eng. J. Article 107241 (2022).

[7.17] G.Y. Gerasimov, Radiation methods in nanotechnology. Journal of Engineering Physics and Thermophysics 84, Article 947 (2011).

[7.18] B. Oryema, E. Jurua, I.G. Madiba, I. Ahmad, S.O. Aisida, F.I. Ezema, M. Maaza, Effects of 7 MeV proton irradiation on microstructural, morphological, optical, and electrical properties of fluorine-doped tin oxide thin films. Surf. and Interf. 28, Article 101693 (2022).

[7.19] H. Shehla, F. T. Thema, A. Ishaq, N.Z. Ali, I. Javed, D. Wan, and M. Maaza: Study on γ-Rays Irradiation Induced Structural and Morphological Changes in Copper Nanowires. Recent Trends in Chemical and Material Sciences 4, pp. 69–78 (2021).

[7.20] R.M. Obodo, A. Ahmad, G.H. Jain, I. Ahmad, M. Maaza, F.I. Ezema, 8.0 MeV copper ion (Cu^{++}) irradiation-induced effects on structural, electrical, optical and electrochemical properties of $Co_3O_4\text{-}NiO\text{-}ZnO/GO$ nanowires. Mat. Sci. Energy Technol. 3, pp. 193–200 (2020).

[7.21] R.M. Obodo, A.C. Nwanya, C. Iroegbu, I. Ahmad, A.B.C. Ekwealor, R.U. Osuji, M. Maaza, F.I. Ezema, Transformation of GO to rGO due to 8.0 MeV carbon (C^{++}) ions irradiation and characteristics performance on $MnO_2–NiO–ZnO@GO$ electrode. Inter. J. Energy Res. 44, pp. 6792–6803 (2020).

[7.22] S.K. Sen, M. Noor, M.A. Al Mamun, M.S. Manir, M.A. Matin, M.A. Hakim, S. Nur, S. Dutta, An investigation of ^{60}Co gamma radiation-induced effects on the properties of nanostructured $\alpha\text{-}MoO_3$ for the application in optoelectronic and photonic devices. Opt. Quantum Electron. 51, pp. 1–15 (2019).

[7.23] Y. Rao, D. Banerjee, A. Datta, S. Das, R. Guin, A. Saha, Gamma irradiation route to synthesis of highly re-dispersible natural polymer capped silver nanoparticles. Radiat. Phys. Chem. 79, pp. 1240–1246 (2010).

138

[7.24] I. Ahmad, A. F. Khan, A. Shah, H. Tabassum, A. Diallo, J. Iqbal, F. I. Ezema, M. Maaza, Gamma irradiation-Induced chemical decomposition related bandgap engineering in SnO_2 nanoparticles. Surface Review and Letters 26, Article1850228 (2019).

[7.25] I.G. Madiba, N. Emond, M. Chaker, F.T. Thema, S.I. Tadadjeu, U. Muller, P. Zolliker, A. Braun, L. Kotsedi, M. Maaza, Effects of gamma irradiations on reactive pulsed laser deposited vanadium dioxide thin films. Applied Surface Science 411, pp. 271–278 (2017).

[7.26] W.J. Croft, N.C. Tombs, R.E. England, Crystallographic data for pure crystalline silver ferrite. Acta Crystallogr. 17, pp. 313–314 (1964).

[7.27] M.N. Mirzayev, S.H. Jabarov, E.B. Asgerov, R.N. Mehdiyeva, T.T. Thabethe, S. Biira, N.V. Tiep, Crystal structure changes and weight kinetics of silicon-hexaboride under gamma irradiation dose. Results Phys. 10, pp. 541–545 (2018).

[7.28] M. Singh, M. Goyal, K. Devlal, Size and shape effects on the band gap of semiconductor compound nanomaterials. J. Taibah Univ. Sci. 12, pp. 470–475 (2018).

[7.29] S.M. Hosseini, H.H-Monfared, V. Abbasi, Silver ferrite-graphene nanocomposite and its good photocatalytic performance in air and visible light for organic dye removal. Appl. Org. Chem. 31, Article e3589 (2016).

[7.30] T. Cele, M. Maaza and A. Gibaud, Synthesis of Platinum nanoparticles by Gamma Radiolysis. MRS Advances 3, pp. 2537–2557 (2018).

[7.31] C. Liu, A. J. Rondinone, Z. Zhang, Synthesis of magnetic spinel ferrite $CoFe_2O_4$ nanoparticles from ferric salt and characterization of the size-dependent superparamagnetic properties. J. Pure Appl. Chem.72, pp. 37–45 (2000).

[7.32] A.G. Kolhatkar, A.C. Jamison, D. Litvinov, R.C. Willson, T.R. Lee, Tuning the magnetic properties of nanoparticles. Int. J. Mol. Sci. 14, pp. 15977–16009 (2013).

[7.33] A. Kumar and A. Singhal, Synthesis of colloidal silver iron oxide nanoparticles—study of their optical and magnetic behavior. Nanotechnology 20, Article 295606 (2009).

[7.34] A. khan, M. Javed, A.R. khan, Y. Iqbal, A. Majeed, S.Z. Hussain, S.K. Durrani, Influence of preparation method on structural, optical and magnetic properties of nickel ferrite nanoparticles. Mater. Sci. Pol. 35, pp. 58–65 (2017).

[7.35] H. Jalili, B. Aslibeiki, A.G. Varzaneh, V.A. Chernenko, The effect of magneto-crystalline anisotropy on the properties of hard and soft magnetic ferrite nanoparticles. Beilstein J. Nanotechnol. 10, pp. 1348–1359 (2019).

[7.36] S. Maiti, A. Pramanik, and S. Mahanty, Interconnected network of MnO_2 nanowires with a "cocoonlike" morphology: redox couple-mediated performance enhancement in symmetric aqueous supercapacitor. ACS applied materials & interfaces 6, pp. 10754–10762 (2014).

[7.37] N. Matinise, K. Kaviyarasu, N. Mongwaketsi, S. Khamlich, L. Kotsedi, N. Mayedwa, M. Maaza, Green synthesis of novel zinc iron oxide (ZnFe$_2$O$_4$) nanocomposite via Moringa Oleifera natural extract for electrochemical applications. Applied Surface Science 446, pp. 66–73 (2018).

[7.38] X. Fuku, N. Matinise, M. Masikini, K. Kasinathan, M. Maaza, An electrochemically active green synthesized polycrystalline NiO/MgO catalyst: Use in photo-catalytic applications. Mater. Res. Bull. 97, pp. 457–465 (2018).

[7.39] E.L. Miler and R.E. Rocheleau, Electrochemical behavior of reactively sputtered iron-doped nickel oxide. J. Electrochem. Soc. 144, pp. 3072–3077 (1997).

[7.40] Y. Yan, F.H. Du, X.P. Shen, Z.Y. Ji, H. Zhou, G.X. Zhu, Porous SnO$_2$-Fe$_2$O$_3$ nanocubes with improved electrochemical performance for lithium-ion batteries, Dalton Trans. 43, pp. 17544–17550 (2014).
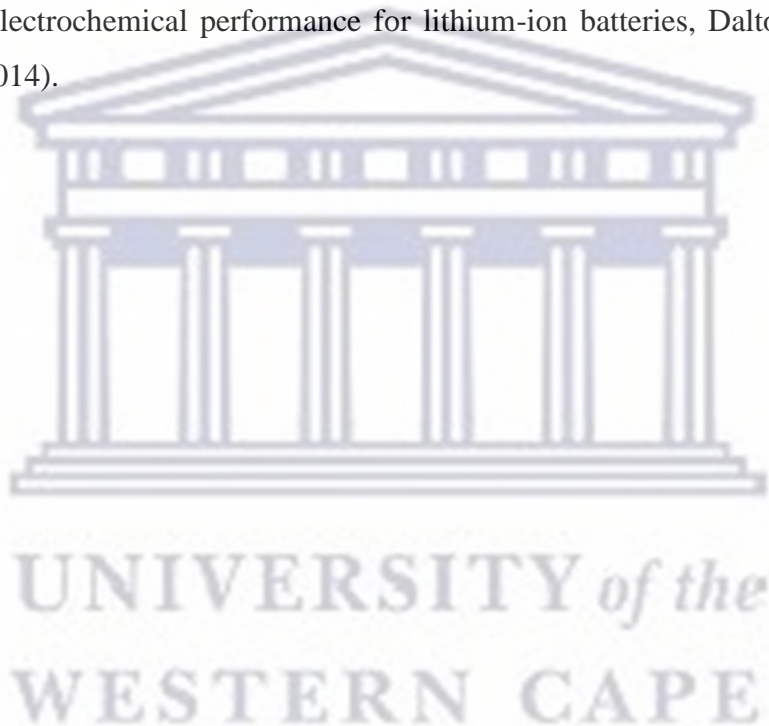
PHYSICAL AND MAGNETIC PROPERTIES OF BIOSYNTHESIZED ZnO/Fe$_2$O$_3$, ZnO/ZnFe$_2$O$_4$, AND ZnFe$_2$O$_4$ NANOPARTICLES

Abstract

For the first time, the physical and magnetic properties of biosynthesized ZnO/Fe$_2$O$_3$, ZnO/ZnFe$_2$O$_4$, and ZnFe$_2$O$_4$ nanoparticles (NPs) from aqueous extract of rosemary leaves extract are reported. The findings demonstrated the green approach as environmentally benign to generate bimetallic alloy NPs from immiscible metals. The crystallographic analyses in line with microscopic observations revealed crystalline, well-agglomerated NPs with hexagonal structures confirming the presence of ZnO. The chemical bonds of Fe-O and Zn-O were detected as well as Fe, Zn, and O elements, showing their existence within the samples. Besides, the magnetic properties portrayed the same paramagnetic behavior due to similar average size distribution whereas the defects coming from oxygen vacancies agreed with the photoluminescence spectroscopy. Overall, the annealing temperature significantly influenced the final structure of generated NPs amongst other parameters.

8.1. Introduction

Bimetallic nanoparticles (NPs) have gained more popularity in the scientific community than monometallic NPs due to their virtuous properties [8.1]. The synthesis of bimetallic NPs from immiscible metals has received little attention in the literature. However, in recent decades, it has piqued considerable concern among scholars due to its valuable physio-chemical properties and potential applications [8.2]. Fe is thermodynamically immiscible with other metals such as Ag, Cu, Pt, Zn, and Au, according to binary phase diagrams [8.3]. There are eight known magnetic iron oxides among hematite (α-Fe$_2$O$_3$) which is the most stable iron oxide under ambient conditions with a rhombohedral structure with black color to steel-grey, or brown to red; magnetite (Fe$_3$O$_4$) which is a ferrimagnetic mineral and a member of the spinel ferrite group and converts to the alpha phase at high temperatures; and maghemite (γ-Fe$_2$O$_3$) the second most stable polymorph of iron oxide, has received considerable attention in recent years due to their ferrimagnetic and oxygen stability properties [8.4]. Because of their polymorphism involving temperature-induced phase transition, unique properties such as electronic, optical, and

141

magnetic that differ from those of their bulk counterparts, and numerous applications such as photocatalytic, magnetic hyperthermia, and biomedical, these three oxides are greatly promising and notorious candidates [8.4, 8.5]. Amongst metal oxides that are immiscible to Fe from the thermodynamic point of view, ZnO seems to be a convenient material for doping. It is a p-type semiconductor with a broad direct bandgap of up to 3.37 eV and high excitation energy of 60 meV, which exhibits high optical transparency and luminescent properties in the near UV and visible regions and is widely employed in electronic and optoelectronic devices, room temperature UV-lasers, short wavelength, and photoconductors [8.6]. The incorporation of Fe into the ZnO lattice is interesting because it fascinates new properties due to synergistic effects which are completely different from their bulk [8.7, 8.8]. However, Fe-Zn alloy is challenging to get as Fe and Zn are immiscible in the bulk phase at equilibrium due to their positive mixing enthalpy of formation observed from their corresponding phase diagram [8.9]. It exists different types of architectures of Fe-Zn such as $Zn_{0.3}$ $Fe_{2.7}O_4$ by hydrothermal method [8.10], $ZnO@Fe_3O_4$ by green process [8.11], ZnO/Fe_2O_3 by microwave-assisted hydrothermal technique [8.12], α-Fe_2O_3-ZnO by wet chemical route [8.13]. Nanotechnology must overcome the intrinsic immiscibility in bimetallic systems because it generates new functional nanomaterials such as $ZnFe_2O_4$-ZnO [8.14, 8.15], and $ZnFe_2O_4$ [8.4, 8.5] with desired properties. This can be achieved by adjusting some parameters to break down the immiscibility aspect such as the materials' composition, methodology, pH, temperature, and volume ratio, which significantly influence the size, shape, and the morphology of final composition of NPs using versatile routes.

Several methods including hydrothermal [8.10], combustion [8.15], hyperthermia [8.5, 8.7, 8.16], sol-gel [8.4, 8.17], solvothermal [8.18], thermal decomposition [8.19], and co-precipitation [8.14, 8.20] are utilized for the synthesis and evaluation of physical, magnetic, thermal, antimicrobial, anneal-tuned, and photocatalytic properties of Fe-Zn NPs. However, these methods contain drawbacks such as cost, efficacy, the requirement of high temperatures, a high vacuum system to evacuate generated harmful wastes, and environmental effects after the treatment. Therefore, it urges selecting an appropriate process to obtain an alloy Fe-Zn by modifying its properties. Thus, the research focus has recently shifted towards the development of one-pot, clean, simple, facile, cheap, reliable, eco-friendly, and cost-effective synthesis protocols by using a nontoxic solvent and reagents under mild conditions to produce the desired NPs. Some scholars have synthesized zinc ferrite nanoparticles using the green process for diverse applications such as the removal of methylene blue from baker's yeast [8.21]; electrochemical applications from *Moringa Oleifera* leaves [8.22]; photocatalytic and

142

antibacterial activities from *acidissima* juice [8.23]; anti-inflammatory and antioxidant activities from *Boswellia carteri* resin [8.24]; anticancer activity from *Lawsonia inermis* [8.25]; biological applications from *Phyllanthus acidus* [8.26]; and biological activity from *Petroselinum crispum* [8.27]. To the best of our knowledge, there is no report so far on *Rosmarinus officinalis* (rosemary) plant [8.28–8.31]. Rosemary is an aromatic medicinal and condiment plant that belongs to the family Labiate. It can be cultivated around the world due to its hardiness. Medicinal uses of rosemary are well documented, and it is primarily used to treat jaundice, hepatitis, circulatory, and cardiovascular diseases with anti-diabetic and neuroprotective properties [8.29]. Because of these biological properties, rosemary has emerged as a potential new therapeutic agent for a range of ailments. Many compounds, including flavones, diterpenes, steroids, and triterpenes, were isolated from rosemary whereby α-pinene, bornyl acetate, camphor, and 1,8-cineole are mainly responsible for the antimicrobial activity [8.30]. Phenolic compounds and other constituents in rosemary extracts (Table 8.1) can play an important role in the capping, reducing, chelating, and stabilizing agents, and viable sources for NP analogs as they could control the growth of generated NPs [8.31].

This study aims to overcome the immiscibility of Fe and Zn by varying some parameters such as volume ratios, pH, and annealing temperature to find out if a bimetallic alloy $ZnFe_2O_4$ could be obtained and assess the physical and magnetic properties.

Table 8.1: Major compounds of agro-waste extracts of rosemary leaves [8.28]

Compounds	Chemical composition
Flavonoids	Pelargonidin-3,5-Diglucoside (I); Cyanidin-3,5-Diglucoside (II); Kaempherol (III)
Monoterpenoids	α- Pinene (IV); 1,8-Cineole; Camphor
Phenolic acids	Rosmarinic acid; Caffein acid
Diterpenoids	Carnosol; Methyl Carnosate; 12-Methoxycarnosic acid; Epi- and Iso-Rosmanol

8.2. Experimental

8.2.1. Material

Rosemary leaves were purchased from Western Cape Province-South Africa. Iron (III) chloride hexahydrate ($FeCl_3.6H_2O$), 270.33 g/mol; iron (II) chloride tetrahydrate ($FeCl_2.4H_2O$), 198.81 g/mol; zinc chloride ($ZnCl_2$), 136.286 g/mol; and sodium hydroxide (NaOH), 39.997 g/mol were purchased as an analytical grade reagent (Sigma Aldrich, Modderfontein, South Africa) and used without further purification.

8.2.2. Methods

8.2.2.1. Synthesis of Fe-Zn [1:3]

A mass of 3 g of rosemary leaves (RL) was immersed in 100 mL of boiled deionized water at 80 °C for 2 hrs. The extract solution was filtered twice with Whatman paper (N°5) to eliminate residual solids. Thereafter, a mass of 1.5 g of $FeCl_2.4H_2O$ and a mass of 4.5 g of $ZnCl_2$, were added to 100 mL of rosemary extract, under the magnetic stirrer at 60 °C for 1 hr. The resultant pH was found to be 4.51. This solution was dried in the oven at 100 °C for 6 hrs 45 min and was black powder color. This powder was annealed at 500 °C in an open-air for 2 hrs with no change of color.

8.2.2.2. Synthesis of Fe-Zn [1:2] and Fe-Zn [2:3]

A mass of 4 g of RL was immersed in 200 mL of boiled deionized water at 80 °C for 2 hrs. The extract solution was filtered twice with Whatman paper (N°5) to eliminate residual solids. Thereafter, a mass of 2 g of $FeCl_2.4H_2O$ and a mass of 2 g of $FeCl_3.6H_2O$ were added respectively to 100 mL of rosemary extract, followed by the addition of a mass of 4 g and a mass of 3 g of $ZnCl_2$, respectively to each extract under the magnetic stirrer at 60 °C for 1 hr. The resultant pH was found to be 1.32 for the first solution with a light green color; and 1.12 for the second solution with a dark green color. A mass of 2 g of NaOH was added to the first solution with a change of color to dark reddish-brown and an increase of pH from 1.32 to 11.24. The resultant solution was dried in the oven at 100 °C for 17 hrs and still dark reddish-brown color. This powder was annealed at 800 °C in an open-air for 2 hrs 30 min and no change of color was observed. Regarding the second solution, no NaOH was added. The solution was dried in the oven at 100 °C for 6 hrs 30 min and was dark green powder color. This powder was annealed at 800 °C in an open-air for 2 hrs 30 min with a change of color to purple.

8.2.3. Techniques

Various techniques were used to investigate the physical and magnetic properties of bio-synthesized iron-zinc nanoparticles.

Field emission capable Zeiss Ultra 55 Scanning Electron Microscope (FESEM) was investigated to study the morphology and shape of the synthesized NPs. The energy-dispersive X-ray spectroscopy (EDS) spectrum was collected using an EDS Oxford instrument X-Max solid-state silicon drift detector set at 20 kV. High resolution transmission electron microscope (HRTEM) using a Joel JEM 4000EX electron microscopy unit with a resolution limit of about 0.12 nm at an accelerating voltage of 200 kV combined with selected area electron diffraction (SAED) was used to study the morphology, shape, and polycrystallinity of NPs. An X-ray diffractometer (model Bruker AXS D8 Advance) with an irradiation line Kα1 of copper ($\lambda CuK\alpha1=1.5406$ Å) operating at a voltage of 40 kV and a current of 35 mA, in the angular range of 20 to 90° was performed to study the crystalline nature and structure of NPs. An attenuated total reflection-Fourier transform infrared (ATR-FTIR) absorption spectrometer (Thermo Nicolet 8700 FTIR spectrometer) in the spectral range 400 to 4000 cm^{-1} was used to determine the surface coating and chemical bonding of NPs. Photoluminescence (PL) was recorded from 200 to 800 nm to understand the effects of quantum size and particle defects with a Varian Cary Eclipse Fluorescence Spectrophotometer with a 372 nm excitation wavelength. Additionally, at room temperature, the magnetic properties were measured using a vibrating sample magnetometer (VSM) (Cryogenic Ltd., UK).

8.3. Results and Discussion

8.3.1. Crystallographic analysis

X-ray diffraction (XRD) of biosynthesized Fe-Zn NPs revealed different structures depending on volume ratio as depicted in Figure 8.1.

ZnO/Fe_2O_3 NPs are obtained at Fe-Zn [1:3] in Figure 8.1 (a), while $ZnO/ZnFe_2O_4$ NPs are obtained at Fe-Zn [1:2] in Figure 8.1 (b), and $ZnFe_2O_4$ NPs at Fe-Zn [2:3] in Figure 8.1 (c). The presence of sharp, well-defined diffraction peaks and crystallographic reflections of iron and zinc with their maxima centered at 2θ (°) = 24.138, 30.007, 31.770, 33.153, 34.422, 35.344, 36.253, 40.855, 42.952, 47.539, 49.480, 53.281, 54.091, 56.796, 62.364, 62.451, 62.864, 67.963, 69.100, and 73.767 fit to the reflections planes of (012), (220), (100), (104), (002), (311), (101), (113), (400), (102), (024), (422), (116), (511), (440), (214), (103), (112), (201),

145

and (533) indicating the highly crystalline nature of rhombohedral Fe_2O_3 (hematite), hexagonal ZnO (zincite), and face-centered cubic $ZnFe_2O_4$ (zinc ferrite) structures, consistent with the JCPDS patterns No. 033-0664 for hematite, No. 036-1451 for zincite, and No. 01-074-2397 for zinc ferrite. These results are following the works of Noukelag et al., 2020 [8.6, 8.31] who synthesized zincite and hematite using an aqueous extract of rosemary leaves, respectively; Jana al., 2019 [8.13] who fabricated zinc oxide coated iron oxide; the findings of Choudhary et al., 2022 [8.14] on the evaluation of physical and photocatalytic properties of $ZnFe_2O_4$-ZnO and Imraish et al., 2021 [8.24] on biomedical activities of $ZnFe_2O_4$.
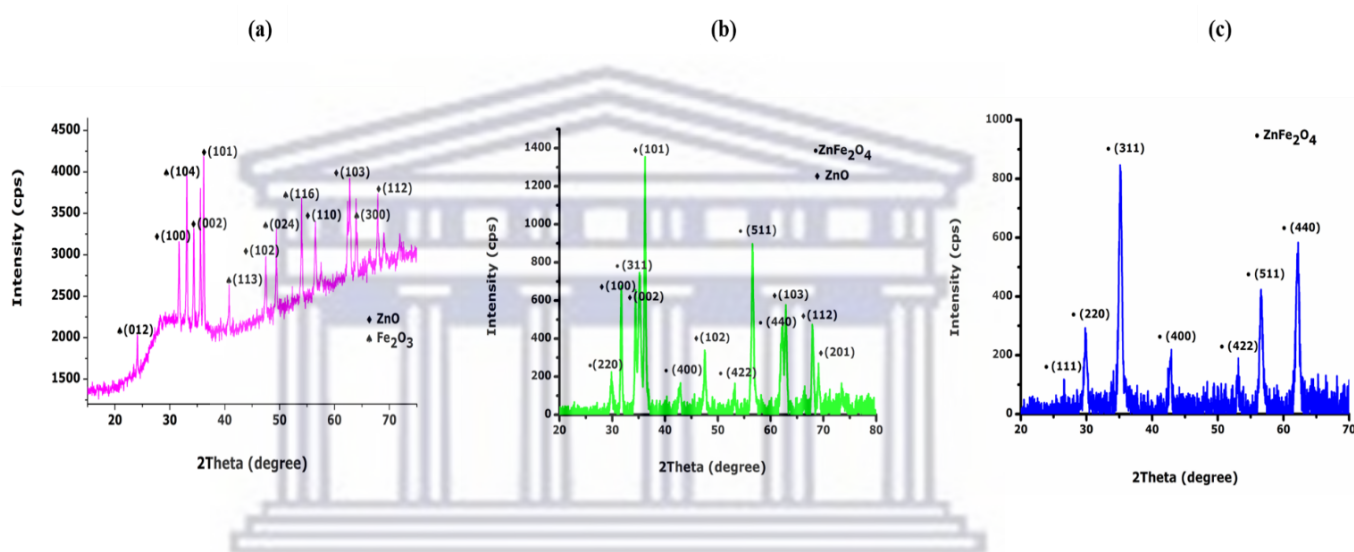
Figure 8.1: XRD results of **(a)** ZnO/Fe_2O_3, **(b)** $ZnO/ZnFe_2O_4$, **(c)** $ZnFe_2O_4$ NPs

The peak position of the doped ZnO samples shifts to smaller angles compared with pure ZnO, and the intensity of the characteristic peak reduces as the Fe doping concentration increases, pointing that Fe has been successfully incorporated into the ZnO matrix, which can be ascribed to the difference in ion radius of Zn^{2+} (0.74 Å) compared with that of Fe^{3+} (0.64 Å). It is demonstrated for $ZnFe_2O_4$ that Fe ions occupy the Zn ions sites in the hexagonal wurtzite structure without any impurity phase in line with the findings of Shirsath et al., 2018 [8.4].

In preliminary works performed at 500° C, Fe-Zn [1:3] generated ZnO, Fe_2O_3; Fe-Zn [1:2] $ZnFe_2O_4$, ZnO, NaCl; and Fe-Zn [2:3] Fe_2O_3, ZnO, $Zn_2OCl_2.2H_2O/ZnO.ZnCl_2.2H_2O$. By increasing the annealing temperature at 800 °C for Fe-Zn [1:2] and [2:3], $ZnFe_2O_4/ZnO$ and $ZnFe_2O_4$ were obtained, respectively.

Fe-Zn [1:3] at pH 4.51, dispersed into two phases namely ZnO and α-Fe_2O_3 whereas Fe-Zn [2:3] at pH 1.12, combined to $ZnFe_2O_4$ by solid-state diffusion showing that Zn preferentially occupied octahedral sites in the strong acid medium [8.32, 8.33].

The results show the influence of volume ratio, pH, as well as annealing temperature on structural properties due to the distribution of Zn^{2+} and Fe^{3+} cations on octahedral and tetrahedral sites as demonstrated by Tamilarasi et al., 2022 [8.34] and Aisida et al., 2020 [8.35].

Using the Debye-Scherrer formula

$$D = \frac{0.9\,\lambda}{\beta Cos\,\theta} \tag{8.1}$$

Where D is the average crystalline size, λ the wavelength, β the full width half maximum, and θ the X-ray diffraction angle; the crystalline size of ZnO/Fe_2O_3, $ZnO/ZnFe_2O_4$ and $ZnFe_2O_4$ NPs presented in Table 8.2 was found within the range 05.070–20.852 nm.

Table 8.2: Major XRD characteristics of the various Bragg diffraction peaks of ZnO/Fe_2O_3, $ZnO/ZnFe_2O_4$ and $ZnFe_2O_4$ NPs

NPs	Miller indices	2θ (degrees)	θ (radians)	FWHM (radians)	Crystalline size<Φ>(nm)
Fe_2O_3	(012)	24.138	0.210	0.0191	07.412
$ZnFe_2O_4$	(220)	30.007	0.262	0.0257	05.585
ZnO	(100)	31.770	0.277	0.0081	19.775
Fe_2O_3	(104)	33.153	0.289	0.0152	09.505
ZnO	(002)	34.422	0.300	0.0113	14.272
$ZnFe_2O_4$	(311)	35.344	0.308	0.0287	05.070
ZnO	(101)	36.253	0.316	0.0169	09.592
Fe_2O_3	(113)	40.855	0.356	0.0152	09.721
$ZnFe_2O_4$	(400)	42.952	0.372	0.0171	08.713
ZnO	(102)	47.539	0.414	0.0114	14.766
Fe_2O_3	(024)	49.480	0.431	0.0151	10.033
$ZnFe_2O_4$	(422)	53.281	0.465	0.0172	09.018
Fe_2O_3	(116)	54.091	0.472	0.0189	08.205
$ZnFe_2O_4$	(511)	56.796	0.496	0.0198	07.960
$ZnFe_2O_4$	(440)	62.364	0.544	0.0230	07.046
Fe_2O_3	(214)	62.451	0.544	0.0191	08.476

ZnO	(103)	62.864	0.548	0.0203	08.894
ZnO	(112)	67.963	0.593	0.0158	11.697
ZnO	(201)	69.100	0.603	0.0089	20.852
$ZnFe_2O_4$	(533)	73.767	0.643	0.0237	07.289

8.3.2. Microscopic observations

The structure, morphology, elemental composition, and average size distribution of biosynthesized Fe-Zn displayed in Figure 8.2, were assessed through FESEM/EDS, and HRTEM/SAED.

The results of Fe-Zn [1:3] or ZnO/Fe_2O_3 NPs in Figure 8.2 (a) with irregular forms from FESEM micrographs because of the difference in the volume ratio of Fe_2O_3 and ZnO, consequently affect the size and morphology. The presence of Zn (yellow), Fe (purple), and O (red) well-distributed in the sample and contaminating elements of Cl, K, and Ca which are hypothesized to come from rosemary leaves, are confirmed by the EDS spectrum and elemental mapping micrographs. The presence of carbon is because of carbon tape utilized to immobilize the NPs. More so, the elemental mapping micrographs were performed to get a more accurate analysis and presented in Figure (vi)-(viii). The extra signal detected, asserted that ZnO/Fe_2O_3 NPs are not highly pure. HRTEM micrographs in agreement with SAED exhibited the hexagonal wurtzite structure of ZnO. The different rings portrayed from SAED corroborated the formation of crystalline ZnO (100), (101), and Fe_2O_3 (104), in line with the XRD spectrum. The findings are consistent with the works of Jana et al., 2019 [8.13], who evaluated the antibacterial and anticancer properties of zinc oxide coated iron oxide by wet chemical route. By fitting the histogram data with a Gaussian distribution from HRTEM micrographs, the average size was found to peak at 18.647 ± 0.247 nm.
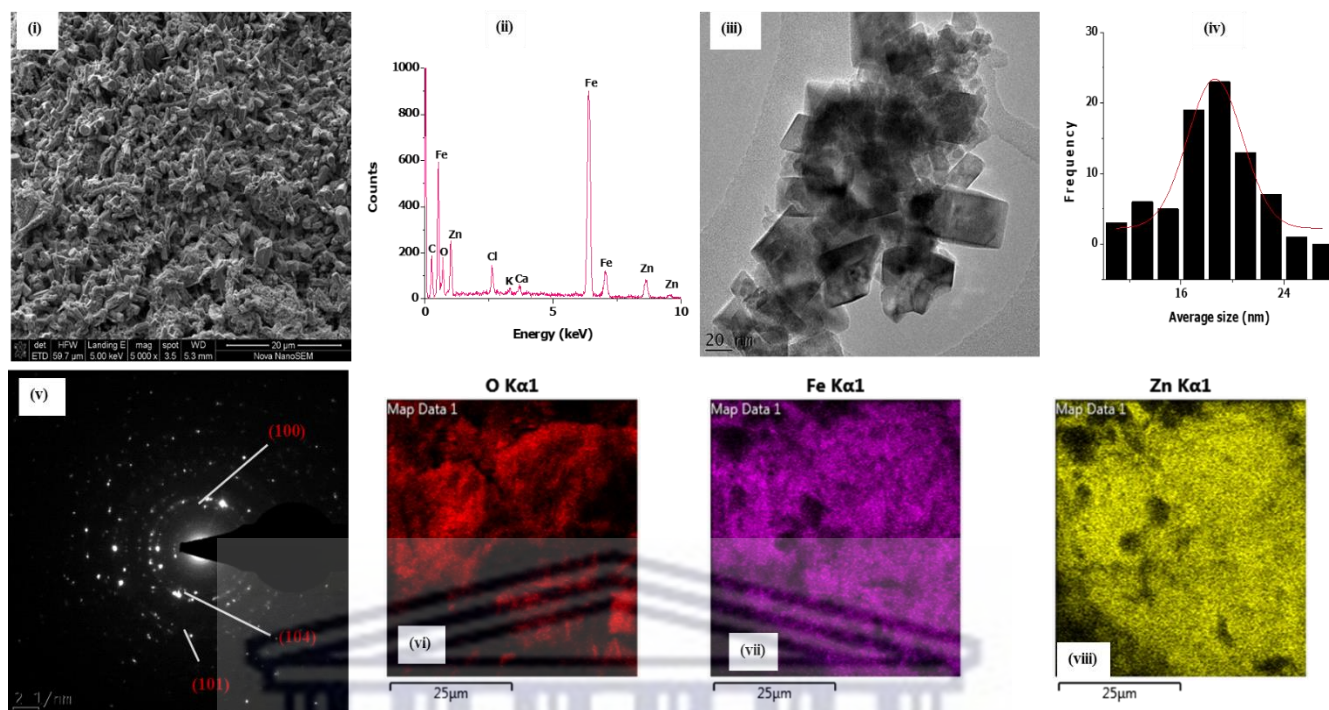
Figure 8.2 (a): (i) FESEM, **(ii)** EDS, **(iii)** HRTEM, **(iv)** Average size, **(v)** SAED of ZnO/Fe$_2$O$_3$ NPs, **(vi)** Elemental mapping extracted of O, **(vii**) Elemental mapping extracted of Fe, **(viii)** Elemental mapping extracted of Zn

Figure 8.2 (b) illustrates the results of Fe-Zn [1:2] or ZnO/ZnFe$_2$O$_4$ NPs with cubic forms from FESEM micrographs in line with XRD analysis. The presence of well-distributed elements Zn (yellow), Fe (purple), O (red) and contaminating element of Na, which is hypothesized to come from rosemary leaves, are displayed by the EDS spectrum and elemental mapping micrographs. The presence of carbon is due to carbon tape utilized to immobilize the NPs as aforementioned. The extra signal detected, asserted that ZnO/ZnFe$_2$O$_4$ NPs are not highly pure. The different rings presented from SAED corroborated the formation of crystalline ZnO (101), ZnFe$_2$O$_4$ (440) and (220), in line with XRD spectrum. The findings are in accordance with the works of Korotkova et al., 2019 [8.27] who synthesized zinc-based nanoparticles zinc ferrite by *Petroselinum crispum* extract. By fitting the histogram data with a Gaussian distribution from HRTEM micrographs, the average size was found to peak at 17.912 ± 0.555 nm.

149
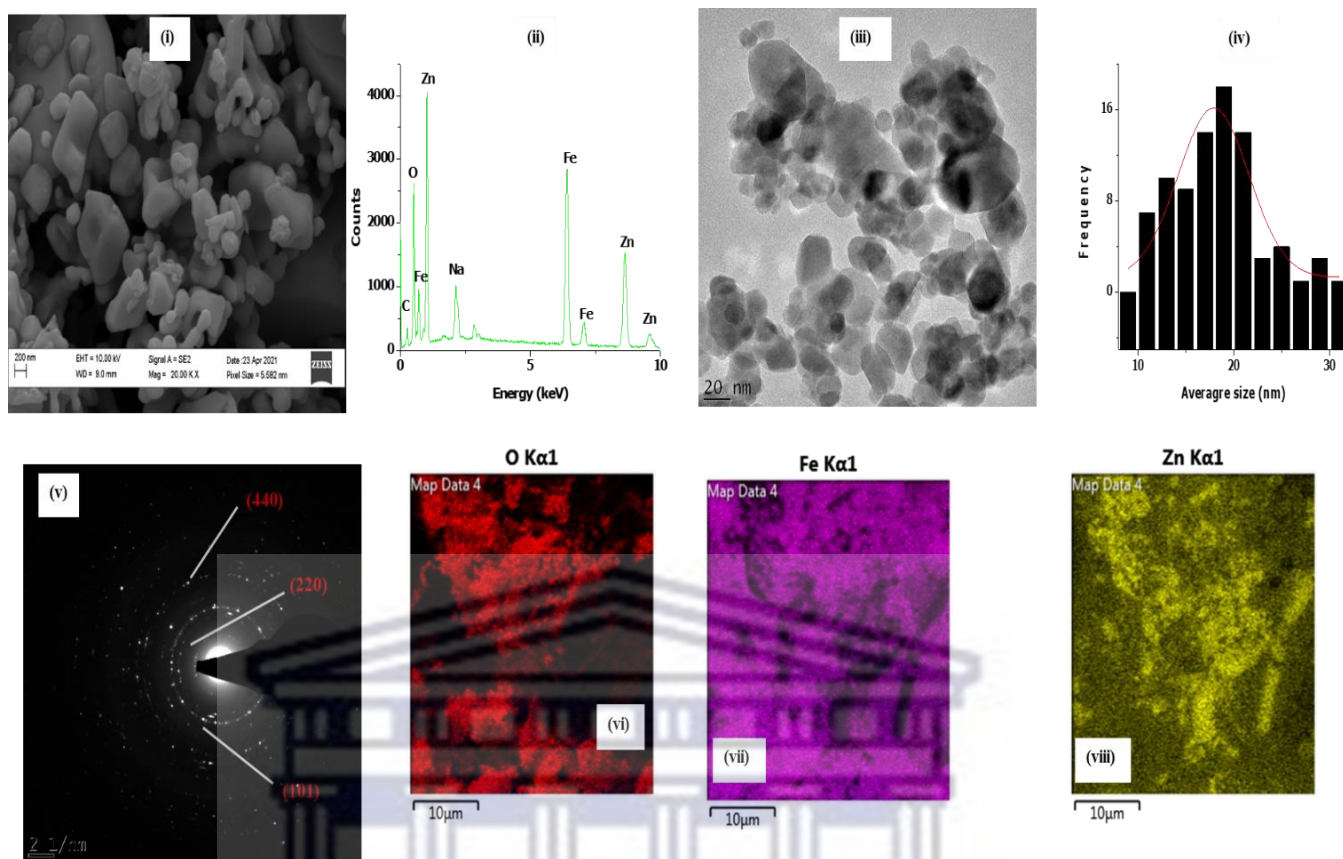
Figure 8.2 (b): (i) FESEM, **(ii)** EDS, **(iii)** HRTEM, **(iv)** Average size, **(v)** SAED of ZnO/ZnFe$_2$O$_4$ NPs, **(vi)** Elemental mapping extracted of O, **(vii)** Elemental mapping extracted of Fe, **(viii)** Elemental mapping extracted of Zn

Figure 8.2 (c) portrays the results of Fe-Zn [2:3] or ZnFe$_2$O$_4$ NPs with hexagonal and cubic forms from HRTEM micrographs. The presence of Zn (yellow), Fe (purple), and O (red) with no extra signal depicted by the EDS spectrum and elemental mapping micrographs confirms the purity of ZnFe$_2$O$_4$ NPs as revealed by the XRD spectrum. The presence of carbon is owing to the carbon tape used to immobilize the NPs. The different rings presented from SAED sustained the formation of crystalline ZnFe$_2$O$_4$ (220), (311), and (440), in line with the XRD spectrum. The results are in accordance with the works of Naik et al., 2019 [8.23] who obtained pure zinc ferrite from *Limonia acidissima* (wood apple) juice. By fitting the histogram data with a Gaussian distribution from HRTEM micrographs, the average size was found to peak at 19.909 ± 0.591 nm.

150

Figure 8.2 (c): (i) FESEM, **(ii)** EDS, **(iii)** HRTEM, **(iv)** Average size, **(v)** SAED of ZnFe₂O₄ NPs, **(vi)** Elemental mapping extracted of O, **(vii)** Elemental mapping extracted of Fe, **(viii)** Elemental mapping extracted of Zn
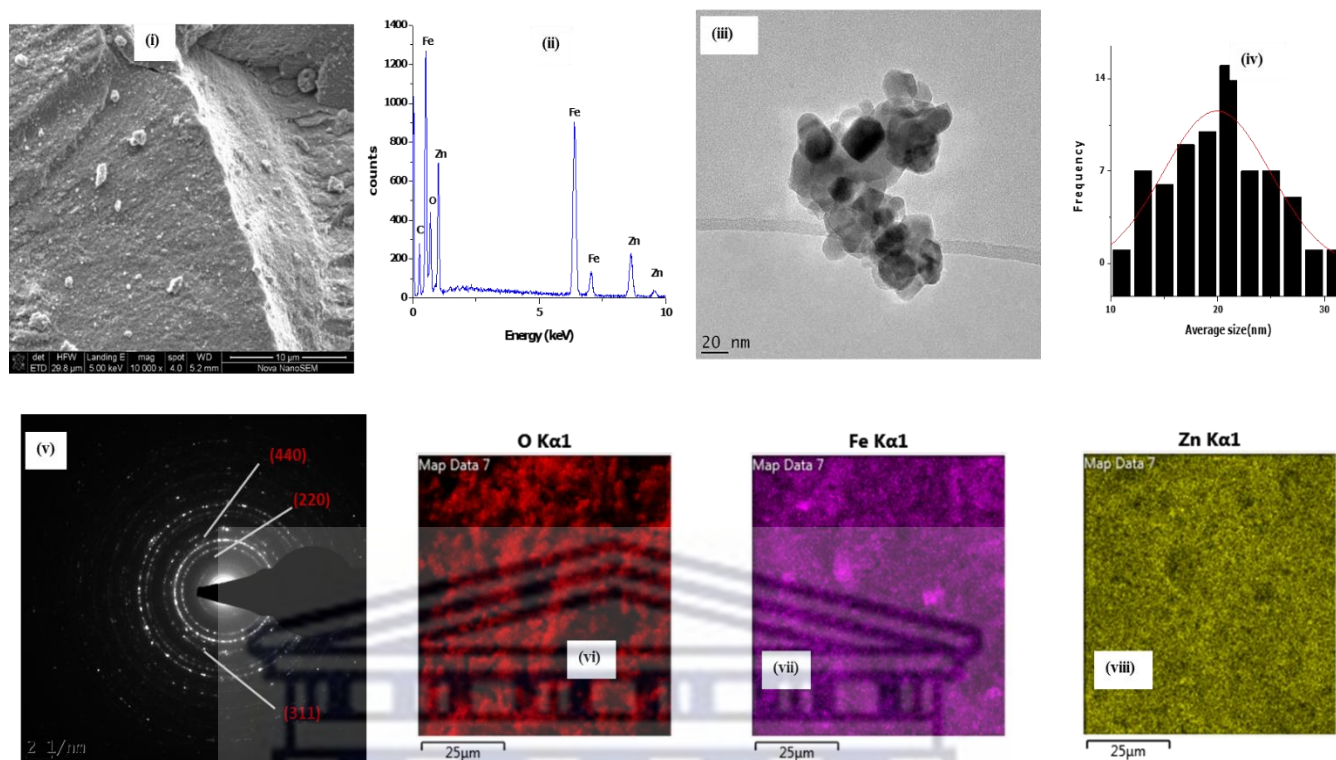
8.3.3. Vibrational properties

To validate again and conclude on the purity of the biosynthesized Fe-Zn, ATR-FTIR studies were carried out to identify the possible biomolecules involved as elucidated in Figure 8.3.

The peaks that appeared around 462, 468, 495 cm⁻¹, are from the iron oxide skeleton (–O–Fe) and 545, 558, 570 cm⁻¹ are from the zinc oxide stretching vibration mode (–O–Zn) which indicate the existence of iron-zinc NPs [8.24, 8.25]. The prominent peaks around 840 cm⁻¹, are attributed to FeOOH and the absorption bands around 1000 cm⁻¹ are attributed to C–N of aliphatic amines or alcohols/phenols [8.31]. The absorption bands located around 1300 and 1600 cm⁻¹ represent the symmetric and asymmetric bending modes of C=O bonds of amino acid and esters, respectively [8.22]. Finally, the wide peaks in the high energy of the spectrum centered around 3435 and 3695 cm⁻¹ are associated with standard H₂O bending modes and OH stretching, respectively [8.6]. These findings are in line with the EDS results which illustrated pure zinc ferrite NPs.

151
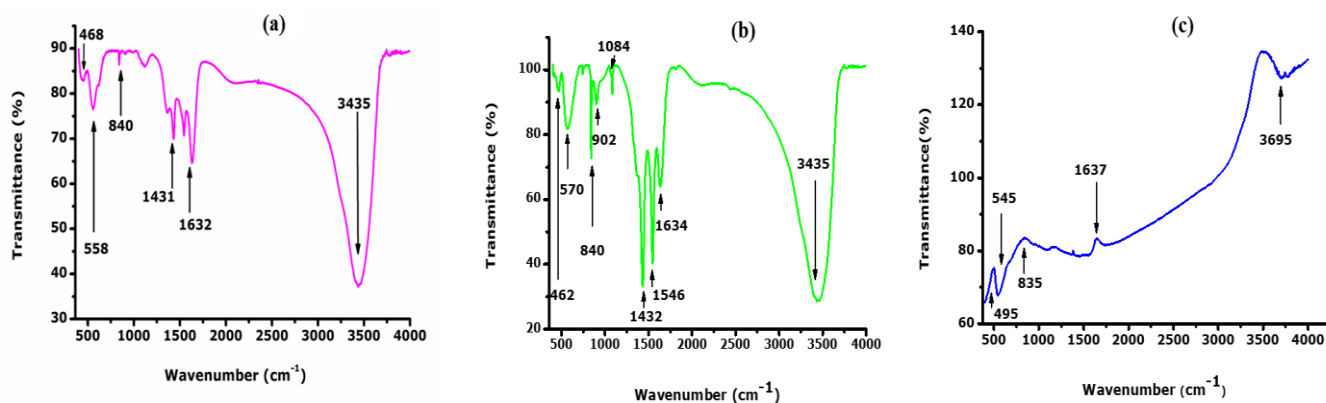
Figure 8.3: ATR-FTIR of **(a)** ZnO/Fe$_2$O$_3$, **(b)** ZnO/ZnFe$_2$O$_4$, **(c)** ZnFe$_2$O$_4$ NPs

8.3.4. Photoluminescence spectroscopy

PL is an essential phenomenon to detect the optical properties that emit light from the material under optical excitation and an effective indicator that reflects the rate of recombination and the life span of photogenerated charge carriers based on fluorescence intensity [8.6]. Besides, the defects and other impurity states of the material are new donor levels formed near the material's conduction band edge, which is the basis of luminescent features in nanomaterials [8.14]. Figure 8.4 depicts the PL of Fe-Zn [1:3] or ZnO/Fe$_2$O$_3$, Fe-Zn [1:2] or ZnO/ZnFe$_2$O$_4$, and Fe-Zn [2:3] or ZnFe$_2$O$_4$ with three clear peaks corresponding to visible emissions, indicating a high surface-to-volume ratio with large surface-states and native defects (vacancies and interstitials) of NPs that cause trap levels responsible for the observed emissions [8.31]. At 432 and 434 nm, very strong blue-green emission peaks are observed, which are like the electronic transition between the conduction band edges to the deep level acceptors. These emission peaks could be ascribed to band-edge emission caused by electron-hole recombination in free excitons [8.23]. The green emission observed at 504 nm could be related to oxygen vacancies as a parameter associated with the defects which decreased the intensity at higher annealing temperatures [8.35].

152
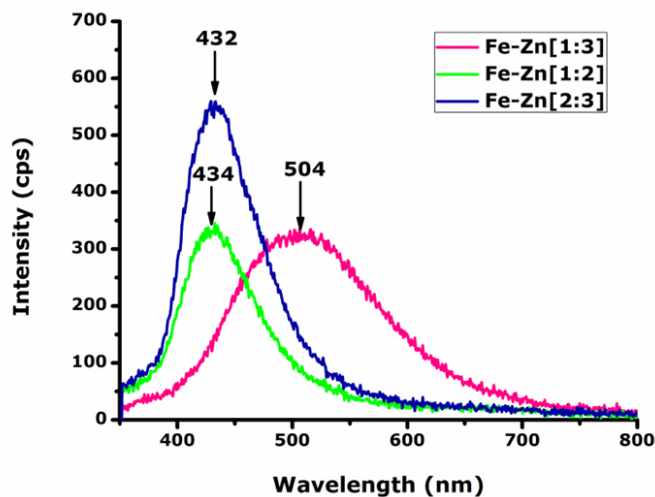
Figure 8.4: PL of ZnO/Fe_2O_3, $ZnO/ZnFe_2O_4$, $ZnFe_2O_4$ NPs

8.3.5. Magnetic properties

Fe-Zn [1:3] or ZnO/Fe_2O_3, Fe-Zn [1:2] or $ZnO/ZnFe_2O_4$, and Fe-Zn [2:3] or $ZnFe_2O_4$ NPs magnetic properties were studied using a VSM. The temperature of the samples was kept constant at 300 K during the measurement. The applied magnetic field from the superconducting magnet varied from -3 T to +3 T, while the vibrating amplitude and frequency of the sample holder were set at 0.2 and 20 Hz, respectively. The behavior can be changed by modifying the proportion between Fe and Zn contents and depending on other parameters such as synthesis method, chemical formula, grain size, amount and distribution of ions, calcination temperature, tilting, oxygen ion occupancy, and anisotropy [8.25, 8.33, 8.35].

The magnetic hysteresis loops (M-H) presented in Figure 8.5 shows a plot of moments versus of applied magnetic field of three samples. One figure is used for the depiction as the same results have been obtained for the three samples, showing that neither the volume ratio nor the pH, nor the annealing temperature influences the magnetic behavior. It is noticeable a linear magnetization without any saturation that indicates the biosynthesized Fe-Zn samples are paramagnetic at room temperature [8.36]. Furthermore, there are no remanent magnetization (M_r) and coercivity (H_c) as well. The same magnetic behavior might be explained by the similar average size distribution of 18.647 ± 0.247 nm for Fe-Zn [1:3], 17.912 ± 0.555 nm for Fe-Zn [1:2], and 19.909 ± 0.591 nm for Fe-Zn [2:3], which is another factor that affects the magnetic

153

properties as well as impurity phases with cationic distribution in spinel structure, surface spin structure of NPs, and oxygen vacancies confirmed by PL spectrum [8.5, 8.37].
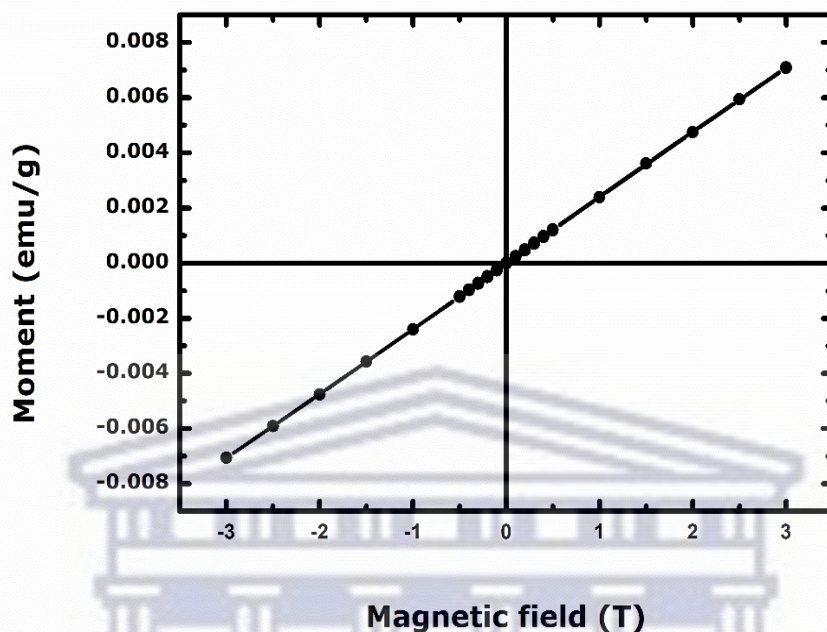
Figure 8.5: Magnetization curve of ZnO/Fe_2O_3, $ZnO/ZnFe_2O_4$, and $ZnFe_2O_4$ NPs

8.4. Conclusion

Overcoming the immiscibility of Fe and Zn in their bulk phase was achieved in this report with the generation of nanoscaled $ZnO/ZnFe_2O_4$ and $ZnFe_2O_4$ at a higher annealing temperature of 800 °C during 2 hrs and 30 min, different volume ratios, in basic and acidic media, respectively through a green approach using *Rosmarinus officinalis* (rosemary) leaves extract, confirming the versatility of nanotechnology. However, the exact mechanism of formation should be further investigated through density functional theory (DFT) calculations and electron paramagnetic resonance (EPR) analyses as the follow-up to this study.

154

8.5. References

[8.1] G. Krishnan, S.D. Graaf, G.H.T. Brink, P.O.Å. Persson, B.J. Kooia, G. Palasantzas, Strategies to initiate and control the nucleation behavior of bimetallic nanoparticles. Nanoscale 9, pp. 8149–8156 (2017).

[8.2] Z. Swiatkowska-Warkocka, A. Pyatenko, F. Krok, B.R. Jany & M. Marszalek, Synthesis of new metastable nanoalloys of immiscible metals with a pulse laser technique. Scientific reports 5, 9849 (2015).

[8.3] B.P. Burton, P. Perrot, Phase Diagrams of Binary Iron Alloys. ed. By H. Okamoto. ASM International, Materials Park, OH, pp. 459–466 (1993).

[8.4] S.E. Shirsath, D. Wang, S.S. Jadhav, M.L. Mane, S. Li, Ferrites Obtained by Sol-Gel Method. In Book: Handwork of Sol-Gel Science and Technology, pp. 695–735 (2018).

[8.5] A. Manohar, V. Vijayakanth, S.V. P. Vattikuti, K.H. Kim, A mini-review on AFe_2O_4 (A = Zn, Mg, Mn, Co, Cu, and Ni) nanoparticles: Photocatalytic, magnetic hyperthermia and cytotoxicity study. Materials Chemistry and Physics 286, Article 126117 (2022).

[8.6] S.K. Noukelag, H.E.A. Mohamed, B. Moussa, L.C. Razanamahandry, S.K.O. Ntwampe, C.J. Arendse & M. Maaza, Investigation of structural and optical properties of biosynthesized Zincite (ZnO) nanoparticles (NPs) via an aqueous extract of *Rosmarinus officinalis* (rosemary) leaves. MRS Advances 5 (45), pp. 2349–2358 (2020).

[8.7] A. Manohar, V. Vijayakanth, K.H. Kima, Influence of Ca doping on $ZnFe_2O_4$ nanoparticles magnetic hyperthermia and cytotoxicity study. Journal of Alloys and Compounds 886, Article 161276 (2021).

[8.8] P.J. Gellings, E.W.D Bree, G. Gierman, Synthesis and Characterization of Homogeneous Intermetallic Fe-Zn Compounds, Part 2. International Journal of Materials Research 70 (5), pp. 315–317 (1979).

[8.9] C. Yang, B.H. Ko, S. Hwang, Z. Liu, Y. Yao, W. Luc, M. Cui, A.S. Malkani, T. Li, X. Wang, J. Dai, B. Xu, G. Wang, D. Su, F. Jiao, L. Hu, Overcoming immiscibility toward bimetallic catalyst library. Sciences Advances 6 (17), eaaz6844 (2020).

[8.10] T. Zargar, A. Kermanpur, Effects of hydrothermal process parameters on the physical, magnetic, and thermal properties of $Zn_{0.3}Fe_{2.7}O_4$ nanoparticles for magnetic hyperthermia applications. Ceramics International 43 (7), pp. 5794–5804 (2017).

[8.11] N. Roy, S.A. Alex, N. Chandrasekaran, K. Kannabiran & A. Mukherjee, Studies on the removal of acid violet 7 dye from aqueous solutions by green $ZnO@Fe_3O_4$ chitosan-alginate nanocomposite synthesized using *camellia sinensis* extract. Journal of environmental management 303, Article 114128 (2022).

[8.12] L.G. da Trindade, G.Y. Hata, J.C. Souza, M.R.S. Soares, E.R. Leite, E.C. Pereira, E. Longo, T.M. Mazzo, Preparation and characterization of hematite nanoparticles-decorated zinc oxide particles (ZnO/Fe_2O_3) as photoelectrodes for solar cell applications. Journal of Materials Science 55 (7), pp. 2923–2936 (2020).

[8.13] T.K Jana, S.K. Jana, A. Kumar, K. De, R. Maiti, A.K. Mandal, T. Chatterjee, B.K. Chatterjee, P. Chakrabarti, K. Chatterjee, The antibacterial and anticancer properties of zinc oxide coated iron oxide nanotextured composites. Colloids surf. B Biointerf. 177, pp. 512–519 (2019).

[8.14] S. Choudhary, D. Hasina, M. Saini, M. Ranjan, S. Mohapatra, Facile synthesis, morphological, structural, photocatalytic and optical properties of $ZnFe_2O_4$-ZnO hybrid nanostructures. Journal of Alloys and Compounds 895, Article 162723 (2022).

[8.15] L.T.T. Nguyen, N.V. Dai-Viet, L.T.H. Nguyen, A.T.T. Duong, H.Q. Nguyen, N.M. Chu, D.T.C. Nguyen, T.V. Tran, Synthesis, Characterization, and application of $ZnFe_2O_4@ZnO$ nanoparticles for photocatalytic degradation of Rhodamine B under visible-light illumination. Environmental Technology & Innovation 25, Article 102130 (2022).

[8.16] A. Manohar, V. Vijayakanth, P. Manivasagan, J. Eue-Soon, B. Hari, M. Gu, K.H. Kim, Investigation on the physico-chemical properties, hyperthermia and cytotoxicity study of magnesium doped manganese ferrite nanoparticles. Materials Chemistry and Physics 287, Article 126295 (2022).

[8.17] M. Atif, S.K. Hasanain, M. Nadeem, Magnetization of sol–gel prepared zinc ferrite nanoparticles: effects of inversion and particle size. Solid State Communications 138 (8), pp. 416–421 (2006).

[8.18] X. Zhang, Z. Chen. C. Wu. J. Zhang, F. Wang, Solvothermal synthesis of spinel $ZnFe_2O_4$ nanoparticles with enhanced infrared radiation property. Chemical Physics Letters 732, Article 136647 (2019).

[8.19] D. Tomar, P. Jeevanandam, Synthesis of $ZnFe_2O_4$ nanoparticles with different morphologies via thermal decomposition approach and studies on their magnetic properties. Journal of Magnetism and Magnetic Materials, Article 170033 (2022).

[8.20] Nikita, A. Rana, and V. Kumar, Investigation on anneal-tuned properties of $ZnFe_2O_4$ nanoparticles for use in humidity sensors. Appl. Phys. A Mater. Sci. Process 127 (8), Article 609 (2021).

[8.21] W. Zhang, Y. Zhang, Development of $ZnFe_2O_4$ nanoparticle functionalized baker's yeast composite for effective removal of methylene blue via adsorption and photodegradation. Journal of Water Process Engineering 37, Article 101234 (2020).

156

[8.22] N. Matinise, K. Kaviyarasu, N. Mongwaketsi, S. Khamlich, L. Kotsedi, N. Mayedwa, M. Maaza, Green synthesis of novel zinc iron oxide ($ZnFe_2O_4$) nanocomposite via *Moringa Oleifera* natural extract for electrochemical applications. Applied Surface Science 446, pp. 66–73 (2018).

[8.23] M.M. Naik, H.S.B. Naik, G. Nagaraju, M. Vinuth, H.R. Naika, K. Vinu, Green synthesis of zinc ferrite nanoparticles in *Limonia acidissima* juice: Characterization and their application as photocatalytic and antibacterial activities. Microchemical Journal 146, pp. 1227–1235 (2019).

[8.24] A. Imraish, T.A. Thiab, W. Al-Awaida, H.J. Al-Ameer, Y. Bustanji, H. Hammad, M. Alsharif, A. Al-Hunaiti, In vitro anti-inflammatory and antioxidant activities of $ZnFe_2O_4$ and $CrFe_2O_4$ nanoparticles synthesized using *Boswellia carteri* resin. Journal of Food Biochemistry 45 (6), article e13730 (2021).

[8.25] E. Sarala, M.M. Naik, M. Vinuth, Y.V.R. Reddy & H.R. Sujatha, Green synthesis of *Lawsonia inermis*-mediated zinc ferrite nanoparticles for magnetic studies and anticancer activity against breast cancer (MCF-7) cell lines. Journal of Materials Science: Materials in Electronics 31, pp. 8589–8596 (2020).

[8.26] A. Karthikeyan, R.N. Hanumanaika, K. Gurushantha, K. Shetty, Plant mediated green synthesis of zinc ferrite nanoparticles and its biological applications. International Journal of Botany Studies 6 (1), pp. 197–200 (2021).

[8.27] A.M. Korotkova, O. B. Polivanova, I. A. Gavrish, E. N. Baranova, S. V. Lebedev, Green synthesis of zinc based nanoparticles zinc ferrite by *Petroselinum crispum*. IOP Conference Series: Earth and Environmental Science 341(1), Article 012175 (2019).

[8.28] J.R. de Oliveira, S.E.A. Camargo, and L.D. de Oliveira, *Rosmarinus officinalis* L. (rosemary) as therapeutic and prophylactic agent. Journal of Biomedical Science 26 (1), 5 (2019).

[8.29] S.K. Noukelag, L.C. Razanamahandry, S.K.O. Ntwampe, C.J. Arendse, M. Maaza, Industrial Dye Removal Using Bio-Synthesized Ag-doped ZnO Nanoparticles. Environmental Nanotechnology, Monitoring & Management 16 (16), Article 100463 (2021).

[8.30] M. Minaiyan, A.R. Ghannadi, M. Afsharipour, P. Mahzouni, Effects of extract and essential oil of *Rosmarinus officinalis* L. on TNBS-induced colitis in rats. Res. Pharm. Sci. 6, pp. 13–21 (2011).

[8.31] S.K. Noukelag, C.J. Arendse, M. Maaza, Biosynthesis of hematite phase α-Fe_2O_3 nanoparticles using an aqueous extract of *Rosmarinus officinalis* leaves. Material Today: Proceedings 43, pp. 3679–3683 (2021).

157

[8.32] M. Xing, L. Xu, J. Wang, Mechanism of Co (II) adsorption by zero valent iron/graphene nanocomposite. Journal of Hazardous Materials 301, pp. 286–296 (2016).

[8.33] M.A. Yousuf, S. Hussain, T. Kousar, A. Anwar, M.A. Shahzad, F. Munawar, M. Imran, F. Hanif & M.F. Warsi, The Impact of pH on Structural and Electrical Properties of E-Substituted $ZnFe_2O_4$ Nanoparticles Synthesized via Wet Chemical Route. J. Supercond. Nov. Magn. 34, pp. 1823–1831 (2021).

[8.34] K. Tamilarasi, P.A. Udhaya, M. Meena, Enhancement on the electrical and optical behaviour of $ZnFe_2O_4$ nano particles via transition metal substitution. Materials Today: Proceedings 64 (5), pp. 1671–1678 (2022).

[8.35] S.O. Aisida, I. Ahmad, Z. Ting-kai, M. Maaza & F.I. Ezema, Calcination Effect on the Photoluminescence, Optical, Structural, and Magnetic Properties of Polyvinyl Alcohol Doped $ZnFe_2O_4$ Nanoparticles. Journal of Macromolecular Science, Part B, 59 (5), pp. 295–308 (2020).

[8.36] B. Issa, I.M. Obaidat, B.A. Albiss, Y. Haik, Magnetic nanoparticles: surface effects and properties related to biomedicine applications. Int. J. Mol. Sci., 14 (11), pp. 21266–21305 (2013).

[8.37] S.K. Jesudoss, J. Judith Vijaya, L.J. Kennedy, P.I. Rajan, A.A. Hamad, R.J. Ramalingam, K. Kaviyarasu, M. Bououdina, Studies on the efficient dual performance of $Mn_{1-x}Ni_xFe_2O_4$ spinel nanoparticles in photodegradation and antibacterial activity. J. Photochem. Photobiol. B Biol. 165, pp. 121–132 (2016).

ANTIMICROBIAL PERFORMANCE OF Fe-Zn NANOPARTICLES AND PHYSICAL PROPERTIES OF Ag-Zn NANOPARTICLES INDUCED BY GAMMA IRRADIATION

Abstract

The antimicrobial performance of Fe-Zn nanoparticles (NPs) and the physical properties of Ag-Zn NPs irradiated at 50 kGy doses using gamma-ray co^{60} as the source are reported. Since pure Ag/ZnO NPs were not produced via crystallographic studies, the photocatalytic activities of gamma-irradiated Ag-Zn NPs are not provided in this chapter for comparison with green Ag-doped ZnO NPs reported in chapter six. However, antimicrobial properties indicated that Fe-Zn [1:2] and Fe-Zn [1:4] were more efficient than Fe-Zn [1:1] and [2:3], in inhibiting the growth of some spoilage yeasts and molds investigated for food safety. These two samples were characterized in addition to Ag-Zn [1:3] to assess their physical and magnetic properties. X-ray diffraction (XRD) in line with field emission scanning electron microscopy (FESEM) portrayed pure crystalline phases of Fe-Zn [1:2] and [1:4]. Energy dispersive X-ray spectroscopy (EDS) substantiated the presence of elements Ag, Zn, Fe, and O in the samples whilst attenuated total reflection-Fourier transform infrared (ATR-FTIR) denoted the chemical bonds of Ag-O around 400 cm^{-1}, Zn-O and Fe-O around 600 cm^{-1}. The decrease of energy bandgap demonstrated the successful insertion of Ag and Fe onto the ZnO lattice from the optical analyses. The magnetic properties assessed via a vibrating sample magnetometer (VSM) did not detect any magnetic moments of Ag-Zn [1:3] whereas the ferromagnetic behavior was observed with Fe-Zn [1:2] and Fe-Zn [1:4].

9.1. Introduction

Microorganisms that are ubiquitous such as yeasts, molds, bacteria, and viruses are associated with stale food, fruit, and beverages during manufacturing, processing, and packaging. The subsequent consequences related to undesirable changes in reputation due to unpleasant flavor, texture, odor, and taste make it harmful to consumers' health, followed by foodborne diseases and death [9.1]. Economic losses on agricultural products are estimated at 1.3 billion tons per

159

year, according to a Food and Agriculture Organization (FAO) report [9.2], emphasizing the necessity for appropriate treatment for food safety and public health issues.

The genera of *Candida*, *Dekkera, Zygosaccharomyces*, *Saccharomyces, Hanseniaspora*, *Debaryomyces*, *Botrytis, Rhizopus*, *Alternaria*, *Fusarium*, *Penicillium*, *Aspergillus,* and *Monilinia, sp.,* are well-known to be responsible for food and fruit spoilage with a major economic effect on human life [9.3–9.10]. With the world's population growing, substantial care should be focused to inhibit the growth of spoilage microorganisms and increase food production. The use of antibiotics is not advisable due to secondary effects on the human body associated with severe clinical risks [9.11], shifting the focus to the use of metal oxide nanoparticles (NPs) [9.12]. Amongst them, CuO, NiO, ZrO$_2$, CeO$_2$, and ZnO, are very important due to their numerous properties and several applications in diverse fields of nanotechnology [9.13], especially ZnO as antimicrobial agents in food decontamination, and eradicator of toxins with the generation of reactive oxygen species (ROS) that damage the spoilage organisms cell membranes via cytoplasmic contents deactivation and disruption of cellular homeostasis without any resistance [9.14]. Besides, ZnO is the most often used as a p-type semiconductor, with a broad direct bandgap of up to 3.37 eV and high excitation energy of 60 meV and diverse properties [9.15]. Nonetheless, to improve its properties, it is quite interesting to dope it with other metals such as gold (Au), silver (Ag), and platinum (Pt), because of their recoverability in numerous technological applications [9.16]. Mostly, Ag NPs are the most broadly explored due to their varied bandgap of around 2.5 eV, absorption of visible light, physicochemical, biological, and geometrical properties, imparted by characteristics associated with the induction of oxygen vacancies, crystalline transformation, and light scattering pattern alterations [9.17, 9.18]. On the other hand, magnetic NPs are considered significant due to their stability, high surface area including recoverability, and higher saturation magnetization especially iron (Fe) with bandgap energy of 2.2 eV [9.19–9.21]. Therefore, ZnO NPs combined with Ag or Fe constituents culminate in several additional unique properties such as electronic, optical, and electrical that make them different from their bulk [9.22, 9.23], and could extend their appeal for antimicrobial, hyperthemia, photocatalytic applications. Many processes were developed to synthesize NPs to multiply innovative food and fruit control systems and satisfy customers' standards. The conventional synthesis methods presented some limitations such as the overall synthesis cost, and high-temperature usage thus, making it high energy consumption particularly when high vacuum systems are used to decontaminate the NPs of harmful by-products during synthesis [9.24–9.26]. Residual waste generated from such a synthesis process contributes to environmental pollution associated with their disposal [9.24]. Henceforth, the

160

development of one-pot, facile, cheap, reliable, and eco-friendly synthesis protocols by using nontoxic solvents and reagents under mild conditions to produce desired NPs is researched. Ionizing radiation seems a promising route to generate such NPs due to the rapidity in action, durability, and efficacy [9.21]. It encompasses charged particles such as electrons, protons, photons (gamma and X-rays), neutrons, and fission fragment ions [9.27, 9.28]. In this regard, the γ-irradiation emitted from cobalt 60 (^{60}Co) or cesium 137 (^{137}Cs), is an ionic non-thermal processing technology widely used. Notably, high-energy gamma Co^{60} ray irradiation emitting photons of 1.17 and 1.33 MeV, is considered as a reliable method for the synthesis and modification of nanomaterials because of miscellaneous benefits [9.29–9.32].

This study aims to assess for the first time the antimicrobial efficacy of 20 % (m/v) of gamma irradiated Fe-Zn samples at different volume ratios through the concept of the volumetric zone of inhibition (VZI) [9.3], expressed in a liter of contaminated solidified media per milliliter of antimicrobial compounds/agents used, i.e., L CSM/mL ACU, for the quantification of their cidal effect against the growth of some spoilage microorganisms, and the characterization of the sample which showed a better antimicrobial performance. Additionally, the characterization of Ag-Zn [1:3].

9.2. Experimental

9.2.1. Material

All the chemicals namely silver nitrate (AgNO$_3$), zinc sulphate heptahydrate (ZnSO$_4$.7H$_2$O), ferrous sulphate (FeSO$_4$.7H$_2$O), zinc nitrate hexahydrate (Zn(NO$_3$)$_2$.6H$_2$O), zinc nitrate hydrate (Zn(NO$_3$)$_2$.xH$_2$O), and isopropyl alcohol (CH$_3$CHOHCH$_3$) were purchased as an analytical grade reagent (Sigma Aldrich, Modderfontein, South Africa) and used without any further purification.

9.2.2. Methods

9.2.2.1. Preliminary works

According to research done in an acidic medium, the wettability of the samples prevented XRD analysis from being completed for Ag-Zn [1:4] and Ag-Zn [1:7] synthesized from metal salt precursors AgNO$_3$ and Zn(NO$_3$)$_2$.xH$_2$O.

9.2.2.2. Synthesis of Ag-Zn [1:3]

250 mg of $AgNO_3$ and 750 mg of $ZnSO_4.7H_2O$ were dissolved into a beaker with 50 mL of distilled water (DW) and stirred for 30 min on a hot plate at 60 °C. The solution was clear, with a pH of 5.18. Thereafter, 15 mL of $CH_3CHOHCH_3$ was added to the colorless solution as a scavenger of OH radicals, followed by another 30 min of stirring on a hot plate at 60 °C. The mixture solution was transferred into a test tube for the irradiation process performed after one week. At room temperature, it was exposed to a 50 kGy dose at a dose rate of 50 kGy/min, using Co^{60} as the source. The hue of the solution changed to green. This green solution was then centrifuged thrice at 4,000 rpm with DW and ethanol every 12 min before drying in an oven at 70 °C for 1 hr.

9.2.2.3. Synthesis of Fe-Zn [1:1] and Fe-Zn [1:4]

1 g and 0.25 g of $FeSO_4.7H_2O$ were dissolved respectively, into a beaker containing 50 mL of DW and stirred for 30 min on a hot plate at 60 °C. Thereafter, 1 g of $Zn(NO_3)_2.6H_2O$ was added to each solution, respectively. Fe-Zn [1:1] had a brown solution with a pH of 1.80 whereas Fe-Zn [1:4] had an orange solution with a pH of 3.02. Following that, 15 mL of $CH_3CHOHCH_3$ was introduced to each beaker as a scavenger of OH radicals, followed by another 30 min of stirring on a hot plate at 60 °C. The final solutions were transferred into test tubes and irradiated after one week, using Co^{60} as the source at 50 kGy dose (dose rate of 50 kGy/min) at room temperature with the orange solution changing color to mud. The solutions were centrifuged thrice at 4,000 rpm with DW and ethanol every 12 min before drying in an oven at 70 °C for 2 hrs.

9.2.2.4. Synthesis of Fe-Zn [1:2]

1 g of $FeSO_4.7H_2O$ and 2 g of $Zn(NO_3)_2.xH_2O$ were dissolved into a beaker containing 50 mL of DW and stirred for 30 min on a hot plate at 60 °C. The solution was yellow with a pH of 2.34. Thereafter, 15 mL of $CH_3CHOHCH_3$ was added as a scavenger of OH radicals, followed by another 30 min of stirring on a hot plate at 60 °C. The final solution was transferred into a test tube and irradiated after one week, using Co^{60} gamma as the source at 50 kGy dose (dose rate of 50 kGy/min) at room temperature. The hue of solution changed to brown. This brown solution was thus centrifuged thrice at 4,000 rpm with DW and ethanol every 12 min before drying in an oven at 70 °C for 2 hrs.

9.2.2.5. Synthesis of Fe-Zn [2:3]

2 g of FeSO$_4$.7H$_2$O and 3 g of ZnSO$_4$.7H$_2$O were dissolved into a beaker with 50 mL of DW and stirred for 30 min on a hot plate at 60 °C. The solution was yellow with a pH of 1.89. Subsequently, 15 mL of CH$_3$CHOHCH$_3$ was introduced as a scavenger of OH radicals, followed by another 30 min of stirring on a hot plate at 60 °C. The final solution was transferred into a test tube and irradiated after one week, using a Co^{60} gamma irradiation source at 50 kGy dose (dose rate of 50 kGy/min) at room temperature without any change of color. The yellow solution was centrifuged thrice at 4,000 rpm with DW and ethanol every 12 min before drying in an oven at 70 °C for 1 hr 30 min.

9.2.2.6. Test microorganisms' origin, culture condition, and inoculum preparation

The spoilage organisms used for the study were obtained from the culture collection of the Fruit, Vine and Wine Institute of the Agricultural Research Council, Stellenbosch, South Africa. The protocol used is the same described in chapter five [9.3, 9.4].

9.2.2.7. Growth inhibition assay and activity quantification

The growth inhibition method used in this study was adapted from [9.3], using grape pomace extract (GPE) agar as a test medium. A mass of 0.2 g of the annealed powders of Fe-Zn [1:1], [1:2], [1:4], and [2:3] was mobilized in a 100 µL volume of sterile distilled water and was tested against selected spoilage yeasts [9.4]. From the resulting mixtures, a volume of 10 µL was spotted in 5 mm diameter and 1.7 mm depth wells created on the test agar plates using an agar driller. Prior to plates inspection for the presence of inhibition zones around the wells, the seeded plates were incubated for 72 hrs at 22 °C. Each sample was tested three times, and the average diameter of the zone of inhibition was used for the quantification of growth inhibition activity.

The growth inhibition effect of the best performing (n=2) NP solutions on mold spore germination was carried out following the aforementioned approach. In three replicates per treatment, the GPE test agar medium was seeded with the corresponding mold spores at the concentration of 10^5 spores/mL. The plates were incubated at 20 °C until a clear zone of inhibition was observed around the 5 mm wells, in which a volume of 10 µL was spotted.

The concept of the volumetric zone of inhibition (VZI) is interpreted as the volume of the contaminated solidified medium at a specific cell or spore concentration that one milliliter of solution of Fe-Zn [1:1], [1:2], [1:4], and [2:3] will be able to completely control, was measured based on the adapted method of Maxwell et al., 2019 [9.33] to quantify the growth inhibition

activity of Fe-Zn [1:1], [1:2], [1:4], and [2:3] solutions against common beverage and fruit spoilage organisms identified, i.e., *C. guilliermondii*, *Z. fermentati*, *Z. florentinus*, *P. expansum*, *B. cinerea,* and *A. alstroemeriae.*

9.2.3. Techniques

Field emission capable Zeiss Ultra 55 Scanning Electron Microscope (FESEM) was investigated to study the morphology and shape of the synthesized NPs. The energy-dispersive X-ray spectroscopy (EDS) spectrum was collected using an EDS Oxford instrument X-Max solid-state silicon drift detector set at 20 kV. An X-ray diffractometer (model Bruker AXS D8 Advance) with an irradiation line Kα1 of copper ($\lambda CuK\alpha1=1.5406$ Å) operating at a voltage of 40 kV and a current of 35 mA, in the angular range of 20 to 90° was performed to study the crystalline nature and structure of NPs. An attenuated total reflection-Fourier transform infrared (ATR-FTIR) absorption spectrometer (Thermo Nicolet 8700 FTIR spectrometer) in the spectral range 400 to 4000 cm^{-1} was used to determine the surface coating and chemical bonding of NPs. Photoluminescence (PL) was recorded from 200 to 800 nm to understand the effects of quantum size and particle defects with a Varian Cary Eclipse Fluorescence Spectrophotometer with a 372 nm excitation wavelength. A vibrating sample magnetometer (VSM) was used to measure the magnetic properties at room temperature (Cryogenic Ltd., UK). Gamma-ray with Co^{60} source type GIK-9-4, S/N 08398 and 56 TBq was used.

9.3. Results and Discussion
9.3.1. Antimicrobial performance of Fe-Zn NPs

9.3.1.1. Screening against spoilage yeasts

The growth inhibition potential of 20 % (m/v) of solutions of Fe-Zn [1:4] (1), [2:3] (2), [1:2] (3), and [1:1] (4), interacting with cells of spoilage yeasts *Candida guilliermondii*, *Zygosaccharomyces fermentati, Zygosaccharomyces florentinus*, was assessed to achieve their different levels of growth inhibition activity, i.e., their antimicrobial function is presented in Figure 9.1. The findings reveal the four solutions exhibited an antimicrobial function and the highest growth inhibition activity was found with Fe-Zn [1:4] solution of VZI values of 18.02, 31.53, and 5.81 L CSM/mL ACU against *C. guilliermondii*, *Z. fermentati, Z. florentinus,* respectively, suggesting that a volume of 1 mL at 20 % (m/v) of Fe-Zn [1:4] solution could suppress the growth of these spoilage yeasts of 18.02, 31.53, and 5.81 L in contaminated

164

food/beverage at a cell concentration of 10^6 cell/mL. However, the lowest level of growth inhibition activity of VZI values of 10.58, 12.63, and 0.40 L CSM/mL ACU against *C. guilliermondii*, *Z. fermentati*, *Z. florentinus*, respectively, was observed with Fe-Zn [1:1] solution. It could be concluded the sample with higher Zn concentration, exhibited better antimicrobial activity, demonstrating the volume ratio affects the efficacy. This assertion is confirmed by the works of (1) Elumalai et al., 2015 [9.34] who reported the zone of inhibition increases when the concentration of green synthesized ZnO NPs using curry leaf extract against *C. albicans* and *C. tropicalis*, is higher with small particle size; Similarly, (2) Ye et al., 2020 [9.35] demonstrated that iron and zinc ions displayed a stronger bactericidal effect due to their smaller ion particle sizes; as well as (3) Swaroop et al., 2015 [9.36] who reported on the antibacterial properties of gamma irradiated ZnO NPs.
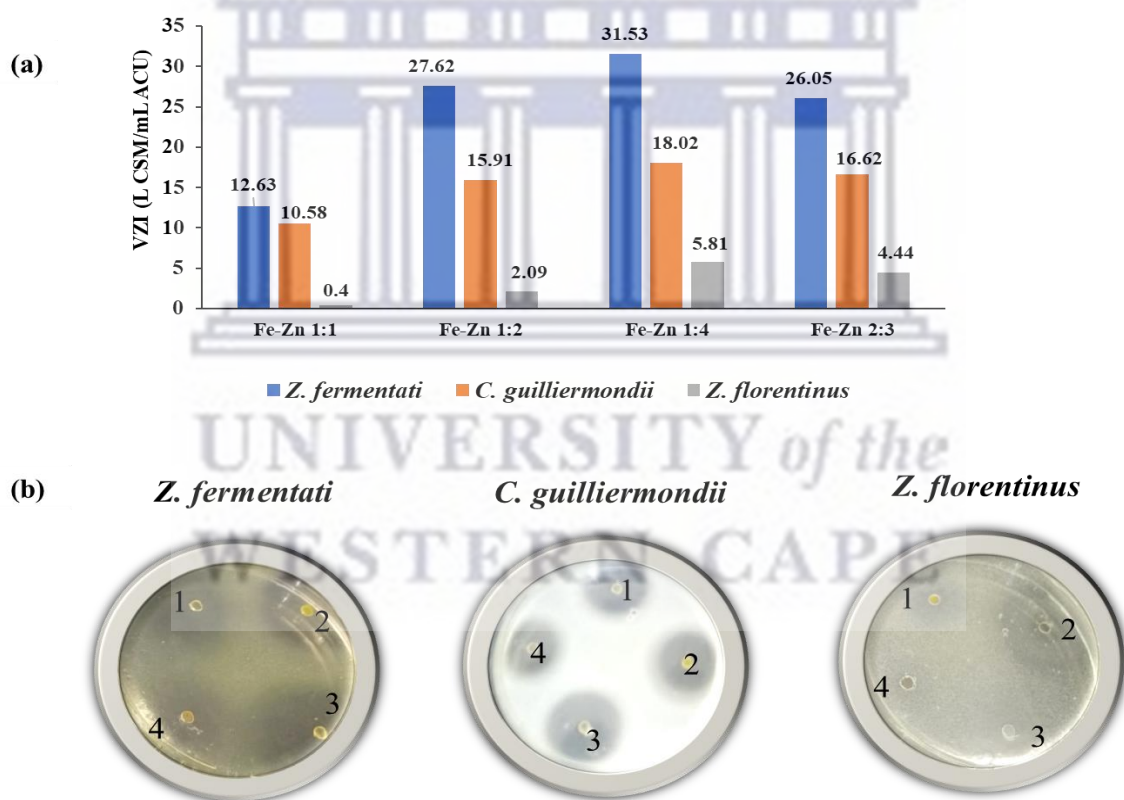
Figure 9.1: (a) The histogram and **(b)** the photograph showing the growth inhibition activity of 20% (m/v) of Fe-Zn [1:4] (1), [2:3] (2), [1:2] (3), and [1:1] (4), against *Z. fermentati*, *C. guilliermondii*, *Z. florentinus*. VZI in L CSM/mL ACU = Volumetric Zone of Inhibition, expressed in Liter of Contaminated Solidified Media per milliliter of Antimicrobial Compound Used

165

9.3.1.2. Screening against spoilage molds

The growth inhibition activity exhibited by the solutions of Fe-Zn [1:4] (1), [2:3] (2), [1:2] (3), and [1:1] (4) against spoilage molds i.e., *Penicillium expansum, Botrytis cinerea, Alternaria alstroemeriae* are presented in Figure 9.2. The Fe-Zn [2:3] and [1:1] solutions did not present any activity whereas Fe-Zn [1:2] solution presented the lowest VZI values L CSM/mL ACU against *P. expansum* and *B. cinerea* of 5.43 and 6.20, respectively, and no activity against *A. alstroemeriae*. Fe-Zn [1:4] solution presented the highest VZI values of 25.15, 9.70, and 9.46 L CSM/mL ACU against *P. expansum*, *B. cinerea,* and *A. alstroemeriae*, respectively. The results are in line with the works of (1) Sharma et al., 2016 [9.37] who demonstrated that ZnO NPs doped with 10 % of Fe ions synthesized by a simple co-precipitation route, exhibited maximum antimicrobial activity against fungi and bacteria than 1 % of Fe ions and pure ZnO; and (2) Fathima et al., 2020 [9.38] who confirmed the antimicrobial activity increases with Fe-doped ZnO NPs than with pure ZnO NPs, which presented a higher inhibition zone for all fungal pathogens.
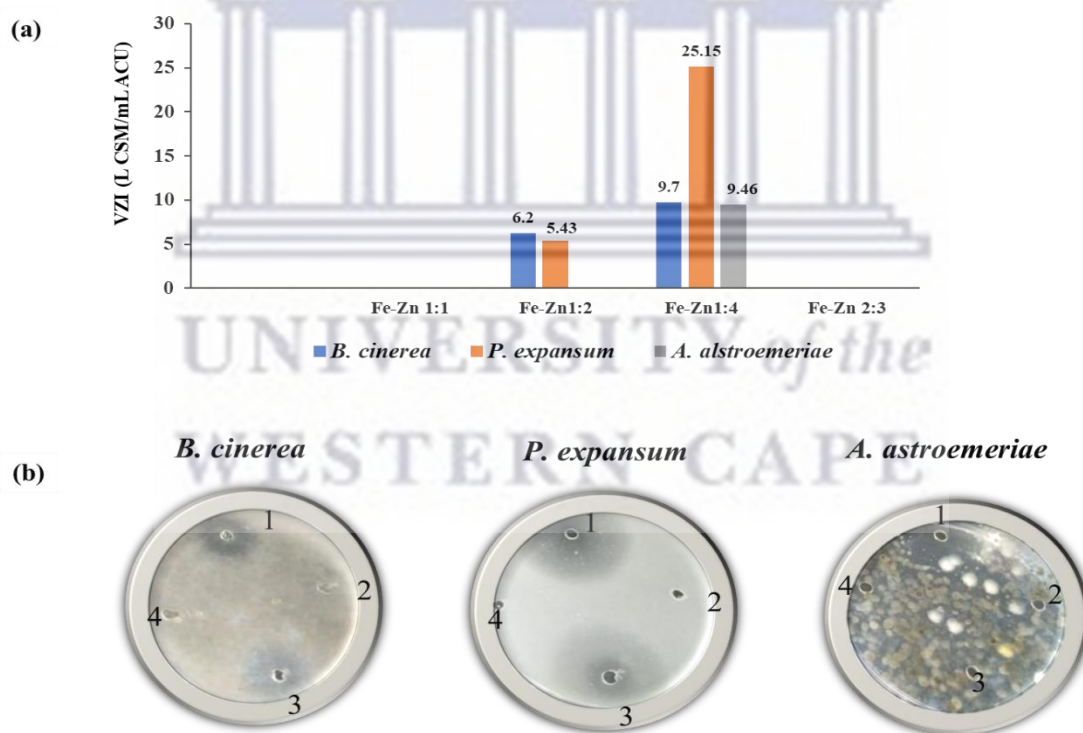
Figure 9.2: (a) The histogram and **(b)** the photograph showing the growth inhibition activity of 20% (m/v) of Fe-Zn [1:4] (1), [2:3] (2), [1:2] (3), and [1:1] (4), against *B. cinerea, P. expansum*, *A. alstroemeriae*. VZI in L CSM/mL ACU = Volumetric Zone of Inhibition, expressed in Liter of Contaminated Solidified Media per milliliter of Antimicrobial Compound Used

166

9.3.1.3. Mechanism of reaction of Fe-Zn NPs on spoilage microorganisms

ROS generated by NPs and free ions are known to deactivate cellular enzymes and deoxyribonucleic acid with the creation of pits in microorganism cells' walls and secretion of toxic elements, leading to enhance permeability which facilitates the capture and killing of cellular by ROS due to the increase of superoxide radicals under visible light exposure as reported by works of Li et al., 2012 [9.12]. The key processes emphasizing the antimicrobial effects of NPs are summarized in four steps: (1) disruption of the microorganism cell membrane; (2) generation of ROS; (3) penetration of the microorganism cell membrane; (4) induction of intracellular antimicrobial effects. The various kinds of interaction between spoilage microorganisms and NPs are the electrostatic attraction, van der Waals forces, receptor-ligand, and hydrophobic interactions [9.14].

Figure 9.3 below depicts the mechanism of the reaction of gamma-irradiated Fe-Zn [1:4] NPs by ROS on spoilage pathogens.
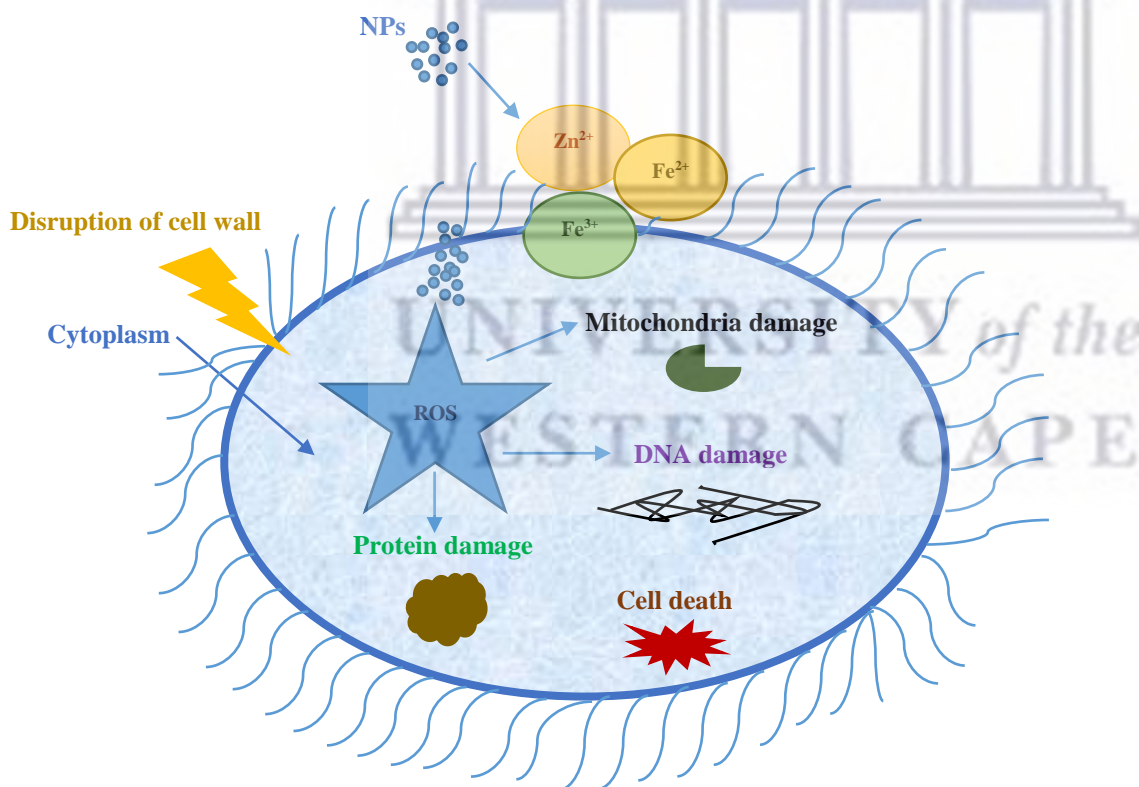
Figure 9.3: Mechanism of reaction of Fe-Zn [1:4] NPs on spoilage microorganisms

It is worth noting the betterment antimicrobial performance with Fe-Zn [1:4] and [1:2] samples, led us to characterize them in addition to Ag-Zn [1:3] sample, to study their physical and magnetic properties, as discussed in the following sections.

9.3.2. Crystallographic analysis

Figure 9.4 (a) shows the X-ray diffraction (XRD) patterns of Ag-Zn [1:3], i.e., hexagonal $Zn(SO_4)(H_2O)$/Ag/ZnO NPs. The presence of intense and well-defined diffraction peaks, is depicted at maxima centered at 2θ (°) = 26.106; 29.513; 35.991; 38.384; 40.934; and 44.351 which are ascribed to the reflections planes of $Zn(SO_4)(H_2O)$ (111); $Zn(SO_4)(H_2O)$ (201); ZnO (101); Ag (111); $Zn(SO_4)(H_2O)$ (102); and Ag (200), respectively. They match with the JCPDS patterns No. 01-080-2210 for Gunningite $Zn(SO_4)(H_2O)$, No. 036-1451 for Zincite (ZnO) and No. 004-0783 for Silver (Ag). The non-identified peaks observed in the spectrum are assigned to impurities, as the metal salt precursor zinc sulphate heptahydrate used is not completely dissolved. It could be remediated by increasing the dose [9.31]. Hence, the phases of Ag-Zn are not pure when compared to other works with a poor crystalline nature [9.17, 9.24, 9.26]. The average crystalline size of $Zn(SO_4)(H_2O)$/Ag/ZnO NPs calculated from the Debye-Scherrer formula $\langle\text{øparticles}\rangle \sim 0.9\lambda/ (\Delta\theta_{1/2} \cos\theta_B)$ was found at 49.011 nm. The values are displayed in Table 9.1.

Table 9.1. Major XRD characteristics of the various Bragg diffraction peaks of Gunningite/Silver/Zincite, i.e., $Zn(SO_4)(H_2O)$/Ag/ZnO NPs

NPs	(hkl)	2θ (degrees)	θ (radians)	FWHM (radians)	Crystalline size D (nm)
$Zn(SO_4)(H_2O)$	(111)	26.106	0.2278	0.0032	40.887
$Zn(SO_4)(H_2O)$	(201)	29.513	0.2544	0.0040	79.684
ZnO	(101)	35.991	0.3140	0.0079	26.715
Ag	(111)	38.384	0.3349	0.0038	38.740
$Zn(SO_4)(H_2O)$	(102)	40.934	0.3572	0.0058	88.971
Ag	(200)	44.351	0.3870	0.0074	19.071

Figures 9.4 (b) and 9.4 (c) exhibit the XRD of Fe-Zn [1:2] and Fe-Zn [1:4], i.e., hexagonal FeOOH/FeO/ZnO and FeO/ZnO NPs, respectively. The presence of intense and well-defined diffraction peaks of iron and zinc with their maxima centered at 2θ (°) = 20.410; 22.374; 26.574;

168

29.388; 30.976; 35.090; 36.100; 39.831; 41.420; 50.402; and 60.528 matches to the reflections planes of (111); (210); (120); (220); (100); (311); (101); (222); (400); (422); and (511) indicating the highly crystalline nature of wustite, zincite, and goethite structures, which are coherent with the JCPDS patterns No. 82-1533 for wustite (FeO), No. 036-1451 for zincite (ZnO), and No. 29-07-13 for goethite (FeOOH). The diffraction peaks were more intensive and narrower, implying that FeO, ZnO, and FeOOH were well-crystalline. Moreover, no impurities were observed. The average crystalline size calculated from the Debye-Scherrer formula was found at 21.260 nm for Fe-Zn [1:2], i.e., FeOOH/FeO/ZnO NPs and 40.582 nm for Fe-Zn [1:4], i.e., FeO/ZnO NPs. The major XRD characteristics are displayed in Table 9.2.

Table 9.2. Major XRD characteristics of the various Bragg diffraction peaks of Wustite/ Zincite/Goethite, i.e., FeO/ZnO/FeOOH NPs

NPs	(hkl)	2θ (degrees)	θ (radians)	FWHM (radians)	Crystalline size D (nm)
FeO	(111)	20.410	0.1781	0.0124	17.117
FeO	(210)	22.374	0.1952	0.0140	52.045
FeOOH	(120)	26.574	0.2319	0.0098	18.828
FeO	(220)	29.388	0.2611	0.0094	27.841
ZnO	(100)	30.976	0.2703	0.0063	22.544
FeO	(311)	35.090	0.3062	0.0093	56.661
ZnO	(101)	36.100	0.3154	0.0132	14.696
FeO	(222)	39.831	0.3475	0.0061	54.543
FeO	(400)	41.420	0.3611	0.0164	31.158
FeO	(422)	50.402	0.4398	0.0130	10.690
FeO	(511)	60.528	0.5282	0.0140	24.350

The peak position of the doped ZnO altered to smaller angles (30.976, 35.991 and 36.100) when compared to pure ZnO (31.770 and 36.253), indicating the successful incorporation of Fe and Ag within the ZnO matrix, and minimization in the intensity of the characteristic peaks [9.39, 9.40].
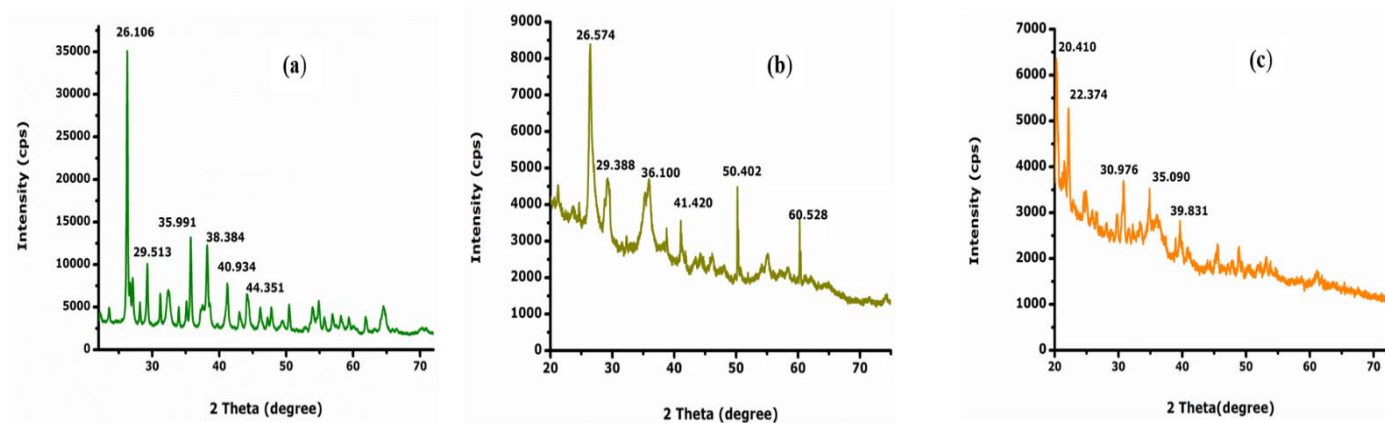
Figure 9.4: XRD of **(a)** Ag-Zn [1:3], **(b)** Fe-Zn [1:2], and **(c)** Fe-Zn [1:4]

9.3.3. Microscopic observations

Figure 9.5 depicts the morphology, composition, size, and crystallinity of Ag-Zn and Fe-Zn NPs using field emission scanning electron microscopy (FESEM) micrographs.

Ag-Zn [1:3], i.e., $Zn(SO_4)(H_2O)/Ag/ZnO$ NPs are hexagonal and spherical, well-agglomerated, and crystalline. The energy dispersive X-ray spectroscopy (EDS) spectrum confirms the presence of Ag, Zn, and O elements in addition to the impurity sulfur (S). The carbon peak is caused by the carbon tape used as grid support to immobilize the NPs and to reduce charging effects. By fitting the histogram data with a Gaussian distribution, the average particle size extracted from FESEM micrographs amounts to 13.369 ± 0.175 nm. Gayathri et al., 2015 [9.24] investigated the physicochemical properties of Ag-doped ZnO nanoparticles prepared by a chemical route, and FESEM micrographs depicted a hexagonal shape. Abedini et al., 2018 [9.31] studied the heterostructure of ZnO/Ag and pure Ag, Zn, and O were depicted in the EDS spectrum in contrast with our findings where some impurities are observed in line with XRD results.

170
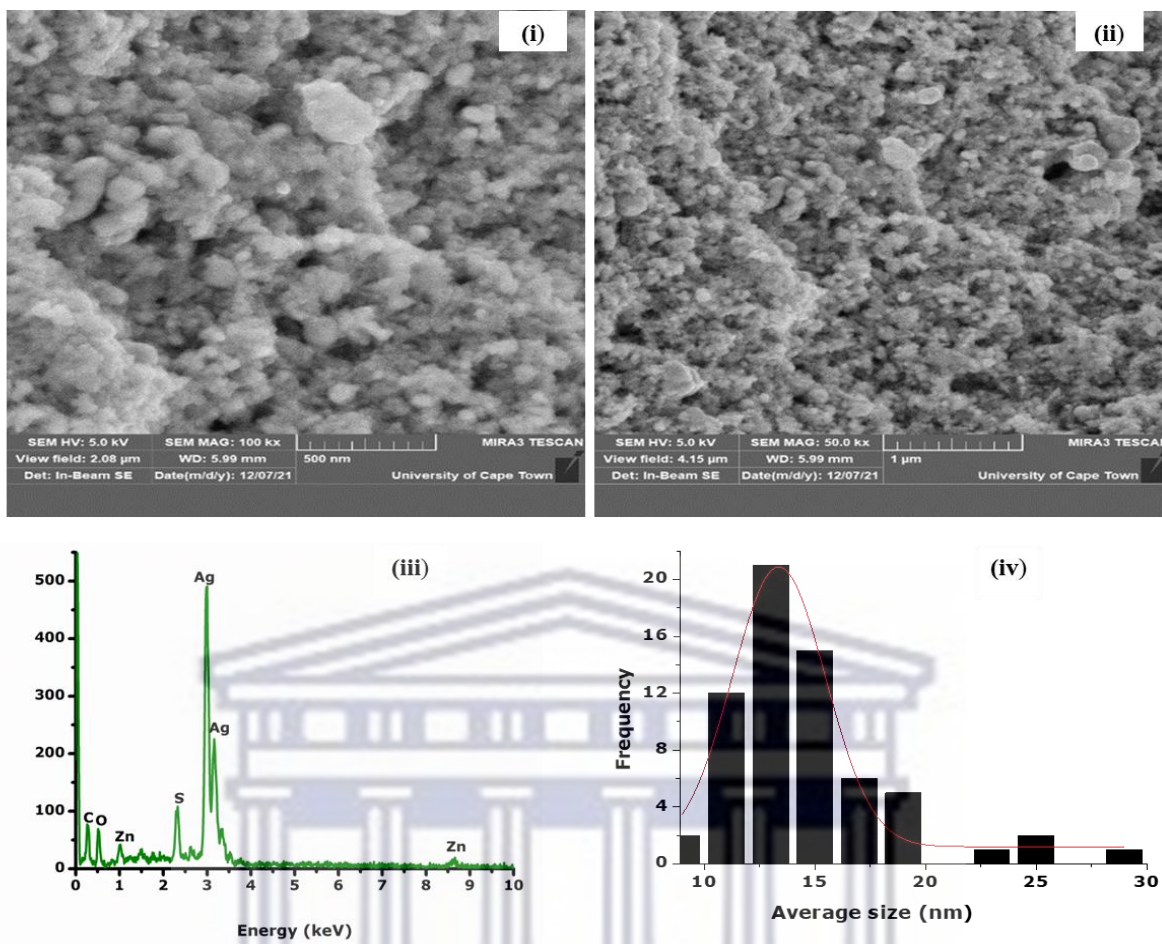
Figure 9.5 (a) : **(i)** FESEM, **(ii)** FESEM, **(iii)** EDS, and **(iv)** Average size of Ag-Zn [1:3]

FESEM show well-agglomerated and crystalline hexagonal Fe-Zn [1:2], i.e., FeOOH/FeO/ZnO and cubic Fe-Zn [1:4], i.e., FeO/ZnO NPs. The EDS spectrum elucidates the presence of Fe, Zn, and O on the sample's surface with some contaminating elements that might come from the FESEM device. The role of the carbon peak was explained previously. By fitting the histogram data with a Gaussian distribution, the average particle size extracted from FESEM micrographs amounts to 12.994 ± 0.462 and 10.745 ± 0.217 nm for FeOOH/FeO/ZnO and FeO/ZnO, respectively.

The microscopic observations are in line with the findings of (1) Reddy et al., 2012 [9.39] who reported on the structural, electron paramagnetic resonance (EPR), photo and thermoluminescence properties of gamma-irradiated ZnO:Fe NPs in the range of 1–5 kGy. They sustained the phase purity of Fe-Zn samples and reduction of particle size; (2) Kumar et

171

al., 2013 [9.41] worked on the alterations in crystallography, microscopy, and optical analyses of ZnO and ZnO:Fe nanoparticles, generated by heavy ion irradiations using 200 MeV Ag^{15+} ion beams. They have proven that properties of ZnO were modified once Fe was inserted into the ZnO lattice; and (3) Liu et al., 2012 [9.42] studied the influence of Fe-doping on the structural, optical, and magnetic features of ZnO nanoparticles. They substantiated that the crystallinity of ZnO is affected by the insertion of Fe.
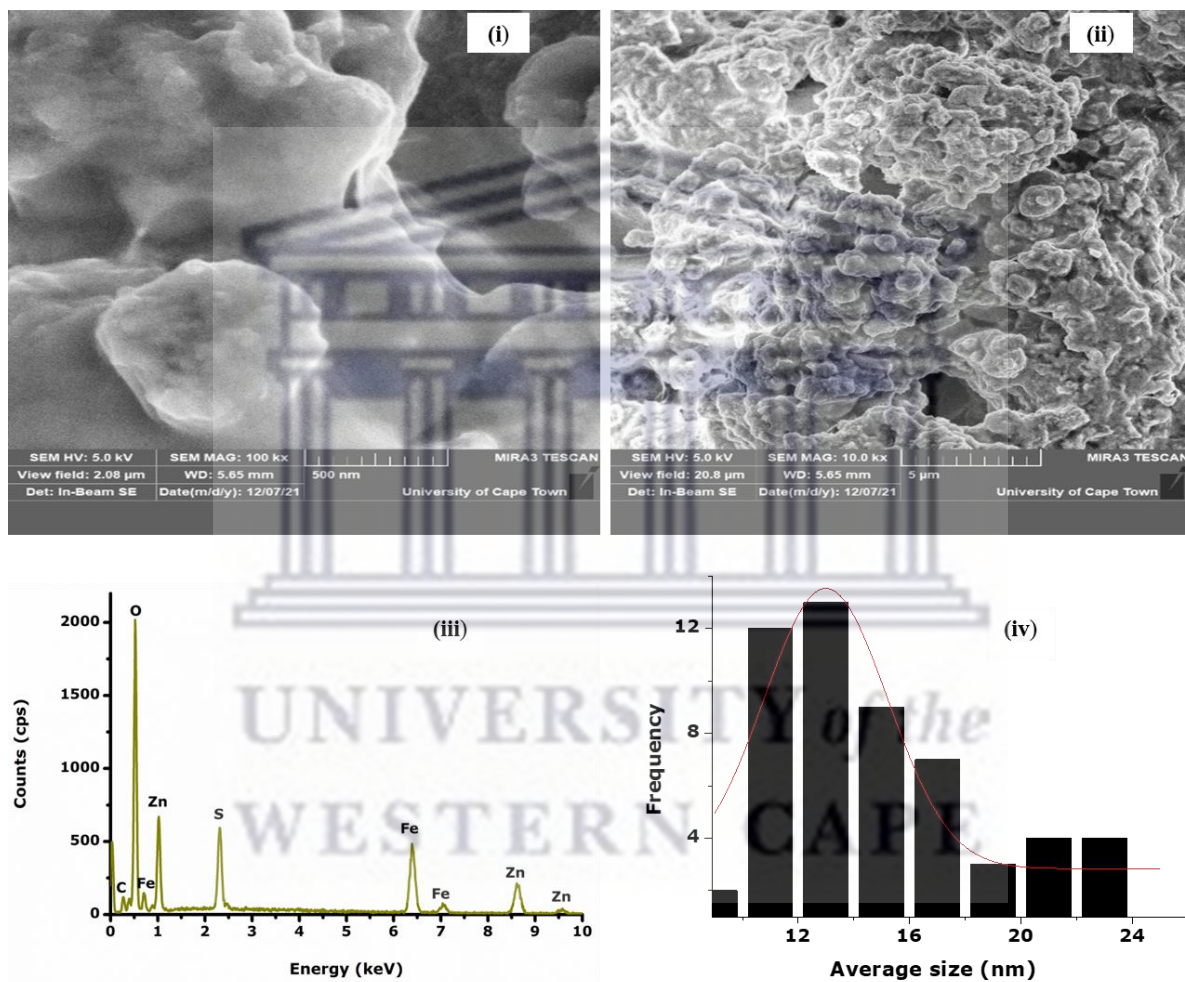
Figure 9.5 (b) : (i) FESEM, **(ii)** FESEM, **(iii)** EDS, and **(iv)** Average size of Fe-Zn [1:2]

172
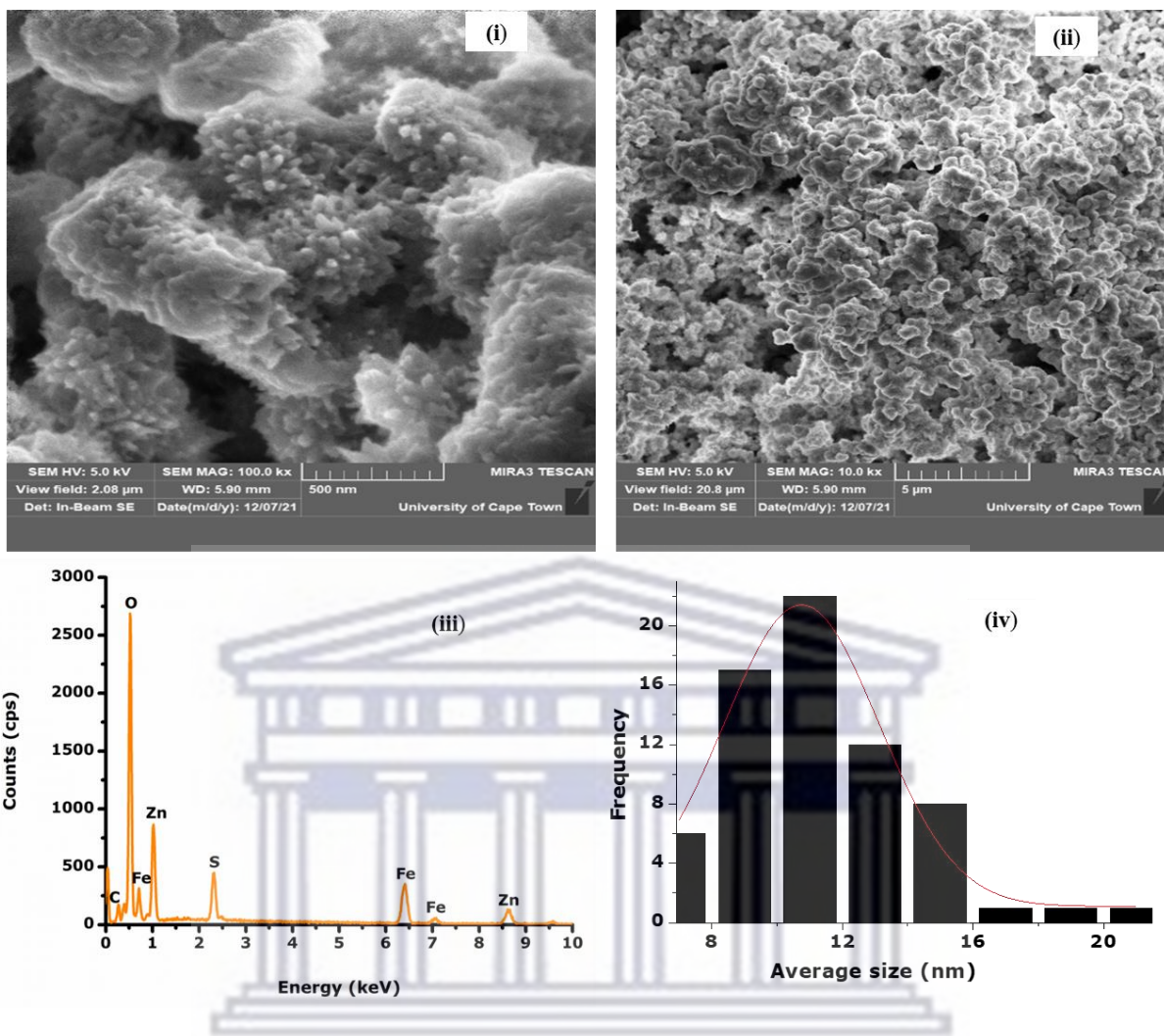
Figure 9.5 (c) : (i) FESEM, **(ii)** FESEM, **(iii)** EDS, and **(iv)** Average size of Fe-Zn [1:4]

9.3.4. Vibrational properties

To validate and to conclude on the purity of Ag-Zn and Fe-Zn, attenuated total reflection-Fourier transform infrared spectroscopy (ATR-FTIR) analysis was performed from 400 to 4000 cm^{-1} at room temperature to determine the potential biomolecules involved in the irradiation and presented in Figure 9.6.

Figure 9.6 (a) denotes ATR-FTIR of Ag-Zn [1:3] where the peaks at 410 and 619 cm^{-1} are ascribed to Ag-O and Zn-O, respectively [9.15, 9.17]. The peak at 1125 cm^{-1} is owing to the oxygen stretching and bending frequency [9.24]. The strong and broad bands centered around 1409 and 1643 cm^{-1} can be assigned to the bending modes of interlayer water molecules [9.40].

173

The broad bands at 2937 and 3578 cm^{-1} are attributed to the hydroxyl groups that originated from moisture content in the sample [9.43].
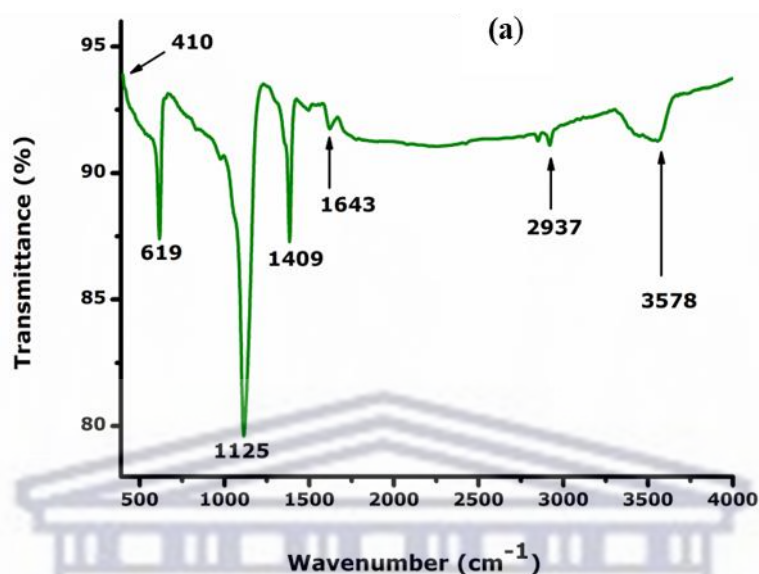
Figure 9.6: ATR-FTIR of (**a**) Ag-Zn [1:3]

Figures 9.6 (b) and 9.6 (c) display the ATR-FTIR of Fe-Zn [1:2] and [1:4], where the peaks around 400 and 600 cm^{-1} are ascribed to Fe-O and Zn-O, respectively [9.39, 9.41]. The peaks between 700 and 1100 cm^{-1} are assigned to the insertion of Fe^{2+} ions into the ZnO lattice. The prominent peaks around 800 cm^{-1} are attributed to FeOOH [9.20]. The strong and broad bands centered around 1400 and 1600 cm^{-1} can be ascribed to the bending modes of interlayer water molecules [9.37]. The broad bands at 2900 and 3500 cm^{-1} are deducted from the hydroxyl groups that originated from moisture content in the sample [9.42].
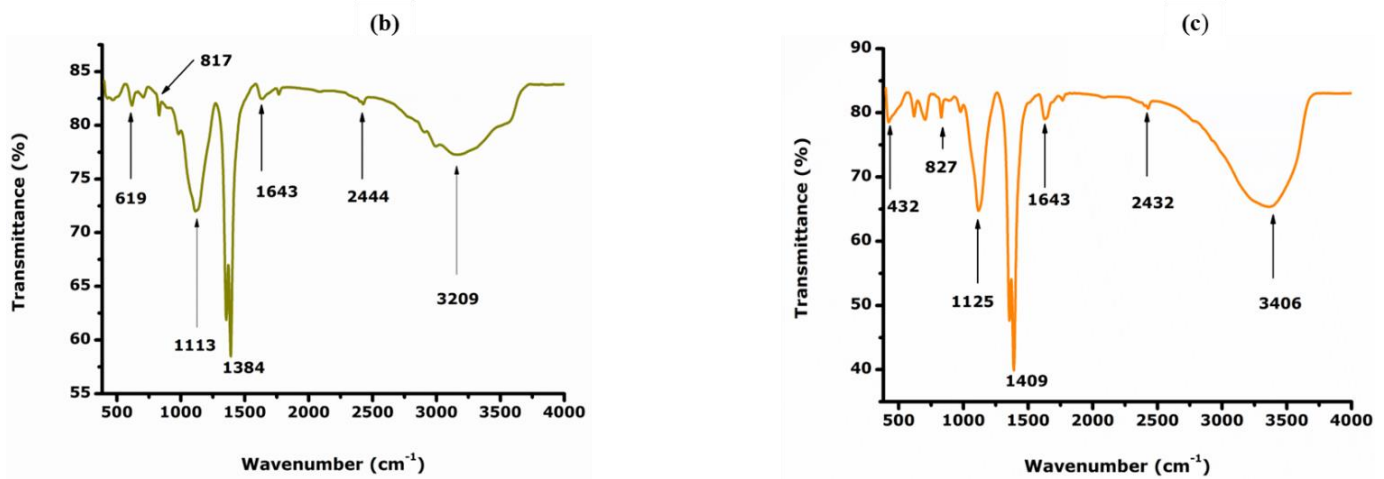
Figure 9.6: ATR-FTIR of **(b)** Fe-Zn [1:2], and **(c)** Fe-Zn [1:4]

9.3.5. Optical properties

9.3.5.1. UV-Visible

The diffuse reflectance spectroscopy (DRS) analysis used to carry out to evaluate the influence of Ag and Fe doping on the optical properties of ZnO NPs, is shown in Figure 9.7. It is noticeable the intense UV absorptions shifted to lower values of 230, 234, and 224 nm, for Ag-Zn [1:3], Fe-Zn [1:2], and [1:4], respectively, in accordance with the XRD results. This phenomenon could be accounted for by the insertion of Ag and Fe within the ZnO lattice. A rearrangement of the neighboring atoms arose to maintain the charge balance, affecting the electronic structure of ZnO lattice, and consequently changing the optical absorption of ZnO NPs [9.40].
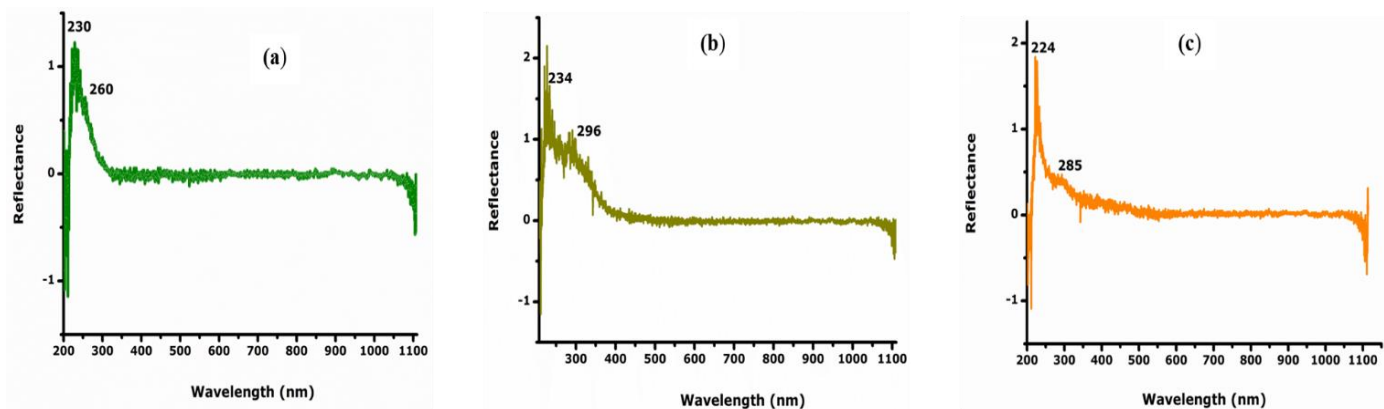
Figure 9.7: UV-Visible of **(a)** Ag-Zn [1:3], **(b)** Fe-Zn [1:2], and **(c)** Fe-Zn [1:4]

175

9.3.5.2. Photoluminescence spectroscopy (PL)

Additional information regarding the surface properties, and structural defects such as oxygen vacancies and metal interstitials, is provided by PL which is a suitable tool to explore the electronic structure, the transfer behavior and recombination rate of photoexcited electron-hole pairs in semiconductors according to its intensity [9.32].

It is well-known that ZnO has an electronic bandgap of 3.37 eV. Generally, the PL of ZnO possesses two peaks around 330 and 390 nm. From Figure 9.8 (a), the PL of Ag-Zn is observed around 505 nm (2.45 eV) showing a shift due to the insertion of Ag into the ZnO lattice. Likewise, the PL spectra of Fe-Zn from Figures 9.8 (b) and 9.8 (c), elucidate two blue emission peaks around 448 nm (2.76 eV) and 468 nm (2.64 eV), ascribed to surface defects due to oxygen deficiency and a green emission peak around 555 nm (2.23 eV), assigned to oxygen vacancies, combined with the radiative recombination process of an electron between the conduction band edges from a deep donor level to an acceptor level [9.39]. The increase of PL intensity is ascertained to a high surface-to-volume ratio with numerous surface-states, native defects (vacancies and interstitials) and Zn-O bonds, on the NPs' surface arising from the modification of the surface which generates the trap levels responsible for the observed emissions [9.18, 9.41]. As Zn concentration arises, the formation of the number of oxygen vacancies arises as well leading to a decrease in the energy bandgap (Eg) values due to more electrons excited from the valence band (VB) to the conduction band (CB) [9.31]. More so, the method of synthesis and experimental conditions can influence several factors including oxygen deficiency, surface roughness, and impurity centers [9.17].
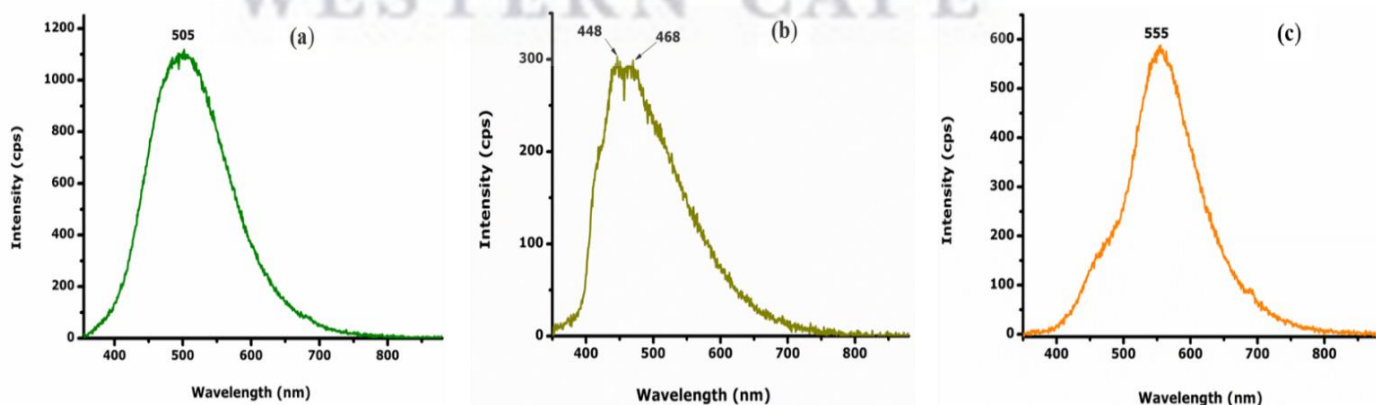

Figure 9.8: PL of **(a)** Ag-Zn [1:3], **(b)** Fe-Zn [1:2], and **(c)** Fe-Zn [1:4]

176

9.3.6. Magnetic properties of Ag-Zn and Fe-Zn NPs

Magnetic measurements were studied using a vibrating sample magnetometer (VSM) where the moments in comparison to the applied magnetic field are denoted in Figure 9.9. The temperature of the samples was kept constant at 300 K during the measurement. The applied magnetic field, from the superconducting magnet, varied from -3 T to +3 T, whereas the vibrating amplitude and the frequency of the sample holder were set at 0.2 Hz and 20 Hz, respectively. The magnetic hysteresis loops (M-H) of Ag-Zn [1:3] did not depict any magnetic moments after measurements whereas Fe-Zn [1:2] and [1:4] suggested a ferromagnetic behavior. The low magnetic saturation magnetization (M_s = 0.0138 and 0.0118 emu/g) for Fe-Zn [1:2] and Fe-Zn [1:4], respectively compared to bulk values of Fe (M_s = 218 emu/g), FeO (M_s = 72 emu/g), Fe_2O_3 (M_s = 74 emu/g), and Fe_3O_4 (M_s = 93 emu/g) may be interpreted as evidence of the effective incorporation of doping iron oxide onto ZnO lattice, as demonstrated by XRD and ATR-FTIR analyses. The results suggested that the number of defects such as oxygen vacancies at the samples' surface may display a charge transfer ferromagnetism in defect-rich regions due to a minimization in superexchange interaction of iron cations in the tetrahedral and octahedral sites [9.30]. Thus, disordered surfaces and oxygen non-stoichiometric of oxide surfaces and consequently, a reduction in the magnetization on the NPs' surface [9.44]. Moreover, the weak ferromagnetism could be explained as the result of three important factors such as impurity phases, cationic distribution, disordered surface spins, crystallinity, particle size, dose, and dose rate [9.45]. This ferromagnetic behavior observed is in line with the works of Liu et al., 2012 [9.42]; Sathya et al., 2017 [9.46] who assessed the magnetic properties of Fe-doped ZnO nanoparticles.
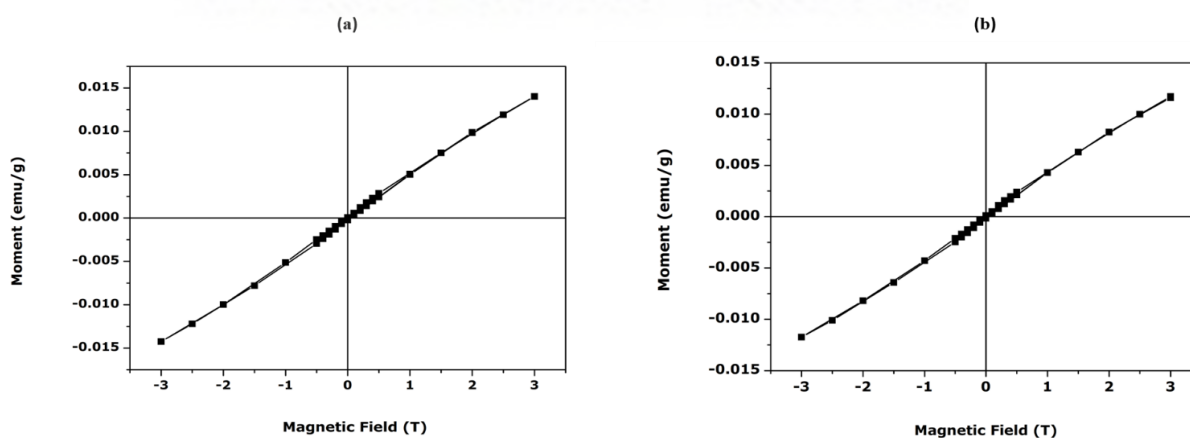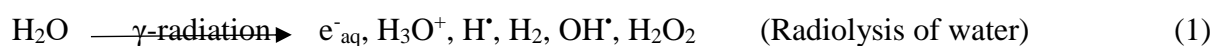

Figure 9.9: Magnetic behavior of **(a)** Fe-Zn [1:2] and **(b)** Fe-Zn [1:4]

9.3.7. Mechanism of formation of FeO/ZnO NPs

The formation of Fe-Zn [1:4], i.e., FeO/ZnO NPs, which showed the best antimicrobial during the radiolytic reduction by gamma irradiation is presented [9.32].

The interaction results in the generation of secondary electrons in an aqueous solution that forms hydrated electrons (e^-_{aq}), hydroxyl radicals ($OH^\bullet$) and hydrogen radicals ($H^\bullet$) as shown in equation 1.

$$H_2O \xrightarrow{\text{γ-radiation}} e^-_{aq}, H_3O^+, H^\bullet, H_2, OH^\bullet, H_2O_2 \qquad \text{(Radiolysis of water)} \qquad (1)$$

The solvated electrons (e^-_{aq}) are strong reducing agents that can reduce Fe (II) and Zn (II) ions into their lower states, as shown in equation 2.

$$Fe^{2+} + 2e^- \rightarrow Fe^0 \qquad\qquad \text{(Reduction and nucleation)} \qquad (2a)$$

$$Zn^{2+} + 2e^- \rightarrow Zn^0 \qquad\qquad \text{(Reduction and nucleation)} \qquad (2b)$$

Isopropyl alcohol, the most commonly used hydroxyl radical scavenger, scavenges hydrogen and hydroxyl radicals, generating a secondary radical with high negative potential.

According to equations 3, 4 and 5, the new radical can now contribute to the reduction of metal ions into their zero-valent form.

$$OH^\bullet + CH_3\text{-}CH(OH)\text{-}CH_3 \rightarrow H_2O + H_3C\text{-}C^\bullet(OH)\text{-}CH_3 \qquad \text{(Radical association)} \qquad (3)$$

$$H^\bullet + CH_3\text{-}CH(OH)\text{-}CH_3 \rightarrow H_2 + H_3C\text{-}C^\bullet(OH)\text{-}CH_3 \qquad \text{(Radical association)} \qquad (4)$$

Thus formed 2-propanol radical can additionally reduce iron (Fe^{2+}), and zinc (Zn^{2+}) ions:

$$Fe^0 + Zn^0 + 2OH^\bullet + 2[CH_3\text{-}CH(OH)\text{-}CH_3] \rightarrow 2[H_3C\text{-}C^\bullet(OH)\text{-}CH_3] + FeO\text{-}ZnO + 2H_2$$

$$\text{(Reduction and nucleation)} \qquad (5)$$
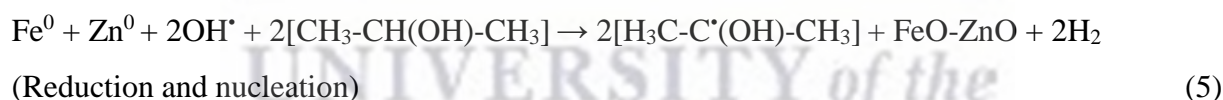
9.4. Conclusion

The gamma radiolysis approach was successfully demonstrated to be versatile in enhancing the antimicrobial performance of Fe-Zn samples. The sample Fe-Zn [1:4], i.e., FeO/ZnO NPs, with a greater Zn content and a smaller particle size of 10.745 ± 0.217 nm, showed the remarkable antimicrobial performance against six spoilage microorganisms tested. This finding will contribute to reducing infectious diseases as well as economic losses in the beverages, fruit, and food industries. The analysis of Ag-Zn [1:3] indicated crystalline impurities but no magnetic behavior. The XRD analyses in agreement with the microscopic observations confirmed polycrystalline, self-assembled, and well-agglomerated NPs. The optical properties

substantiated the insertion of Ag and Fe within the ZnO lattice by obtaining lower Eg values. Besides, the photoluminescence spectroscopy revealed certain defects with oxygen vacancies, which were corroborated by magnetic properties, suggesting a weak ferromagnetic behavior of Fe-Zn NPs. The best antimicrobial performance of FeO/ZnO NPs should be considered for further work in other biomedical applications such as antiviral or antioxidant.

9.5. References

[9.1] J.M. Lorenzo, P.E. Munekata, R. Domínguez, M. Pateiro, J.M.A. Saraiva, and D.J.F. Ruiz, Main Groups of Microorganisms of Relevance for Food Safety and Stability. In Book: Innovative Technologies for Food Preservation, pp. 53–107 (2018).

[9.2] S.A. Cichello, Oxygen absorbers in Food preservation: a review. Journal of Food Science and Technology 52, pp. 1889–1895 (2015).

[9.3] M. Mewa-Ngongang, H.W du Plessis, U.F. Hutchinson, L. Mekuto, S.K.O Ntwampe, Kinetic modelling and optimization of antimicrobial compound production by *Candida pyralidae* KU736785 for control of *Candida guilliermondii*. Food Sci. Technol. Inter. 23 (4), pp. 1–13 (2017).

[9.4] B.S. Chidi, V.I. Okudoh, U.F. Hutchinson, M.M. Ngongang, T. Maphanga, B.S. Madonsela, K. Shale, J.W. Lim, S.K.O. Ntwampe, A Perspective on Emerging Inter-Disciplinary Solutions for the Sustainable Management of Food Waste. Appl. Sci. 12, Article 11399 (2022).

[9.5] G.H. Fleet, Yeasts in foods and beverages: Impact on product quality and safety. Current Opinion in Biotechnology 18 (2), pp.170–175 (2007).

[9.6] J.I. Pitt & A.D. Hocking, Fungi and food spoilage. New York: Springer-Verlag (2009).

[9.7] B. Williamson, B. Tudzynski, P. Tudzynski, & J.A.V. Kan, Botrytis cinerea: the cause of grey mould disease. Molecular Plant Pathology 8 (5), pp. 561–580 (2007).

[9.8] R.R. Sharma, D. Singh, R. Singh, Biological control of postharvest diseases of fruits and vegetables by microbial antagonists: A review, Biological Control. 50 (3), pp. 205–221 (2009).

[9.9] M. Koopmans & E. Duizer, Foodborne viruses: An emerging problem. International Journal of Food Microbiology 90 (1), pp. 23–41 (2004).

[9.10] B. Anne-Laure, T.J. Ward, G.J.V. Coller, B. Flett, S.C. Lamprecht, K. O'Donnell, A. Viljoen, Analysis of the Fusarium graminearum species complex from wheat, barley and maize in South Africa provides evidence of species-specific differences in host preference. Fungal Genetics and Biology 48 (9), pp. 914–920 (2011).

[9.11] A.H. Shah, M.A. Rather, Pharmaceutical residues: New emerging contaminants and their mitigation by nano-photocatalysis. Advances in nano research 10 (4), pp. 397–414 (2021).

[9.12] Y. Li, W. Zhang, J. Niu, and Y. Chen, Mechanism of photogenerated reactive oxygen species and correlation with the antibacterial properties of engineered metal-oxide nanoparticles. ACS Nano 6 (6), pp. 5164–5173 (2012).

[9.13] E.D. Sherly, J.J. Vijaya, L.J. Kennedy, A. Meenakshisundaram, M. Lavanya, A comparative study of the effects of CuO, NiO, ZrO_2 and CeO_2 coupling on the photocatalytic activity and characteristics of ZnO. Korean J. Chem. Eng. 33 (4), pp. 1431–1440 (2016).

[9.14] K.R. Raghupati, R.T. Koodali, A.C. Manna, Size dependent bacterial growth inhibition and mechanism of antibacterial activity of zinc oxide NPs. Langmuir 27, pp. 4020–4028 (2011).

[9.15] S.K. Noukelag, H.E.A. Mohamed, B. Moussa, L.C. Razanamahandry, S.K.O. Ntwampe, C.J. Arendse & M. Maaza, Investigation of structural and optical properties of biosynthesized Zincite (ZnO) nanoparticles (NPs) via an aqueous extract of *Rosmarinus officinalis* (rosemary) leaves. MRS Advances 5 (45), pp. 2349–2358 (2020).

[9.16] G. Habibullah, J. Viktorova & T. Rumi, Current Strategies for Noble Metal Nanoparticle Synthesis. Nano Res. Lett. 16, Article 47 (2021).

[9.17] S.K. Noukelag, L.C. Razanamahandry, S.K.O. Ntwampe, C.J. Arendse, M. Maaza, Industrial Dye Removal Using Bio-Synthesized Ag-doped ZnO Nanoparticles. Environmental Nanotechnology, Monitoring & Management 16 (16), Article 100463 (2021).

[9.18] H. Thabit, N. Kabir, N.M. Ahmed, Synthesis and thermoluminescence characteristics & structural and optical studies of ZnO/Ag/ZnO system for dosimetric applications. Journal of Luminescence 236, Article 118097 (2021).

[9.19] L. An-Hui, E.L. Salabas, and F. Schüth, Magnetic Nanoparticles: Synthesis, Protection, Functionalization, and Application. Angewandte Chemie (International ed. In English) 46 (8), pp. 1222–1244 (2007).

[9.20] S.K. Noukelag, C.J. Arendse & M. Maaza, Biosynthesis of hematite phase α-Fe_2O_3 nanoparticles using an aqueous extract of *Rosmarinus officinalis* leaves, Material Today: Proceedings 43, pp. 3679–3683 (2021).

[9.21] A. Abedini, A.R. Daud, M.A.A. Hamid, & N.K. Othman, Radiolytic formation of Fe_3O_4 nanoparticles: influence of radiation dose on structure and magnetic properties. PloS one 9 (3), Article e90055 (2014).

[9.22] D. Sahu, B. S. Acharya, and A. K. Panda, "Role of Ag ions on the structural evolution of nano ZnO clusters synthesized through ultrasonication and their optical properties." Ultrasonics Sonochemistry 18 (2), pp. 601–607 (2011).

[9.23] S.K. Noukelag, F. Cummings, C.J. Arendse, M. Maaza, Physical and magnetic properties of biosynthesized ZnO/Fe_2O_3, $ZnO/ZnFe_2O_4$, and $ZnFe_2O_4$ nanoparticles. Results in Surfaces and Interfaces 10, Article 100092 (2023).

[9.24] S. Gayathri, O.S.N. Ghosh, S. Sathishkumar, P. Sudhakara, J. Jayaramudu, S.S. Ray, K. Viswanath, Investigation of physicochemical properties of Ag doped ZnO nanoparticles prepared by chemical route. Applied Science Letters 1 (1), pp. 8–13 (2015).

[9.25] O. Muktaridha, M. Adlim, S. Suhendrayatna and I. Ismail, Synthesis of iron-doped zinc oxide (Fe-ZnO) nanoparticles by using several stabilizers. Journal of Physics: Conference Series 1882, Article 012109 (2020).

[9.26] T.S. Vijayakumar, S. Karthikeyeni, S. Vasanth, A. Ganesh, G. Bupesh, R. Ramesh, M. Manimegalai, P. Subramanian, "Synthesis of Silver-Doped Zinc Oxide Nanocomposite by Pulse Mode Ultrasonication and Its Characterization Studies". Journal of Nanoscience 2013, Article 785064 (2013).

[9.27] G.G. Flores-Rojas, F. López-Saucedo, E. Bucio, Gamma-irradiation applied in the synthesis of metallic and organic nanoparticles: A short review. Radiation Physics and Chemistry 169, Article 107962 (2020).

[9.28] Q. Yun, A. Kimura, M. Taguchi, E. Miyako, Sonication – and γ-ray – mediated biomolecule-liquid metal nanoparticlization in cancer optotheranostics. Applied Materials Today 26, Article 101302 (2022).

[9.29] S.D. Raut, V.V. Awasarmol, B.G. Ghule, S.F. Shaikh, S.K. Gore, R.P. Sharma, P.P. Pawar, R.S. Mane, γ-irradiation induced zinc ferrites and their enhanced room temperature ammonia gas sensing properties. Materials Research Express 5 (3), Article 033702 (2018).

[9.30] S. K. Noukelag, M. Mewa-Ngongang, S. Ngqoloda, L. Kotsedi, L. C. Razanamahandry, S.K.O. Ntwampe, C.J. Arendse, M. Maaza, Influence of synthesis method on structural, morphological, magnetic, and antimicrobial properties of Fe-Ag nanoparticles. Journal of Inorganic and Organometallic Polymers and Materials 33, pp. 159–169 (2023).

[9.31] A. Abedini, M. Saraji, A.A.A. Bakar, P.S. Menon, S. Shaari, Gamma-Radiation-assisted synthesis of luminescent ZnO/Ag heterostructure core-shell nanocomposites. Plasmonics 13 (3), pp. 771–778 (2018).

[9.32] S.K. Noukelag, S. Ngqoloda, L.K. Chester, C.J. Arendse, M. Maaza. Investigation of physical, magnetic, and electrochemical properties of silver-iron nanoparticles synthesized by gamma radiolysis. Applied Physics A 128 (3), pp. 1–10 (2022).

[9.33] M. Mewa-Ngongang, H.W du Plessis, E. Hlangwani, S.K.O Ntwampe, B.S. Chidi, U.F. Hutchinson, and P.N. Neil, Activity Interactions of Crude Biopreservatives against Spoilage Yeast Consortia. Fermentation 5 (3), Article 53 (2019).

[9.34] K. Elumalai, S. Velmurugan, S. Ravi, V. Kathiravan, S. Ashokkumar, Bio-fabrication of zinc oxide nanoparticles using leaf extract of curry leaf (*Murraya koenigii*) and its antimicrobial activities. Materials Science in Semiconductor Processing 34, pp. 365–372 (2015).

[9.35] Q. Ye, W. Chen, H. Huang, Y. Tang, W. Wang, F. Meng, H. Wang, & Y. Zheng, Iron and zinc ions, potent weapons against multidrug-resistant bacteria. Applied Microbiology and Biotechnology 104 (12), pp. 5213–5227 (2020).

[9.36] K. Swaroop, S. Sheikh, K.R. Chandrashekar, H.M. Somashekarappa, Antibacterial studies of gamma irradiated zinc oxide nanoparticles on *Klebsiella pneumoniae* and *Pseudomonas aeruginosa*. IOSR Journal of Applied Physics 7 (4), pp. 58–63 (2015).

[9.37] N. Sharma, S. Jandaik, S. Kumar, M. Chitkara, & I.S. Sandhu, Synthesis, characterization and antimicrobial activity of manganese and iron-doped zinc oxide nanoparticles. Journal of Experimental Nanoscience 11 (1), pp. 54–71 (2016).

[9.38] A.F. Fathima, R.J. Mani, K. Sakthipandi, K. Manimala, A. Hossain, Enhanced antifungal activity of pure and iron-doped ZnO nanoparticles prepared in the absence of reducing agents. Journal of inorganic and organometallic polymers and materials 30 (7), pp. 2397–2405 (2020).

[9.39] A.J. Reddy, M.K. Kokila, H. Nagabhushana, S. Sharma, J.L. Rao, C. Shivakumara, B.M. Nagabhushana, R.P.S. Chakradhar, Structural, EPR, photo and thermoluminescence properties of ZnO:Fe nanoparticles. Materials Chemistry and Physics 133 (2–3), pp. 876–883 (2012).

[9.40] M. Kouhail, Z. El Ahmadi & A. Benayada, Effect of Ag, Ca, and Fe on photocatalytic activity of ZnO nanoparticles to remove textile dyes under sunlight irradiation. Reac. Kinet. Mech. Cat. 135, pp.169–182 (2022).

[9.41] S. Kumar, K. Asokan, R.K. Singh, S. Chatterjee, D. Kanjilal, and A.K. Ghosh, Structural and Optical properties of ZnO and ZnO:Fe nanoparticles under dense electronic excitations. Journal of Applied Physics 114 (16), Article 164321 (2013).

[9.42] C. Liu, D. Meng, H. Pang, X. Wu, J. Xie, X. Yu, L. Chen, X. Liu, Influence of Fe-doping on the structural, optical, and magnetic properties of ZnO nanoparticles. Journal of magnetism and magnetic materials 324 (20), pp. 3356–3360 (2012).

[9.43] M.A. Kareem, I.T. Bello, H.A. Shittu, P. Sivaprakash, O. Adedokun, S. Arumugam, "Synthesis, characterization, and photocatalytic application of silver doped zinc oxide nanoparticles". Cleaner Materials 3, Article 100041 (2022).

[9.44] J.M.D. Coey, K. Wongsaprom, J. Alaria, M. Venkatesan, Charge-transfer ferromagnetism in oxide nanoparticles, J. Phys. D: Appl. Phys. 41 (13), pp. 134012–134018 (2008).

[9.45] A. Sharaf, Synthesis Characterization and Gamma Irradiation Effect on Cobalt Doped ZnO Diluted Magnetic Semiconductor. Arab Journal of Nuclear Sciences and Applications 55 (3), pp. 62–73 (2022).

[9.46] B. Sathya, V Porkalai, D.B. Anburaj, G Nedunchezhian. Low Temperature Ferromagnetism and Optical Properties of Fe Doped ZnO Nanoparticles Synthesized by Sol-Gel Method. Mechanics, Materials Science & Engineering Journal 9 (1), ISSN 2412–5954 (2017).

184

SUMMARY, RECOMMENDATIONS AND FURTHER WORK

10.1. Summary

The main objective of this thesis was to synthesize and characterize bimetallic immiscible alloy nanoparticles (NPs) via versatile and efficient routes, namely green and gamma radiolysis for environmental remediation applications. Several factors were explored to determine the conditions of possible miscibility from immiscible metals, including the mass of rosemary leaves, volume of isopropyl alcohol, annealing temperature, pH, metal salt precursor type, volume ratio, dose, and dose rate. The strategy for breaking down the immiscibility and getting an alloy structure was successfully achieved via the two methods reported in chapters seven and eight, respectively.

In chapter five, three synthesis methods were used to create Fe-Ag and Fe-Zn NPs with varying volume ratios. Superparamagnetic green Ag/Fe_2O_3 NPs produced at Fe-Ag [3:1], annealing temperature 800 °C, basic medium, rosemary extract 2 g, synthesized from silver nitrate and iron chloride hexahydrate, depicted the best antimicrobial activity. Ferromagnetic $ZnSO_4/Zn(SO_4)(H_2O)/Fe_2O_3$ generated at Fe-Zn [2:3], annealing temperature 600 °C, acidic medium, synthesized from iron chloride hexahydrate and zinc sulphate heptahydrate with distilled water, showed lower antimicrobial properties whereas ferromagnetic gamma irradiated Ag/Fe_3O_4 NPs obtained at Fe-Ag [7:1], basic medium, 50 kGy dose, 10 mL of isopropyl alcohol, synthesized from silver nitrate and ferrous sulphate, portrayed the lowest antimicrobial activity.

In chapter six, green Ag-doped ZnO NPs were synthesized from silver nitrate and zinc chloride and utilized as a photocatalyst at Ag-Zn [1:9] volume ratio, annealing temperature 500 °C, basic medium, rosemary extract 2 g, for the removal of hazardous pollutants in a dye coming from clothing company industry. The preliminary tests revealed this dye was extremely polluted, upsurging a swift treatment to alleviate the environmental concern. However, the percentage of degradation of 63 % after 100 min by the green photocatalyst Ag/ZnO could be improved by using hydrogen peroxide H_2O_2 as a scavenger for further work.

In chapter seven, bimetallic Fe-Ag NPs were performed at volume ratio [1:7], basic medium, 10 mL of isopropyl alcohol, at 25 and 50 kGy doses, to find out if the thermodynamic immiscibility of Fe and Ag could be overcome. The formation of AgCl NPs at 25 kGy dose and superparamagnetic $AgFeO_2$ NPs at 50 kGy dose, was consistent with the literature on the effect of dose. The gamma radiolysis route herein substantiated its versatility for production of bimetallic Fe-Ag alloy NPs in this thesis. Furthermore, the prominent electrical conductivity properties exhibited by $AgFeO_2$ NPs after the electrochemical measurements, ascertained their possibility to be explored for energy storage in various devices as further work.

In chapter eight, Fe-Zn samples with varying volume ratios, pH, and 2 and 3 g of rosemary extract were synthesized. From the thermodynamic point of view, Fe and Zn are immiscible in their bulk form. As a result, the target aimed to find out the optimal parameters for generating bimetallic Fe-Zn alloy NPs. No alloy Fe-Zn NPs were obtained at annealing temperatures of 500 and 600 °C. Nevertheless, by raising the annealing temperature to 800 °C, $ZnO/ZnFe_2O_4$ and $ZnFe_2O_4$ NPs were obtained at volume ratios of [1:2] and [2:3], rosemary extract 2 g, in basic and acidic media, respectively. This finding demonstrated herein the significance of using a green method approach to manufacture bimetallic Fe-Zn alloy NPs by breaking down their immiscibility.

In chapter nine, the screening was carried out using four solutions of Fe-Zn samples at different volume ratios against six spoilage microorganisms. The goal was to identify the sample with the best antimicrobial activity, and the results revealed ferromagnetic gamma irradiated FeO/ZnO NPs, obtained at volume ratio [1:4], acidic medium, 50 kGy dose, 5 mL of isopropyl alcohol, synthesized from ferrous sulphate and zinc nitrate hexahydrate, with a higher concentration of Zn and smaller particle size. These findings in line with the previous studies, confirmed the effect of volume ratio on the antimicrobial properties. On the other hand, photocatalytic properties of gamma irradiated Ag-Zn samples were not performed since pure Ag/ZnO NPs were not produced.

Overall, the findings demonstrated the method and conditions of synthesis such as volume ratio, metal salt precursor type, concentration extract, isopropyl alcohol, dose, annealing temperature, and pH, alter the final structure and features of generated NPs as reported in chapter two. The type of combination is also important because the synthesis of Fe-Zn NPs with a lower volume of isopropyl alcohol in an acidic medium was more efficient than the synthesis of Fe-Ag NPs

186

with a higher volume of isopropyl alcohol in a basic medium for the growth inhibition of the same spoilage yeasts and molds using the gamma radiolysis approach. Hence, getting bimetallic alloy NPs from immiscible metals via versatile methods opens the floor to alternative applications not explored in this thesis, such as nanofluids for enhanced thermal conductivity.

10.2. Recommendations and Further work

While there are few reports in the literature, the perspective of this research is to develop more and more bimetallic alloy NPs from immiscible metals using gamma radiolysis method. Still, the following points should be considered for further work.

1. The mechanism of formation of NPs arising through the interaction of biomolecules from rosemary leaves extract with metal salt precursors, leading to their nucleation, formation, and stability.

2. The synthesis of gamma irradiated Fe-Zn NPs by increasing the dose or volume of isopropyl alcohol/volume ratio to assess if $ZnFe_2O_4$ alloy NPs could be generated.

3. The combination of green and gamma radiolysis approaches for the synthesis and characterization of bimetallic alloy NPs derived from immiscible metals to define whether the new properties generated are far better for environmental remediation applications.

List of Publications

Research papers

1. Sandrine Kamdoum Noukelag, Maxwell Mewa-Ngongang, Siphelo Ngqoloda, Lebogang Kotsedi, Lovasoa Christine Razanamahandry, Seteno K.O. Ntwampe, Christopher J. Arendse, Malik Maaza, **Influence of synthesis method on structural, morphological, magnetic, and antimicrobial properties of Fe-Ag nanoparticles.** Journal of Inorganic and Organometallic Polymers and Materials 33, pp. 159–169 (2023).

2. Sandrine Kamdoum Noukelag, Siphelo Ngqoloda, Lebogang Kotsedi Chester, Christopher J. Arendse, Malik Maaza, **Investigation of physical, magnetic, and electrochemical properties of silver-iron nanoparticles synthesized by gamma radiolysis.** Applied Physics A 128 (3), pp. 1–10 (2022).

3. Sandrine Kamdoum Noukelag, Lovasoa Christine Razanamahandry, Seteno K.O. Ntwampe, Christopher J. Arendse, Malik Maaza, **Industrial dye removal using bio-synthesized Ag-doped ZnO nanoparticles.** Environmental Nanotechnology, Monitoring & Management 16, Article 100463 (2021).

Conference papers

1. Sandrine Kamdoum Noukelag, Franscious Cummings, Christopher J. Arendse, Malik Maaza, **Physical and magnetic properties of biosynthesized ZnO/Fe_2O_3, $ZnO/ZnFe_2O_4$, and $ZnFe_2O_4$ nanoparticles**. Results in Surfaces and Interfaces 10, Article 100092 (2023).

2. S.K. Noukelag, C.J. Arendse & M. Maaza, **Biosynthesis of hematite phase α-Fe_2O_3 nanoparticles using an aqueous extract of Rosmarinus officinalis leaves**. Material Today: Proceedings 43, pp. 3679–3683 (2021).

3. S.K. Noukelag, H.E.A. Mohamed, B. Moussa, L.C. Razanamahandry, S.K.O. Ntwampe, C.J. Arendse & M. Maaza, **Investigation of structural and optical properties of biosynthesized Zincite (ZnO) nanoparticles (NPs) via an aqueous extract of Rosmarinus officinalis (rosemary) leaves.** MRS Advances 5 (45), pp. 2349–2358 (2020).

International Conferences

1. Attended and participated in the 10th AMRS International Conference, 10–13 December 2019 (Arusha–Tanzania): **Poster presentation** on biosynthesized ZnO nanoparticles.

2. Attended and participated in the 4th African Nano Conference/ Workshop in applications of nanotechnology, 18–23 July 2021 (Nsukka–Nigeria): **Oral presentation** on biosynthesized ZnO/Fe_2O_3, $ZnO/ZnFe_2O_4$, and $ZnFe_2O_4$ nanoparticles.
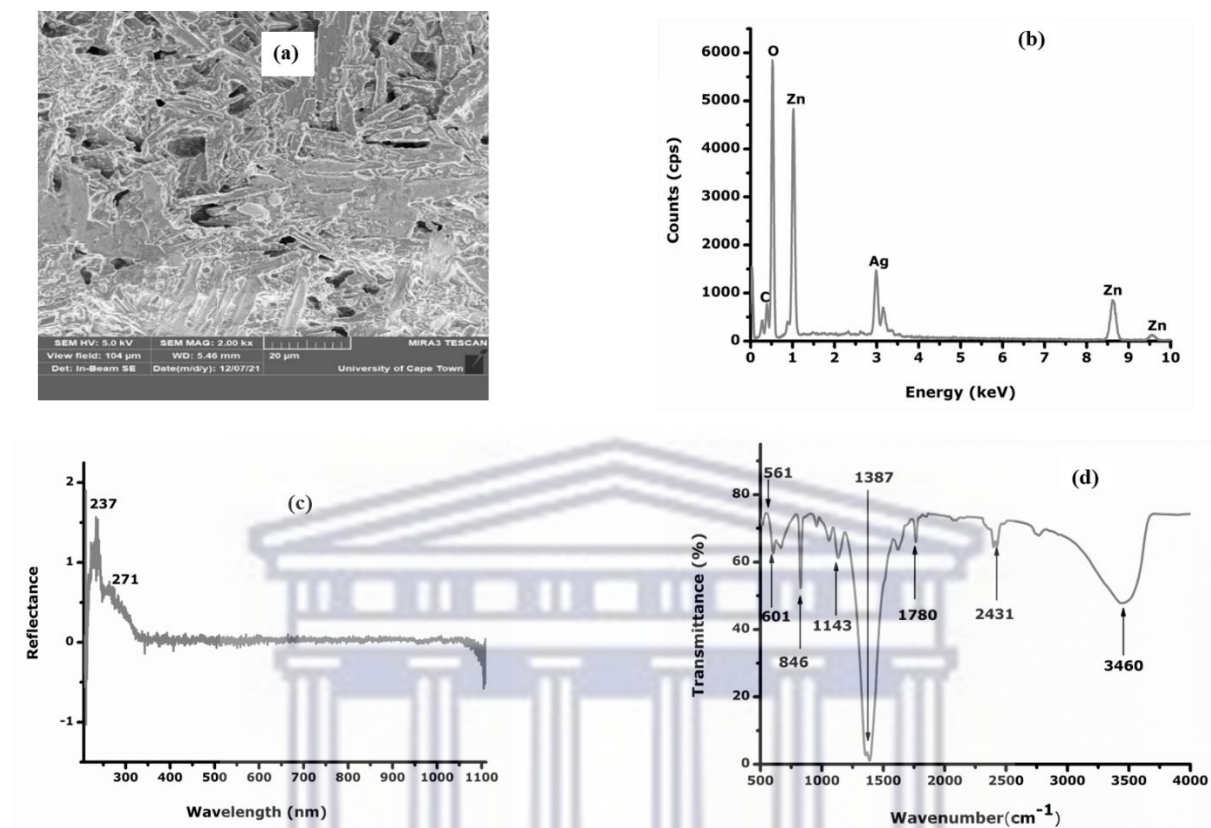
Figure S1 : (**a**) FESEM, (**b**) EDS, (**c**) UV-Visible, (**d**) ATR-FTIR of gamma irradiated Ag-Zn [1:7]